Contribution to real-time long-range erupting volcanoes monitoring based on infrasound

Tese de Doutoramento

Sandro Branquinho de Matos

Doutoramento em

Geologia

Ponta Delgada
2025

Contribution to real-time long-range erupting volcanoes monitoring based on infrasound

Tese de Doutoramento

Sandro Branquinho de Matos

Orientadores

Doutor Nicolau Maria Berquó de Aguiar Wallenstein

Doutor Maurizio Ripepe

Doutora Paola Campus

Tese de Doutoramento submetida como requisito parcial para obtenção do grau de Doutor em Geologia

Thesis submitted to the University of the Azores in fulfilment of the requirements for the degree of Doctor in Geology, specialty in Volcanology

This research was supported by FCT – Foundation for Science and Technology

Sandro Branquinho de Matos was supported by PhD Grant from Foundation for Science and Technology UI/BD/151384/2021

To Catarina and Guilherme

… always there.

TABLE OF CONTENTS

ANNEXES

APPENDICES

LIST OF FIGURES

LIST OF TABLES

LIST OF EQUATIONS

LIST OF ACRONYMS

AVO - Alasca volcano Observatory

CEA/DASE – Commissariat à l'Energie Atomique et aux energies alternatives, Departement Analyse, Surveillance, Environnement

CF - Central Facility

CMSCG - Santa Cruz da Graciosa Municipality

CTBT - Comprehensive Nuclear-Test-Ban Treaty

CTBTO - Preparatory Commission of the Comprehensive Nuclear-Test-Ban Treaty Organization

CVARG - Centre of Volcanology and Geological Risks Assessment

DA – Data Availability

DIA – Deelen Infrasound Array

DTK-GPMCC – Dase Tool Kit - Graphical Progressive Multi-Channel Correlation

ECMWF - European Centre for Medium-Range Weather Forecasts

EOI – Event of Interest

FDTD - Finite-difference time-domain

GA – Global Association

GCI - Global Communication Infrastructure

GCP - great circle path

GPS - Global Positioning System

GVP - Global Volcanism Program

ICAO - International Civil Aviation Organization

IDC - International Data Centre

IMS - International Monitoring System

IS - Infrasound Station

IVAR - Instituto de Investigação em Vulcanologia e Avaliação de Riscos

KIGAM - Korea Institute of Geoscience and Mineral Resources

LEB - Late Event Bulletin

LVDT - Linear Variable Displacement Transducer

MDR - Mass Discharge Rate

MER - Mass Eruption Rate

NOAA - National Oceanic and Atmospheric Administration

NRL- G2S - Naval Research Laboratory Ground to Space Ground-to-Space

OSI - On-Site Inspections

PDC - Pyroclastic Density Current

PDF – Probability Density Function

PE – Parabolic Equations

PMCC - Progressive Multi-Channel Correlation

PSD - Power Spectral Density

PTBT - Partial Test Ban Treaty

PTS - Provisional Technical Secretariat

REB - Reviewed Event Bulletin

SEL - Standard Event Lists

SREA - Serviço Regional de Estatística dos Açores

SSO – Single Sigh On

VAAC - Volcanic Ash Advisory Centres

VEI - Volcanic Explosivity Index

VSAT - Very Small Aperture Terminal

WNRS - Wind-Noise-Reducing System

ACKNOWLEGDMENTS

No academic endeavour is tackled alone. This doctoral thesis is the outcome of many shared moments, thoughtful mentoring and continuous positive support from a broad group of people and institutions. I am deeply grateful to all of those who made their time, knowledge or sympathy accessible throughout this path.

With sincere gratitude, I would like to express my deepest appreciation, in particular, to:

- to the Portuguese Foundation of Science and Technology (FCT) for the scholarship during my PhD studies from 2021 to 2025.

- to the University of the Azores and the Faculty of Science and Technology for the facilities granted.

- to the Geosciences Department of the University of the Azores and to the Institute of Research in Volcanology and Risk Assessment For the opportunity to pursue this doctoral degree and the resources provided to carry out this work.

- to Professor Nicolau Wallenstein, for his supervision and unwavering willingness to guide this work - from helping define the object of study to providing thorough critical revisions of the text. I am deeply grateful for his insistence on method and rigor, his insightful comments, clarifications, and suggestions, as well as his valuable advice. I also thank him for the cordiality, encouragement, and trust he has consistently shown throughout this process, and for the genuine interest and continued support he has demonstrated throughout my academic journey.

- to Professor Maurizio Ripepe and Dr Paola Campus, for their supervision and for their willingness to guide this work. I am truly grateful for their help, collaboration, and support throughout the development of this thesis. Their expertise and encouragement were fundamental at every stage of this journey, and their contributions enriched both the scientific and personal dimensions of this work.

- to Dr Emanuelle, for the generous support during my research stay at UniFi in Florence. I am especially grateful for the opportunity to learn from his expertise in data analysis, and for the clarity and precision with which he shared his knowledge. His availability and encouraging words were of great value throughout this period. I sincerely appreciate the time he dedicated to our discussions.

- to my Italian friends from the University of Florence, especially Dr. Duccio Gheri and Dr. Giacomo Belli, for their constant support, thoughtful encouragement, and sincere friendship, which helped

sustain my motivation throughout the journey of this thesis, and to all the colleagues from UniFI who shared their support and kindness throughout along the way.

- to my Lab. colleague, Linda Inês Silva, for her valuable support and assistance, particularly in helping with the preparation of important details related to this thesis. Her collaboration, sense of fellowship, and friendly support were deeply appreciated during the final stages of this work.

- to the Preparatory Commission for the Comprehensive Nuclear-Test-Ban Treaty Organization (CTBTO), for all the support provided for my participation in workshops and training programs.

- I would like to extend my sincere gratitude to Duarte Silva, my colleague and the local operator of the IS42 station, for his unwavering support in maintaining the station and ensuring its continuous and proper functioning, which was essential for securing valid data for analysis. I am especially thankful for the many hours he dedicated, the numerous trips he undertook, and the phone calls he answered at any time, always ready to assist in resolving the various technical challenges that arose throughout the process.

- to my colleagues, for the solidarity, friendship, and mutual support we shared throughout this journey. Their presence made the challenges lighter and the achievements more meaningful

- to my family, whose unwavering belief in my potential and steadfast support remained constant, even across distances and during challenging times. Their encouragement, confidence, and thoughtful presence—however near or far—were invaluable throughout this journey. To each of them, I extend my deepest respect, sincere appreciation, and heartfelt gratitude.

- to all those who, in one way or another, contributed to the success of this journey — through acts of support, words of encouragement, shared knowledge, or simple gestures of friendship — I extend my most sincere and heartfelt thanks. Every contribution, no matter how small, played a meaningful role in the completion of this work.

At the end - and above all else - my deepest gratitude goes to those who stood by my side every single day, through both the good times and the challenging ones: to my life partner, Catarina, for her love, patience, understanding, and unwavering support throughout this journey. And to my son, Guilherme, his smile, joy, and quiet strength illuminated even the most difficult moments and reminded me every day of what truly matters. This thesis is dedicated to them, with all my love, for being the true reason why this all makes sense.

ABSTRACT

According to the Smithsonian Institution's Global Volcanism Program (GVP) database, in January 2025, there were 1,281 potentially active volcanoes and tens of thousands of dormant volcanoes worldwide. It is important to realize that only a fraction of the world's active and potentially active volcanoes is monitored in real-time, and only for few of them multiparametric networks are available. For volcanoes located in remote regions, lacking local ground-based monitoring systems, remote-sensing techniques are the only available means of volcanic surveillance.

Different styles of volcanic eruptive activity represent different types of volcanic hazards, ranging from local (< few km) to regional (< few hundreds of km) scales. In a risk mitigation perspective, recent studies have demonstrated how the use of infrasound technology (remote sensing technology) can contribute to the detection, location, characterization of volcanic eruptions. Ash clouds produced by major volcanic explosive eruptions can be blown by winds and spread hundreds or thousands of kms away from the volcanic edifice, crossing national and international borders, and can represent a serious threat to aviation. Volcanic Ash Advisories Centres (VAACs) perform extensive use of satellite images and interact with volcano observatories worldwide. However, due to the resemblance of volcanic and meteorological clouds, and the satellite data access data possible delay, it is critical to find an alternative to know when a major volcanic eruption occurs as it might potentially inject ash in the atmosphere. Indeed, when a volcano erupts, it releases energy in the form of pressure waves into the atmosphere, generally with low frequency (<20Hz), below the audible range of human hearing. Large-scale volcanic eruptions have the potential to generate atmospheric pressure waves that propagate around the Earth, and the use of infrasound provides a valuable working tool for monitoring volcanic activity, both in the near- and far-field.

The objective of this work was to assess the effectiveness of the remote detection of explosive volcanic activity using infrasound monitoring. An automatic detection algorithm was applied to eruptions reported in the GVP database for the period 2011-2020, with a Volcanic Explosivity Index (VEI) ≥ 3. A total of 46 active volcanoes were selected from 11 volcanic regions, adopted by the GVP based on its geodynamic framework. The analysis was based on data from 43 infrasound stations of the International Monitoring System (IMS), operated by the Comprehensive Nuclear-Test-Ban Treaty Organization (CTBTO), in a maximum distance of 4,500 km from the selected volcanoes.

The methodology workflow followed a sequential and structured approach, from the identification of eruptions to the results validation. In the initial phase, explosive eruptions were identified, and an Event List was compiled, comprising information such as date, onset time, location, and eruption

classification for each event. At the same time, data from the infrasound stations were retrieved and processed. The resulted detections were compiled into Station Detection Lists (Bulletins), with key signal parameters such as arrival time, back-azimuth, length and amplitude.

A space-time correlation was then carried out between the Event Lists and the Station Detection Lists, with the aim of identifying detections potentially associated with the reported eruptions. This filtering step allowed us to reduce unrelated signals and highlight those most likely to be associated with volcanic activity.

To assess the detection capability and improve the association between signals and volcanic events, a specific algorithm was developed based on the Progressive Multi-Channel Correlation (PMCC) method. This algorithm was adjusted to consider the state of the atmosphere at the time of each event, by incorporating meteorological reanalysis data from the ECMWF models (ERA-Interim and ERA5) and the Ground-to-Space (G2S) empirical model for application of ray tracing techniques to simulate infrasonic signal propagation.

A set of MATLAB® scripts was created to automate the following processing steps: (1) association between infrasonic detections and volcanic events; (2) atmospheric parameters, including temperature, zonal and meridional wind components, also calculating adiabatic and effective sound speeds; and (3) generation of $V_{eff\text{-}ratio}$ maps and attenuation patterns; The resulting scripts outputs are generated in parallel and integrated in the final stage of the detection algorithm, allowing for a dynamic analysis sensitive to atmospheric conditions.

The algorithm's robustness was then assessed by a cross comparison with the bulletins produced by the International Data Centre (IDC), from CTBTO, offering an independent external reference for evaluating the workflow's effectiveness and the detections' confidence of explosive volcanic activity.

The obtained results were organized into eight detection classes, based on the source's distance from the station that registered the signal, with the aim of evaluating the performance of the monitoring network and the propagation range of the infrasonic waves. These classifications were used to discuss the effectiveness of the proposed algorithm in the detection of explosive volcanic events. The performance of the algorithm was evaluated in terms of the eruptions' duration and magnitude, volcano’s location in the different regions, and the constraints on event detection, in particular the network coverage and, above all, the atmospheric conditions, that limits the propagation.

Overall, the proposed algorithm detected successfully 50 out of the 67 recorded eruptions and 128 of the 186 associated discrete events (VEI ≥ 3), from 30 volcanoes, representing an effectiveness of 75% for eruptions and 69% for discrete events.

RESUMO

De acordo com a base de dados do *Global Volcanism Program* (GVP) da Smithsonian Institution, existem atualmente 1 281 vulcões potencialmente ativos e dezenas de milhares de vulcões dormentes no Planeta Terra. É importante destacar que apenas uma pequena parte dos vulcões ativos e potencialmente ativos do planeta é monitorizada em tempo real, e apenas uma minoria dispõe de redes multiparamétricas instaladas. Para os vulcões situados em regiões remotas que carecem de sistemas locais de monitorização, as técnicas de deteção remota são os únicos recursos viáveis para a vigilância vulcânica.

Diferentes estilos de atividade eruptiva representam distintos tipos de perigos vulcânicos, com impacto numa escala local (na ordem de alguns quilómetros), até a uma escala regional ou global (superior a vários milhares de quilómetros). Do ponto de vista da mitigação de riscos, estudos recentes demonstraram que o uso da tecnologia com base em infrassons (uma técnica de deteção remota) pode contribuir significativamente para a deteção, localização e caracterização de erupções vulcânicas. As nuvens de cinzas geradas por grandes erupções explosivas podem ser transportadas pelos ventos a centenas ou milhares de quilómetros do vulcão emissor, atravessando fronteiras nacionais e internacionais, e representando uma ameaça séria para a aviação. Os Centros de Vigilância e Alerta que monitorizam nuvens de cinzas vulcânicas, (*Volcanic Ash Advisory Centres*-VAACs) fazem uso extensivo de imagens de satélite e interagem com observatórios vulcânicos em todo o mundo; no entanto, devido à semelhança entre nuvens vulcânicas e meteorológicas, e o possível atraso aos dados de satélite, é essencial encontrar uma alternativa para se saber exatamente quando ocorre uma erupção com o potencial de injeção de cinzas na atmosfera. Com efeito, quando um vulcão entra em erupção, liberta energia sob a forma de ondas de pressão na atmosfera, geralmente em frequências muito baixas (< 20 Hz), abaixo do limiar audível para o ouvido humano. Erupções de grande escala podem gerar ondas de pressão atmosférica que se propagam à volta da Terra, sendo os infrassons uma ferramenta valiosa para a monitorização da atividade vulcânica, tanto a pequenas como a longas distâncias.

O objetivo deste trabalho foi o de avaliar a eficácia da deteção remota de atividade vulcânica explosiva através da monitorização com base em infrassons. Foi elaborado um algoritmo de deteção automática e aplicado a erupções registadas na base de dados do GVP no período de 2011 a 2020, com Índice de Explosividade Vulcânica (VEI) ≥ 3. A análise baseou-se em dados recolhidos de 43 estações de infrassons da rede do Sistema Internacional de Monitorização (*International Monitoring System* - IMS), operada pela Comissão Preparatória da Organização do Tratado de Proibição Total de Ensaios Nucleares (*Comprehensive Nuclear-Test-Ban Treaty Organization* - CTBTO), numa distância máxima de 4 500 km dos vulcões selecionados.

A metodologia seguida adotou uma abordagem sequencial e estruturada, desde a identificação das erupções até à validação dos resultados. Numa fase inicial, foram identificadas as erupções explosivas, tendo sido compilada uma Listas de eventos *Event List*, com informações como a data, hora de início, localização e classificação da erupção, para cada evento. Simultaneamente, foram adquiridos e processados dados das estações de infrassons. As deteções resultantes foram compiladas em boletins (*Station Detection Lists*), com informações sobre parâmetros-chave do sinal, tais como o tempo de chegada, azimute inverso, duração e amplitude.

Foi então efetuada uma correlação espaciotemporal entre as Listas de eventos e as Listas das deteções da Estação (*Station Detection Lists)*, com o objetivo de identificar deteções potencialmente associadas às erupções previamente identificadas. Esta etapa de filtragem permitiu reduzir falsas deteções, ruido ambiente e destacar sinais mais prováveis de estarem associados à atividade vulcânica.

Para avaliar a capacidade de deteção e melhorar esta relação entre os sinais e eventos, foi desenvolvido um algoritmo específico baseado no método de Correlação Progressiva Multi-Canal (*Progressive Multi-Channel Correlation* - PMCC). Este algoritmo foi adaptado para ter em consideração o estado da atmosfera no momento de cada evento, através da incorporação de dados de reanálise meteorológica dos modelos do ECMWF (ERA-Interim e ERA5) e do modelo empírico *Ground-to-Space* (G2S), que permite a aplicação de técnicas de traçados de raios (*ray tracing)* para simular a propagação de sinais de infrassons.

Foi elaborado um conjunto de scripts em MATLAB® para automatizar as seguintes etapas do processamento: (1) associação entre deteções de sinais de infrassons e eventos vulcânicos; (2) criação dos mapas de rácios de velocidade $V_{\_eff}$ e padrões de atenuação; e (3) parâmetros atmosféricos, incluindo a temperatura e componentes do vento zonal e meridional e calculando, ainda, as velocidades do som adiabática e efetiva. Os resultados destes scripts são gerados em simultâneo e integrados na fase final do algoritmo de deteção, permitindo uma análise dinâmica e sensível às condições atmosféricas.

A robustez do algoritmo foi posteriormente avaliada por meio de uma comparação cruzada com os boletins de eventos produzidos pelo *Internacional Data Centre* (IDC), da CTBTO, proporcionando uma referência externa independente para avaliação da eficácia do fluxo de trabalho e o grau de confiança das deteções relativas à atividade vulcânica explosiva.

Os resultados obtidos foram organizados em oito classes de deteção, com base na distância entre o vulcão e as estações que registaram o sinal, com o objetivo de avaliar o desempenho da rede de monitorização e o alcance da propagação das ondas infrassónicas. Estas classificações serviram de base para a avaliar a eficácia do algoritmo proposto na deteção de eventos vulcânicos explosivos, em função da duração e magnitude das erupções, da localização dos vulcões nas diferentes regiões e das

limitações à deteção dos eventos, em particular a cobertura da rede e, sobretudo, as condições atmosféricas que condicionam a propagação eficaz.

De forma geral, o algoritmo proposto detetou, com sucesso, 50 das 67 erupções registadas, e 128 dos 186 eventos discretos associados (VEI ≥ 3), de 30 vulcões, representando uma eficácia de 75% para as erupções e 69% para os eventos discretos.

PREAMBLE

I. Motivation

Volcanoes, through their impressive explosive activity, disrupt the atmosphere and generate low-frequency acoustic waves, imperceptible to the human ear, known as infrasound. These waves can be propagated over long distances through atmospheric waveguides and registered at remote monitoring stations. From Hawaiian to Plinian eruption styles, infrasound has proven to be an effective tool in the detection and the monitoring of volcanic activity, especially in regions without a dedicated monitoring network.

This thesis was motivated by the need to enhance global detection of volcanic eruptions using infrasound data from the International Monitoring System (IMS). Taking advantage of this infrasound infrastructure network for Earth Science applications provides new opportunities and challenges, mainly in terms of signal detection, network coverage and atmosphere propagation variability to enhance volcanic monitoring capabilities at regional and global scales.

II. Research objectives

The main objective of this research is to develop and validate an automatic detection algorithm capable of identifying infrasound signals associated with volcanic eruptions, using data from the IMS network and tested on volcanoes with eruptive activity reported on GVP, between 2011 and 2020, for events with VEI 3 or higher.

III. Research goals

The primary objective of this thesis is to assess the feasibility and effectiveness of long-range infrasound-based detection algorithm. Specifically, the research aims to:

- Develop a global database of explosive volcanic events that occurred between 2011 and 2020.
- Propose methodological improvements for near real-time infrasound-based monitoring.
- Contribute to the advancement of volcanic hazard mitigation strategies and the broader scientific understanding of explosive volcanism.

The dissertation is structured into six chapters:

Chapter 1 – **Global volcanism and volcano infrasound**: Introduces fundamental concepts of how infrasound signal associated with explosive volcanic activity are generated, providing the geophysical context for this research.

Chapter 2 –**Infrasound monitoring of volcanic eruptions**: Presents an overview of the International Monitoring System (IMS) infrasound network and describes how the IS42 array data is effectively processed. It also discusses local, regional, and global infrasound detection characteristics, including recent advances in long-range infrasound monitoring.

Chapter 3 – **Infrasound Propagation**: Explores the physical properties of infrasound and its propagation through atmosphere, establishing the theoretical bases necessary for interpreting detection results.

Chapter 4 – **Data and methods**: Details the methodology developed to identify coherent infrasound detections associated with explosive volcanic eruptions, together with the validation employed to ensure reliability

Chapter 5 – Results: Provides a comprehensive overview of the results, evaluates the algorithm's performance, and compares the outcomes with the events listed in IDC bulletins.

Chapter 6 – Discussion and conclusions: Interprets the results within the context of global volcano monitoring, highlighting the algorithm's ability to detect volcanic events of VEI ≥ 3. The chapter conclude with remarks on the general relevance of the outcomes and the potential applications in operational monitoring systems using infrasound.

Note: While the annexes included were produced by the author, they have been designated as “annexes” in this volume for practical purposes of organization.

CHAPTER 1 |

Global volcanism and volcano infrasound

At the time of writing, there are at least 20 volcanic eruptions occurring somewhere on planet Earth.

There are more than 1,200 potentially active volcanoes worldwide (1,281 volcanoes according to the Smithsonian Institution Global Volcanism Program (GVP) database VOTW4.22), and tens of thousands of dormant volcanoes, mainly distributed in the four major linear volcanic belts along tectonic plates boundaries: the Circum-Pacific Volcanic Belt, the Mid-Oceanic Ridge Volcanic Belt, the Mediterranean-Himalayan Volcanic Belt, and the East African Rift Valley Volcanic Belt.

Volcanic eruptions take many forms, from effusive events (*e.g.*, fluid lava flows or lava domes) to violent explosive eruptions that produce rapidly eruptive columns, expanding volcanic clouds and pyroclastic density currents. These different styles of volcanic eruptive activity represent different types of volcanic hazards, ranging from local (< few km) to regional (< few hundreds of km) scales. Ash clouds produced by major volcanic explosive eruptions can be blown by winds and spread hundreds of kms away from the volcanic edifice, crossing national and international borders, and can represent a serious threat to aviation. This led the International Civil Aviation Organization (ICAO) to establish 9 Volcanic Ash Advisory Centres (VAAC) that have the duty to identify volcanic clouds and to issue related hazard alerts to the aviation. VAACs

perform extensive use of satellite images and interact with volcano observatories worldwide (Evans 1994). However, due to the resemblance of volcanic and meteorological clouds, it is critical to know when a major volcanic eruption occurs as it might potentially inject ash in the atmosphere.

Despite considerable progresses in building real-time and multiparametric monitoring networks have been achieved over the past decades, it is important to realize that only a fraction of the world's active and potentially active volcanoes is monitored in real-time, and only for few of the networks are available (Pallister and McNutt, 2015). Many active volcanoes, especially the ones located in remote regions, lack local conventional, ground-based monitoring systems. Here, remote-sensing techniques provide the only practical means of volcanic surveillance.

In the past 30 years infrasound technology was boosted by the opening for signature of the Comprehensive Nuclear-Test-Ban Treaty (CTBT) in November 1996. Although not supported by the treaty, parallel scientific work study volcanoes as sources of severe atmospheric events with explosion yields compatible with nuclear explosions, to perform infrasound propagation studies and network coverage. This led to its increasing contribution to monitoring volcanoes, complementing other geophysical (seismic, geodetic) and fluid geochemistry tools (gas, water), enhancing the characterization and understanding of volcanic physical processes (Johnson 2019, Matoza *et al.* 2019). Nowadays, infrasound is getting more and more common in permanent volcano surveillance (see Chapter 2).

One component of the CTBT comprehensive verification regime is the International Monitoring System (IMS), which currently consists of 337 monitoring facilities encompassing four verification technologies (seismic, hydroacoustic, infrasound and radionuclides), to monitor the planet for signs of nuclear explosions underground, in the atmosphere and oceans. As of January 2024, the IMS Infrasound network consists of 53 certified stations (see Chapter 2, Section 2.1). Other pillar of the verification regime is the International Data Centre (IDC) at the Comprehensive Nuclear-Test-Ban Treaty Organization (CTBTO) headquarters in Vienna, which receives data from the global monitoring stations. The data are processed and distributed to the CTBTO's Member States in both raw and analysed form. Automatically detected events are distributed in the form of IDC bulletins called Standard Event Lists (SELs). Review processes by IDC analysts are then carried out, resulting in the Late Event Bulletin (LEB) and, after applying event definition criteria, the final waveform product, the Reviewed Event Bulletin (REB).

1.1 Global volcanism and related hazard

According to their level of activity, volcanoes can be classified as active (currently erupting), dormant (not currently erupting, but could erupt in the future), and extinct (no eruptions in the last 10 thousand years). Worldwide, around 80% of the active volcanoes are concentrated in the circum-Pacific region and countries such as Indonesia, Japan and the Philippines (at the south-western edge of the Pacific Plate). Volcanoes can be found on land and on the ocean seafloor (*i.e.*, seamount volcanoes). Most of the land or island volcanoes on Earth are on volcanic arcs (*e.g.,* the Circum-Pacific Volcanic Belt, the Mid-Oceanic Ridge Volcanic Belt, the Mediterranean-Himalayan Volcanic Belt, and the East African Rift Valley Volcanic Belt) above subduction zones (Figure 1.1). Even if they only represent approximately 10 to 20% of all volcanoes on Earth, these subaerial volcanoes interact directly with the atmosphere (*e.g.,* by releasing gases), so their eruptions can affect the surrounding areas, most of which are densely populated and considered high-risk regions.

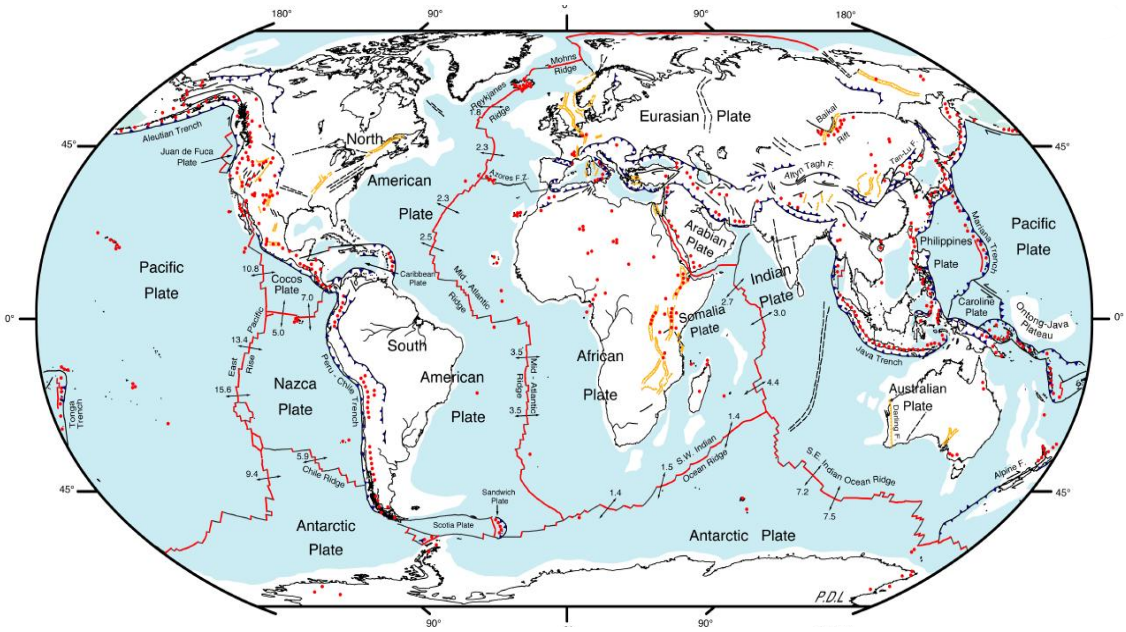

Figure 1.1. Map showing the distribution of the world's known volcanoes (red dots), tectonic plates, and active ridges and faults. Image adapted from Paul D. Lowman Jr., NASA GSFC illustration. Van der Grinten projection.

Eruptive activity can be categorized according to its magnitude. Tsuya (1955) proposed a scale based on the logarithm of the pyroclastic ejecta volume, which categorised eruptions into different magnitude classes (I-IX). A new revised scale was proposed by Newhall and Self (1982), referred to as the Volcanic Explosivity Index (VEI) (Table 1.1). The VEI uses an integer scale from 0 to 8 to widely describe the volume erupted (magnitude) and the eruption plume height

(intensity). This scale is now widely used, since it was adopted by GVP for use in its catalogues of volcanic eruptions over the last 10,000 years (Siebert et al. 2010).

Traditionally, eruptive activity has been broadly assigned to eruption styles, whose differences are mainly a function of magma composition and temperature, magma volatile content and crystallinity, exsolution and degassing processes, magma feeding and discharge rates, conduit geometry and mechanical strength, magma reservoir pressure and the presence of external water (Bonadonna *et al.* 2016). All these aspects are somehow reflected in eruption explosivity and the height of the eruptive column and affect the fragmentation index and dispersal area of their deposits. Based on the fragmentation index and dispersal area, eruptive styles were differentiated into Hawaiian, Strombolian, Vulcanian, Sub-Plinian, Plinian and Ultra-Plinian (Walker 1973, 1980, Bonadonna *et al.* 2016).

Table 1.1. Categories of the Volcanic Explosivity Index (*Adapted from Newhall and Self 1982, Mason *et al.* 2004, Siebert *et al.* 2010, and Brown *et al.* 2014).

Index	0	1	2	3	4	5	6	7	8
Bulk tephra volume (m^3)	$<10^4$	$<10^6$	$<10^7$	$<10^8$	$<10^9$	$<10^{10}$	$<10^{11}$	$<10^{12}$	$>10^{12}$
Eruption plume column height (km)	<0.1	0.1- 1	1-5	3-5	10-25	>25			
Qualitative description	Gentle	Effusive	Explosive		Cataclysmic, Paroxysmal				
Stratospheric injection	None	None	None	Possible	Certain				
Percentage of known eruptions in the past 10,000 years	13	16	49	14	5	2	<1	<0.1	0
Typical recurrence interval	Days to Weeks			0.3 years	3 years	20 years	80 years	500 years	$7 * 10^5$ years

As the world's population has grown, so has the number of people living near active volcanoes. Studies show that approximately 58 million people live within 10 km of ≈1,281 Holocene volcanoes (or volcanic field sources), more than 300 million live within 30 km, and more than 14.3% of the world's 8.11 billion people live within 100 km of an active volcano (Freire *et al*. 2019). Although not very frequent, moderate to large eruptions are events with the potential for high consequences, both immediately for neighbouring populations, due to the various phenomena associated (*e.g.,* pyroclastic flows, lava flows, ash deposition, *etc.*), and for those who are living or travelling hundreds of kilometres away. The eruption of the Eyjafjallajökull volcano in Iceland in 2010 demonstrated that even modest eruptions in relatively remote locations can have global impacts on the economy and society (Freire *et al.* 2019).

1.2 Volcano Infrasound

Throughout the 20th century several articles were published referring to pressure waves studies, either of low frequencies (<1 Hz), using meteorological barometers and arrays of infrasound microphones (Fee and Matoza 2013), or, since the 1980s, of higher frequencies (1-20 Hz) caused by volcanic explosions on a regional and global scale (Johnson and Ripepe 2011). Examples of such studies are: Mount Pelé, Martinique, 1902 (Anderson and Flett 1903); Bezymianny, Russia, 1956 (Gorshkov 1959); Mount Agung, Bali Island, 1963 (Goerke *et al.* 1965); Mount St. Helens, USA, 1980 (Reed 1987); Sakurajima, Japan, 1982 (Tahira 1982); El Chichon, Mexico, 1983 (Mauk 1983); Mount Tokachi, Japan, 1988 (Iguchi and Ishihara 1990); Mount Pinatubo, Philippines, 1991 (Tahira *et al.* 1996); Stromboli, Italy, 1991 (Braun and Ripepe 1993); Erebus, Antarctica, 1994-1998, (Rowe *et al.* 2000); Arenal, Costa Rica, 1997 (Garcés *et al.* 1998); Karymsky, Kamchatka, Russia, 1997 (Johnson *et al.* 1998); Etna, Italy, 1998 (Ripepe *et al.* 2001*b*); Shishaldin, Aleutian Islands, 1999, (Caplan-Auerbach and McNutt 2003); Tungurahua, Ecuador, 2004 (Ruiz *et al.* 2006); Fuego, Guatemala 2005-2007 (Lyons *et al.* 2010) and many other volcanoes.

While the early studies focused on the audible band of the sound spectrum in volcanic recordings (Richards 1963, Woulff and McGetchin 1976), studies carried out in the 1990s showed that the most intense sounds produced by volcanoes with frequent eruptions or in constant activity are in the near infrasound band, becoming the main focus of volcano infrasound research and leading to a growing body of vast literature in the last decade of the 20th century (Johnson and Ripepe 2011, Watson *et al*. 2022).

Large-scale volcanic eruptions have the potential to generate atmospheric pressure waves that propagate around the Earth (Dabrowa *et al.* 2011), such as reported examples of the Krakatau volcano eruption in 1883 (Yokoyama 1981), the Bezymianny volcano in 1956 (Murayama 1968), Mount Saint Helens in 1980 (Bolt and Tanimoto 1981; Donn and Balachandran 1981), or the 15 January 2022 Hunga Tonga-Hunga Ha'apai (Vergoz *et al*. 2022) volcano's explosive eruption.

The earliest observations of acoustic waves produced by volcanic eruptions were recorded with analogue microbarometers with the capability to measure frequencies lower than 1 Hz and with temporal resolution from seconds to tens of seconds (Johnson and Ripepe 2011).

In the audible range of acoustic signals (> 20 Hz), the first acoustic signals originating from volcanic systems were probably recorded by Frank Perret using microphones with mobile coils in Teide Volcano, Canary Islands, Spain (1909); Campi Flegrei, Etna, Stromboli, and Vesuvius Volcanoes, Italy (1906-1921); Sakurajima Volcano, Japan (1914); Kilauea, Hawaii (1912); and Pelé, Martinique (1929) (Perret 1950).

On August 26th, 1883, the Krakatau volcano paroxysmal eruption (South-East of Sumatra Island, Indonesia) was the origin of the first remote detection of a volcanic eruption through

atmospheric disturbances. The low-frequency pressure signals were recorded on barometers around the world (Symons 1888). The eruption was so energetic (later classified as VEI 6) that it produced waves that circled the Earth seven times, being waves recorded with a peak pressure of 883 Pa at 160 km distance (Symons 1888), and audible sounds reached distances up to 5,000 km (Simkin and Fisk 1983).

In 1912, Fusakichi Omori, using barometers and seismometers, conducted a pioneering study on Mount Asama in order to distinguish airborne explosions from earthquake signals, elaborating a map of acoustic wave propagation and shadow zones (Omori 1912, Fee and Matoza 2013).

In 1959, Gorshkov used pressure records at local and regional distances (> 250 km) to estimate the explosive yield of the Bezymianny eruption of 1959. In the late 1960s, a network of seven microphones was installed in Antarctica in order to monitor atmospheric infrasonic waves between 0.01 Hz and 0.1 Hz. Multiple acoustic channels in the eruption of the Redoubt volcano (Alaska) among other events were identified. This network was also used to identify and locate the eruptive activity of Trident volcano (Wilson 1967, 1971).

The May 18th 1980, Mount St. Helens VEI 5 eruption produced high-intensity, both audible and low-frequency, atmosphere-to-ground coupled airwaves recorded around the world (Don and Balachandran 1981; Johnson and Malone 2007), with associated ≈375 Pa infrasound recorded 54 km away from the vent as well audible sound heard as far as 80 km from the source (Reed 1987; Fairfield 1980). Also, the El Chichón VEI 5 eruption in 1982 was recorded on microbarometers from the United States of America (USA), and the eruption parameters were calculated based on long-period waves (Mauk 1983).

A deployment of an array of microphones near Sakurajima volcano (≈700 km distant), in Japan, allowed for the detection of recurrent explosions, as well as the VEI 6 eruption of the Mount Pinatubo Volcano in the Philippines in 1991. The high-frequency infrasound signals from this event were recorded close to 2770 km away from the source (Tahira 1982, 1988; Tahira *et al.* 1996).

It was shown that using infrasound to gather data from large volcanic eruptions was possible, even at long distances from the source. Also, as in the case of the Mount Pinatubo eruption, long-distance detections proved to be able to provide information on the eruptive history of the explosive sequence when visual and other instrumental observations close to the volcano were not possible due to the severe conditions (Tahira *et al.* 1996).

1.2.1 The sound wave

A sound wave is a longitudinal mechanical wave produced by the vibration of particles travelling in the

same direction of propagation in solid, liquid and gaseous media, whose speed of propagation depends on the characteristics of the medium in which it propagates. These types of waves induce compression and rarefaction in a medium and are seen as pressure variations in relation to their equilibrium. A restoring force proportional to the pressure disturbance restores the medium to its initial state, which is why they are also known as pressure waves (Hansen 2001). As a sound wave, infrasound is a low-pressure elastic wave in the acoustic spectrum of frequencies lower than the acoustic threshold of human hearing (16-20 Hz) and above the Brunt-Väisälä lower acoustic limit cut-off frequency (3-10 mHz). The temperature-dependent acoustic cut-off frequency (NA) marks the lower limit (Figure 1.2) - approximately 3.3 mHz at 20°C. This intermediate frequency range (below NA and up to the Brunt-Väisälä frequency (NB)) varies with altitude and is known as the acoustic gravity waves, where the restoring forces are both buoyancy and pressure (Gossard and Hooke 1975).

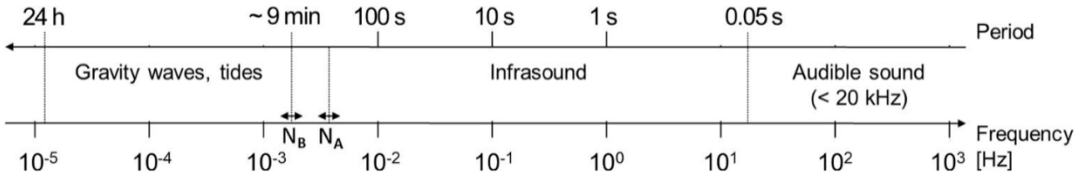

Figure 1.2. Frequency and period range of infrasound and gravity waves. N_A is the acoustic cut-off frequency and N_B is the Brunt-Väisälä frequency (Hupe 2018).

Acoustic waves occur in the atmosphere when a periodic vibration causes alternating adiabatic compression and expansion of air and are defined (among other characteristics) by their frequency, period, amplitude and speed of propagation. Acoustic waves travel at the speed of sound, 343 m/s at 20°C in air, increasing with temperature and with a favourable wind field (downwind) due to advection and vice versa. This velocity depends on the medium and on the state of the medium. Velocities higher than the speed of sound generate shock waves, generally recorded near the source and produced by energetic events, which propagate as nonlinear waves and, as the shock energy dissipates, become acoustic linear waves (Needham 2010). On the other extreme, low-frequency waves in the atmosphere, known as gravity waves, have velocities lower than the speed of sound with wind speed velocities of around 1-10 m/s (Evers and Haak 2010).

The state of the atmosphere strongly dictates infrasound propagation (see Chapter 3), controlled mainly by a) the attenuation due to the absorbing properties of the atmosphere, b) the refraction heights driven by sound-speed gradients, c) reflections by the ground terrain, d) scattering by atmospheric turbulence, and e) the azimuthal deviation due to winds (de Groot-Hedlin 2008), *i.e.*, it loses energy through absorption and geometric spreading, is deflected by the wind, and is refracted according to its velocity profile.

Different studies have consistently demonstrated a correlation between the pressure waves, frequency and magnitude and the characteristics of the source that generates them.

Only nuclear explosions (*e.g.,* Donn and Shaw 1967), large volcanic eruptions (*e.g.,* Kanamori *et al.* 1994, Ripepe *et al.* 2010a), or large meteoroids (*e.g.,* de Groot-Hedlin and Hedlin 2014) can displace a greater volume of air and generate acoustic-gravitational waves.

In addition, a wide variety of natural and anthropogenic sources generate oscillatory processes that interact directly with the atmosphere with the capability of producing infrasound signals (Campus 2004). Natural sources of infrasound include **auroras** (*e.g.,* Wilson 1971, Pasko 2012, Chrzanowski *et al.* 1961, Procunier 1971, Wilson and Olson 2005, Liszka 2008, Campus 2004), **avalanches,** (*e.g.,* Bedard 1989, Ancey 2001, Scott *et al*. 2007, Marchetti 2019); **calving of icebergs and glaciers,** (*e.g.,* Campus 2004, 2010, Richardson *et al.* 2010); **convective storms,** (*e.g.,* Goerke and Woodward 1966, Georges 1973, Assink *et al.* 2008, Mialle 2007); **coastal surf** (*e.g.,* Garcés *et al.* 2003, 2006, Le Pichon *et al* 2004, Arrowsmith and Hedlin 2005); **earthquakes (***e.g.,* Grover and Marshall 1968, Cook 1971, Young and Greene 1982, Olson *et al.* 2003, Le Pichon *et al.* 2003, 2006, Campus 2004, Mutschlecner and Whitaker 2005); **explosive volcanoes** (*e.g.,* Dibble 1989, Braun and Ripepe 1993, Vergniolle and Brandeis 1994, Buckingham and Garcés 1996, Johnson *et al.* 1998, Ripepe *et al.* 2007, Dabrowa *et al.* 2011, Fee and Matoza 2013, Matoza *et al.* 2019, Marchetti *et al.* 2019, among others); **icequakes; landslides** (Fu *et al.* 2020); **debris flow/Avalanches** (Kogelnig *et al.* 2014, Shimmel *et al.* 2018, Marchetti *et al.* 2019); **lahar (**Marcial *et al.* 1996, Johnson *et al.* 2023)**; lightning** (*e.g.,* Dessler 1973, Balachandran 1982, Few 1985, Campus 2004, Assink *et al.* 2008, Liszka 2008, Farges and Blanc 2010); **meteors** (*e.g.,* ReVelle 1976, Chimonas 1977, Ceplecha 1998, Evers and Haak 2010, Brown *et al.* 2002, Campus 2004, Edwards *et al.* 2006, Arrowsmith *et al.* 2008, Le Pichon *et al*. 2013, Silber *et al*. 2015, Pilger *et al.* 2020); **microbaroms** (*e.g.,* Benioff and Gutenberg 1939, Posmentier 1967, Arendt and Fritts 2000, Landès *et al.* 2014, De Carlo *et al.* 2021); **mountain air waves** (Chimonas 1977, Campus and Christie 2010, Larson *et al.* 1971); **sprites** (Liszka 2004, Farges *et al.* 2005); **tornadoes** (*e.g.,* Bedard 1998, Bedard *et al.* 2004); **tsunamis** (Le Pichon *et al*. 2005b); or **waterfalls** (Bedard 1988).

Examples of man-made infrasonic sources include **chemical explosions** (*e.g.,* Evers *et al.* 2007, Lizka 1995); l**ocal mines** (*e.g.,* Wallenstein and Campus 2017); **nuclear explosions** (CTBTO 2009); **rockets launching and space shuttle re-entry** (*e.g.,* Balachandran and Donn 1971, Posmentier 1971); **subsonic aircraft** (*e.g.,* Balachandran *et al.* 1977, Donn and Rind 1979, Le Pichon *et al.* 2002, Gainville *et al.* 2007, Liszka 2008). Industrial equipment such as wind turbines, diesel engines, compressors, boilers, forms of transport (*e.g.,* aeroplanes, helicopters, ships, trains, and trucks), and other cultural sources are also sources that may generate infrasound (Bass *et al.* 2003, Campus and Christie 2010).

1.2.2 Infrasound signals from eruptive volcanoes

From the works listed above, it can be stated that the frequency band between 0.1 and 20 Hz is very diversified regarding the acoustic signals associated with different types of volcanic processes. Following the classification of seismo-volcanic signals, infrasound signals can be classified into three main categories in volcanic areas: (1) infrasound tremor, (2) discrete transient explosions, and (3) sustained volcanic explosions (jet noise). A fourth category of infrasound signal can be related to surface mass movements at volcanoes.

1.2.2.1 Infrasound tremor

Infrasound tremor is a common and variable volcanic acoustic signal defined as a continuous vibration of the atmosphere that can last from tens of seconds to months (Fee and Matoza 2013). There are several types of tremors, generally characterised by their time domain and frequency characteristics (Konstantinou and Schlindwein 2002). These include **volcanic, harmonic,** or **"chugging"** (frequency spectrum with a spectral peak and harmonic movements associated), **gliding** (smooth and continuous variation in the frequency of the infrasound signal, reflecting changes in the behaviour of the eruption), **monochromatic** or **monotonic** (containing only one spectral peak over a narrow frequency band), **broadband** (wide frequency range without continuous strong spectral peaks with amplitude variation or spaced in time), **banded** (characterised by the occurrence of blasts separated in time by periods of inactivity), **spasmodic** (a continuous tremor with great amplitude variation), or a **tremor storm**, a short-lived tremor that overlaps seismic activity background. Due to the limited amplitude of infrasound tremor, generally below a few Pa at local distances (less than hundreds of meters), the maximum range of observation of the eruption tremor generally ranges from a few tens to a few hundreds of meters (Fee and Matoza 2013).

1.2.2.2 Discrete transient explosions

Some eruptions are described as transient explosions resulting in fast, large-scale expansion (compression) of the atmosphere, followed by rarefaction (decompression), with a short coda lasting on the order of seconds to minutes (Morrissey and Chouet 1997, Fee and Matoza 2013). The results of this sudden release of pressure generate a shockwave with N-shapes, a very common feature of this kind of explosive eruption (Fee *et al.* 2010a, Johnson and Ripepe 2011). This kind of explosive event is typically associated with volcanian and strombolian eruptions but can occur during almost any style of volcanic activity.

Volcanic eruptions (especially explosive ones) are dynamic phenomena whose behaviour varies continuously, changing throughout the course of the eruption, sometimes making it very difficult to classify

them in terms of style. Despite exhibiting a range of styles within a single explosive episode, they can be categorised according to the main styles they exhibit. Different volcanic signals identified during an eruptive event reflect these shifts in eruptive dynamics.

Hawaiian

Hawaiian-style eruptions are low-viscosity basaltic magma events, often with effusive phases but occasionally with explosive phases or degassing bursts, and are often characterised by fissural eruptions or lava fountains (Taddeucci *et al.* 2015).

Infrasound during effusive phases has tremor-like characteristics, ranging from harmonic to broadband spectra, while infrasound produced during explosive phases can have complex signatures (Figure 1.3). Lava fountains can produce sustained and broadband infrasound signals in which the frequency content, amplitude, and duration vary with the distance from the source and the intensity of the eruption (Fee and Matoza 2013, Marchetti *et al.* 2019).

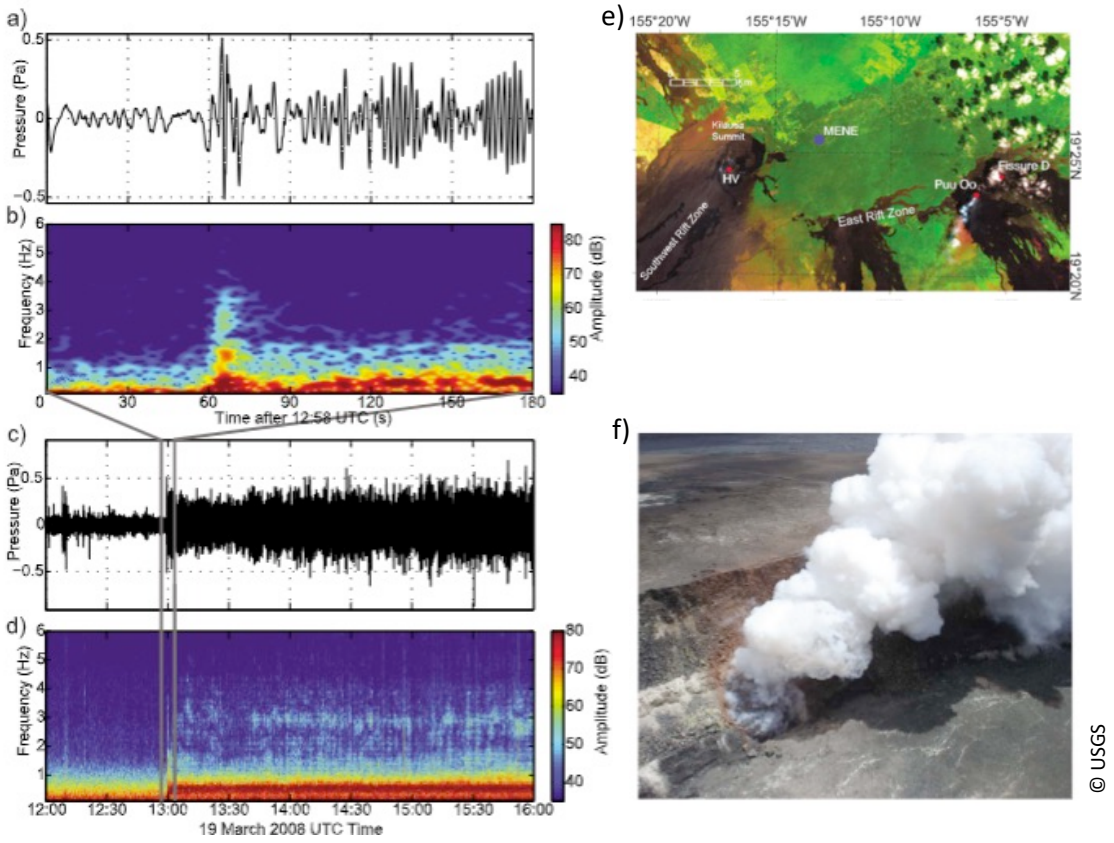

Figure 1.3. 19th March 2008 degassing burst waveforms and spectrograms from Halema'uma'u Crater, Kilauea Volcano, recorded by MENE infrasound array: **(a)** beamed waveform (0.1–10 Hz); **(b)** beamed spectrogram (0.1–6 Hz); **(c and d)** beamed waveform and spectrogram of the start of the explosion at 1259:00 UTC, which is broadband, followed by a tremor over the next 4 hours; **e)** Area overview map and: blue dot denotes the MENE infrasound array (≈7 km NE of Halema'uma'u) red dots refer to Pu'u 'O'o, Fissure D and two other infrasound sources and **f)** Halema'uma'u on 1st August 2008 (from Fee *et al.* 2010a).

Strombolian

These eruptions are characterised by distinctive explosions of basaltic to andesitic magma, in which the ascent of a gas slug in a relatively open system results in an explosive release of gas and incandescent magma fragments. Small tephra cones (ash cones) can form, and sometimes lava flows erupt from low openings on the flanks of small cones. Strombolian eruptions are recurrent, short-lived explosions of variable frequency and intensity, considered to be moderately explosive, producing low-altitude eruptive columns and pyroclastic fallout deposits (Taddeucci *et al.* 2015).

Strombolian explosions produce impulsive, short-lived infrasound signals associated with gas overpressure and the volume of gas released (*e.g.*, Chouet 1974). Acoustic source mechanisms can be related to explosions from the bursting of a gas slug at the surface (due to overpressure; otherwise, “puffing” events occur), followed by low, short-lived amplitude jetting or degassing through sealed caps (Figure 1.4) (Fee and Matoza 2013).

Infrasound waveforms from Strombolian explosions are characterised by initial sharp compressional onsets, followed by a slightly longer duration rarefaction and coda of a few to tens of seconds (*e.g.,* Firstov and Kravchenko 1996, Ripepe *et al.* 1996, Johnson 2003, Ripepe and Marchetti 2002b, Ripepe *et al.* 2007, Johnson *et al.* 2008, Jones *et al.* 2008). These short-lived bipolar pulses are often shaped like N waves, which resemble a chemical explosion shock wave after it has been turned into an acoustic wave (Johnson and Ripepe 2011).

As examples, explosions (both lower and high amplitude signals) at Stromboli, Italy, are understood to result from the coalescence of bubbles in the conduit in a foam at depth and the consequent rise of this gas as a slug flow and the subsequent bursting at the magma surface (Harris and Ripepe 2007). If a bubble ascends in the magma column and moves through a zone with a much lower density, the bubble will expand rapidly and violently, exceed its equilibrium radius, and collapse, starting a new explosion/contraction cycle. This pressure disturbance (explosion) is then transmitted to the ground as a seismic wave and, in the presence of an open vent system, to the atmosphere as acoustic waves (Buckingham and Garces 1996).

The Karymsky volcano, in Russia, exhibits signal variations from its explosions and degassing throughout the sealed summit, including episodes consisting of a series of discrete pulses (intermittent or continuous) that are like harmonic tremors, called "chugging" (Johnson and Lees 2000, Lees *et al.* 2004). Infrasonic tremor is common in Strombolian systems (*e.g.,* Garces *et al.* 1998) and may be due to gas release at the lava/air interface (Ripepe *et al.* 1996).

Studies of infrasound recordings on volcanoes such as Stromboli (*e.g.,* Lacanna and Ripepe 2013), Yasur (*e.g.,* Marchetti *et al.* 2013), and Erebus (*e.g.,* Johnson *et al.* 2008) exhibit classic Strombolian explosion behaviour that has remained relatively unchanged for years.

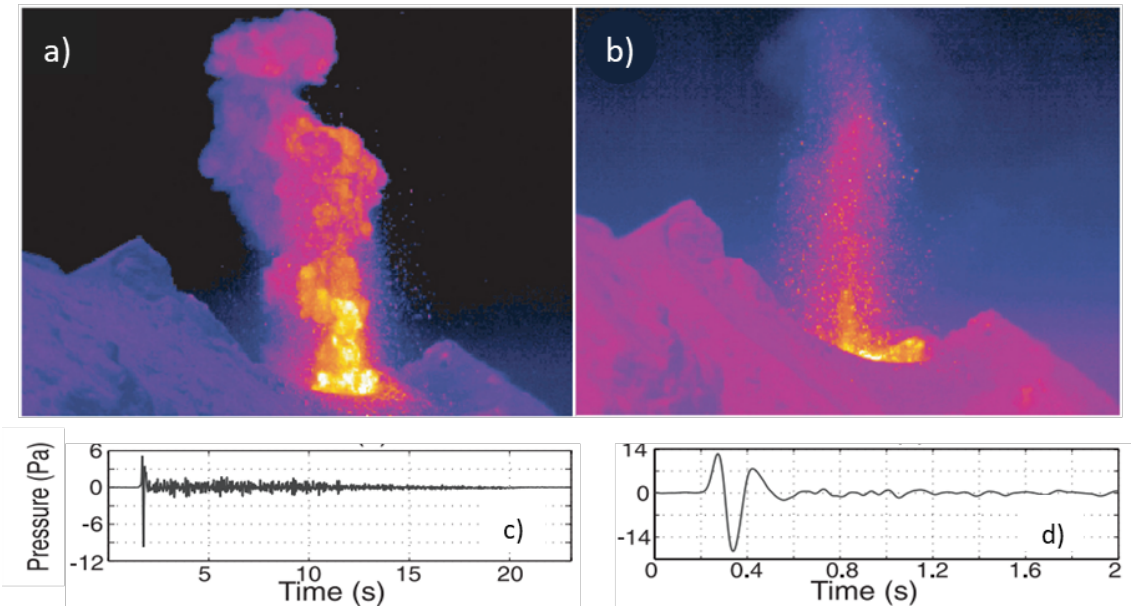

Figure 1.4. Examples of Stromboli thermal images showing **(a)** fragment-rich explosions at the NE crater and **(b)** ash-rich explosions at the SW crater. Acoustic signals produced by the explosions are shorter and more energetic **(c)** at the NE crater than **(d)** at the SW crater, where the longer duration of the acoustic signal indicates a longer mass discharge process (from Ripepe *et al*. 2008).

Vulcanian

Vulcanian eruptions occur because of the abrupt decompression of a volcanic vent containing highly pressurised, crystallised, and bubbling magma of intermediate composition (Clarke *et al.* 2015). They usually begin when a cohesive magma cap or dome sealing the conduit is suddenly disrupted due to a high enough pressure in the underlying magma (up to 10e15 MPa, but usually <5 MPa, based on the strength of typical magmas). This disruption produces a decompression wave, followed by a fragmentation front that propagates through the conduit, while a compression shock propagates into the atmosphere (Clarke *et al.* 2015). This means that the vesicular magma is fragmented into a mixture of gas and pyroclasts, driven upwards, and projected from the vent into the atmosphere as an impulsive and unstable outburst jet at sonic to supersonic speeds. The transition to the subsonic regime can occur quite rapidly above the vent, so the jet can evolve into a buoyant plume (typical “mushroom” shape), collapse gravitationally to form pyroclastic density currents (PDC), or both can occur simultaneously. Vulcanian activity differs from Plinian activity in duration and from Strombolian activity in dynamics. In most Vulcanian explosions, in impulsive ejections that last for seconds to minutes, a significant portion of the ejected material rises in a plume, typically between 1 and 15 km in height, with material falling out from this (Bonadonna *et al.* 2002).

Acoustic signals from Vulcanian eruptions typically consist of short-duration, high-amplitude impulsive blast waves (compression and subsequent rarefaction), often followed by a longer-duration coda with harmonic spectra (gliding) up to tens of minutes.

Major Vulcanian eruptions can also generate non-linear shock waves characterised by N-shaped compression and rarefaction (Morrissey and Chouet 1997) with a very rapid compressional rise time (characteristic of supersonic propagation), compared to the slower impulsive compressional rise times of typical and Strombolian and Vulcanian infrasound signals. Figure 1.5 illustrates an example of an infrasound signal from the large volcanic explosion at the Augustine volcano in Alaska. The impulsive, high-amplitude onset represents significant overpressure and an outburst at the source, while the long-lived coda probably represents jetting or tremor.

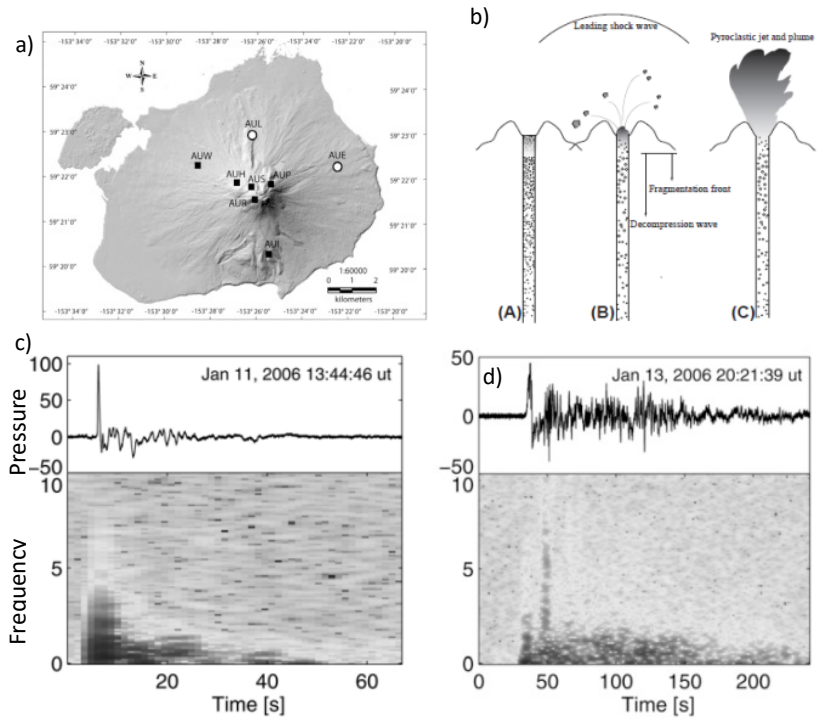

Figure 1.5. Map of Augustine Volcano showing the permanent AVO (Alasca volcano Observatory) monitoring network stations (white circles); b) Vulcanian explosion mechanism, as explained by Clarke *et al.* (2015); (c and d) Acoustic signals associated with the Augustine January 2006 explosive eruptions recorded at AUE station. Acoustic pressure in Pa (top) and spectrogram (bottom) of the impulsive pressure signal recorded at AUE in January 2006 (acoustic onsets: 11-Jan-06 13:44:55 UT, Petersen *et al.* 2006).

Infrasound signals, with emergent beginnings and peak amplitudes, observed after the onset of "vulcanian" eruptions are associated with the possibility of subsequent gradual collapse of the dome (*e.g.,* Petersen *et al.* 2006, Fee *et al.* 2011b). Despite the similarity in characteristics between the acoustic signals originating from Vulcanian and Strombolian explosions, Marchetti

et al. (2009) have shown how the use of infrasound and thermal infrared data can help to discriminate between the styles and give an idea of the dynamics of the jet and the plume.

Infrasound recordings from volcanoes such as Sakurajima (*e.g.,* Yokoo *et al.* 2009, Fee *et al.* 2014, Kim *et al.* 2015) and Santiaguito (*e.g.,* De Angelis *et al.* 2016) show Vulcanian behaviour.

Vulcanian explosions occur at many volcanoes around the world (Morrissey and Mastin 2000) and can precede large Plinian eruptions (*e.g.*, Mt. Pinatubo, Philippines, 1991); produce dangerous pyroclastic flows (*e.g.,* Mount St. Helens, USA, 1980, or Soufriére Hills Volcano, Montserrat, 1997); and present a significant hazard to aircraft (*e.g.,* Galunggung, Indonesia, 1982, or Redoubt, Alaska, 1989). At several volcanoes around the world, including Semeru (Indonesia), Sakurajima (Japan), and Karymsky (Russia), Vulcanian eruptions occur daily and can persist for years.

1.2.2.3 Sustained volcanic eruptions

Another category of continuous signal is produced by sustained volcanic explosions, often associated with sub-Plinian, Plinian, or phreatomagmatic eruptions. This type of high-amplitude sustained (minutes to hours) broadband infrasound signal resembles to a low-frequency jet noise signal and is often recorded up to thousands of kilometres from the source (Fee and Matoza 2013).

Plinian

Some of the largest, most infrequent, and most dangerous eruptions are generally classified as Plinian eruptions and are characterised by a quasi-steady, sustained, and high-speed ejection into the atmosphere of a highly volatile mixture of solid, liquid, and gaseous particles (solid fragments of preexisting rocks, multiphase magma, and gas), produced by the fragmentation of andesitic to rhyolitic magma. The mixture creates a buoyant vertical column that can rise to tens of kilometres high (Cioni *et al.* 2015). These complex successions of volcanic pulses in the convective plumes result in an alternation and overlap of pulsatory explosions of varying styles, intensities, and dynamics (from volcanic explosions to phases of prolonged ash emission to phreatomagmatic activity to the emission of lava flows or domes).

When it is at maximum height, the column eventually (due to winds) spreads laterally like an "umbrella" cloud, maintaining its shape for hundreds of kilometres. In the reverse scenario, when the eruptive column loses its buoyancy, the basal part collapses in a sustained cloud of hot gases and PDCs that disperses around the volcano.

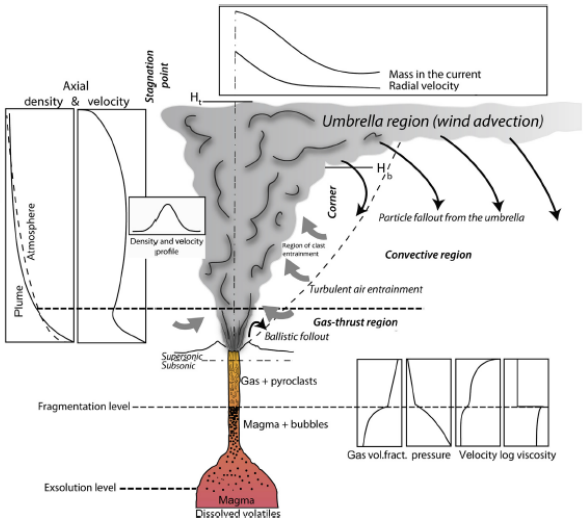

Figure 1.6. General scheme of eruptive regimes for a strong plume, and variation of physical parameters during Plinian eruptions (adapted from Cioni *et al.* 2015).

All eruptive events that share this Plinian regime are commonly summarised under the term "Plinian eruptions", which includes the sub-Plinian, Plinian and ultra-Plinian styles (Cioni *et al.* 2015). These Plinian eruptions are characterised by VEI values in the 4-7 range, with recurrence times per century of roughly 30-40 sub-Plinian events (VEI 4) and 10 Plinian events (VEI 5-6), in contrast to the recurrence rate of less than 1 per 1000 years for ultra-Plinian eruptions (VEI 7).

Sub-Plinian eruptions have lower values of magnitude (M = 4) and intensity (I = 10), while Plinian and ultra-Plinian eruptions share common eruption dynamics but different values of magnitude (4 to 8) and eruption intensity (10 to 12), according to Pyle (2000).

Sub-Plinian eruptions are generally unstable events marked by phases of short-period oscillations (minutes) with time intervals that can be reproduced multiple times over longer periods (days, weeks). In most events, the vertical convective column has a moderate velocity (weak plumes), can be clearly tilted in the presence of a strong wind and usually does not cross the tropopause.

In Plinian and ultra-Plinian eruptions, variations in Mass Discharge Rate (MDR) or in the parameters that control eruption dynamics (*e.g.,* magma gas content, total grain-size distribution, conduit and vent geometry, and exit velocity) often take place on a longer time scale than the typical times of the distinct processes that dominate magma ascent, magma fragmentation, and plume development, playing a key role in determining the course of the eruptive column. Ultra-Plinian events are distinguished from typical Plinian eruptions only by their greater mass flow rate, reflected in taller columns and wider dispersion (dispersive power), which can reach heights of up to 55 km and commonly generate PDCs due to the subsequent

collapse of the column. These massive eruption columns penetrate the tropopause and disperse into the stratosphere.

Infrasound from these types of eruptions is frequently high amplitude, sustained (minutes to hours) emergent broadband signals, commonly recorded up to thousands of kilometres from the source (Fee and Matoza 2013). The spectral content of broadband infrasonic tremor depends on multiple factors (*e.g.,* size and shape of eruptive column, volume of erupted material, or speed and direction of winds) and is comparable to the low-frequency form of jet noise (broad spectral peak and a distinctive shape of attenuation at high frequencies).

Determining the parameters of the volcanic jet has been shown to be feasible by using the Strouhal number, St:

$$St = \frac{f_{j+}\, D_j}{U_j} \qquad \text{(Eq. 1.1.)}$$

where f_j is the peak frequency of the jet noise, D_j is the expander jet diameter (*i.e.*, vent diameter), and U_j is the jet velocity. Evaluating the Strouhal numbers of the flows, it is possible to compare different jet noise spectra from man-made and volcanic jets (if both types of flows have a peak Strouhal number), enhancing the possibility of estimating the diameter and speed of volcanic jets (or at least their relationship) using infrasound data (Fee and Matoza 2013, McKee *et al.* 2017).

1.2.2.4 Surface mass movements at volcanoes

Surface mass movements are a common occurrence in volcanic environments as a result of magmatic processes or the action of liquids, hot fluids, and gases and can occur both during periods of eruptive activity and during periods of volcanic quiescence (Allstadt *et al.* 2018). Surface mass wasting events comprise **lahars and outburst floods**, a type of mudflow or debris flow extremely destructive with high infrasonic frequencies (> 10 Hz); **PDCs - Pyroclastic Density Currents,** *e.g.,* the tracking of trajectories and velocities of PDCs in the Soufriere Hills Volcano, were recorded ranging from 0.4 to 7 Hz, with durations ranging from 400 to 1500 s and peak amplitudes of 40 to 80 Pa (Ripepe *et al.* 2010a, Delle Donne *et al.* 2014); **Large rockfalls**, associated with the stronger infrasound signal sources during an eruption, produce complex seismic and infrasonic signals in the range of 0.1 to 1 Hz frequency, with an approximately 50 s period and infrasonic pulses (10.4 to 11 Pa) (Moran *et al.* 2008); **Debris, rock and ice avalanches**, which are highly mobile and extremely rapid flows of fragmented rock, ice, and/or debris with typical velocities ranging from 20 to 90 m/s (Scott *et al.* 2001) and high frequencies (>1 Hz);

Edifice collapses, which are rare events, distinct from debris avalanches due to their exceptional size, and can be subdivided into sector collapses and flank collapses. The infrasound signals generated by these kinds of surface events can provide important information for research and real-time monitoring.

CHAPTER 2 |

Infrasound monitoring of volcanic eruptions

Since 1990, infrasound-based technology has been included in the geophysical toolkit and incorporated by worldwide observatories for volcano monitoring, rapidly evolving from an academic research area into a usable, well-established, and valuable real-time monitoring tool.

Seismo-acoustic geophysical technologies are complementary in research and monitoring of volcanoes (Matoza and Roman 2022). While volcanic seismology aims to analyse, understand, and model seismic signals generated by magmatic, hydrothermal, and fault processes occurring on and around active volcanoes and from deep in the mantle to the surface (*e.g.*, Chouet and Matoza 2013), infrasound data complements seismic observations by offering clear and unambiguous evidence of shallow subsurface and subaerial activity, such as explosive eruptions, shallow degassing, surface flow and mass wasting (Watson *et al.* 2022).

Compared to other monitoring technology (*e.g.*, satellite-based optical sensing or classic terrestrial monitoring techniques), infrasound recording is not affected by reduced visibility (due to clouds or gas/grey shelves) and data latency for short distance (usually less than a few tens of seconds), becoming more effective and proving to be a powerful tool for detection and characterization of explosive activity (Cannata *et al.* 2009).

Several studies related to eruption dynamics, using infrasound techniques in the vicinity of volcanic systems, have proved their ability to detect and locate explosions and to contribute, with records and relevant valid data, to better understanding pre-eruptive processes (Ripepe *et al.* 2001b,

2002a, Johnson *et al.* 2004, Genco and Ripepe 2010, Cannata *et al.* 2015) and the volcanic processes at their origin (Dibble *et al.* 1984, Iguchi and Ishihara 1990, Braun and Ripepe 1993, Vergniolle and Brandeis 1994, Johnson and Ripepe 2011, Fee and Matoza 2013, TailpiedTalpied *et al.* 2013, among others). By providing quantitative eruption source parameters (*e.g.*, Vergniolle and Caplan-Auerbach, 2006) like explosion pressure, gas concentration, eruption magnitude (Morrissey and Chouet 1997), volumetric and mass flow rates (*e.g.,* Harris *et al*. 2013, Kim *et al*. 2015, Fee *et al*. 2017), directionality of eruptive blasts (*e.g.*, Kim *et al*. 2012, Jolly *et al.* 2017, Iezzi *et al*. 2019), plume height (*e.g.,* Lamb *et al.* 2015, Caplan-Auerbach *et al*. 2010, Ripepe *et al*. 2013, Perttu *et al*. 2020), infrasound allows to discriminate among multiple close-spaced sources (Ripepe *et al*. 2007, Fee *et al*. 2021) or to help forecast eruptions (Garcés *et al*. 1999, Ulivieri *et al*. 2013, Johnson *et al*. 2018, Ripepe *et al.* 2018).

However, only a small fraction of the roughly 1,281 Holocene active volcanoes are effectively well instrumented, some of them poorly instrumented, while the vast majority are not instrumented at all (Pallister and McNutt 2015). Many of these volcanoes are in remote areas and have scarce or no field observations or no deployed instrumentation (Matoza *et al.* 2011a, Fee and Matoza 2013), thus, the use of infrasound-based techniques for remote monitoring is increasingly widespread (Ripepe *et al.* 2010b, TailpiedTalpied *et al.* 2013, Ulivieri *et al.* 2013). Monitoring volcanoes at regional and global levels in the infrasound band has proved to be effective, allowing the identification of periods of eruptive activity on several volcanoes (Johnson and Ripepe 2011, Dabrowa *et al.* 2011, Fee and Matoza 2013).

Real-time monitoring of a volcano's eruptive activity is extremely important in assessing the potential risk of eruption and in identifying potential risks to aviation (Fee and Matoza 2013).

Infrasound networks have become essential resources with valuable data for a wide range of geophysical hazard warning systems across the world, enabling enhanced monitoring, mitigation, and assessment of potential damage from surface earthquakes, landslides and avalanches, as well as global warming and global volcanic activity (Campus and Christie 2010).

Automatic systems are presently used on an operational basis, and further developments will enhance this technique, particularly when combined with other ground or space observations. The development and establishment of the IMS infrasound network of the CTBTO has demonstrated the capability of detecting volcanic eruptions at a wide range of energies at very large source-receiver distances (*e.g.,* Campus and Christie 2010, Dabrowa *et al.* 2011), high temporal resolution data on ongoing activity at remote volcanoes (*e.g.,* Matoza *et al.* 2011a), and global coverage for different scale volcanic eruptions (Dabrowa *et al.* 2011).

2.1.The infrasound network of the IMS

2.1.1.Historical Review: Infrasound and the Comprehensive Nuclear-Test-Ban Treaty

Two remarkable pre-nuclear events, the August 1883 Krakatoa volcano paroxysmal eruption in the West Indies (Verbeek 1884) and the June 1908 Great Tunguska (or Siberian) Meteor (Whipple 1930), generated fluctuations in air pressure that were recorded in sensitive barometers and microbarographs around the world (*e.g.*, Symons 1888).

The infrasound shockwaves generated by these events sparked the interest in the infrasound technology, which led to the construction of the first microbarometers, but it was only with the growth of nuclear weapons testing programs in the 1940s and 1950s that the first scientific papers based on infrasound data appeared (Gutemberg 1945, Yamamoto 1954).

During the Cold War, global infrasound technique-based network arrays were established and used to detect, locate, and monitor atmospheric nuclear explosions. Those studies have shown that both acoustic gravitational waves and infrasound not only allow to identify their sources but also contain information about the state of the atmosphere (Evers and Haak 2010).

With the increase in nuclear testing by the superpowers, the escalation of the arms race by the USA and the USSR, as well as its proliferation among regional powers, became evident. With growing global concern, the issue of banning nuclear tests, proposed by a group of countries (known as the non-aligned countries), was put on the agenda of the UN Disarmament Council for 1955.

With the signature of the Partial Nuclear-Test-Ban Treaty (PTBT) in 1963 in Moscow by USSR, USA and UK, in which it was agreed to ban all nuclear tests in the atmosphere, underwater and in outer space, interest in infrasound-based monitoring gradually waned, with the last nuclear test in the atmosphere being carried out on 16 October 1980. From 1945 to 1980, 520 nuclear tests occurred with an estimated total yield of 545 Mt of TNT equivalent (Pavlovski 1998). However, the treaty did not ban underground nuclear tests. To avoid satellite observation, an emerging technology since the 1960s, nuclear tests were then carried out underground and monitored using data from seismic stations.

Always bearing in mind the importance of reducing stockpiles of nuclear weapons and preventing the proliferation of nuclear weapons, the Comprehensive Nuclear Test Ban Treaty (CTBT) was adopted on 10 September 1996 and opened for signature 14 days later. This treaty bans all types of nuclear explosions in all environments: on the Earth's surface, in the atmosphere, underwater and underground, carried out by any organisation and in any location, whether for military or peaceful purposes (CTBTO 2021).

The Preparatory Commission (PrepCom) for the Comprehensive Nuclear-Test-Ban Treaty Organisation (CTBTO) was established with the purpose of developing the verification regime of the Comprehensive Nuclear-Test-Ban Treaty (CTBT) in preparation for the Treaty's entry into force, as well as promoting its universality (CTBTO 2024).

To ensure that no nuclear explosion goes undetected, the CTBT has a unique and comprehensive verification regime based on three pillars: the International Monitoring System (IMS), the International Data Centre (IDC) and the On-Site Inspections (OSI) (not considered in the scope of this work; more information at https://www.ctbto.org/our-work/on-site-inspection).

Since 1996, 187 UN Member States have signed the Treaty (out of a total of 196) and 178 have ratified it (CTBTO 2024).

2.1.2. The International Monitoring System (IMS) network

The IMS network will comprise 337 monitor facilities worldwide using four state-of-the-art technologies (see Figure 2.1): seismic (170 stations), hydroacoustic (11 stations), infrasound (60 stations) and radionuclide (80 stations plus 16 laboratories), as well as a Global Communication Infrastructure (GCI) between these stations and the IDC, located in Vienna, Austria, providing a steady flow of real-time data. Ninety percent of the facilities are presently certified.

In addition to its main objective of monitoring compliance with the Treaty, the IMS produces data that can be used both to prevent and mitigate the effects of natural disasters and to potentially contribute to sustainable development, the expansion of knowledge, and human well-being through a wide range of applications in civil and scientific fields. That’s the case of this study that will use data from the IMS infrasound stations network.

Figure 2.1. Global distribution of the seismic, hydroacoustic, infrasound and radionuclide IMS stations (CTBTO 2021).

2.1.2.1. The IMS infrasound network

Under the IMS, the aim of the infrasound network layout is to ensure reliable detection and location of any atmospheric explosions anywhere in the globe with a yield greater than 1 kiloton (1 kT) equivalent of trinitroluene (TNT; 1 kt of TNT = 4.185 x 10^{12} J) by at least two stations (LePichon *et al.* 2009, Christie and Campus 2010, Green and Bowers 2010). Previous studies have shown that IMS detection capacity already meets its design goal (*e.g.,* LePichon *et al.* 2021).

As of January 2025, the IMS infrasound network consists of 54 certified stations, and when fully operational, the IMS infrasound network will be deployed strategically across 35 countries (Figures 2.2 and 2.3) with a medium distance between the nearest stations of around 2,000 km (LePichon *et al.* 2012, Hedlin and Walker 2012).

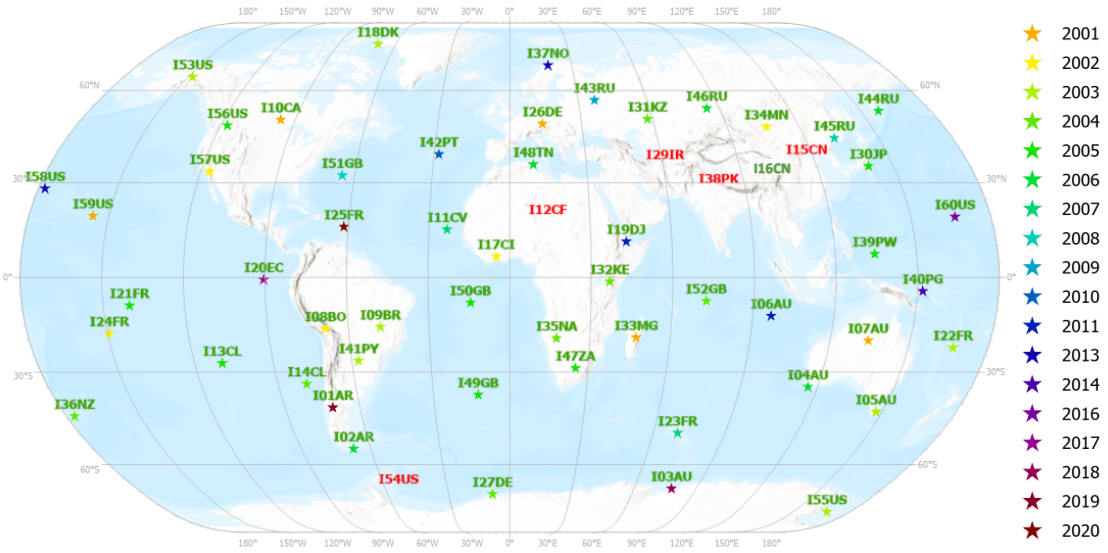

Figure 2.2. Map of the IMS infrasound network with certified stations (green) and planned, under construction or installed stations (red). The location of one of the 60 stations has not been determined yet (as of January 2025).

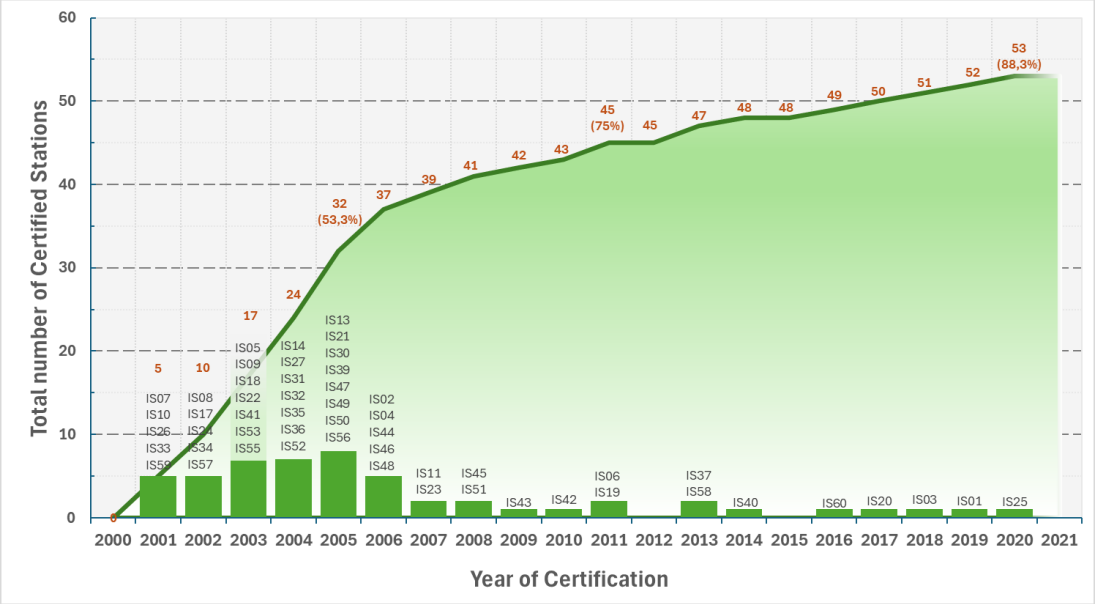

Figure 2.3. IMS certified stations by year (green bars). Total number of certified stations installing between 2000 and 2021 (green curve).

To take part in the International Monitoring System (IMS), all IMS stations have to fulfil all the technical specificities and meet all the requirements established by the Treaty.

In general, an IMS infrasound station (or array) comprises several infrasound array elements (sites), ranging from 4 to 15 (the majority of stations have 4 or 8 elements), spatially distributed over a diameter area between 1 and 4 kilometres, arranged in different geometric layouts (*e.g.*, a pentagonal outer main array surrounding a small triangular sub-array, a triangular outer main array

that surrounds a small central sub-array (4 to 5 elements), or a larger aperture array outside a small aperture array).

Each site is equipped with a vault to ensure the protection of all equipment against the environment (*e.g.*, temperature, water, fire), animals and human activities. Equipment comprises one (or two, for calibration) infrasound sensor, a wind noise reduction system (WNRS), power and Data Acquisition Systems (DAS) and communication technology. Meteorological measurements (temperature, wind speed and direction) are also recorded at one of the array's sites to provide information on the station's environmental conditions.

The sensor measures the variation in atmospheric pressure. It is a high-sensitivity absolute pressure microbarometer and must be able to detect pressure variations of less than 1 mPa (with instrumental noise of less than 2 mPa between 0.02 and 4 Hz) and operate between -10 and +45°C. The sensor's self-noise must be 10 dB lower than the minimum acoustic noise at 1 Hz (Ponceau and Bosca, 2010), with a maximum pressure level of ± 5 hPa and a dynamic range of 108 dB.

For the WNRS, different methods and techniques have been developed over the last few decades, with the rosette-shaped pipe arrays being the IMS standard at present, by which all other technologies are compared. More common pipe array designs such as radial, star, or hexagonal closed pack (HPC) are also in use in IMS infrasound stations (Christie *et al.* 2001; Marty *et al*. 2012).

Data are forwarded from the sites to the Central Facility (CF), generally transmitted using radio or fibre optic communication systems. In the CF, data received is buffered, formatted with a secure digital signature, converted into a proper transmission format, and then forwarded to the IDC via GCI using integrated satellite communication equipment.

Therefore, the number of sites, their locations and deployment on the ground, and the types and standards of sensors and transmission technology, as well as the proper operation and maintenance of all the equipment, make IMS infrasound station conception a compromise between detection and an accurate estimation of wave parameters (Marty 2019).

The continuous improvement of the stations with the deployment of robust WNRS, an increase in sensors and developments in array geometry, as well as standardised station procedures, has boosted data quality and the network's detection capability. A continuous timely data availability transmission over 98% is required to be received at the IDC with a maximum delay of 5 minutes (CTBTO Manual), which demands an effective preventive maintenance.

The IMS infrasound network is a worldwide infrasound network that not only provides important near real-time data for monitoring nuclear explosions but also offers a unique potential for continuous information useful for monitoring extreme atmospheric events (*e.g.*, volcanic activity) along with other scientific applications (Marty 2019).

In section 2.2 the IS42 station, located in the Azores archipelago, Portugal, will be presented as an example of an IMS infrasound station in what concerns characteristics, performance, and event detections.

2.1.3. The International Data Centre (IDC)

Data from the IMS infrasound stations, together with state-of-health information, are continuously transmitted to the IDC through GCI, a communication system based on VSAT technology that enables global coverage using 5 geostationary satellites (Figure 2.4).

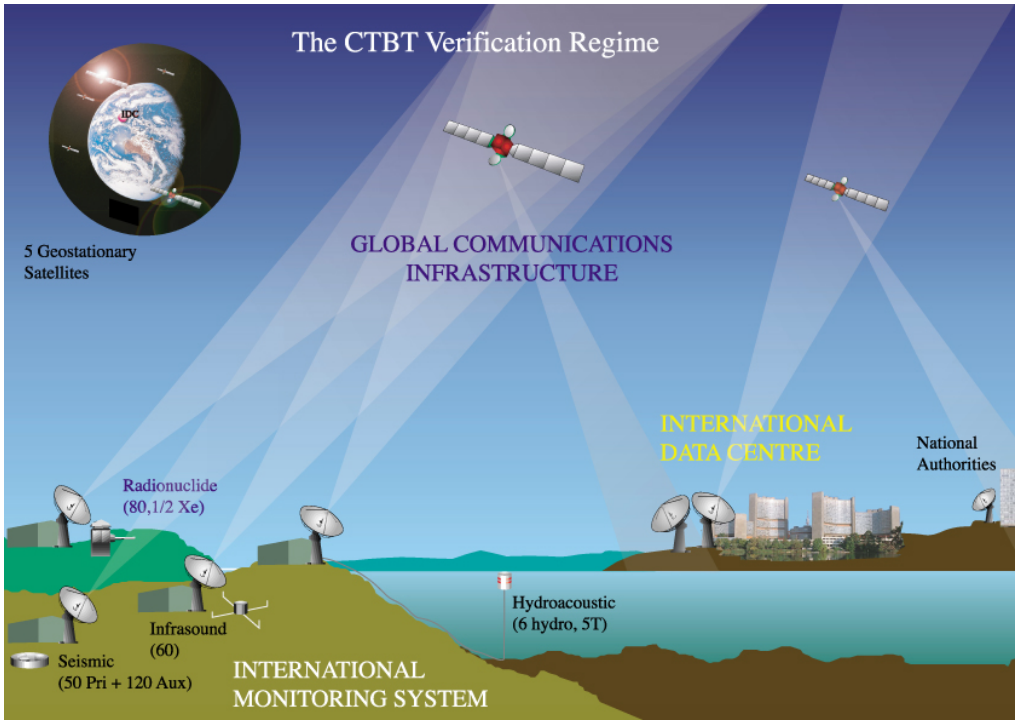

Figure 2.4. GCI - Global Communications Infrastructure (Kebeasy 2008).

Data are automatically processed and referenced in the IDC database in near real time, interactively reviewed and sent to National Data Centres (NDCs) on request to support CTBT signing states in fulfilling their verification responsibilities by providing objective analyses and specific services (CTBTO 2021).

After a first stage of automatic processing, in which the data from the Seismic, Hydroacoustic, and Infrasound (SHI) stations are processed individually, the network process (2nd stage) is initiated based on the results obtained to identify events based on the three SHI technologies (Brachet *et al.* 2010). These events are then reported in IDC bulletins referred to as Standard Events Lists 1, 2 and 3 (SEL1, SEL2 and SEL3), formed within 1, 4 and 6 hours, respectively (Figure 2.5). The automatic late bulletin SEL3 contains the infrasound signals associated with waveform events. The results of a later

interactive review process are included in the Late Event Bulletins (LEB) on which event definition criteria are applied to produce the Reviewed Event Bulletin (REB), the final waveform product of the IDC, nowadays within a timeline target of 10 days (Mialle et al 2019). More detailed information will be provided in Chapter 4, Section 5, which will cover all these procedures and the software used.

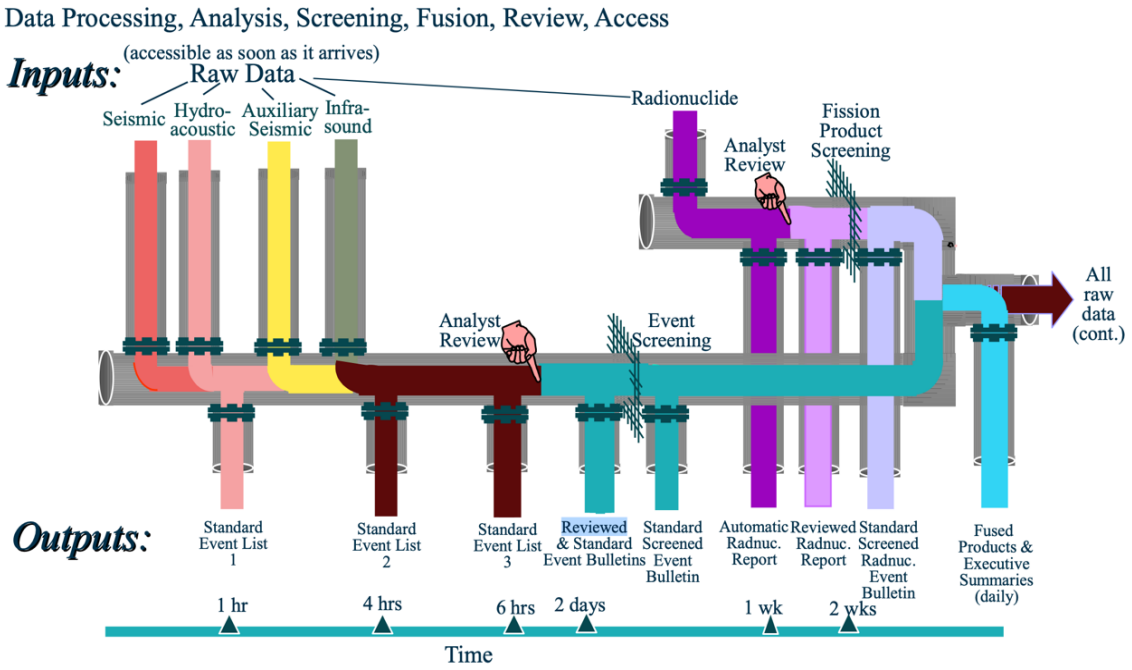

Figure 2.5. Schematics of the operational pipeline at the IDC illustrating the flow of data and the processing stages carried out for generating the IDC Products provided to state Signatories (adapted from Kebeasy 2008).

2.2. The IS42 infrasound array

As stated before, an example of an IMS infrasound station is described here, in what concerns characteristics, performance, and event detections.

According to the Treaty, the infrasound station IS42 was initially planned to be installed on São Miguel Island, in the Azores archipelago, Portugal. Due to environmental and security reasons, it was decided to deploy it on Graciosa Island of the same archipelago.

After all the technical specificities were met and all the requirements established by the Treaty fulfilled, the construction and installation of the infrasound station (Treaty code IS42, IDC code I42PT) was made possible through collaboration between the CTBTO, the Government of the Azores Autonomous Region (GRA), the Santa Cruz da Graciosa Municipality (CMSCG), and Centro de Vulcanologia e Avaliação e Riscos (CVARG) of the University of the Azores.

Being installed in August, the station was certified by the CTBTO's PTS on December 2nd, 2010 and integrated into IDC's operations. With its key position in the North Atlantic Ocean, it plays an

important role, along with the other infrasound stations (IS11 - Cape Verde Islands; IS25 - Guadeloupe; IS51 - Bermuda; IS18 - Greenland), in covering this important area for CTBTO monitoring purposes (Figure 2.1 – IMS network).

2.2.1. Location

The Azores archipelago is located about 1,370 km west of mainland Portugal, in the middle of the North Atlantic Ocean, and is composed of nine volcanic islands that span for approximately 600 km in a NW-SE trend, between the latitudes 36°55' and 39°43' N and the longitudes 24°46' and 31°16' W. The islands are arranged into three geographical groups: the Eastern (São Miguel and Santa Maria), the Central (Terceira, Graciosa, São Jorge, Pico, and Faial), and the Western (Flores and Corvo) groups (Figure 2.6).

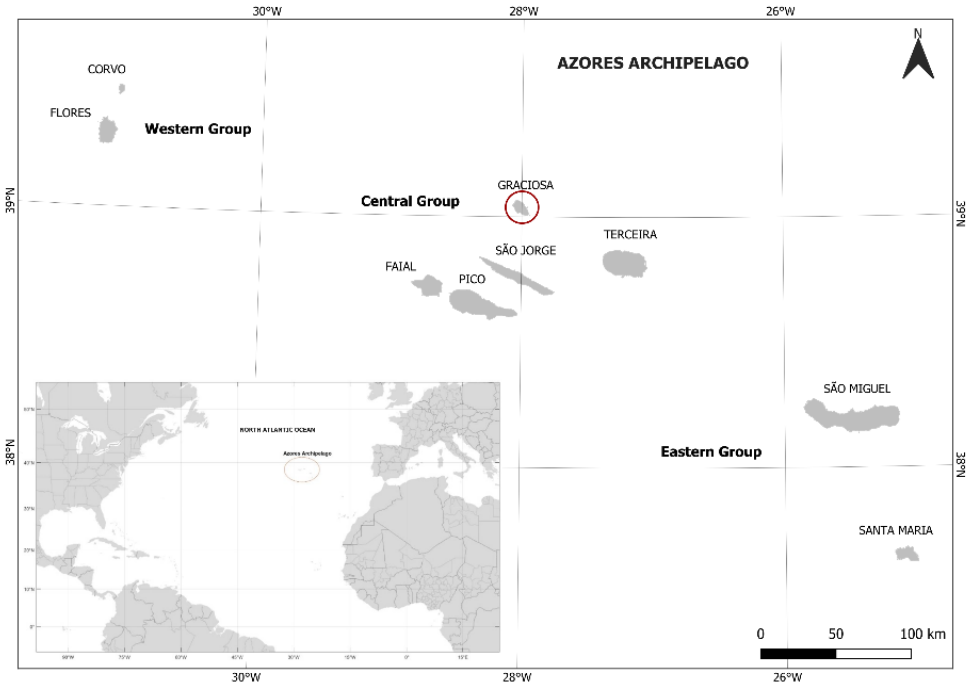

Figure 2.6. Geographical location of the Azores archipelago (Esri 2025, Mercator projection). The red circle encloses Graciosa Island, where IS42 is located.

Graciosa Island (Figure 2.7) is the northernmost island of the Central Group. It is the second smallest island of the archipelago with an area of 61.2 km^2. Only 5% of its area rises 300 m *a.s.l.*, with its highest point in the eastern part of Caldeira at an altitude of 405 m. With a maximum length of 12.6 km and a maximum width of 7.0 km, the island extends along a NW-SE orientation (Gaspar 1996). The estimated resident population in 2021 was 4,090 inhabitants (SREA 2024), which represents a density of ≈66 inhabitants per km^2.

Figure 2.7. Graciosa Island and IS42 station array sites location (Base GVP Image -12549, Planet Labs Inc., 2019).

2.2.2. Array geometry and technical features

The IS42 station array comprises 8 array elements and a Central Facility (CF) (Figure 2.8) where data is received, integrated, and converted into a proper transmission format and then forwarded via GCI to the IDC in Vienna (Wallenstein *et al.* 2011). All the station's components are located at altitudes between ≈90 and ≈250 m *a.s.l*. in a heavily forested area that shields all the infrastructure from winds that are frequently very strong. The array layout is arranged in a pentagonal outer main array of approximately 2,000 m in aperture that surrounds a triangular sub-array with an aperture of around 200 m (Figure 2.8). All the sites are connected by fibre optics to the CF to guarantee reliability, robustness, and high performance. Each of the sites consists of (1) an equipment vault with an external GPS antenna and energy supply circuit breakers and (2) a Wind Noise Reduction System (WNRS). At site I42H1, meteorological instruments such as an anemometer or a thermometer are also installed. All the sites are supplied by 230 V grid energy and are enclosed by security fences.

Figure 2.8. Graciosa Island and IS42 station array sites location (Base GVP Image -12549, Planet Labs Inc. 2019).

2.2.3. Noise level

The signal-to-noise ratio of IS42 is directly influenced by the wind-generated micro-pressure fluctuations linked to turbulent eddies within the atmospheric boundary layer. This can present a significant issue at certain times of the day for infrasound stations in the IMS network, as they occupy the primary and secondary monitoring passbands (Walker and Hedlin, 2010). Winds at the IS42 infrasound elements are expected to be weak in the summer, with speeds are ranging from 0.1 to 0.4 m/s, though up to 7 m/s during storms. The rest of the year, the projected average wind speeds are between 0.3 and 1 m/s. Infrasonic microbarom waves (in the 0.12 - 0.35 Hz passband) are another major source of noise; the surf (usually at frequencies above 1.0 Hz) is common in the waveforms due to the proximity of the station to the coastal areas. Fortunately, infrasonic noise from anthropogenic activities such as industries, traffic, or other cultural sources is not an issue in this case.

In addition to being deployed within a dense and stable forested area, a WNRS with 4 rosette shapes, with 96 inlet ports and a total length of 20 m, was assembled in each of the 8 array elements to reduce the impact of wind noise. It is made of stainless-steel pipes (tubing) set on pre-levelled ground (Figure 2.9).~´

Figure 2.9. WNRS pipes and manifold (Matos 2018).

To reduce wind turbulence and enhance thermal isolation and component shielding, all pipes and inlet ports are covered with a 10 cm thick layer of washed gravel, with approximately 20/25 mm in size (Figure 2.10).

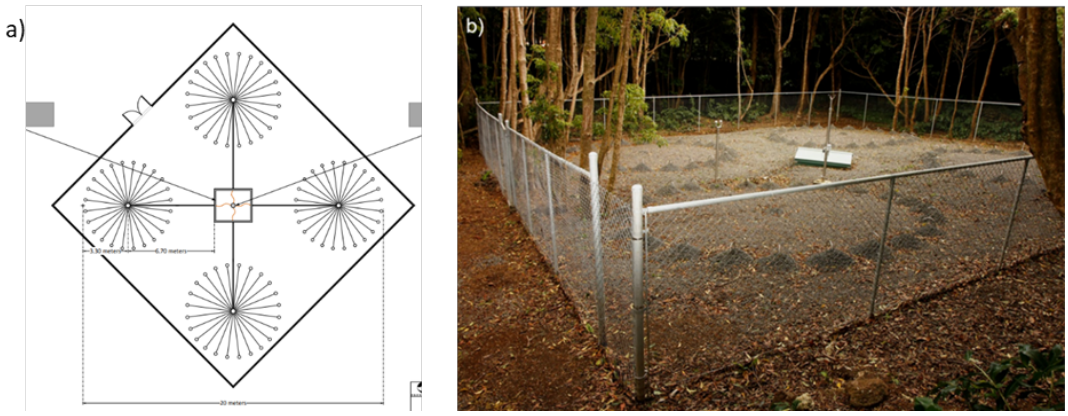

Figure 2.10. a) The IS42 rosette pipe array design for all sites (Christie and Campus 2010). **b)** I42H6 station element after putting gravel over stainless steel pipes and inlet ports (Matos 2018).

In each vault, a high-sensitivity absolute pressure microbarometer (CEA MB2005) is installed to measure the atmospheric pressure variation. This deformation is measured by a Linear Variable Displacement Transducer (LVDT) sensor, able to sense pressure variations under 1 mPa, with instrumental noise being less than 2 mPa at 0.02 to 4 Hz. The maximum pressure level is approximately ± 100 hPa for a sensitivity of 1 mV/Pa, which gives the sensor a dynamic range of 134 dB. The sensor sensitivity is generally set to 20 mV/Pa to be adapted to the digitizer's range.

The maximum pressure level is then ± 5 hPa and the dynamic range is 108 dB. The MB2005 frequency response is therefore highly stable over time (Figure 2.11).

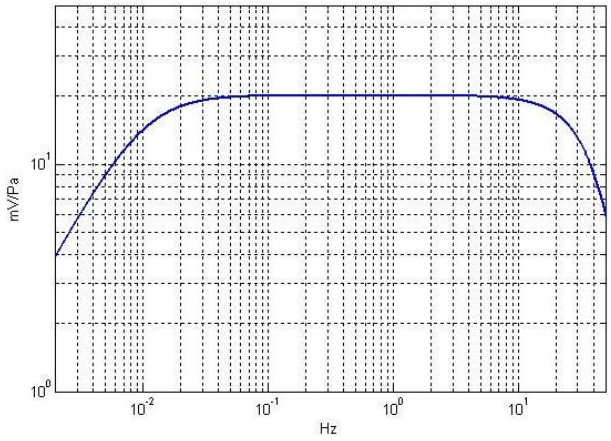

Figure 2.11. Frequency response of the MB2005 sensor (CEA-DASE 2017).

2.2.4. IS42 efficiency

The Root Mean Square (RMS) and Power Spectral Density (PSD) methods were applied to analyse the IS42 response, measuring the station's background noise level over time and how the signal is spread across different frequencies, respectively. Also, an empirical noise-amplitude Probability Density Function (PDF) graphic is presented.

The root of the average of the squares of the sound pressure levels over time (RMS) measurements were performed on daily data from all IS42 sites for a detailed understanding of how background noise levels change over the course of the day (Figure 2.12). These measurements were also applied to the period covered by this work (2011 to 2020) for identifying long-term patterns in background ambient noise that can be influenced by factors such as weather or seasonal activities (Figure 2.13).

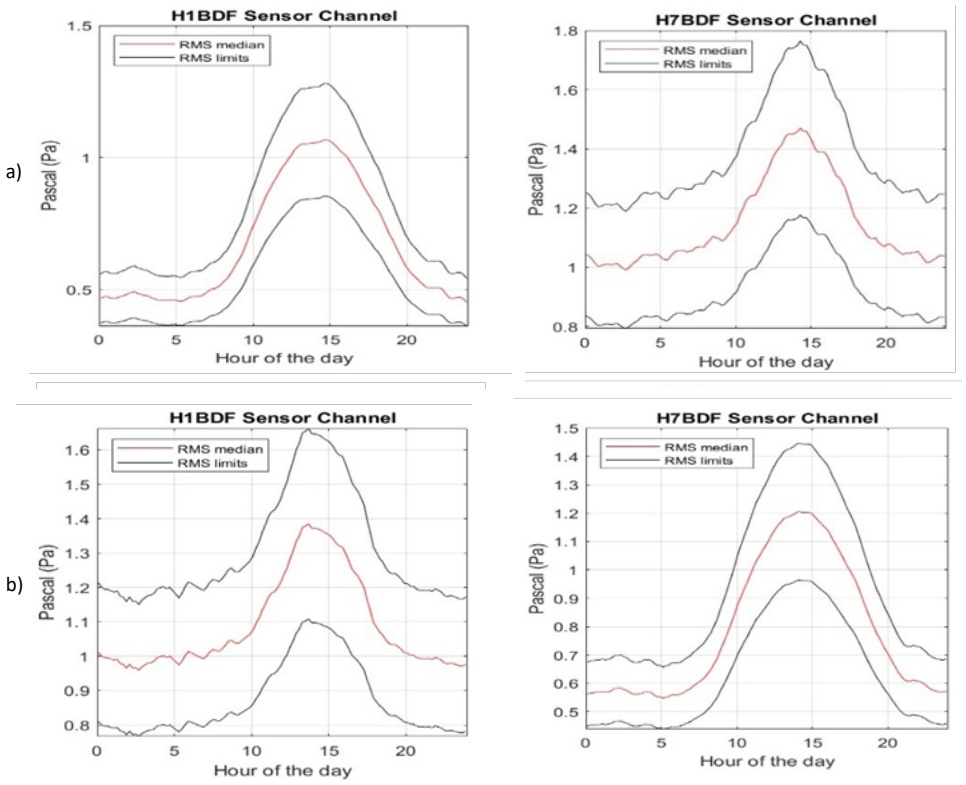

Figure 2.12. Example of a daily median RMS (red line) for IS42H1 and IS42H7 BDF sensors, between 2011-2020, during; a) Oct-March and b) Apr-Sep. Variation is clearly visible throughout the day. Higher RMS values are between 11:00 and 15:00 UTC.

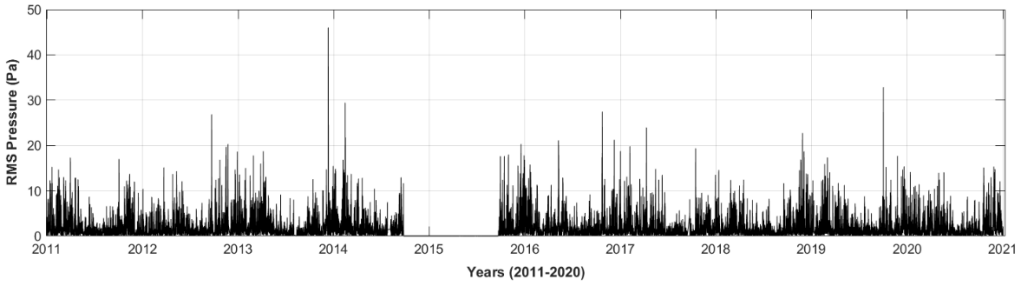

Figure 2.13. 2011-2020 time series showing IS42 station RMS infrasound variation. It was not possible to process data from due to several faulty array elements.

When analysing RMS measurements throughout the day, the intensity of acoustic energy is strongly correlated with the increase in human labour typically linked to agricultural activity, such as milking systems, cooling compressors, generators, and pumps, which often operate intensively during daytime, particularly between mid-morning and early afternoon. Tractors and other machinery used in agriculture also contribute significantly to the low-frequency noise increase. Cattle are most active during feeding and milking cycles, and the vibrations caused by their movements can contribute to structural resonance (when in enclosed spaces) or to the increase in ambient noise transmitted through the ground.

Additionally, temperature gradients and atmospheric stability vary throughout the day due to factors such as solar heating of the surface, variation in moisture, or turbulent eddies (surface winds), potentially causing constructive interference that amplifies the RMS values. Moreover, in this island environmental context, midday conditions typically present more intense wind-wave interactions due to high wind speeds and thermal uplift, which leads to an increase in low-frequency background noise generated by stronger coastal waves.

The analysis shows significant seasonal variations in the average sound pressure levels (RMS) measured at the IS42 station over the years, both in terms of amplitude and the dominant sources of background noise during the summer and winter periods. Observed RMS values show a clear daytime pattern, with a gradual increase observed from 08:00 UTC, reaching a daytime peak between 11:00 and 15:00 UTC, and then decreasing to lower levels from 20:00 UTC, which become stable during the night until the following morning.

During the daytime peak period, the average RMS values show seasonal variation, ranging from 1.4 to 1.6 Pa in winter and from 0.9 to 1.4 Pa in summer. The high values observed in winter are mainly associated with natural acoustic sources, such as intensified ocean activity (*e.g.*, wave breaking and coastal swell), frequent storms, and strong winds. In addition, atmospheric conditions, such as thermal inversions, play a significant role by increasing the low-frequency sound propagation and concentrating the acoustic energy near the ground. Summer values, while influenced by increased anthropogenic activity, have an acoustic energy that is typically more tonal, short-lived, and localized, resulting in lower average RMS levels than winter.

Night measurements from around 20:00 UTC to 08:00 UTC emphasise the seasonal trend. Throughout the winter, RMS levels tend to remain high, standing between 1.0 and 1.2 Pa, while in summertime, values drop significantly to mean levels between 0.4 and 0.5 Pa. This variation can be explained by the persistence of natural acoustic sources during the winter months, like coastal wave action and wind-generated turbulence, which produce continuous broadband infrasound throughout the night. Furthermore, nocturnal thermal inversions play a significant role in trapping low-frequency sound near the ground, resulting in elevated RMS measurements, even in the absence of direct anthropogenic sources. In contrast, the calmer weather and reduced marine agitation typical of summer nights contribute to significantly lower ambient sound levels during the same hours.

A frequency-domain analysis, such as Power Spectral Density (PSD), examines how much of the signal's power is distributed at different frequencies to evaluate the infrasound background noise level at each site. The PSD was estimated for the period between January 1st 2011 and December 31st 2020, through 24 consecutive hourly data segments. The spectral amplitudes of the filtered data were calculated for all the array sensors (H1BDF to H8BDF) using Welch's method (1967) with a Hann function. A data file is then recorded in the form of the base 10 logarithm of the PSD for each array

sensor. The sample rate is 20 samples per second, with an analysis window of 180 seconds (3,600 data samples). A monthly and yearly average were also recorded on data datafiles. As an example, raw data for the IS42H5 BDF sensor during the month of June are shown in figure 2.14.

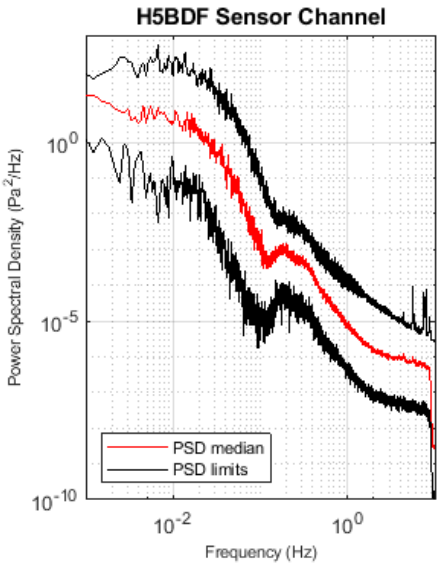

Figure 2.14. PSD for IS42H1 BDF sensor during the month of June.

Noise PSD plots were made for April to September (spring/summer) (Figure 2.15) and for October to March (autumn/winter) (Figure 2.16) seasons for the eight sensors of the array (H1 to H8). All sensors show a power variation of 2 orders of magnitude at all frequencies. The microbarom peak is distinctly observed around 0.2 Hz in all sensors across seasons, being more visible in the spring/summer season, and varies by 1 order of magnitude. Noise at 0.2 Hz varies annually and is higher during the local autumn/winter because of station location and the Atlantic Ocean winter storms that generate microbaroms.

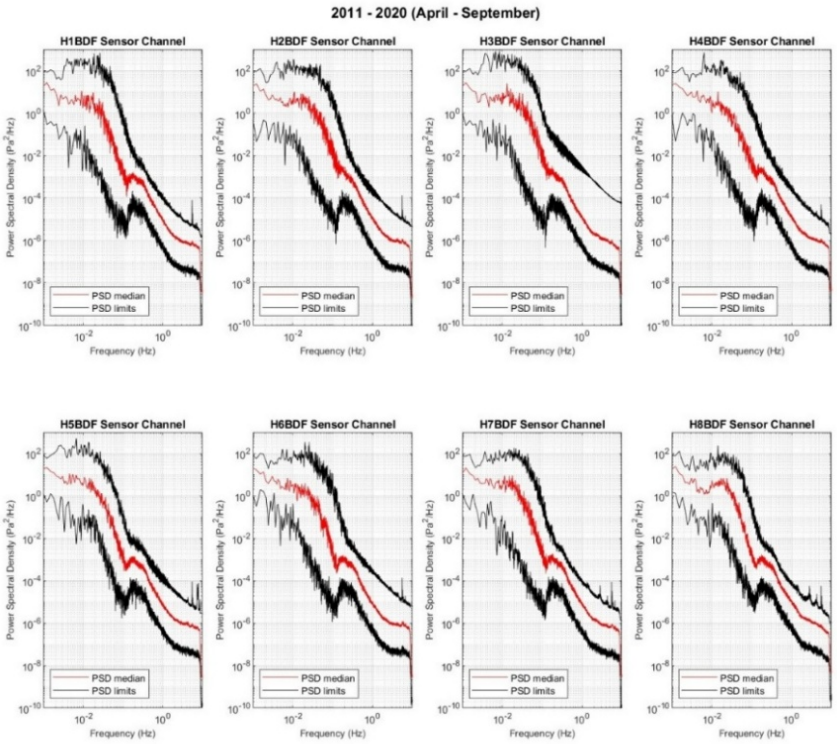

Figure 2.15. PSD plots for IS42 BDF channel sensors between April to September (Spring/Summer) covering the 2011-2020 period.

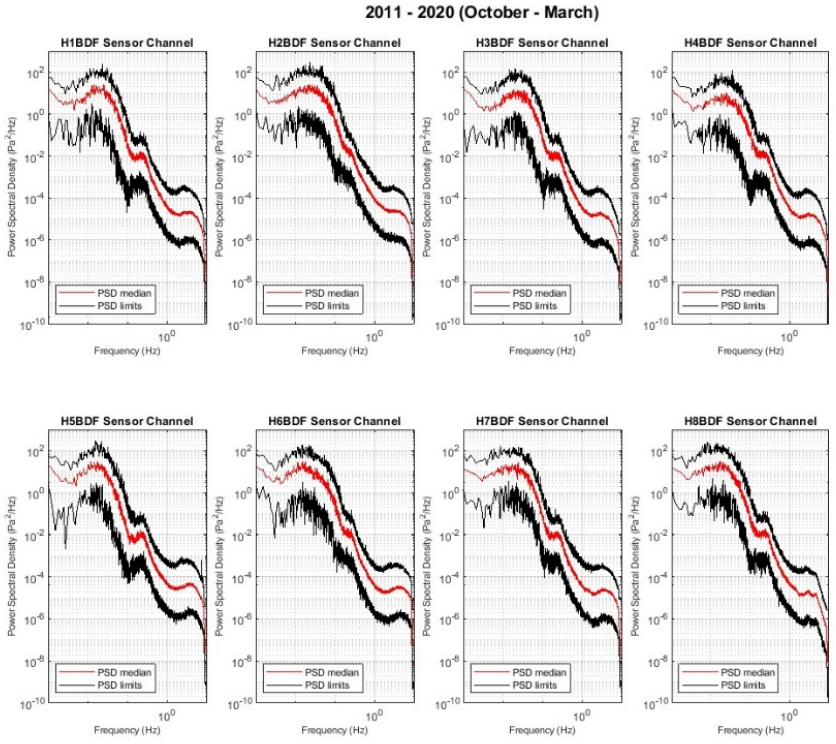

Figure 2.16. PSD plots for IS42 BDF channel sensors between October and March (Autumn/Winter) covering the 2011-2020 period.

The Probability Density Function (PDF) illustrates the distribution of noise and is valuable for predicting the signal-to-noise ratio for signals of specified amplitude (Bowman *et al.*, 2005). A PDF example for infrasound station channel sensor I42H1BDF as a function of noise power for each frequency band is shown in figure 2.17. The Power Spectral Densities (PSDs) are computed over a 1-h period using Welch's method and are corrected from the system response, including WNRS, sensor, and data acquisition system.

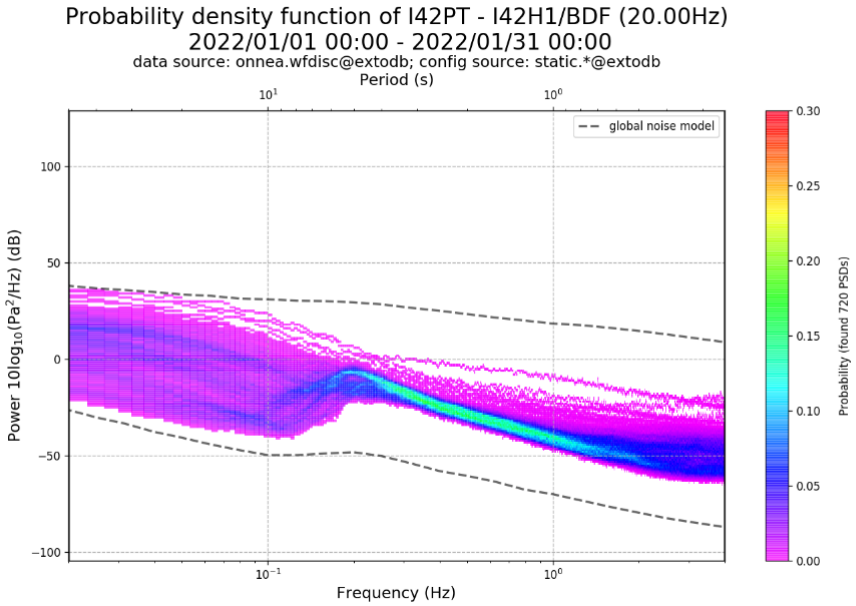

Figure 2.17. PDF in January 2022 for Infrasound Station Channel Sensor I42H1BDF. The grey-dashed lines represent a high- and low-noise model according to Bowman *et al.* (2005) infrasound noise models (In: Marty, 2019).

In the example above (Figure 2.17), the spectral levels of background noise observed are, on average, between -60 dB and 40 dB. The microbarom peak is visible around 0.2 Hz, with spectral levels mostly concentrated in the mid-range amplitude (around -5 Pa^2/Hz). The amplitude range narrows to about half beyond 0.2 Hz. A drop in the upper part of the amplitude range is also observed around 0.07 Hz, with a linear slope between 0.2 and 1 Hz, a result of the station being installed in a dense forest that acts as a windbreak and encloses standard WNRSs.

Overall, ambient infrasound is highly variable from station to station due to its location, time of day or season of the year (Bowman *et al.* 2005, Marty 2019).

2.2.5. Processing of infrasound data

The CTBTO provides technical assistance to support Member States in dealing with IMS data and IDC products (*e.g.,* LEB, SEL3 or REB). This includes the distribution and support of the NDC-in-a-Box

software package. This package covers a wide range of features, including software to retrieve, process, and analyse Seismic, Hydroacoustic, and Infrasound (SHI) wave data and Radionuclide (RN) data. Among the software features used for data analysis, the highlights are CDTools, Geotool, DTK-GPMCC, NMS Client, and PostgreSQL databases.

Geotool software is used to monitor station data, analyse data integrity, overall quality, and coherency between BDF channel signals, as well as check waveforms and perform spectral analyses. When an Event of Interest (EOI) is identified, data is processed with the DTK-GPMCC to identify and characterise the sources of detections recorded by the station. DTK-GPMCC is a graphical user interface that performs the Progressive Multi-Channel Correlation (PMCC) algorithm (see Chapter 4, Section 2.1), retrieves the results, and provides them for further analysis with data from other IMS stations and with IDC products (LEB, SEL3 and REB) and, in the end, saves them in a local Network Attachment Storage (NAS) unit.

IS42 station presents detections from natural and anthropogenic infrasound sources, such as extreme atmospheric events and meteorological phenomena (hurricanes and meteors), seismic and volcanic activity, as well as chemical and mine explosions or rocket launches to the atmosphere, throughout the North Atlantic and Mediterranean region.

2.2.6. I42PT events examples

Long-term observations of IS42 data between 2011 and 2020 (Figure 2.18), displayed in Data-Interpolating Variational Analysis (DIVA) software (CEA version 3.4.3), allow the spatial interpolation of data and show the most coherent source azimuths. These results also include recurrent coherent infrasound detections associated with seismic, atmospheric and anthropogenic activity. Seasonal fluctuations in dominating sources at low (microbaroms) and high (surf) frequencies indicate the impact of the zonal wind. In summertime, most detections are located between 0° and 180° (east-west propagation) and in winter between 200° and 350° (west-east propagation).

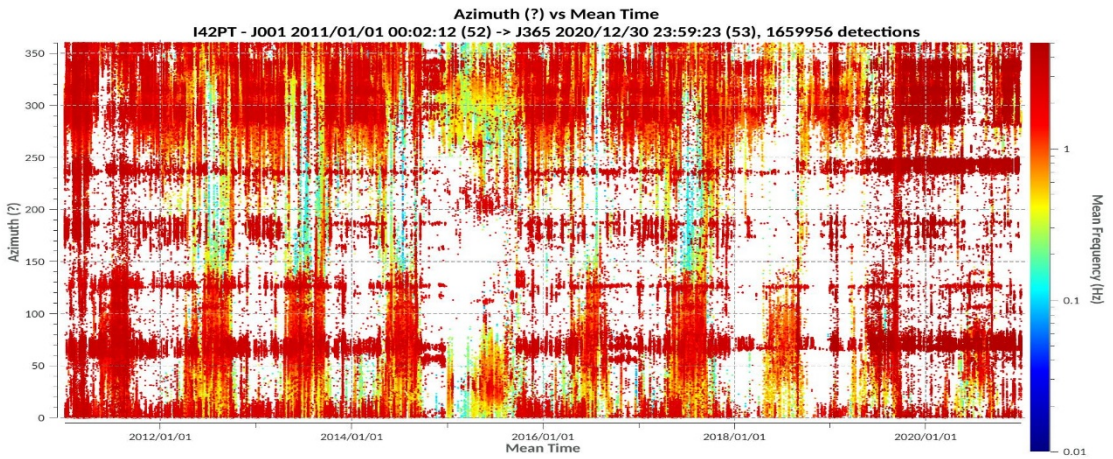

Figure 2.18. IS42 detections in the period of 2011 – 2020 by azimuth and mean frequency.

Over this 10-year period, a total of 1,704,994 detections were recorded by IS42 (Figure 2.19). According to the classification of detections into three frequency groups observed by Le Pichon *et al.* (2010) and Ceranna *et al* (2019) and followed by Hupe *et al.* (2022), 80% of all IS42 detections had frequencies above 0.5 Hz. Most of the near-field sources (on a local and regional scale) that produce infrasound can be identified in this frequency range; 19 percent of detections are between 0.1 and 0.5 Hz, where volcanic explosive activity or military explosions have been documented, despite the dominant band of recurrent North Atlantic microbaroms (0.2-0.3 Hz) and the stratospheric winds; less than 1% of detections referred to frequencies below 0.1 Hz, where infrequent events like Mountain Air Waves (MAW) or auroras were observed.

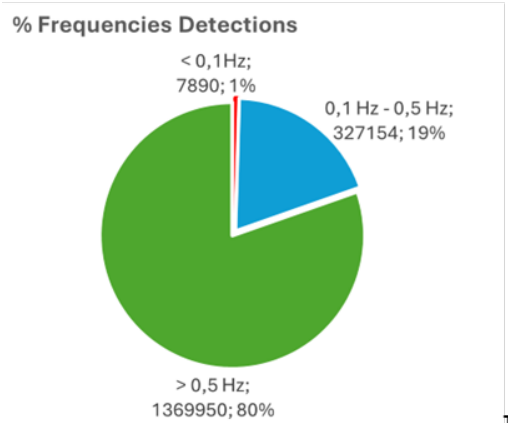

2011 - 2020	
Year	**I42 detections**
2011	349,079
2012	185,968
2013	211,617
2014	137,544
2015	100,467
2016	179,455
2017	172,677
2018	23,115
2019	146,422
2020	198,650
Total Events	**1,704,994**

Figure 2.19. Chart showing the total amount of detections classified by frequency and detections over 10 years period.

Concerning the IDC bulletins, in SEL3, 2,975 detections from IS42 were analysed, of which 1,792 were associated with acoustic events, 601 with seismoacoustic events and 398 with hydroacoustic

events. In REB, 163 events were analysed, 72 of which were associated with acoustic events and 91 with seismoacoustic events. Detections cluster in SEL3 and associated events in REB can be observed related to natural events and anthropogenic activity (Figure 2.20).

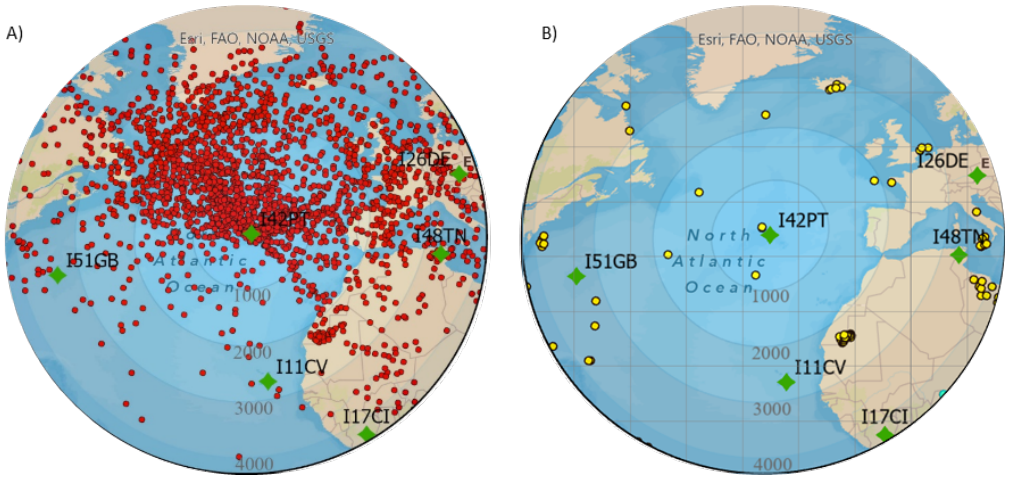

Figure 2.20. IS42 detections between 2011 – 2020 listed on a) SEL3 and b) REB IDC bulletins. REB clusters events can be associated to volcanic activity in Sicily and Iceland or explosions at quarries in Northwest Africa or rockets launches in United States coast (cartographic base ESRI2023).

The following examples illustrate some computed results of infrasound recordings at IS42 through the PMCC algorithm.

2.2.6.1 Stromboli paroxysm, July 3rd, 2019

Stromboli volcano, located on a small Italian island in the Mediterranean Sea with the same name (Figure 2.21), is probably the world's best-known volcano due to its spectacular basaltic explosions occurring every ≈10 minutes (strombolian eruptive style).

At 14:45:43 UTC on July 3rd, 2019, a very strong explosive event (paroxysm) occurred, with two explosions, one from the SW crater and the other from the Central crater. Data from IMS stations (I48TN and I26DE) at source-receptor distances ranging from approximately 500 to 3,600 km were also analysed (Figure 2.22).

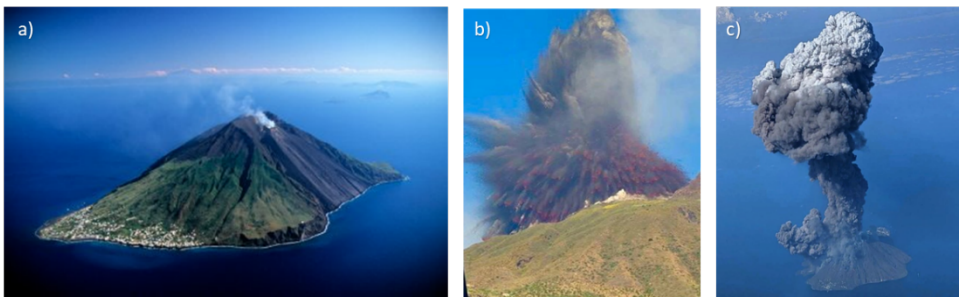

Figure 2.21. a) Stromboli Island and Volcano (Marani et al, 2004); b) *(Fabrizio Schiano photo)* and c) *(Anil Charley image)*: strong explosive event (paroxysm) images.

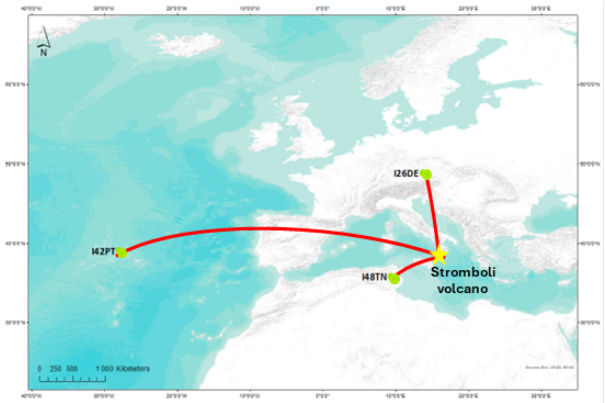

Stromboli volcano explosive activity event		
LOCATION	38.789° N, 15.213° E	
EVENT TIME	July 3rd 2019, 14:45 UTC	
STATIONS	Source Distance	Source Back-az.
I48PT	≈ 500 km	≈ 54.9°
I26DE	≈ 1,100 km	≈ 176.0°
I42PT	≈ 3,680 km	≈ 76.0°

Figure 2.22. Volcano source location and stations distance and back-azimuth. (Matos et al 2019).

About 3 hours after the event, IS42, located 3,680 km from Stromboli and with a back-azimuth of 76.4°, started to detect signals with a coherent back-azimuth from Stromboli volcano, a mean speed of 0.352 km/s, a mean frequency of 1.43 Hz, and a max amplitude of 0.010 Pa. Figure 2.23 shows 35 minutes of data with the respective spectrogram and beamforming arrivals consistent with stratospheric propagation(Matos 2019).

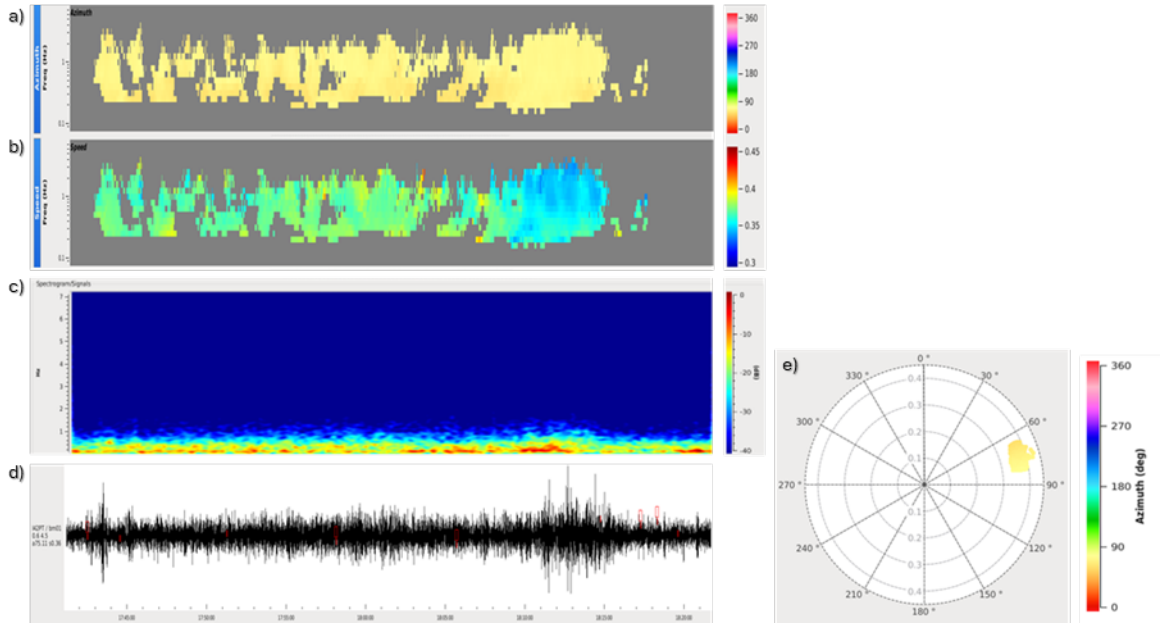

Figure 2.23. July 3rd, 2019, at 18:05 UTC event with 10 families corresponding to 4,423 pixel detections. a) a back-azimuth range from 70° to 80° (yellow pixels); b) speed from 0.324 to 0.380 (km/s); c) a spectrogram with a frequency close to 1 Hz; d) a band-pass filtered beam between 0.6 and 4.5 Hz with a max amplitude of 0.12 Pa; e) a polar plot with azimuths (polar angle) and trace velocities (polar radius), with a mean back-azimuth of 76.4° and 0.352 km/s speed (yellow dots).

Based only on detections from the stations (Table 2.1), the obtained source location falls within the Region of Interest (ROI) included in the uncertainty ellipse, whose centre is 55 km distant from the event ground truth (Figure 2.24). Moreover, there was consistency between the obtained results and the IDC REB bulletin (which also included seismic data) associated event, as well as a compliance with the Civil Protection agencies' reports and bulletins.

Table 2.1. Resume of Infrasonic detection parameters.

Station	REB time (UTC)	REB ba (°)	Number of pixels	Number of families	Azimuth range (°)	Mean Azimuth (°)	Mean Frequency (Hz)	Mean Speed (km/s)	Max Amplitude (Pa)
I48PT	15:17:14	54,9	6322	5	46 - 58	53.1	1.97	0.367	1.87
I26DE	15:44:18	179,5	2782	1	9 - 12	176.3	0.723	0.352	0.17
I42PT	18:05:42	79,9	4423	10	71 - 81	76.4	1.07	0.352	0.12

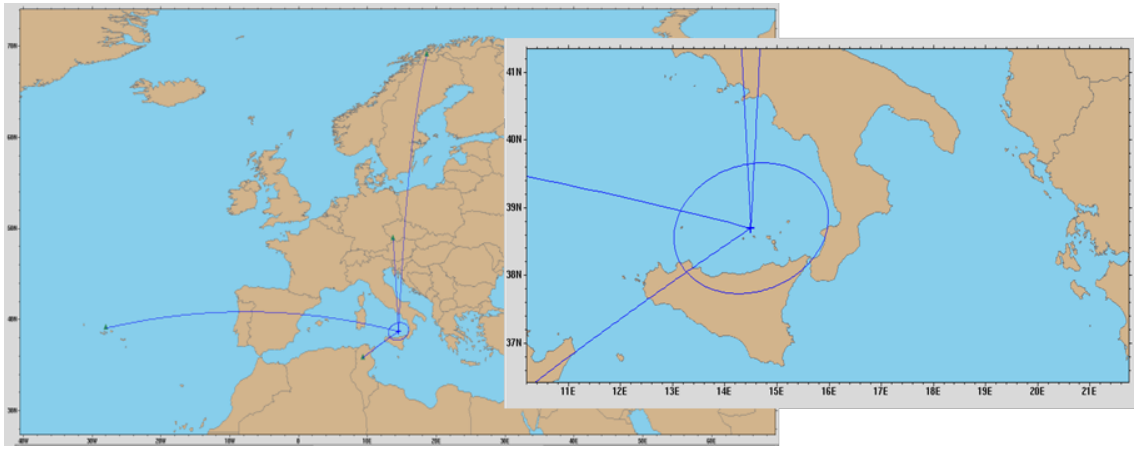

Figure 2.24. Event location results processed in Geotool and DTK-GPMCC analysis tool, based on the detection parameters and associated arrivals.

2.2.6.2 São Jorge Island seism, April 5th, 2022

During the 2022 seismo-volcanic crisis in the western part of São Jorge Island, Azores, station IS42 recorded an event with the 7 operational sensors on April 5th at 21:25:24 UTC. Data was band-pass filtered between 1 and 8 Hz with an overlap of 98%. The detections recorded were characterized by a peak amplitude of 0.02 Pa, a mean speed of 0.350 km/s, and a mean back-azimuth of 203.25° (Figure 2.25).

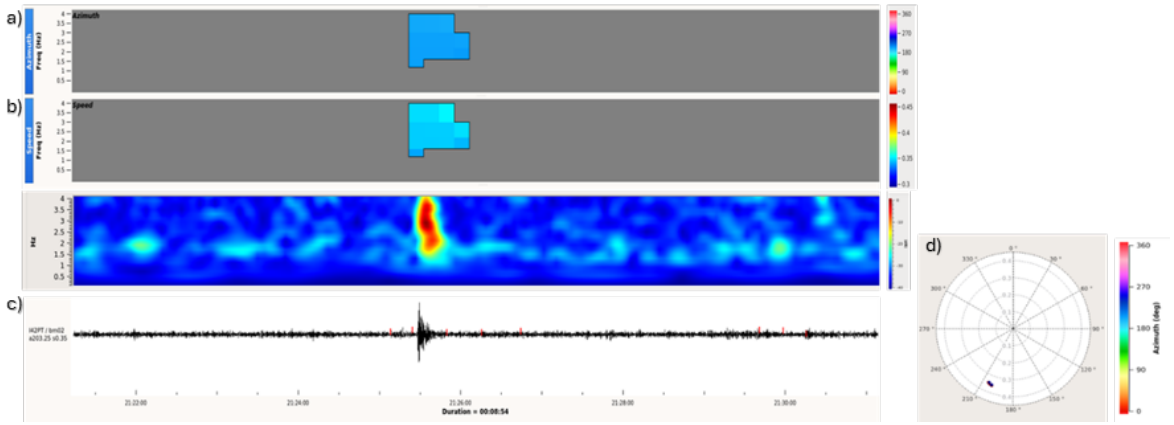

Figure 2.25. April 5th event at 21:25 UTC: a) back-azimuth range from 200° to 205° (blue pixels) b) frequency between 0.685 and 4.5 Hz; c) band-pass filtered beam (0.6 - 4.5 Hz); d) polar plot with back-azimuths (polar angle) and trace velocities (polar radius), with average values of 203.25° and 0.350 km/s speed (blue and red dots).

These results were then correlated with the infrasound arrivals also recorded by the 130 m aperture SJ1 portable array deployed on São Jorge Island, consisting of 4 differential pressure transducers (400 mV/Pa in the frequency band 0.01-200 Hz) (Figure 2.26).

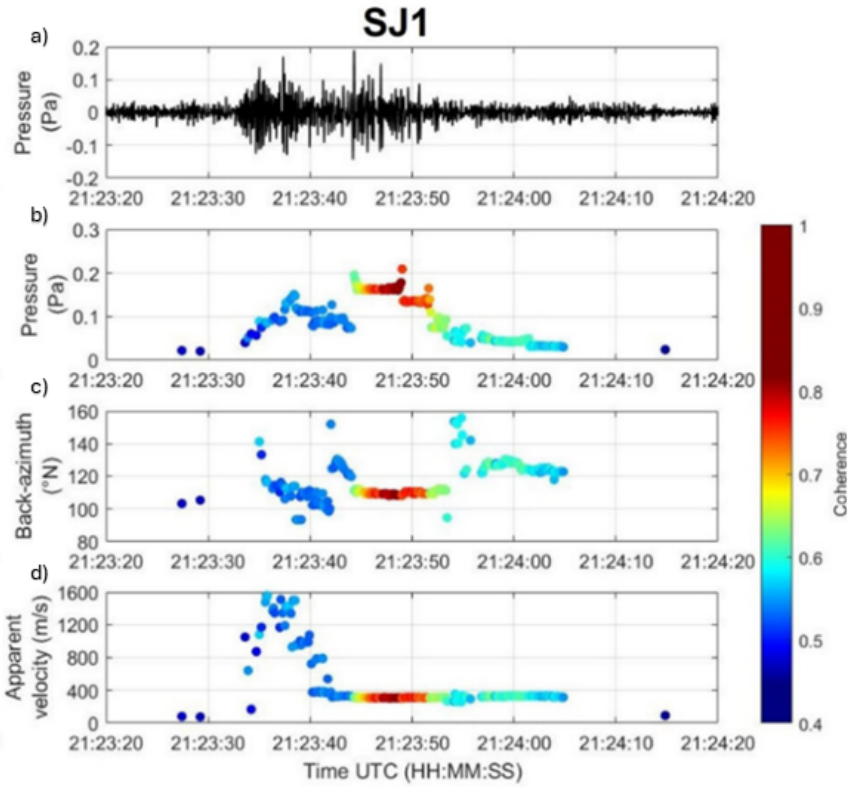

Figure 2.26. April 5th event at 21:25 UTC: Infrasonic tracks and array processing results at SJ1: a) filtered infrasound signal; b pressure (Pa); c back-azimuth (°); d) apparent velocity (m/s); each point in b, c and d represents an infrasonic detection defined with the array processing.

SJ1 array data was band-pass filtered between 1 and 10 Hz with an overlap of 98%. Results revealed a signal with a peak amplitude of 0.2 Pa and a back-azimuth variation between 110° and 130°. The apparent velocity had a distinctive pattern, with an infrasonic detection cluster of approximately 1000-1500 m/s in the first ≈5 s, and an apparent velocity of ≈340 m/s on the latter part of the signal (25 s) (Jesus *et al.* 2024).

A grid-search analysis based on the IS42 and SJ1 allowed locating the source of the signal (Figure 2.27). Recording times and location were correlated with CIVISA's daily events list, which verified consistency with a ML 2.1 earthquake (intensity of III MM1956) with the epicentre located in the NW part of São Jorge Island and recorded on the same day at 21:23:32 (UTC) (Jesus *et al.* 2024). The location by infrasound data is within 1 km of the epicentre and is consistent with source-to-receiver distances and recording times to the arrays, considering the 0.340 km/s speed of sound.

According to Marchetti *et al.* (2016), the ground movement associated with the earthquake coupled with the atmosphere allows the seismic wave to be transferred to the atmosphere as an infrasound wave (Ichiara *et al.* 2012), and therefore to affirm with confidence that the recorded signals represent the acoustic waves generated by the earthquake event itself (Jesus *et al.* 2024).

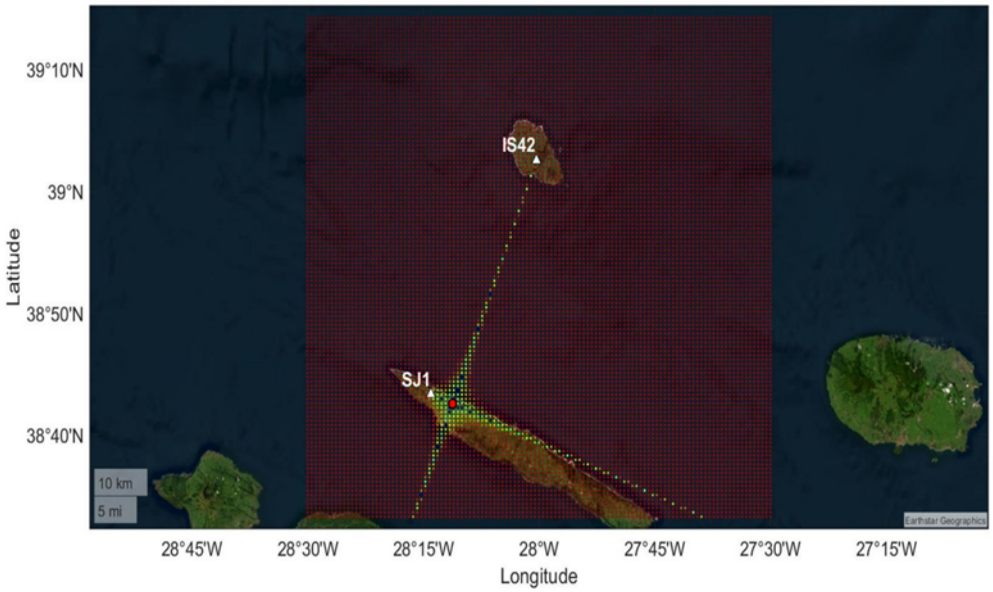

Figure 2.27. Grid search analysis, with 1 km resolution and assuming direct infrasound wave propagation at constant velocity (340 m/s). The red dot represents the real earthquake's epicentre. Dark blue nodes in the grid represent the best fitting reconstructed source locations (Jesus *et al.* 2024).

2.2.6.3 Unreported fireball in the Azores region, June 29th, 2022

On June 29th 2022, routine visual inspections of waveforms at CIVISA's seismic network stations reported seismic signals throughout São Miguel Island at 02:06 UTC. Similarly, anomalous signals were recorded on infrasound arrays on the Graciosa (IS42) and São Jorge Islands (SJ1), ≈200 km away. No other registers or reports have been found. Detections from IS42 show three coherent detected signals with good correlation in what concerns back-azimuths and horizontal trace velocity (Figures 2.28 and 2.29). A follow-up study by Hicks *et al.* (2023), supported by detailed modelling based on a 3D ray-tracing of the infrasonic waves (Belli *et al.* 2021, Blom and Waxler 2012) and on seismic observations, confirmed a fireball source for the anomalous signal detected over the Azores Islands (Figure 2.30).

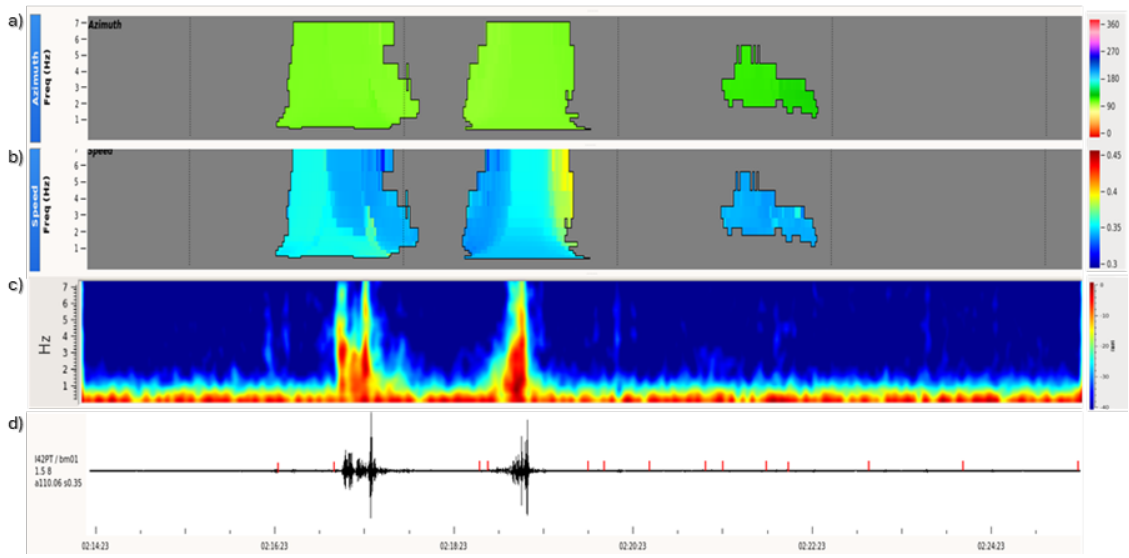

Figure 2.28. June 29th, 2022 event between 02:17 and 02:22 UTC. Three wave trains (at 02:16:48 UTC, 02:18:33 UTC, and 02:20:58 UTC) corresponding to 460, 431, and 131 pixel detections respectively, are shown. a) a back-azimuth range from 100° to 130° (green pixels); b) speed from 0.340 to 0.355 (km/s); c) spectrogram and d) band-pass filtered beam between 0.6 and 4.5 Hz (Hicks *et al.* 2023).

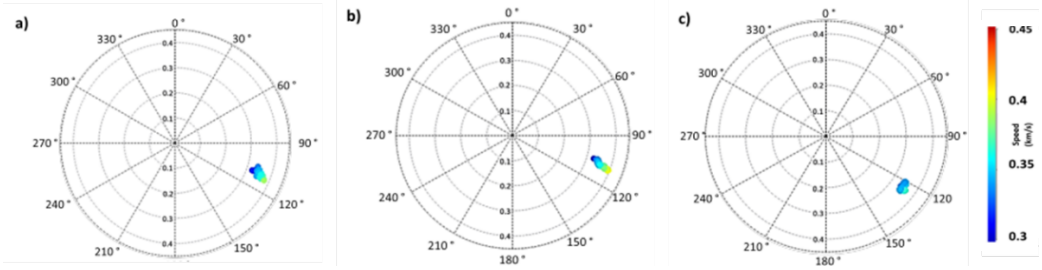

Figure 2.29. IS42 infrasound station polar plots according to azimuth (polar angle) and horizontal trace velocity (polar radius) related to the three wavetrains recorded in the infrasound station IS42: a) The first wave train back-azimuths span from 105.9° to 113.1°; b) second wavetrain back-azimuths span from 105.9° to 110.7°; c) third wavetrain back-azimuths span from 120.8° to 127.4° (Hicks *et al.* 2023).

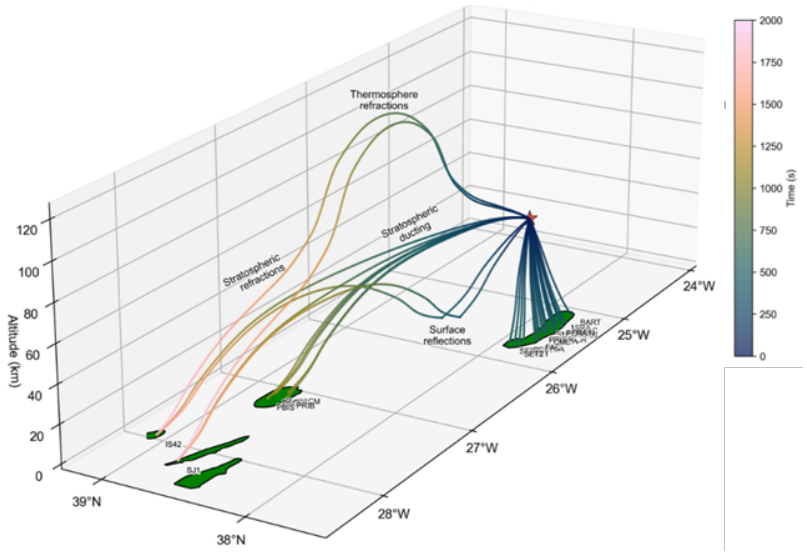

Figure 2.30. Perspective view from the SW of the source position derived using infrasound array data, displaying the 3-D raypaths traced in a realistic atmosphere model (coloured by time) (Hicks *et al.* 2023).

The fireball source was located ≈60 km NE of São Miguel Island, at ≈40 km altitude, with a diameter of ≈0.1-0.4 m and an estimated 10^{-3} kT TNT equivalent energy. This was later correlated with an unidentified flash captured by the Geostationary Lightning Mapper (GLM) on the same day, at 02:02:10 (UTC). It should be noticed that a faster and simpler location was possible only using infrasound data recorded at IS42 and SJ1, without any information about the origin. A 3 km mesh grid search based on estimated back-azimuth (Figure 2.31) showed that the reconstructed source location is within 10 km of the GLM flash spot presented in Hicks *et al.* (2023) and less than 12 km from the ray-tracing-based location by Hicks *et al.* (2023), which demonstrates the great accuracy of the analysis.

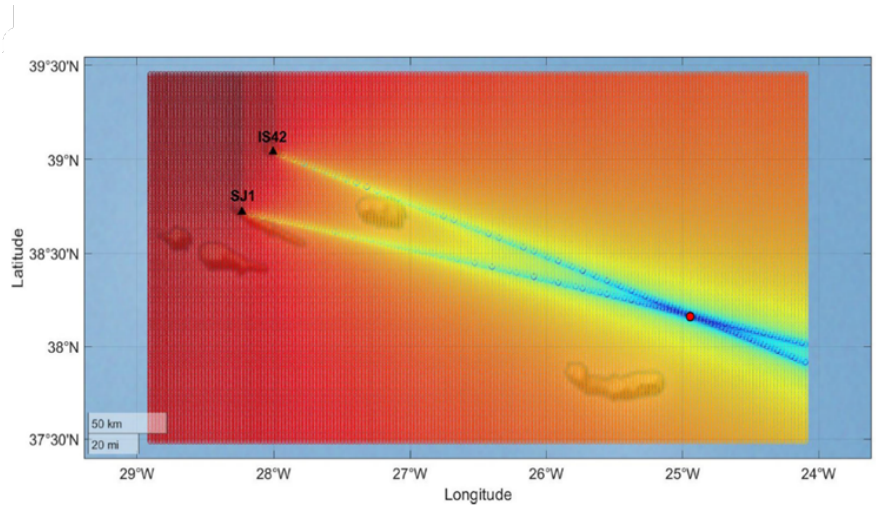

Figure 2.31. Grid search analysis (3 km resolution). The red dot marks the reconstructed source location from the GLM flash (Hicks *et al.* 2023). The grid's merged blue nodes correspond to the best-fit reconstructed locations (in Jesus *et al.* 2024).

Those are a few event examples detected by the IMS IS42 station. Several other research studies already carried out concerning explosive volcanic events (see Section 2.4) and other extreme events in the atmosphere reveal that, beyond its prime purpose of detecting nuclear explosions, data from the CTBT's International Monitoring System (IMS) has the potential to be used for broader civil and scientific purposes, which can bring larger gains to society.

2.3. Local, regional and global infrasound

Low-frequency acoustic waves can be recorded at distances up to several thousand kilometres from their source, making it possible to study volcanoes at multiple ranges, spanning from local (< 15 km) to regional (15-250 km) to global (> 250 km) (Fee and Matoza 2013).

Although major volcanic explosions can often be recorded using seismic networks, detection and higher precision source location of minor surface events are better attained with individual or array infrasound sensors (Fee and Matoza 2013). Local data has the advantage of being more representative of source processes, allowing for the detection of minor transient signals and low-amplitude tremors, which may not be energetic enough to propagate to distant recording sites due to the effects of long-distance atmospheric transmission.

At regional and global distances, infrasound arrays present significant potential for the detection and identification of far-field volcanic infrasound signals within incoherent wind noise (Walker and Hedlin 2010) and coherent infrasonic clutter (Matoza *et al.* 2013), contributing to the monitoring of remote volcanoes that are not easily accessed (Walker *et al.* 2010*,* Lyons *et al.* 2020). Looking to provide additional information on the long-term dynamics of volcanic activity, considerable advances are being made in the deployment of individual infrasound sensor networks or seismic and infrasound sensor pair networks (Nishida and Ichihara 2016*,* Matoza *et al.* 2019).

While at local distances, topography has been proven to have a direct effect on the recorded waveform (*e.g.*, Kim and Lees 2011, Lacanna and Ripepe 2013), the atmosphere's influence is progressively more crucial as the wave propagates further away from the source (*e.g.*, Drob *et al.* 2003).

2.3.1. Local infrasound

Local infrasound studies on volcanoes, using a single sensor or networks of sensors (*e.g.,* Braun and Ripepe 1993, Garcés *et al.* 1999, Johnson 2003, Fee *et al.* 2014), a single array or networks of arrays of different layouts (*e.g.*, Ripepe and Marchetti 2002b, Garcés *et al.* 2003, Matoza *et al.* 2011b*,* Taisne *et al.* 2012*,* Tailpied *et al.* 2013), are suitable for detecting open vents degassing, accurately

locating surface activity (De Angelis *et al.* 2012) and detecting and tracking moving flows in real or near real time (*e.g.*, Cannata *et al.* 2009*,* Johnson and Ripepe 2011*,* Fee and Matoza 2013*,* Johnson and Palma 2015*,* De Angelis *et al.* 2019). These sensors are deployed in different configurations, according to their purpose, near or on the volcanoes flanks that produce high-amplitude transient signals, implying that the acoustic transmission from the vent to the receiver is practically line-of-sight and without refraction into the stratosphere.

With regard to the source process, infrasound studies carried out on volcanoes tend to assume that the atmosphere in the proximity of the source is based on a relatively simple Green's function, which at a short distance from the source (<5 km) is generally assumed to be a homogeneous medium with no structures capable of altering the acoustic wave field (Lacanna and Ripepe 2013). Conceptual triangulation algorithms and the waveform semblance technique were applied to identify the source of volcanic infrasound (Ripepe *et al.* 2007*,* Jones and Johnson 2011).

However, the propagation of infrasound is strongly influenced by reflection and diffraction resulting from irregular topographical features such as craters, domes, valleys, or ridges (Kim and Lees 2011*,* Kim *et al.* 2012*,* Lacanna and Ripepe 2013). One approach to research aims to minimise the impact of topography using finite-difference time-domain (FDTD) algorithms. A simple FDTD algorithm made it possible to model the substantial distortion found along the crater rim of the Karymsky volcano (Kim and Lees 2011, 2014), and later, the use of FDTD algorithm modelling, accounting for 3D effects (3D FDTD model), to obtain the full 3D Green's functions that account for topographically generated waveform distortion (source-to-receiver path response).

At the Stromboli volcano, with a 2-D FDTD modelling approach to take into account the effects of topography, a source amplitude reduction of up to 11 dB compared to hemispherical acoustic scattering was observed for a station that is not within line of sight of the source. Diffraction and topographic reflections along the path are the cause of the amplitude reductions (Lacanna and Ripepe 2013).

The propagation of infrasound waves from volcanic sources is within the atmospheric boundary layer, controlled by temperature and wind gradients, whose variations can result in variable acoustic ducting and significant distortion of the waveform. When acoustic energy is strongly refracted upwards into the upper atmosphere, it can cause non-detection of signals at stations located several kilometres from the vent (Matoza *et al.* 2019).

These effects are not well defined by numerical weather forecasting models in the first few kilometres of altitude, so further studies are needed to better estimate the meteorological conditions near the volcano.

2.3.2. Regional and Global infrasound

Infrasound generated by volcanoes has been widely used for remote sensing of the upper atmosphere since many of them are powerful and consistent sources of infrasound (Matoza *et al.* 2019).

The state of the atmosphere controls infrasound propagation at regional and global distances, and the effective speed of sound is usually applied to characterise its propagation in long-range infrasound studies (see Chapter 3). Soundwaves loses energy through absorption and geometric (or cylindrical) spreading, being deflected by the wind and refracted according to its velocity profile winds (de Groot-Hedlin 2008). Geometric propagation is frequency-independent and occur when the sound spreads spherically from its source, diminishing in amplitude by 1/r (where r is the radial distance from the source). Under certain conditions, cylindrical scattering can also occur with amplitudes decreasing by $1/\sqrt{r}$.

The atmospheric low absorption at infrasonic frequencies allows infrasound to propagate thousands of kilometres from the source, as the acoustic waves are channelled through ducts or waveguides between the ground and the upper atmosphere (*e.g*., Georges and Beasley 1977). Three distinct atmospheric waveguides can be identified in the troposphere, stratosphere and thermosphere, depending on where the acoustic energy refracts towards the Earth's surface (see Chapter 3, Section 3.4). Atmospheric propagation modelling can be applied to identify the potential paths (conduits) that infrasound energy is expected to take from the source to the receiver, using ground-to-space atmospheric reconstruction models such as NRL-G2S (Drob *et al.* 2003) and AVO-G2S (Schwaiger *et al.* 2019) taking in account empirical models for wind, *e.g*., Horizontal Wind Model (HWM) (Hedin *et al.* 1996*,* Drob *et al.* 2008, 2015) and temperature, *e.g*., NRLMSISE-00 (Picone *et al.* 2002). Atmospheric propagation modelling (see Chapter 3, Section 3.4) involves ray tracing, *e.g*., GeoAc (Blom 2014), the parabolic equation (Waxler *et al.* 2015) and normal modes (Waxler *et al.* 2017).

At regional and global distances, infrasound arrays present significant potential for the detection and identification of far-field volcanic infrasound signals contributing to the monitoring of remote volcanoes (Walker *et al.* 2010*,* Lyons *et al.* 2020).

Previous studies have shown that remote infrasound arrays can be used to detect, locate, and characterise remote volcanic explosive events (e.g., Caudron *et al.* 2015, Dabrowa *et al.* 2011, Green *et al.* 2013, Le Pichon *et al.* 2011, Matoza *et al.* 2011a,b), and early warning systems were increasingly being developed (De Angelis *et al.* 2012, Garcés *et al.* 2008, Fee *et al* 2010b, Kamo *et al.* 1994*,* Matoza *et al.* 2007, Ulivieri *et al.* 2013, Gheri *et al.* 2023).

More recent work has looked towards the potential of the International Monitoring System (IMS) infrasound network to offer a global quantitative catalogue of explosive volcanic activity (Matoza *et al.* 2017) and automatic notifications of eruptions to Volcanic Ash Advisory Centres (Mialle *et al.* 2015).

Some studies of long-range infrasound detections generated by volcanic events are presented and discussed in the next section.

2.4.Recent studies on long range infrasound

Infrasound recorded from erupting volcanoes are being studied for three main purposes: (1) The study of the eruption dynamics, through a better understanding of the volcanic processes at the source and the location and characterization of the acoustic signals associated to the various types; (2) Volcanic activity monitoring, in order to evaluate and mitigate its associated risks: and (3) Probing the atmosphere due to the fact that infrasound propagation in the atmosphere is considered relatively homogeneous and isotropic (Johnson 2011, Fee and Matoza 2013).

Powerful volcanic eruptions can disturb the middle and upper atmosphere due to the large amount of released energy. These infrasound signals, recorded at regional and global distances, have great potential as a remote sensing tool to probe the atmosphere and understand how low-frequency acoustic waves refract in the stratosphere and thermosphere (Wilson *et al.*, 2006) or, for example, in which direction and with what intensity winds blow (*e.g.,* Chunchuzov *et al.* 2015).

The influence of zonal crosswinds on the recorded back azimuth was analysed by Evers & Haak during the summer 2001, when they investigated the detectability of infrasound with origin on volcanic eruptions on Mount Etna (Italy), on the 16-element Deelen Infrasound Array (DIA) in the Netherlands. The results were then compared with the detections obtained on the IS26 IMS array in Germany. They found that the use of infrasound as a monitoring technology was highly dependent on the array layout geometry and that the frequency versus spatial coherence of the signals also played a key role in detecting low signal-to-noise ratio events (Evers and Haak 2005).

The research of Le Pichon *et al.* (2005a), demonstrated the capability of measuring fine temporal wind fluctuations in the upper stratosphere and mesosphere thanks to a continuous monitoring of three active volcanoes (Yasur, Lopevi and Ambrym) in Vanuatu archipelago (New Hebrides islands) through IMS I22FR infrasound station (New Caledonia) located at ≈500 km. A comparison of the predicted azimuth deviations obtained using raytracing modelling techniques, combined with data from the NRL-ground to space (Naval Research Laboratory Ground to Space - NRL-G2S - semiempirical atmospheric model up to the stratosphere) climatological database, shows broadly seasonal trends over a period of almost a year, with a maximum azimuthal deviation of 15° being

observed from summer to winter. Considerable daily fluctuations in azimuths were also observed, considering the variability of atmospheric tides. From these comparisons, it is shown that the climatological models used are inadequate for predicting accurate atmospheric changes above the stratosphere (underestimated mesospheric zonal winds). The achieved results gave a more comprehensive understanding and quantification of the atmosphere's specifications and observed acoustic propagation.

Although relatively quiet, Augustine is one of the most potentially threatening Alaskan volcanoes. During the 2006 January eruption 13 large explosive events occurred and produced ash-rich plumes that reached up to 14 km *a.s.l* (Petersen *et al.* 2006). The blast events produced atmospheric pressure waves and intense infrasound signals that were registered through a microphone installed at 3.2 km from the active vent. The variety of recorded waveforms included sharp N-shaped with durations of a few seconds, impulsive signals followed by complex codas, and extended signals with emergent character and durations up to minutes (Petersen *et al.* 2006). This data collection is one of the few examples of continuous monitoring of a whole eruptive sequence by using a local sensor and, along with IMS station I53US, at Fairbanks, offers a unique opportunity for the infrasound community to enhance acoustic propagation studies (Petersen *et al.* 2006).

Sustained, broadband infrasound recordings from the 2008 Plinian eruptions of Okmok (July 12) and Kasatochi (August 7-8) volcanoes, in Alaska's Aleutian Arc (Fee *et al.* 2010c), were recorded at over six IMS arrays from a distance range between ≈1,700 km and ≈4,750 km to Okmok and ≈2,100 km - ≈5,250 km to Kasatochi volcanoes respectively (Figure 2.32), providing an opportunity to test the viability of the IMS infrasound network for monitoring and characterizing large and distant eruptions (Fee *et al.* 2010c). Although most of the seven IMS stations used in the study were closer to the Okmok volcano, only three were able to detect signs of eruptive activity while seven stations were able to detect signs of eruptive activity from Kasatochi, even both ejected ash at similar heights in the stratosphere (15-17 km). A probably first reason is the way volcanoes release gases and ash into the atmosphere. While Okmok's explosive activity (basaltic magma composition) was a sustained eruption (≈10 h longer), most likely a high-velocity but low-pressure ejection at the source, the Kasatochi eruption, with andesitic magma composition (Waythomas *et al.* 2010), produced a sequence of five short but powerful (higher pressure) explosions (≈26 to 68 min each), generating stronger infrasound signals with shorter durations registered at larger distances (Arnoult *et al.* 2010, Fee *et al.* 2010c).

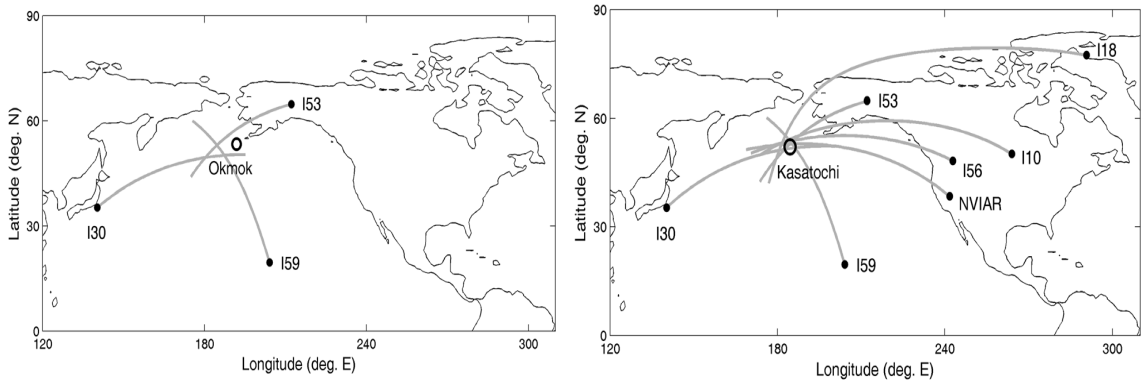

Figure 2.32. Simple back azimuth projections along the great circle paths from IMS stations results: a) in an average location that is approximately 500 km west of Okmok and encompasses a region approximately 450 km wide; b) in an average location that is approximately 200 km west of Kasatochi and encompasses a region several hundred kilometers wide (Fee *et al.* 2010c)

The deviations in measured azimuths of arrival for the estimated locations of the Okmok and Kasatochi eruptions varied by around 500 and 200 km respectively, with inaccuracies of hundreds of kilometres likely due to the presence of atmospheric winds. Possible approaches to minimising inaccuracies in the estimated location should include the use of an atmospheric propagation model that integrates the wind and propagation effects and the installation of infrasound arrays closer to the sources, thus reducing the distance over which wind can affect signal propagation.

The explosive phase of the 2009 Redoubt eruption generated a considerable number of infrasound recorded at a local station and in multiple IMS infrasound arrays (Figure 2.33). The availability of local infrasound data offered a unique opportunity to evaluate the use of infrasound to characterise volcanic eruptions, in this case the waveform representation of the acoustic source (Fee *et al.* 2011b).

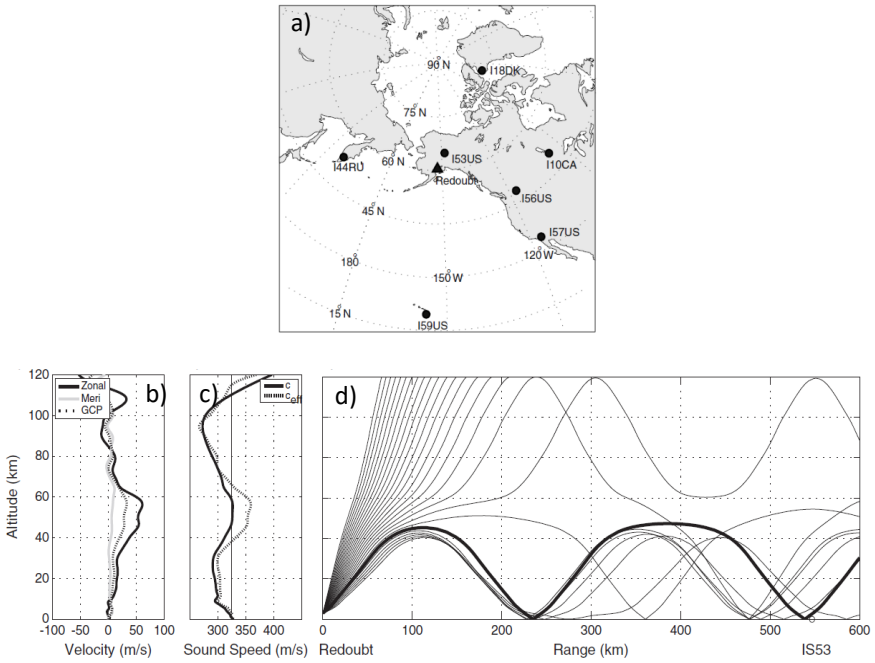

Figure 2.33. Map of Alaskan Redoubt volcano (black triangle) and IMS stations (black circles) in a 4,600 km radius. Profiles and ray tracing from Redoubt to I53US; b) Winds above Redoubt for 28 March 06:00: Zonal winds (solid black line), Meridional winds (gray line) and great circle path (GCP) winds (dotted black line); c) typical high-latitude shape of sound speed (solid black line) above Redoubt and effective sound speed (dotted black line) with a broad maximum in the stratosphere (due to the zonal winds); d) Ray tracing from Redoubt to I53US, with most rays being refracted in the stratosphere. The eigenray (dark black line) is refracted at approximately 45 km height and has a single ground reflection around 225 km (from Fee *et al.* 2011b).

The station closest to the source (I53US), located in Fairbanks, Alaska (547 km), was used to derive source constraints for the explosive events. Local and remote acoustic data were compared to determine the accuracy of these constraints. Basic propagation modelling and analysis of atmospheric models were also carried out to help understand the remote data and comparisons with local stations (Fee *et al.* 2011b). This research demonstrates the potential of using remote infrasound arrays in the detection and characterisation of energic volcanic eruptions, and shows how, under typical meteorological conditions, can accurately represent the acoustic source. High-resolution, near-real-time G2S models may also be used to estimate the quantity of ducts and the estimated waveform integrity (Fee *et al.* 2011b).

The June 2009 eruption of Sarychev Peak, in Kuril Islands, Russia, produced significant infrasound that was recorded on six stations of the IMS infrasound network and several stations of the Korea Institute of Geoscience and Mineral Resources (KIGAM) infrasound network at ranges of ≈640 – 6,400 km (Figure 2.34). After performing median back-azimuth cross-bearings from the three closest stations, IS44 (643 km), IS45 (1,690 km), and IS30 (1,774 km), the source location was determined with a mean source centroid of ≈33 km from the true location of Sarychev Peak, with no atmospheric propagation correction was applied. This error was reduced to ≈15 km using the infrasonic first

arrivals and an atmospheric propagation correction based on 3D ray-tracing and hindcast predictions from the European Centre for Medium-Range Weather Forecasts (ECMWF).

This study also showed that the geometry at the source, the event duration, diffraction and scattering from atmospheric inhomogeneities can affect the propagation path of infrasound from large-scale explosive volcanic eruptions. It was also concluded that the current coverage of the Kuril Islands region by IMS stations is already adequate to provide important information for volcanic monitoring (Matoza *et al.* 2011b). The June 2009 Saryshev Peak eruption ash clouds are an example of how volcanoes can inject substantial ash into the atmosphere and disrupt air traffic in the region (Salinas 2010).

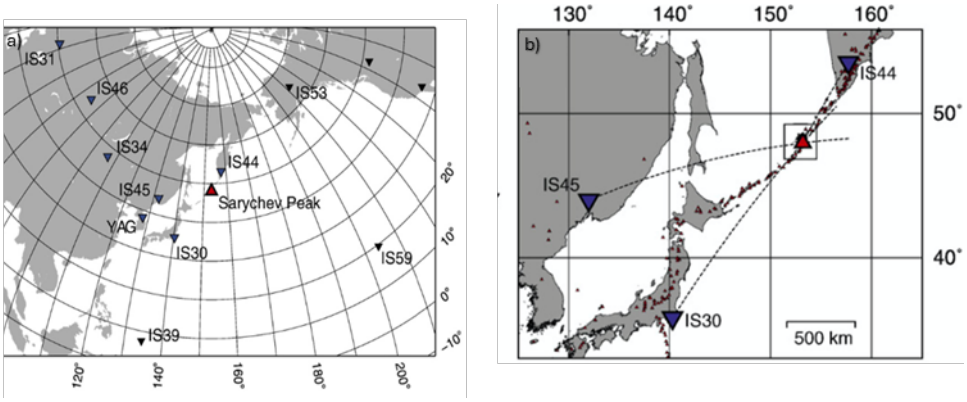

Figure 2.34. Map with the location of Sarychev Peak (SP, red triangle), where blue inverted triangles refer to the array stations that registered the eruption signal and black inverted triangles the stations that did not register the eruption signal (from Matoza *et al.* 2011b).

In 2010, the April–May Eyjafjallajökull summit eruption, Iceland, was recorded by 14 infrasonic stations (Figure 2.35). Four of them (IS18, IS26, IS43, IS48) are stations belonging to the IMS global network, and the other 10 stations (BKNI, LYCK, KIRU, DBN, JAMT, IGADE, FLERS, ARCI, SODA, ADBF) operated by different European research institutes. The mean centroid of the maximum intersection signal back-azimuths projected back from each station points to ≈50 km north of the true location of Eyjafjallajökull (Matoza *et al.* 2011a).

The onset of the eruption took place on 14 April and the highly explosive activity that continued over the next 3 days generated an ash plume that extended up to altitudes of about 9.5 km *a.s.l.* (Gudmundsson *et al.* 2010). Due to the uncommonly sustained anticyclonic meteorological pattern in the south of Iceland, the ash drifted mostly to the south and southeast, leading to great disruption in commercial air traffic over Europe (*e.g.,* Petersen 2012).

Although variations in atmospheric propagation and background noise levels in the sensors generate fluctuations in signal-to-noise ratios and signal detectability, array processing techniques successfully discriminated between volcanic infrasound and coherent and incoherent ambient noise

(*e.g.,* microbaroms), thus indicating that infrasound from medium-sized eruptions can propagate for thousands of kilometres in atmospheric waveguides.

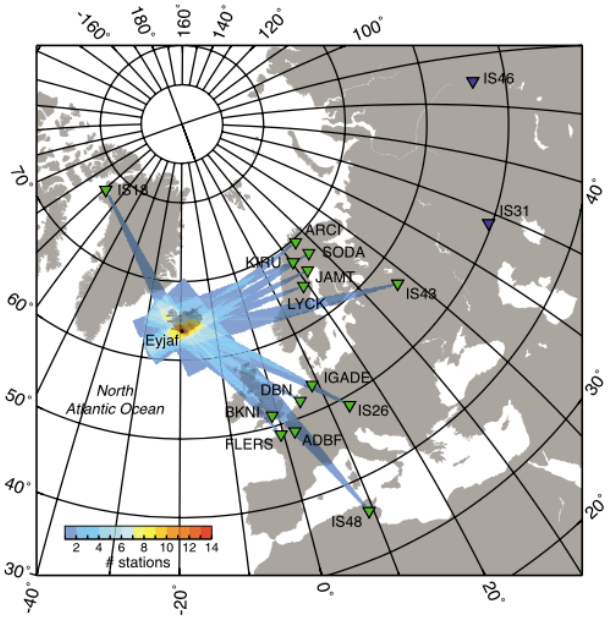

Figure 2.35. Map showing the 14 remote infrasonic arrays (green inverted triangles) that registered the Eyjafjallajökull eruption in April-May 2010, ranging from ≈1,745 km (BKNI, United Kingdom) to ≈3,666 km (IS48, Tunisia). The colour scale indicates the number of intersecting back-azimuths with an average infrasound signal of ± 3° registered at each station and associated with Eyjafjallajökull (from Matoza *et al.* 2011a).

Matoza *et al.*, 2011a, highlight the remarkable long-distance propagation of infrasonic signals from Eyjafjallajökull and use it to emphasize the potential of infrasonic data for detecting explosive volcanic activity in remote regions of the planet where terrestrial-base monitoring techniques are scarce.

Infrasound signals generated by the eruption of the Eyjafjallajökull volcano have also provided an overview of the effect of stratospheric tidal motions on acoustic propagation over distances ≥ 1,500 km, suggesting that, for propagation over long distances, the region of weakest stratospheric ducting will control the amplitude of the signal reaching the station (Green *et al.*, 2012). Independent factors can affect the diurnal variations of the signal bandwidth, such as an increase in the acoustic duct strength, since the reinforcement of the diurnal tidal wind in the stratosphere can enhance the signal-to-noise ratio and incoherent ambient noise at the receiver. Diurnal variations of the turbulence near the ground can reduce the noise at night and consequently enhance the signal-to-noise ratio and the detectability of the signal.

To date, these long-range studies have been focused on individual volcanoes or a small set of volcanoes, mainly studying the characteristics of a specific eruption or evaluating sound propagation models and atmospheric features.

Dabrowa *et al.* (2011) explored the potential of the IMS infrasound network to provide chronologies of remote global explosive volcanism, with the potential to set source parameters for ash transport and dispersal. This was the first study to bring together general trends in the global characteristics of volcanic infrasound to demonstrate how an estimate of eruption intensity could be made using only long-range infrasound data. Using the Smithsonian Institute's volcanic eruption database, they compiled a catalogue of 39 volcanoes and 110 individual volcanic events between 2002 and 2009 (Figure 2.36). Considering the results detections delay and the location capability of the network, Dabrowa *et al.* (2011) investigated the size of the eruption that we could expect to detect on the network at a given distance. This large dataset and global view enabled the identification of new relationships between volcanic infrasound and important eruption parameters, which were found to be consistent across a wide variety of eruption styles.

For each volcanic explosive activity, data from the two closest stations to the volcano (if available) were analysed and, if an event was detected, i.e. if a coherent infrasonic signal received from a suitable back azimuth range (within ±5° in 86% of events and always within ±10°) with acceptable apparent velocities between (300 - 400 m/s), more distant stations were added until no signal was identified at two successive stations.

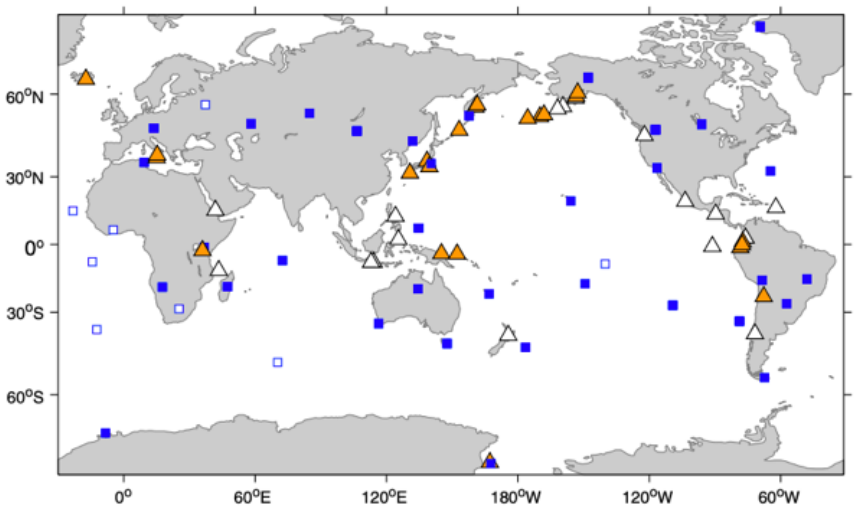

Figure 2.36. Map of the studied volcanoes (triangles) and the IMS infrasound stations used (filled squares), in operation since 1 January 2010. Highlighted volcanoes (filled triangles) produced infrasound that was detected by at least one IMS station during the study while the open triangles show the volcanoes from which no infrasound was detected (Dabrowa *et al.* 2011).

Of the 39 volcanoes investigated 56% were detected by a minimum of one IMS station during at least one event. Of the 110 individual events analysed and related to plume heights, of the 66 events with plume heights of more than 6 km, 48 were detected by at least one infrasound station and 39 were detected at maximum distances of more than 1,616 km. In contrast, of the remaining 44 events

with maximum plume heights of 6 km, only 20 were detected by at least one IMS station. Just 38% of individual events analysed were not detected at any station.

This study indicated that the distance at which an event is detectable increases by approximately 1,000 km for every 4 km increase in the maximum plume height suggesting that events producing tall plumes also generate infrasound with high amplitudes enabling their detection at greater distance (Figure 2.37). Events that produce plumes of greater than 6 km height may be detectable on the IMS if the closest station to the volcano is within approximately 1,600 km along with other factors that could promote detection at greater distance like wider frequency range or a longer duration, giving the signal a greater chance of being detected either at a frequency or during a time period with low background noise (Dabrowa *et al.*, 2011).

An important step in monitoring explosive volcanic activity at a global level was taken by Matoza *et al.* (2017), who developed a new method to systematically search through multi-year data (2005–2010) from the IMS infrasound network. This signal association and location method algorithm (IMS_vASC) uses array processing results to automatically recognize detections and catalogue global explosive volcanic signals occurring anywhere on Earth (Figure 2.38).

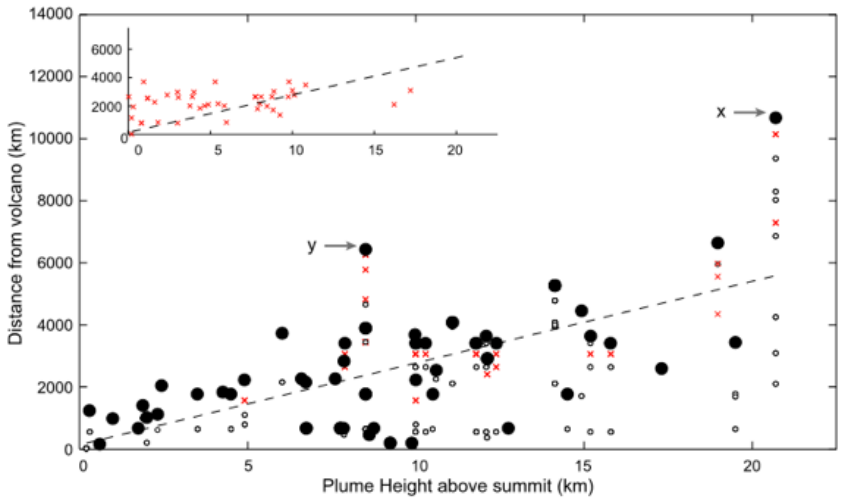

Figure 2.37. Detections (circles) and non-detections (crosses) of volcanic infrasound from eruptions in the study. The dashed lines represent the linear best-fit line to the maximum detected distances. The minimum source–receiver distance is shown on the inset plot (Dabrowa *et al.* 2011).

Compared to the previous work of Dabrowa *et al.*, (2011), which analysed systematically, although manually, infrasound data records for periods related to known eruptions (from the GVP database), in this work, the researchers developed these efforts by carrying out automated searches trying to backtrack from the infrasound data to detect possible evidence of volcanic eruptions.

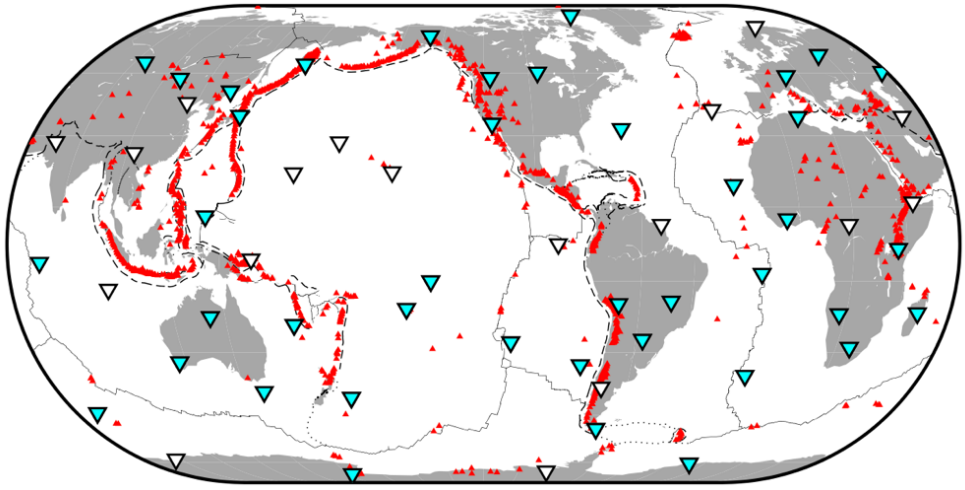

Figure 2.38. Global map with Holocene potentially active volcanoes (red triangles) and the IMS infrasound network (inverted triangles), where the stations included in this study (41 stations), are shown in cyan (from Matoza *et al.* 2017).

They create array processing detection lists by using PMCC method (see Chapter 4, Section 4.2), and estimate the wavefront parameters (*e.g.*, back-azimuth, apparent velocity, and root-mean-square (RMS) amplitude) of coherent plane waves using correlation time delays between successive array element triplets or subnetworks (*Cansi*, 1995).

For each time interval (2 or 10 days) the authors performed a grid of trial source nodes on the Earth's surface with a regular spacing in latitude and longitude of 0.2° and sort all available stations with respect to distance from the trial source node (Figure 2.39). For the detections of each station, using a log frequency band configuration ranging from 0.01 Hz to 5 Hz (more suitable for broadband volcanic signals), arrival times were adjusted assuming a constant celerity of 0.33 km/s and a back-azimuth deviation tolerance of 2°, 5° or 10° depending of the case. The different grids created by the algorithm were then compared and the results compiled in a global explosive volcanic events catalogue (Figure 2.40).

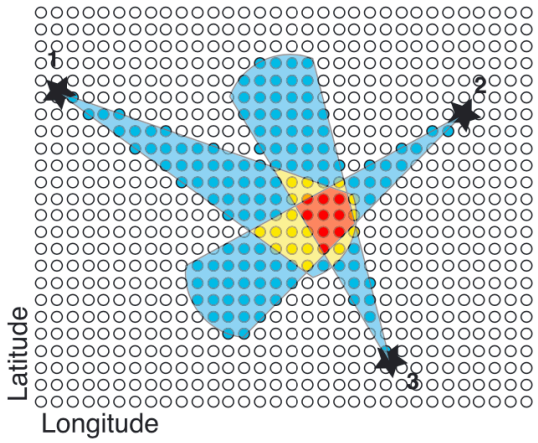

Figure 2.39. Infrasound signal association and source location using a brute force, grid search and cross-bearing approach algorithm. A grid of trial source nodes has been defined on the Earth's surface with a regular spacing in latitude and longitude (0.2°). Three stations are indicated by black stars. The back azimuth of an array detection from each station was used within a given azimuth deviation tolerance and for a maximum great circle distance. In this illustration, the blue, yellow and red test source nodes (grid points) have values of 1, 2 and 3 respectively (from Matoza *et al.* 2017).

The algorithm detected automatically, associated and located 3 of the 7 VEI 4 eruptions reported globally during this period by the Smithsonian GVP bulletins (Siebert and Simkin, 2002; Global Volcanism Program, 2025). However, only 3 of the 31 of the VEI 3 reported events in the GVP, were included in the catalogue.

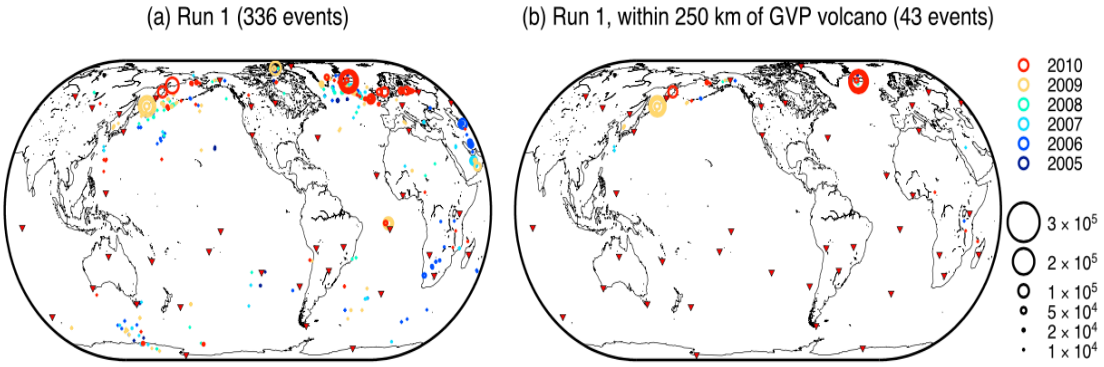

Figure 2.40. Global infrasound catalogues for data from 1 April 2005 to 31 December 2010. Infrasound events are shown as circles coloured by the year of occurrence (see legend on right). Red inverted triangles show the 41 stations used; b) represent the same catalogues as a), but where only events within 250 km of a known GVP volcano (Siebert and Simkin, 2002; Global Volcanism Program, 2025) are shown (from Matoza *et al.* 2017).

CHAPTER 3 |

Infrasound propagation

3.1. Physical properties of sound waves

3.1.1. Sound wave

A sound wave is a pressure variation or oscillation in an elastic medium such as gas (air), solid or liquid, generated by a vibrating surface or a turbulent liquid flow (Hansen 2001). Sound propagates in the form of longitudinal elastic waves (i.e. the motion of the particles is parallel to the direction in which the wave is moving) in a successive pattern of regions of high pressure (condensation or compression) and regions of low pressure (rarefaction). It moves away from the source of sound with the propagation velocity of the acoustic waves (speed of sound).

Figure 3.1 illustrates an image of a wave radiating from a source point with a pressure p(x) at a fixed time t. If we select two points x_1 and x_2, the sound from these points p(t) and q(t) are distinct but come from the same source, with a time difference (Δt) between them:

$$p(t) = q(t \pm {}^{r}/_{c}) \qquad \text{(Eq. 3.1)}$$

where if we consider that sound propagates at a speed of c, we can say that Δt = r/c where r is the distance between the two points, c is the propagation velocity of the sound wave and their ratio r/c corresponds to the time difference Δt required for the sound to propagate from p to q.

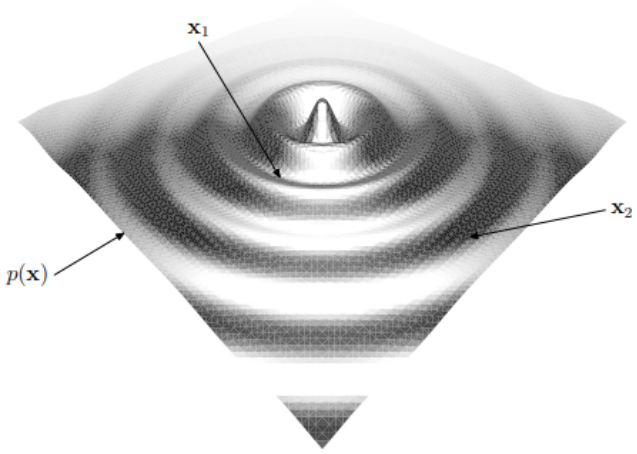

Figure 3.1. Sound pressure *p* at a fixed time (Carley 2011).

The propagation of sound waves is controlled by the properties of medium they travel in, which can lead to reflection, refraction and signal attenuation. For a given temperature, the relation between density and pressure, will define the speed of sound (c) of the medium as:

$$c = \sqrt{\frac{dp}{d\rho}} \qquad \text{(Eq. 3.2)}$$

where *dp* is the change in pressure and *dρ* is the change in density.

A sound wave is fully characterized by its speed, period, frequency, amplitude and wavelength. As a result of particle motion, pressure perturbations are created and can propagate within a medium. In theory, all the sources of sound can be represented by closed surfaces around the source and assuming a perfect coupling.

3.1.2. Pulsating sphere

Through the Navier Stokes equations, it can be inferred three main statements about the characteristics of sound: 1) the sound at instant t depends on the sound at instant t -r/c; 2) the waveform remains unchanged and 3) the pressure magnitude decreases as the wave is propagated. Acoustic sources can be modelled as closed surfaces around them, assuming an ideal coupling. The simplest three-dimensional acoustic model that can be recognised is the radiated sound of a pulsating sphere (*e.g.*, a bubble or an approximation to a body of variable volume).

Taking the linearised momentum equation (Kinsler *et al.* 2000), it is obtained a relation between the acceleration and the pressure gradient:

$$\nabla p = -\rho_0 \frac{\partial \mathrm{v}}{\partial t} \quad \text{(Eq. 3.3)}$$

Considering a sphere of radius a and vibrates with a velocity of amplitude V and a frequency ω, its radial surface velocity v and pressure p can be expressed as:

$$v = Ve^{-jwt} \quad \text{(Eq. 3.4)}$$

$$p = Pe^{-jwt} \quad \text{(Eq. 3.5)}$$

Applying equations (3.4 and 3.5) to the linearized acceleration-pressure gradient relation, the result can be given as:

$$p = \frac{f(t - {}^{r}/_{c})}{r} = \frac{Ae^{-jw(t-{}^{r}/_{c})}}{r} \quad \text{(Eq. 3.6)}$$

where r the distance from the centre of sphere, t is the time, c is the velocity of sound in the medium, □ is the angular frequency of sphere vibration and A is its amplitude to be found from the boundary condition at a (the sphere surface). The pressure gradient can be written as:

$$\nabla p = \frac{A}{r^2}\left[\frac{jwr}{c} - 1\right] e^{-jw(t-{}^{r}/_{c})} \quad \text{(Eq. 3.7)}$$

and applying the boundary condition:

$$\frac{A}{a^2}\left[\frac{jwa}{c} - 1\right] e^{-jw(t-{}^{a}/_{c})} = jw\rho_0 V e^{-jwt}$$

we can define the constant A as:

$$A = \frac{(ka)(ka - j)\rho_0 Vca}{(ka)^2 + 1} e^{-jka}$$

where k = ω/c is the wave number.

The pressure output is then:

$$p = \frac{ka}{r}\frac{ka - j}{(ka)^2 + 1}(\rho_0 Vca)e^{-jk(r-a)}e^{-jwt} \quad \text{(Eq. 3.8)}$$

where ρ_0 is the equilibrium density of the medium. The parameter ka is a non-dimensional characteristic called compactness. Two different approaches can be taken to simplify this equation. When ka ≪ 1 (*i.e.*, when the sphere is small or it vibrates at low frequency), equation 3.8 can be written:

$$p \approx -j\frac{\rho_0 cka^2}{r} V e^{jkr} e^{-jwt} \quad \text{(Eq. 3.9)}$$

When ka ≫ 1 (*i.e.*, when the sphere is large or vibrating at high frequency):

$$p \approx \frac{\rho_0 V c a}{r} e^{jk(r-a)} e^{-jwt} \quad \text{(Eq. 3.10)}$$

When ka is small, the source is point-like and can be treated as a simple source; when it is large, the acoustic field becomes more complicated (Johnson 2003).

3.1.3. Monopole source mechanism

The vibrating sphere model is useful to calculate the noise radiated by a point source (Vergniolle and Caplan-Auerbach 2006). When the sphere vibrates, it injects momentum into the fluid as:

$$M = \rho_0 4\pi a^2 V e^{-jwt} \quad \text{(Eq. 3.11)}$$

where *a* is sphere of radius, V is the velocity of oscillation and *ω* is the angular frequency of sphere vibration. The rate of change of momentum is:

$$\frac{\partial M}{\partial t} = -j\rho_0 w 4\pi a^2 V e^{-jwt}$$

Since ω = kc, and compare it with equation 3.6, sound is generated by fluctuation in moment, and express it in terms of a source strength $q = \rho_0 v(t)$, came:

$$p = \frac{\partial}{\partial t} \frac{q(t - {}^{r}/_{c})}{4\pi r} \quad \text{(Eq. 3.12)}$$

This equation defines the pressure at time t and distance r resulting from a monopole source (Lighthill 1978). A monopole (or single point) is the most common source modelled in infrasound studies and represents the mass flow rate fluctuation in a compressed source region, generating sound that is equally radiated in all directions. Multipole infrasound source mechanism can be described as the sum of the pressure fluctuations of individual sources.

3.1.4. Sound pressure level

Also, the velocity amplitude V is given by:

$$V = \frac{p}{\rho_0 c a} \quad \text{(Eq. 3.13)}$$

where p is related to the Sound Pressure Level (SPL) by:

$$SPL = 20 log_{10} \frac{p}{p_0} \quad \text{(Eq. 3.14)}$$

where p_0 is the reference pressure level (reference sound pressure of air is 20 μPa). This shows that the intensity of the sound influences the amplitude of the acoustic wave's velocity and subsequently, this affects the pressure variation around the acoustic source, as shown in equation 3.13.

3.1.5. Acoustic wave equation

Similarly to how waves in the water are perceived as disturbances on a flat surface, acoustic waves in the atmosphere can be perceived as small disturbances in an environment's background fluid. The linear wave equation governs the propagation of small (linear) disturbances in a compressible fluid. The Navier-Stokes equations are then applied to represent continuity and momentum for an immiscible fluid:

$$\frac{\partial \rho}{\partial t} + \nabla.(\rho \mathrm{v}) = 0 \qquad \text{(Eq. 3.15)}$$

$$\rho \frac{\partial \mathrm{v}}{\partial t} + \nabla p + \rho \mathrm{v} \nabla \mathrm{v} = 0 \qquad \text{(Eq. 3.16)}$$

These equations show that matter is conserved (conservation of mass (Eq. 2.3.19)) and that Newton's laws apply to both fluid and solid particles (conservation of momentum (Eq. 2.3.20)). Assuming that the fluctuations of the fluid's dynamic quantities are small, when deriving the wave equation, their products can be neglected. When decomposing the quantities:

$$\rho = \rho_0 + \rho'(t)$$

$$\mathrm{v} = \mathrm{v}'(t)$$

$$p = p_0 + p'(t)$$

where pedix *0* represents a mean value and the apex' a fluctuation.

Applying this premise to the continuity and momentum equations (3.18 and 3.19) and neglecting the second-order terms (products of small quantities), the linear Euler equations are obtained:

$$\frac{\partial \rho'}{\partial t} + \rho_0 \nabla.\mathrm{v}' = 0 \qquad \text{(Eq. 3.17)}$$

$$\rho_0 \frac{\partial \mathrm{v}'}{\partial t} + \nabla p' = 0$$

derive the equation and remove the velocity v':

$$\frac{\partial}{\partial t}\left(\frac{\partial \rho'}{\partial t} + \rho_0 \nabla . \mathrm{v}'\right) - \nabla\left(\rho_0 \frac{\partial \mathrm{v}'}{\partial t} + \nabla p'\right)$$

$$= \frac{\partial^2 p'}{\partial t^2} - \nabla^2 p' = 0$$

To deal with only one quantity at a time, it must be found (and linearised) a relationship between density and pressure:

$$p' = p - p_0 \approx \frac{\partial p}{\partial \rho}\Big| \quad (\rho - \rho_0) = c^2 \rho'$$

$$c^{2=} \frac{\partial p}{\partial \rho}\Big|_{\rho=\rho_0}$$

and finally, the wave equation for the acoustic pressure can be written:

$$\frac{1}{c^2}\frac{\partial^2 p}{\partial t^2} - \nabla^2 p = 0 \qquad \text{(Eq. 3.18)}$$

where *c* is the speed at which a small disturbance (*p*) propagates through a fluid. This is the fundamental equation in acoustics and gives a full description of the acoustic wave propagation properties in space and time and how these properties evolve.

3.1.6. Adiabatic speed of sound

The speed of sound is independent of the sound wave frequency (Worland and Wilson 1999); however it depends on the thermodynamic properties of the fluid, and it can be calculated based on the premise that sound propagation is adiabatic. For an adiabatic ideal gas process (*i.e.*, without heat transfer), a relation between pressure (p) and density can be established:

$$p = k\rho^{\gamma} \qquad \text{(Eq. 3.19)}$$

where γ is the ratio of the specific heats, k is the bulk modulus (resistance a uniform compression). Replacing p in equation 3.19:

$$= \gamma k \rho^{\gamma - 1} = \frac{\gamma p}{\rho},$$

$$p = \rho R T$$

So that:

$$c^2 = \gamma RT$$

$$c = \sqrt{\gamma RT}$$

where c is the speed of sound in an ideal gas, R is the molar constant, γ is the adiabatic index 1.4 for air and T the absolute temperature, therefore the adiabatic speed of sound can be written as:

$$c = 20.05\sqrt{T}\ (m/s) \qquad \text{(Eq. 3.20)}$$

The propagation speed of infrasonic waves is given by the medium in which they travel and the temperature.

3.1.7. Effective sound speed

Winds control the advection and refraction of sound. Horizontal winds have an essential role to play in the atmospheric ducting of acoustic energy. The vertical component of the wind is neglectable since vertical motions are very small compared to horizontal ones (Drob *et al.* 2013). As lower frequencies are involved the travel distances will be longer due to the low attenuation (Sutherland and Bass 2004). In a horizontally stratified atmosphere, the wind's effects on the speed of sound can be explained through the effective speed of sound, v_{eff} (e.g., Wilson 2003, Evers 2008, Hupe 2018):

$$v_{eff} = c_T + w_\alpha \approx 20.05\sqrt{T} + w_\alpha\ (m/s) \qquad \text{(Eq. 3.21)}$$

where C_T is the adiabatic speed of sound and $w_\alpha = v_h.\hat{n}_\alpha$ is the wind component in the direction of wave propagation. Considering α clockwise relative to the North, w_α can be obtained by projecting the horizontal wind vector, v_h, in α direction using the unit vector normal to the wavefront, $\hat{n}_\alpha$:

$$w_\alpha = \begin{pmatrix}\sin\alpha\\ \cos\alpha\end{pmatrix}.\begin{pmatrix}u\\ v\end{pmatrix} = u.\sin\alpha + v.\cos\alpha$$

Following Snell's law, gradual refraction of sound is controlled by effective sound speed. In case of an increase of effective sound speed with height, controlled both by temperature and winds, sound is refracted downwards, and inversely, in case of a decrease of effective sound speed sound is refracted upwards.

The effective sound speed ratio, $v_{eff-ratio}$, can be defined for a given layer according to the equation:

$$v_{eff-ratio} = \frac{v_{ff(z)}}{v_{ff(z_0)}} \quad \text{(Eq. 3.22)}$$

where $v_{ff(z)}$, is the effective sound speed at a reference altitude z, and $v_{ff(z_0)}$ the effective sound speed at the ground, z_0 = 0 km, (*e.g.*, Le Pichon *et al.* 2012). Refraction of an upward-propagating signal towards the ground is predicted when $v_{eff-ratio} \geq 1$.

3.2. Linear and non-linear propagation

The pressure disturbances generated by most acoustic phenomena in daily life are very small compared with the ambient pressure of the medium and can be accurately predicted with the linear wave equation (eq. 3.18), that assumes that the amplitude of the sound is infinitesimally small. As an example, the amplitude of a dialogue between two persons is approximately 0.02 Pa (60 dB relative to 20 µPa), compared to atmospheric pressure at sea level of around 101 kPa (194 dB relative to 20 µPa) (Pierce 1981). However, there are many cases where the sound amplitude is so great that the linear theory doesn't apply (Atchley 2005).

In linear acoustics, it is assumed that a) the speed of propagation is independent of amplitude and frequency of the sound wave, b) the speed of the medium (wind velocity) is assumed to be substantially less than the speed of sound, c) the medium bounces back to its original state after the wave has flown through it, and d) the principle of superposition holds for the interaction of multiple sound waves, *i.e.,* the total effect is the sum of the individual effects (Atchley 2005).

In the case of geometric propagation, each frequency component will lose amplitude at the same rate (*e.g.*, 1/r for spherical propagation waves) in function of its absorption coefficient in the medium (Pierce 1981, Sutherland and Bass 2004).

If these assumptions are valid and properties of the medium are known, the pressure time history recorded at a given distance allows to calculate the pressure time history at the source (*e.g.*, explosion yield of a man-made source or the mass flow rate of a volcanic explosion).

When the amplitude of the pressure disturbance is greater than the ambient pressure of the medium, the principle of linear propagation no longer prevails. Sound waves produced by very

high amplitude acoustic sources can travel faster than the speed of sound (*i.e.*, supersonic) and propagate non-linearly.

The passage of a sound wave at high differential pressures has non-negligible impacts on the medium (*e.g.*, changes in temperature and particle velocity) (Atchley 2005). Because of this, the waveform deforms as it moves, and when the compression phase (high amplitude) moves faster than the rarefaction phase (negative), it generates a sharp discontinuity in pressure known as a shock wave (Kinney and Graham 1985).

The Friedlander equation (Friedlander 1946) is commonly applied to define the pressure of a shock wave, (p(t)):

$$p = P_0 \ e^{-\frac{t}{t^*}} \left(1 - \frac{t}{t^*}\right) \qquad \text{(Eq. 3.23)}$$

where P_0 is the overpressure at the source and t* is when rarefaction starts after compression back to ambient pressure (relaxation time). The amplitude of these non-linear waves decays after some distance and is transformed into linear sound waves.

Similarly, the end of the wave may overtake the lowest amplitude (rarefaction) portion of the wave, leading to the formation of sawtooth or N-waves (Wright 1983*,* Maher *et al.* 2020).

Non-linear propagation has a far less impact on the waveforms recorded locally at volcanoes than the effects of winds and topography (Maher *et al.* 2020) and a greater effect on the frequency of the recorded waveform compared to the amplitude as the infrasound propagates away from the source (deGroot-Hedlin 2016).

The assumption of linear acoustic propagation is most likely valid in a wide spectrum of studies.

3.3. The role of atmosphere

The Earth's dry atmosphere is the relatively thin gaseous envelope that encloses the planet, primarily composed of nitrogen (N_2, 78%), oxygen (O_2, 21%), Argon (Ar, 0.9%), water vapor (H_2O, 0-4%) and trace amounts of other gases (important in the atmosphere's thermodynamic and radiative heat) such as carbon dioxide (CO_2), Neon (Ne), Helium (He) and Hydrogen (H_2). The ozone layer (O_3) lies between 30 km and 50 km altitude (Arhens 2009). The Earth atmosphere extends from the terrestrial surface to about 560 – 1000 km of altitude (thermopause). It is structured in layers defined according to their physical and chemical characteristics, gas concentration and temperature profile in troposphere, stratosphere, mesosphere and thermosphere, limited by three transition zones known as tropopause, stratopause and mesopause. (NOAA 2017).

The temperature gradient profile in a standard atmosphere (Figure 3.2) shows a sequence of positive and negative temperature gradients as well as constant temperature zones.

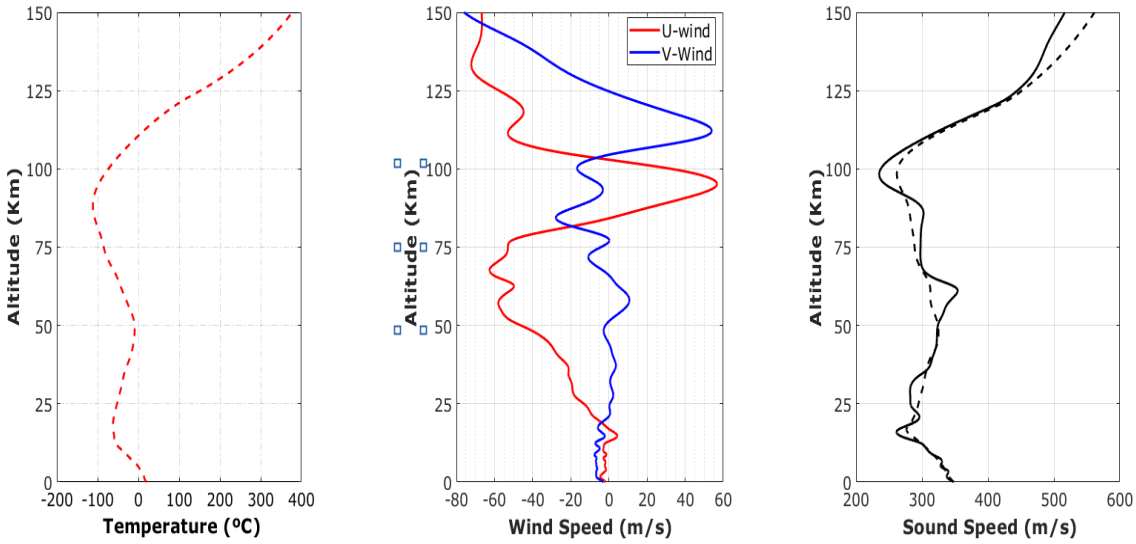

Figure 3.2. Atmospheric vertical profile at IS42 station (Lat: 39.04 N, Long: -28.0 W) shown as a climatological mean for 22 January 2022 (blue) temperature and the meridional (N-S) and zonal (E-W) wind velocities, red and blue respectively. Data were obtained from NASA MERRA-2, NRLMSISE-00 and HWM empirical models.

The troposphere is limited by the Earth's surface and the tropopause. The thickness varies between 7 km during summer in the poles, up to 17 km in the equatorial regions, and concentrates 75% of the atmospheric mass and 99% of humidity. Due to the role of water vapour, it is the region where most of the storms and other meteorological phenomena (rain, hail, snow, cloud formation, lightning, *etc*.) occur. The troposphere is a region with strong negative gradient of pressure and temperature, the latter steady decreases (6 °C per km) with the increase of the altitude, from an average of 15 °C to 20 °C on the Earth's surface to -51 °C near the tropopause (Figure 3.3). Consequently, the speed of sound decreases with increasing altitude. Its upper limit is defined where a thermal inversion occurs, implying a change in the direction of both the temperature and the sound speed gradients.

The mesosphere is the third layer of the atmosphere, between 50 km and 90 km of altitude. It is the coldest region of the atmosphere where the temperature decreases with the increasing altitude, dropping to the absolute minimum near -110 °C at mid-latitudes (-160 °C above summer pole) at the top of the layer. This negative temperature gradient accelerates the infrasound propagation towards its outer layers. The mesosphere is less stable than the stratosphere and

presents with vertical mixing. At its upper limit, the mesopause, from 90 to 100 km above the Earth's surface, is the transition zone between the mesosphere and the thermosphere.

The stratosphere, stratopause, mesosphere, and mesopause form the middle atmosphere.

Commonly referred to as the upper atmosphere, the thermosphere is the upper layer of the atmosphere, above 90 kms in altitude and limited by the thermopause, which marks the transition to the exosphere, occurring at heights that varies between 560 kms and 1000 kms due to the prevailing solar activity. In the thermosphere the molecules absorb high energy from ultraviolet and x-ray radiation and the temperature varies from -100 °C near the mesopause to 2000 °C near the thermopause (Figure 3.3). From 100 to 120 km of altitude the temperature and consequently the sound speed, gradually increase until remains constant at exobase, and above 120 km air particles are so rare (vacuum) that sound waves cannot propagate.

The different incidences of the sun induce a temperature gradient from the warm summer pole to the cold winter pole. For this geostrophic motion, the Coriolis force balances the horizontal pressure gradient, while the thermal balance of the wind relates the vertical wind shear to the horizontal temperature gradient (Muench 1965, Kriester 1972, Smets 2018).

During the winter, the poles become much colder than the tropics, resulting in a strong meridional temperature gradient. The low-pressure region above the pole is enclosed by a belt of strong high-altitude westerly stratospheric winds, known as the polar night jet stream (around 50°- 60° latitude), and collectively form the Stratospheric Polar Vortex (SPV). The lower part of the vortex is the zonal wind pattern, commonly named the stratospheric jet, at altitudes of 50 - 60 km, reaching speeds of around 45-55 m/s and shifting direction twice a year. The strength of the stratospheric polar circulation, whether weak or strong, is a major player in stratosphere–troposphere coupling and in weather and climate variations at northern mid- and high-latitudes (Holton *et al.* 1995*,* Douville 2009), with sudden stratospheric warmings (SSW) being the most impressive dynamical events. At approximately 2-year cycles, the Arctic stratospheric vortex is disrupted by planetary-scale waves (Kelvin and Rossby) propagating from the troposphere and breaks down as a consequence of the temperature increase of tens of degrees in a few days, leading to the typically strong westerly winds being swapped by weak easterly winds (e.g., Baldwinn *et al.* 2021).

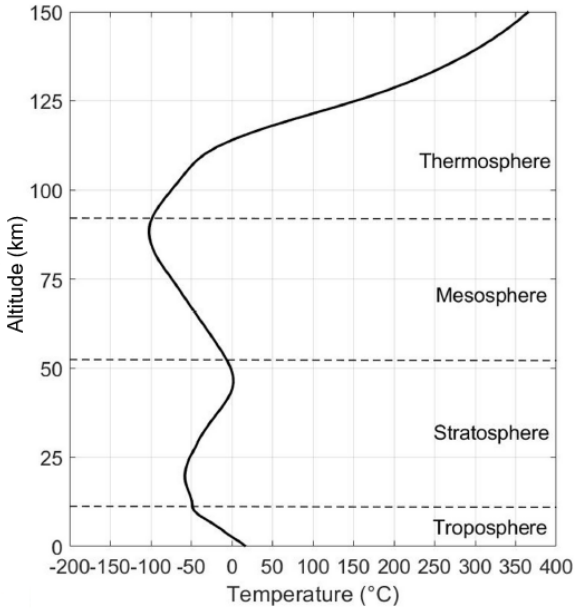

Figure 3.3. Vertical Thermal structure of the Atmosphere.

3.4. Infrasound propagation

The state of the atmosphere strongly governs infrasound propagation, mainly by a) the attenuation due to the absorbing properties of the atmosphere; b) the refraction heights driven by sound-speed gradients; c) reflections by the ground terrain; d) scattering by atmospheric turbulence; and e) the azimuthal deviation due to winds (de Groot-Hedlin 2008). In general, infrasound loses energy through absorption and geometric spreading, is deflected by the wind and refracted according to the velocity profile of the atmosphere.

In a horizontally stratified atmosphere infrasound propagation can be approximated to first order by the effective speed of sound *c*eff = *cT* + *wa* (Figure 3.4), resulting as the sum of the adiabatic speed of sound (*cT)* and the horizontal wind in direction of propagation (*wa*) (Godin 2002).

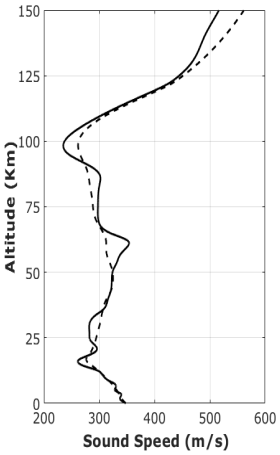

Figure 3.4. Adiabatic (dashed line) and effective (solid line) sound speed at IS42 station for 22 January 2022 (Lat: 39.04 N, Long: -28.0 W).

The refraction of infrasonic signals is conditioned by the speed of sound gradient variations (Brekhovskikh and Godin 1999). The refractivity or ducting of the atmosphere can be expressed by the ratio between the effective sound speed at a given altitude and the effective sound speed on the ground. When this ratio is greater than one, refraction is predicted and the signal is expected to refract towards the ground, indicating that we are in the presence of an atmospheric waveguide or duct (e.g., Wilson 2003, Le Pichon *et al.* 2012).

Looking at the effective sound speed profile in Figure 3.4, it is clear that any wave reaching the thermosphere (around 110 km) will be refracted downward, as the effective sound speed (>350 ms) is larger than the one at the ground. Therefore, a thermosphere duct is always expected. The stratopause is also a good candidate. Here, the adiabatic sound speed is typically just lower that the one at the ground, but the effect of stratospheric jets can increase the effective sound speed to exceed the one at the ground and establish a seasonal stratospheric duct. In the troposphere, adiabatic sound speed is generally lower than the one at the ground (Figure 3.4) but high wind can strongly affect the effective sound speed and allow downward refraction of infrasound waves.

The establishment of such ducts, commonly known as waveguides (de Groot-Hedlin *et al.* 2010), allows infrasound waves to propagate over long distances, ranging from hundreds to thousands of kilometers, due to multiple reflections in the various atmospheric layers (Drob *et al.* 2003) and the low attenuation in acoustic waveguides (Sutherland and Bass 2004, Evers and Haak 2010).

3.4.1. Waveguides

Established between the ground and high temperature and wind speed regions in the troposphere, stratosphere, and thermosphere, three dominant atmospheric waveguides can be distinguished on downwind direction for propagation of distances greater than 1,000 kilometres (Le Pichon *et al.* 2012), by: 1) signals that refract in the troposphere (0-16 km), mainly bound by the mid-latitude jet stream around the tropopause (~10 km); 2) signals that refract in the stratosphere (10-60 km) as the result of the wind and the temperature increase, induced by the presence of ozone; and 3) signals that refract in the thermosphere (110-160 km) where infrasound attenuation is naturally stronger (Garcés *et al.* 2004, Assink *et al.* 2012).

In the troposphere, the influence of winds (jet stream winds) is great enough to occasionally compensate the decrease in the speed of sound, while in the thermosphere, where the waveguide is more absorptive, temperature is the only variable that controls the speed of sound and is therefore not as important as in the other ducts. The ground-to-stratosphere duct is the most important for the propagation of acoustic energy, due to the importance of specific temperature and the strong gradient variations in stratospheric zonal winds (strength and direction), particularly during equinoxes (Drob *et al.* 2003).

In tropospheric and stratospheric waveguides, the absorption is minimal and propagation in opposite directions to the tropospheric and stratospheric wind is possible, but ducting is not. Tropospheric waveguides depend mainly on diurnal variations in temperature and wind speeds, while stratospheric waveguides are influenced by the presence of seasonal variations in stratospheric zonal winds (blowing from east to west and vice versa), thus indicating that long-range infrasound propagation depends predominantly on stratospheric duct (de Groot-Hedlin *et al.* 2011).

3.4.2. Infrasound phases

Depending on the waveguide through which they propagate or the refracting layer, infrasonic signal arrivals are divided into phases and referred to as *Iw, Is,* and *It* phases in terms of waves returned from the troposphere, stratosphere, and thermosphere, respectively. They are characterized by their trace velocity and celerity (*e.g.*, Ceranna *et al.* 2009*,* Vergoz *et al.* 2019).

Dependent on the tropospheric winds as well as on the nature of the local weather below the tropopause, *Iw* phases have a trace velocity in the range of the speed of sound (≈330 m/s) and celerity values around 340 m/s.

Stratospheric phases, *Is*, are seasonal arrivals due to the seasonal variation of the winds in the stratosphere (Brown *et al.* 2002), with trace velocities around 360 m/s and celerities range between 280 and 310 m/s with an average of 300 m/s (Le Pichon *et al.* 2006).

Waves propagating between the ground and the lower thermosphere, *It*, have trace velocities larger than 350 m/s and are characterized by low celerity of 250 to 280 m/s. Due to the strong attenuation in the upper atmosphere, only powerful infrasound sources, like major volcanic eruptions, can generate observable thermospheric returns (de Groot-Hedlin *et al.* 2011) (Figure 3.5). Depending on the atmospheric conditions, the same source may generate multiple arrivals that have been reflected several times between the boundary layer and the ground, with a subsequent number being assigned (*e.g.*, Iw2).

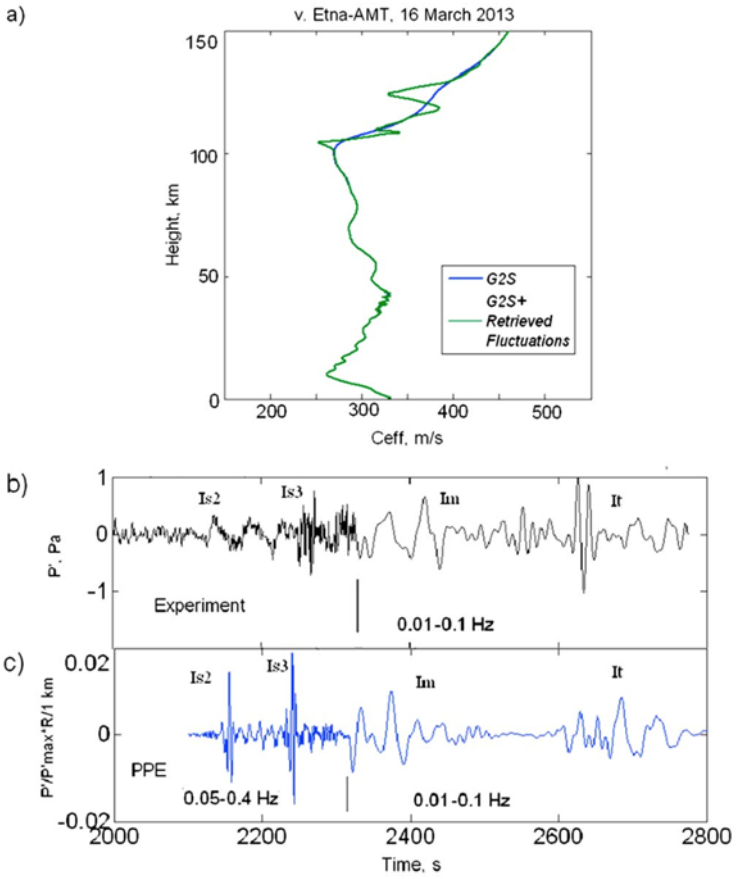

Figure 0.1. Atmospheric profile (a) considering effective sound speed (blue) and wind fluctuations (green). Experimental (b) and theoretical (c) waveforms showing multiple arrivals (stratospheric, mesospheric and thermospheric) of infrasound produced by an explosion at Etna volcano and recorded in Central Italy at a source-to-receiver distance of 632 km (from Chunchuzov *et al.*, 2015).

3.4.3. Ray tracing

Ray tracing is an efficient method for studying infrasound propagation in the Earth's atmosphere (*e.g.*, Blom and Waxler 2012, Lonzaga *et al.* 2015). Ray tracing is based on the principles of geometric acoustics (high frequency approximation applied to fluid mechanics

equations) and assumes that space and time scales of atmospheric properties (temperature, wind, density) are much larger than acoustic wave scales (Gainville *et al.* 2012). It assumes that sound waves travel in straight lines until they encounter a limit or a change in the medium that causes them to refract or reflect.

When a sound wave moves through the atmosphere, it crosses different layers, which causes changes in its speed and, therefore, in ray direction. The incidence angle to the layer boundary, along with the differences in temperature gradients and the adiabatic speed of the sound, will allow defining the refraction angle through the Snell's law. Hence, the sound wave's path (eigenrays) can be tracked, and its expected arrival time and amplitude can be calculated at a chosen location.

Eigenrays provide many important simulated parameters, such as travel time or array features like back azimuth and apparent velocity, and are also relevant for event analysis (*e.g.*, Evers *et al.* 2012*,* Assink *et al.* 2016) and inversion studies (*e.g.*, Assink *et al.* 2014*,* Smets *et al.* 2016), linking observations with atmospheric conditions (Blom and Waxler 2017).

Although an analytical solution for eigenrays can be determined for a stratified atmosphere (*e.g.*, Brekhovskikh and Godin 1999*,* Assink *et al.* 2012), it is not trivial for the proposed ray equations in a moving non-homogeneous atmosphere. Since the propagation is non-planar, inclination and azimuth angles are sought to produce a ray that returns to the ground at a specified location (Blom and Waxler 2017). A grid search is hence proposed to search for approximate solutions within a certain threshold and iteratively reduce the error in comparison to the real (shortest path) eigenray (Figure 3.6).

Consider a source at location x_s and an arbitrary receiver x_r, whereas $x_0 = x_s$, the Euclidean distance *l* between the source and the receiver will be:

$$l = \|x_r - x_s\| \qquad \text{(Eq. 3.24)}$$

A ray S launched from the source x_s with initial angles ϕ and θ in the direction of the receiver x_r is illustrated in x_l is the location when distance *l* is reached (due to atmospheric propagation effects), resulting in the offset '*d* ' from the receiver, thus the distance between the real source and x_l :

$$d = \|x_r - x_l\| \qquad \text{(Eq. 3.25)}$$

Ray *S* (ϕ, θ) is declared an eigenray when x_l falls within a threshold offset of the array, $d < d_{min}$, with minimum offset d_{min} roughly equal to the array aperture.

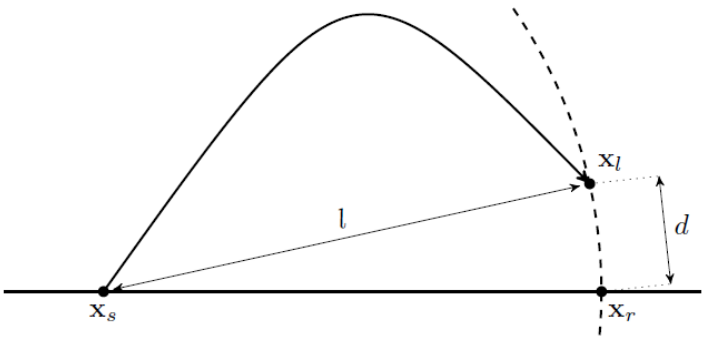

Figure 3.6. Eigenray grid research method (Gheri et al 2023).

3.4.4. Attenuation

The attenuation of atmospheric infrasound waves can be attributed to the acoustic energy transmission loss due to distance from the source, atmospheric absorption, and other. A total attenuation A_t in decibels (dB), can be described as a sum of three independent terms:

$$A_t = A_s + A_a + A_e \qquad \text{(Eq. 3.26)}$$

Where A_s is the attenuation due to geometric spreading, A_a is the attenuation due to atmospheric absorption and A_e is the attenuation due to other effects (that may not be present or necessarily act independently), such as ground attenuation; attenuation by diffraction and reflection of an obstacle; and reflection or scattering due to turbulence.

Wave propagation is subject to the geometric spreading loss (A_s) of the wavefront, and at a distance *r* from the source, is described respective to a reference distance of 1 km as:

$$A_s(r) = 20\ G \log\left(\frac{1}{r}\right) \qquad \text{(dB)} \qquad \text{(Eq. 3.27)}$$

where *G* describes the geometry, ranging from zero (no spreading loss) for plane wave propagation to one for spherical propagation (G=1/2 for cylindrical propagation).

During classical geometrical spreading, which is independent of the frequency and weather, atmospheric absorption is proportional to the squared frequency as well as attenuates infrasound signals due to thermal conductivity, viscosity and molecular relaxation effects (Sutherland and Bass 2004).

When sound waves propagate through the atmosphere, inhomogeneities, random fluctuations in temperature, and wind gradients scatter the acoustic energy in different directions. Also, turbulence produces fluctuations in the sound pressure level and direct

attenuation of sound by scattering energy out of a highly directed beam. As the atmosphere's density decreases drastically with increasing altitude, the acoustic pressure decreases proportionally to the square root of the density, while conversely, the particle velocity increases, proportional to the inverse square root of the density. As a direct consequence, the acoustic attenuation is greater, as well as tends to amplify nonlinearities of the signal propagation, which lead to signal steepening and lengthening (Lonzaga *et al.* 2015*,* Sabatini *et al.* 2016). In other words, the complex interaction among all these variables often poses challenges for predicting long-range infrasound pressure attenuation.

Numerical approaches for atmospheric infrasonic propagation studies have naturally been based on simplified equations. Ray tracing (Gainville *et al.* 2012*,* Lonzaga *et al.* 2015), parabolic models (Lingevitch *et al.* 1999*,* Le Pichon *et al.* 2012), and the normal mode theory (Haskell, 1951*,* Pierce *et al.* 1981) have been the most commonly used techniques.

Based on the linear wide-angle PE method, Le Pichon *et al.* (2012) provide an attenuation relation to probe a wide variety of realistic propagation conditions in the frequency band of interest for the detection of explosions.

This technique accounts for diffraction effects (near shadow zone boundaries), scattering (by minor inhomogeneities in the atmosphere), and wind convection, applying a range-independent effective sound speed computed in the propagation direction. The inputs from classical losses (translation and diffusion) and relaxation (rotation and vibration) were considered in the absorption model chosen. The proposed equation (Le Pichon *et al.* 2012) is:

$$A_p\left(f, V_{eff-ratio}\right) = \frac{1}{R}\ 10^{\frac{\alpha(f)R}{20}} + \frac{R^{\beta(f,V_{eff-ratio})}}{1+10^{\frac{\delta-R}{\sigma(f)}}} \qquad \text{(Eq. 3.28)}$$

where A_p is the pressure wave attenuation coefficient at a source-to-receiver distance R (km).

The equation can be de-composed into two terms, where the first one (near-field term) represents the attenuation in the shadow zone by spherical geometric propagation coupled with an exponential decay, while the second term (far-field term) represents the attenuation in the geometrical acoustic duct region. The four parameters α, β, δ and σ, were calculated using a multidimensional curve-fitting approach, where:

α - is the dissipation of direct waves (km $^{-1}$)

β - accounts for the geometrical spreading and dissipation of stratospheric and thermospheric waves

δ - width of the shadow zone (km), assumed to be constant

σ - is a scaling distance (km) controlling the strength of the attenuation in the shadow zone

The main difference of this equation with previous empirical yield amplitude scaling relations (*e.g.*, Whitaker, 1996) is the effect of stratospheric winds on attenuation, as the PE modelling accounts for an approximately binary variation in attenuation for V_{eff} ratios below and above 1.

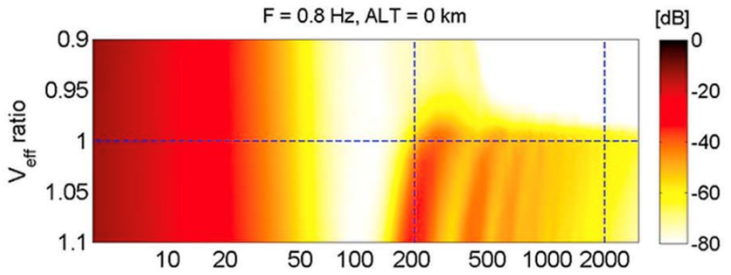

Figure 3.7. Expected attenuation for an infrasound wave with peak frequency of 0.8 Hz (from Le Pichon *et al*. 2012).

CHAPTER 4 |

Dataset and methods

This chapter presents the methods developed on the behalf of this work for obtaining coherent detections in IMS infrasound stations for volcanic activity, aiming to evaluate the capabilities of the IMS infrasound network in the detection and timely reporting of explosive volcanic events. For this, three major workflow phases were defined.

Phase 1 – Compilation of an Explosive Volcanic Activity Database: Build-up of a volcano database, based on GVP reports, by identifying and selecting active volcanoes that had eruptive activity with VEI≥ 3, from 2011 to 2020 (see Section 4.1).

Phase 2 – Infrasound Data Processing and Propagation Analysis: Processing data from 43 IMS infrasound stations at a source-receiver distance of up to 4,500 km from the selected volcanoes, to analyse their potential for detection and monitoring. The analysis involved array processing techniques (*e.g.*, back-azimuth and trace velocity estimation), and the identification of coherent detections potentially associated with volcanic sources (see Section 4.2). As complement and for comparisons with observational data and their validation, ECMWF atmospheric reanalysis datasets (ERA-Interin and ERA5) were used to assess stratospheric specifications (*e.g.*, temperature and horizontal wind components), for subsequent parameters calculations such as the adiabatic speed of sound, $V_{eff\text{-}ratio}$ or attenuation (A_t). Additionally, the empirical Ground-2-Space model was also used to apply raytracing techniques between the selected volcano and the nearest station, to analyse the possible arrival of infrasonic rays from the expected back-azimuth (see Section 4.3).

Phase 3 - Cross-Validation with IDC Bulletins: The IDC CTBTO bulletins (LEB, SEL3 and REB) were investigated to assess their ability to register and provide information on events that could be correlated with the volcanic events detected and processed on the previous step (see Section 4.4).

4.1. Volcanoes Database

The Global Volcanism Program (GVP) includes comprehensive list of the 1281 Earth's active volcanoes and their eruptions over the last 12,000 years. In this work, the database of the Smithsonian Institute's GVP portal was scrutinized to identify all volcanoes that had eruptive activity between 2011 and 2020. The selection was performed by reviewing records of volcanic activity available through the Bulletins of the Global Volcanism Network (GVP, 2025) and considering 4 criteria to be fulfilled:

a) Eruptive volcano must have an assigned name. Volcanoes which have not yet been named, simply listed as 'Unnamed', were not considered;

b) Eruptive activity must be confirmed during the period. Discredited and uncertain eruptions were not taken into account;

c) Although the eruptive period may start before or during the chosen period, only events that effectively have occurred within the selected period's range were considered;

d) The eruptive activity had to be associated with a minimum Volcanic Explosivity Index (VEI) value of 3.

During the period of interest (2011-2020), 360 eruptions (or confirmed eruptive activity) occurred from 138 volcanoes. Among those, 69 confirmed eruptions originated from 46 volcanoes (Figure 4.1) had VEI ≥ 3 and were therefore selected for this study (55 events were ranked with VEI = 3, 13 events with VEI = 4 and 1 event with 1 VEI = 5).

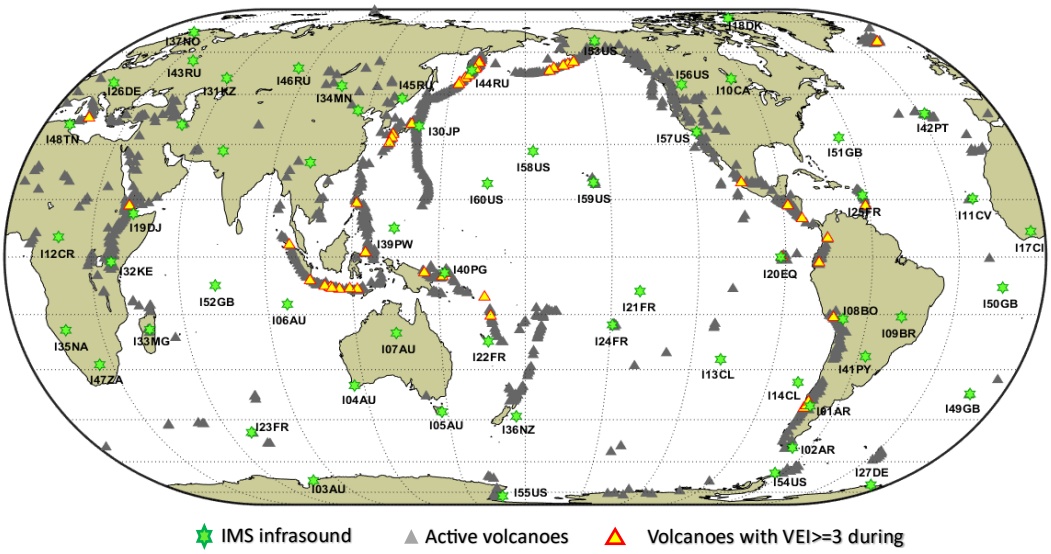

Figure 4.1. Selected volcanoes and IMS infrasound station's locations.

Following the 46 volcanoes selection, these were grouped into 11 pre-defined GVP zones (Table 4.1), according to their geography and geodynamic setting. The terminology employed was based on the GVP, to ensure consistency in the later data analysis.

Table 4.1. GVP Volcanic Regions Groups.

GVP Volcanic Region group	Number of volcanoes
Northwest Pacific Volcanic Regions	9
Sunda-Banda Volcanic Regions	8
South America Volcanic Regions	6
Western Pacific Volcanic Regions	6
North America Volcanic Regions	5
Southwest Pacific Volcanic Regions	5
Middle America-Caribbean Volcanic Regions	3
Atlantic Ocean Volcanic Regions	1
Eastern Africa Volcanic Regions	1
Eastern Pacific Volcanic Regions	1
European Volcanic Regions	1

A general overview of each volcano was compiled in a table (Table 4.2) with the following characteristics: the permanent unique identifiers GVP Number, Volcano Name, location coordinates (latitude and longitude), the Eruption time periods and duration and the VEI.

Table 4.2. Volcanoes characteristics overview grouped by region.

GVP number	Volcano_Name	Lat	Lon	Eruption period time	VEI	Duration
Northwest Pacific Volcanic Region - 9 volcanoes						
300250	Bezymianny	55,972	160,595	2012 Feb 12 - 2013 Jun 20	3	1 y, 4 m, 8 d
				2016 Dec 5 - 2021 Feb 1	3	4 y, 1 m, 27 d
290360	Chikurachki	50,324	155,461	2015 Feb 16 - 2015 Feb 18	3	3 d
290260	Chirinkotan	48,98	153,48	2016 Nov 29 - 2017 Apr 7	3	4 m, 9 d
300010	Kambalny	51,306	156,875	2017 Mar 24 - 2017 Apr 23	3	30 d
300130	Karimsky	54,049	159,443	2017 Jun 4 - 2018 Sep 30	3	1 y, 3 m, 26 d
				2020 Apr 1 - 2022 Aug 7	3	2 y, 4 m, 6 d
300260	Klyuchevskoy	56,056	160,642	2013 Aug 15 - 2013 Dec 20	3	4 m, 5 d
				2015 Aug 28 - 2018 Jul 14	3	2 y, 10 m, 16 d
290250	Raikoke	48,292	153,25	2019 Jun 22 - 2019 Jul 1	3	10 d
300240	Tolbachik	55,832	160,326	2012 Nov 27 - 2013 Sep 5	3	9 m, 9 d
300120	Zhupanovsky	53,589	159,15	2014 Jun 6 - 2015 Aug 6	3	1 y, 2 m
				2015 Nov 28 - 2016 Mar 25	3	3 m, 26 d
				2016 Nov 20 - 2016 Nov 20	3	1 d
Western Pacific Volcanic Region - 6 volcanoes						
282110	Asosan	32,8849	131,085	2016 Oct 7 - 2016 Nov 12	3	1 m, 5 d
282090	Kirishimayama	31,934	130,862	2011 Jan 19 - 2011 Sep 7	3	7 m, 19 d
				2018 Mar 1 - 2018 Jun 22	3	3 m, 21 d
282050	Kuchinoerabujima	30,443	130,217	2015 May 29 - 2015 Jun 19	3	22 d
				2018 Oct 21 - 2019 Feb 3	3	3 m, 13 d
				2020 Jan 11 - 2020 May 13	3	4 m, 2 d
283040	Ontakesan	35,893	137,48	2014 Sep 27 - 2014 Oct 14	3	17 d
266030	Soputan	1,112	124,737	2011 Jul 3 - 2011 Aug 15	3	1 m, 12 d
				2012 Aug 26 - 2012 Sep 19	3	25 d
				2015 Jan 6 - 2015 Mar 9	3	2 m, 3 d
				2016 Jan 2 - 2016 Feb 7	3	1 m, 5 d
				2018 Oct 2 - 2018 Dec 16	3	2 m, 14 d
273070	Taal	14,0106	120,9975	2020 Jan 12 - 2020 Jan 22	4	11 d
Southwest Pacific Volcanic Region - 5 volcanoes						
257030	Ambae	-15,389	167,835	2017 Sep 6 - 2018 Oct 30	3	1 y, 1 m, 24 d
251020	Manam	-4,08	145,037	2010 Aug 10 - 2013 Dec 15	3	3 y, 4 m, 5 d
				2014 Jun 29 - 2018 Jan 10	4	3 y, 6 m, 12 d
252140	Rabaul	-4,2459	152,1937	2014 Jul 7 - 2014 Sep 18	4	2 m, 11 d
256010	Tinakula	-10,386	165,804	2017 Oct 21 - 2017 Oct 26	3	6d
252120	Ulawun	-5,05	151,33	2019 Jun 26 - 2019 Oct 5	4	3 m, 9 d
Eastern Pacific Volcanic Regions - 1 volcano						
353020	Wolf	0,02	-91,35	2015 May 25 - 2015 Jul 16	4	1 m, 21 d

Sunda-Banda Volcanic Region - 8 volcanoes						
264020	Agung	-8,343	115,508	2017 Nov 21 - 2019 Jun 13	3	1 y, 6 m, 23 d
263280	Kelud	-7,935	112,314	2014 Feb 13 - 2014 Feb 15	4	3 d
262000	Krakatau	-6,1009	105,4233	2018 Jun 18 - 2020 Apr 17	3	1 y, 9 m, 30 d
263250	Merapi	-7,54	110,446	2013 Nov 18 - 2013 Nov 18	3	1 d
				2014 Mar 9 - 2014 Apr 20	3	1 m, 11 d
				2018 May 11 - 2020 Jun 21	3	2 y, 1 m, 10 d
264150	Paluweh	-8,32	121,708	2012 Oct 8 - 2013 Oct 31	3	1 y, 23 d
264050	Sangeang Api	-8,2	119,07	2014 May 30 - 2015 Nov 5	4	1 y, 5 m, 6 d
263300	Semeru	-8,108	112,922	2017 Jun 6 - 2024 Dec 19 (ongoing)	4	7 y, 6 m, 13 d
261080	Sinabung	3,17	98,392	2013 Sep 15 - 2018 Jun 22	4	4 y, 9 m, 7 d
				2019 Feb 6 - 2019 Jun 9	4	4 m, 3 d
Eastern Africa Volcanic Region - 1 volcano						
221101	Nabro	13,37	41,7	2011 Jun 13 - 2012 Jun 3	4	11 m, 21 d
Atlantic Ocean Volcanic Region - 1 volcano						
373010	Grimsvotn	64,416	-17,316	2011 May 21 - 2011 May 25	4	5 d
European Volcanic Region - 1 volcano						
211060	Etna	37,748	14,999	2010 Aug 25 - 2013 Apr 27	3	2 y, 8 m, 2 d
				2013 Sep 3 - 2022 Jun 17	3	8 y, 9 m, 14 d
North America Volcanic Region - 5 volcanoes						
311300	Bogoslof	53,93	-168,03	2016 Dec 20 - 2017 Aug 30	3	8 m, 10 d
311240	Cleveland	52,825	-169,944	2016 Apr 16 - 2019 Jan 20	3	2 y, 9 m, 4 d
				2020 Jun 1 - 2020 Jun 1	3	1 d
312030	Pavlof	55,417	-161,894	2013 May 13 - 2013 Jun 26	3	1 m, 13 d
				2014 May 31 - 2014 Jun 6	3	7 d
				2014 Nov 12 - 2014 Nov 15	3	4 d
				2016 Mar 27 - 2016 Jul 30	3	4 m, 3 d
311360	Shishaldin	54,756	-163,97	2019 Jul 23 - 2020 May 4	3	9 m, 11 d
312070	Veniaminof	56,17	-159,38	2013 Jun 13 - 2013 Oct 12	3	3 m, 29 d
Middle America-Caribbean Volcanic Region - 3 volcanoes						
341040	Colima	19,514	-103,62	2013 Jan 6 - 2017 Mar 7	3	4 y, 2 m, 1 d
343100	San Miguel	13,434	-88,269	2013 Dec 29 - 2014 Jul 28	3	6 m, 29 d
345070	Turrialba	10,025	-83,767	2015 Mar 8 - 2019 Dec 7	3	4 y, 8 m, 29 d
South America Volcanic Region - 6 volcanoes						
358020	Calbuco	-41,33	-72,618	2015 Apr 22 - 2015 May 26	4	1 m, 4 d
351020	Nevado del Ruiz	4,892	-75,324	2012 Feb 22 - 2013 Jul 12	3	1 y, 4 m, 20 d
357150	Puyehue Cordon Caulle	-40,59	-72,117	2011 Jun 4 - 2012 Apr 21	5	10 m, 17 d
354006	Sabancaya	-15,787	-71,857	2016 Nov 6 - 2024 Dec 19 (ongoing)	3	8 y, 1 m, 13 d
352080	Tungurahua	-1,467	-78,442	2011 Apr 20 - 2011 May 26	3	1 m, 6 d
				2011 Nov 27 - 2012 Sep 4	3	9 m, 8 d
				2012 Dec 14 - 2016 Mar 16	3	3 y, 3 m, 2 d
357120	Villarrica	-39,42	-71,93	2014 Dec 2 - 2024 Dec 13 (ongoing)	3	10 y, 11 d

From Table 4.2, it is clear that duration of eruptive events is extremely variable, spanning from a minimum of 1 day to a decade. Therefore, in order to create a comprehensive dataset of events required to investigate global infrasound data, a further analysis of the selected eruptions is required to identify discrete events. Figure 4.2 shows the adopted procedure that, for each volcano, can be summarised as follows:

(1) Eruptive activity search - all eruptive periods are retrieved from the database. These periods outline the temporal scope for identifying discrete eruptive events;

(2) Selection of events based on VEI – for each period all events with VEI ≥ 3 are extracted;

(3) Catalogue Structuring – extracted discrete events are compiled in a structured format, grouped by volcano into a dataset (Events List) including the following parameters: eruption date, VEI, volcano name, Latitude, Longitude and a list of events characterized by their respective onset time (t_o).

Out from the 69 confirmed eruptions originated from 46 volcanoes, we select 186 discrete events (see Annex 2).

To ensure comprehensive processing, the script applies a set of routine logical checks to handle cycle iterations, *e.g.*, if no more events were found in the current eruptive period, the script checks for the presence of additional eruptive periods for the same volcano; if there are no additional periods, it moves on to the next volcano in the list. Once all volcanoes are investigated, the final catalogue is saved in a structured output format for further analysis. This catalogue of events forms the basis for the correlation phase, where the start time of each event (t_o) is compared with the infrasound detection records of the IMS stations to assess detectability, temporal coincidence and potential source-station associations.

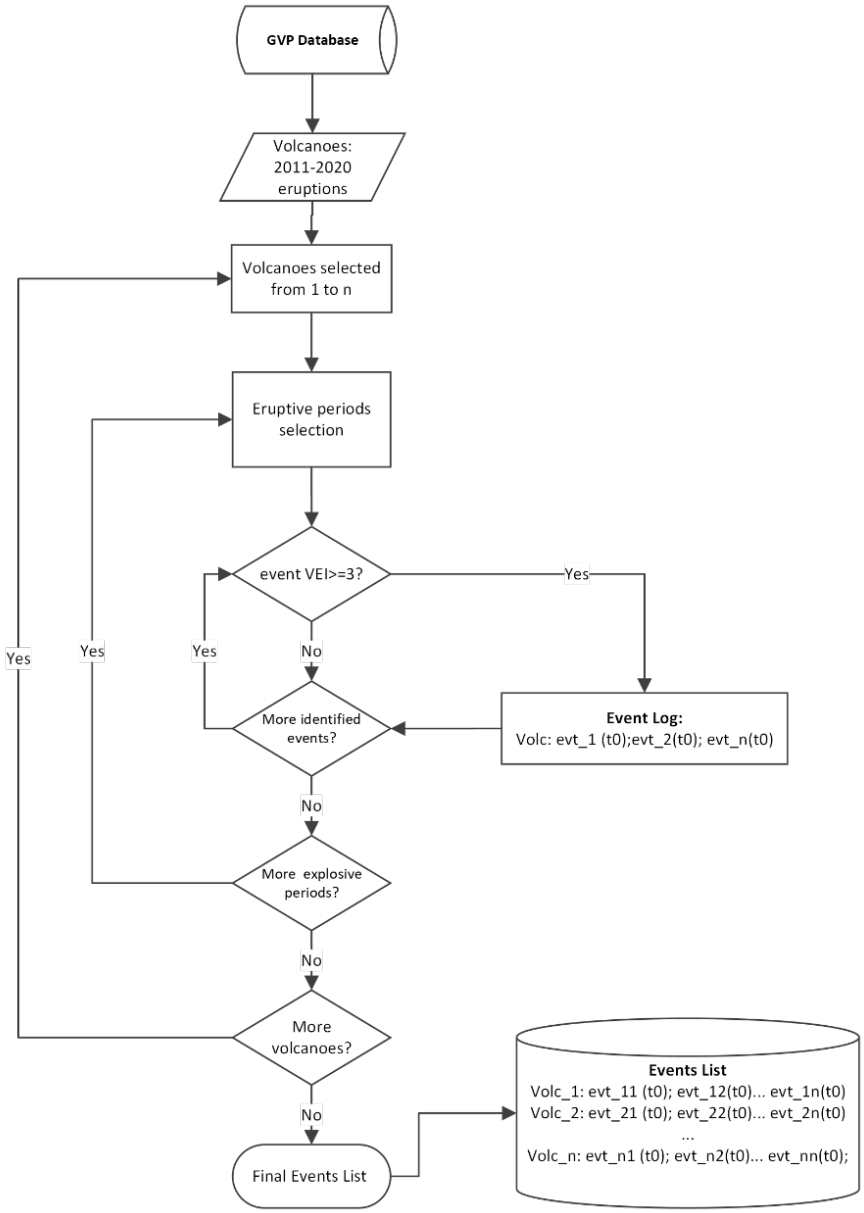

Figure 4.2. Flowchart illustrating Phase 1 of the method used to build the volcanic event catalogue from the GVP database. The workflow starts by identifying volcanoes with eruptions between 2011 and 2020, then by identification of eruptive periods, and selection of events with VEI ≥ 3. Results are logged by volcano as a list of events with their onset times (t_o). These onset times will be used in the next phase in combination with station detection logs.

4.2. IMS Infrasound Database

In order to investigate detection capabilities of volcano infrasound with the infrasound IMS network we selected 43 arrays that were active in the period of analysis and positioned up to 4,500 km from the selected volcanoes. This distance was chosen to ensure, for each volcano, infrasound data analysis for at least three IMS array. Therefore, 17 IMS stations were not considered in this work: 8 that are not available yet (IS01, IS12, IS15, IS16, IS28, IS29, IS38

and IS54), and 9 whose maximum distance from any of the volcanoes of the database doesn't comply with the established criteria (IS21, IS23, IS24, IS47, IS49). Further information of the 53 certified stations.

In general, the selected arrays have a median aperture of 2.15 kilometres (distance between the most apart sensors) spanning from 1.13 kilometres (IS32) to 3.37 kilometres (IS60). The number of elements of each array varies from 4 to 10 (see Table 4.3 and Figure 4.3).

Table 4.3. Distribution of the number of array elements on the IMS arrays used.

Arrays	Number of elements
14	4
1	5
2	6
5	7
18	8
2	9
1	10

The daily volume of raw data from an eight-element array (18 arrays), is greater than 13.8×10^6 samples, while for a four-element array (14 arrays) it is half of that value. The other arrays comprise between 5 and 10 sensors, with a total number of 63.9×10^6 samples per day. Altogether, the daily volume of raw data reaches more than 508×10^6 samples.

Data was processed to retrieve wave parameters by applying the Progressive Multi-Channel Correlation (PMCC) array processing algorithm.

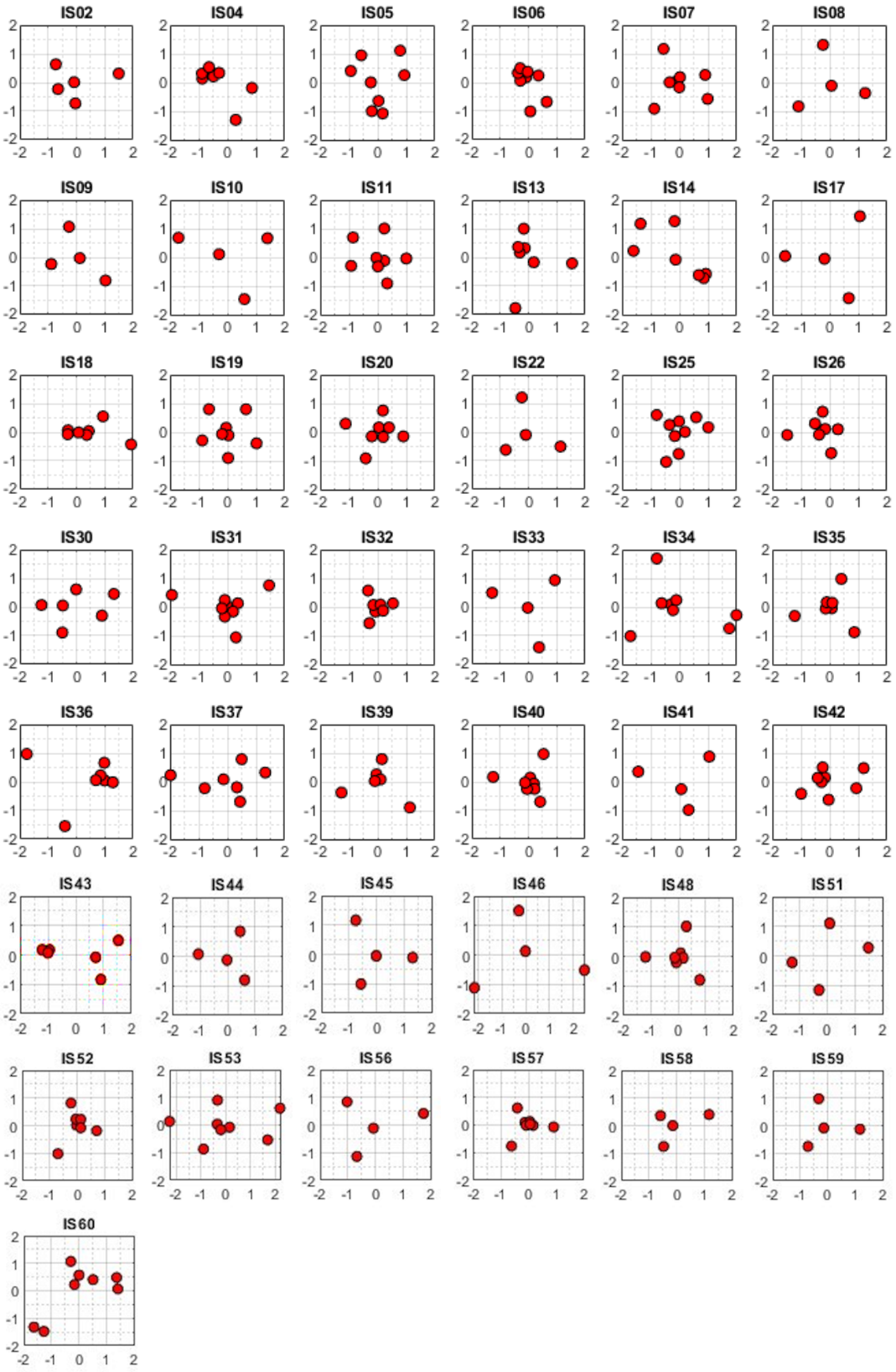

Figure 4.3. Array layouts of analysed stations. Red dots, represents the array elements.

4.2.1. The Progressive Multi-Channel Correlation (PMCC) algorithm

The Progressive Multi-Channel Correlation (PMCC) algorithm is an array processing method for detecting coherent low-amplitude acoustic waves within non-coherent noise (Cansi 1995). A signal in the time domain (t) can be represented in the frequency domain by its Fourier transform:

$$S\,(f) = A(f)e^{i\varphi(f)} \qquad \text{(Eq. 4.1.)}$$

where $A(f)$ is the spectral amplitude and $\varphi(f)$ is the phase. The background noise is characterized by a rapid variation of both spectral amplitude and phase from one sensor to another, even if they are separated by less than one wavelength (Cansi and Le Pichon 2008).

For a signal crossing the sensor array, the only difference between the data recorded by any two sensor elements is a time delay depending upon the relative positions of the sensors and the incident azimuth signal and trace velocity (Cansi and Klinger 1997).

Based on these two premises and since spectral amplitudes and phases evolve between sensors, it is necessary to find similarities in the signals to evaluate the delay between the sensors. This degree of similarity is estimated by the correlation function between $s_i(t)$ and $s_j(t)$, where the maximum correlation is obtained for the value of the desired delay (Mialle 2007). The correlation function Cor_{ij} is:

$$Cor_{ij}(\Delta t_{ij}) = \int_{T/2}^{-T/2} \mathrm{s_i}\,(t) s_j(t + \Delta t_{ij}) dt \qquad \text{(Eq. 4.2.)}$$

where T is the period of the wanted signal.

The correlation is processed in a time window with a given length, where the channel data of sensor $s_i(t)$ is shifted over the channel data of sensor $s_j(t)$. This function is calculated in the time domain and normalized to values ranging from -1 to 1.

The first stage in the implementation of the PMCC method (**Detection**) calculates the correlation between all pairs of signals, $s_i(t)$ and $s_j(t)$ in each triangular sub-array (triplet) of sensors to measure time delay Δt_{ij} (Cansi 1995).

A schematic illustration example of a wavefront arrival at a triplet is show in Figure. 4.4. The time delays (*e.g.*, Δt_{12}) and distances (*e.g.*, r_{12}) among the sensors allow the PMCC algorithm to determine the apparent phase velocity (v_{app}) and the direction of origin, as well the back-azimuth, β (as opposed to the propagation direction, α).

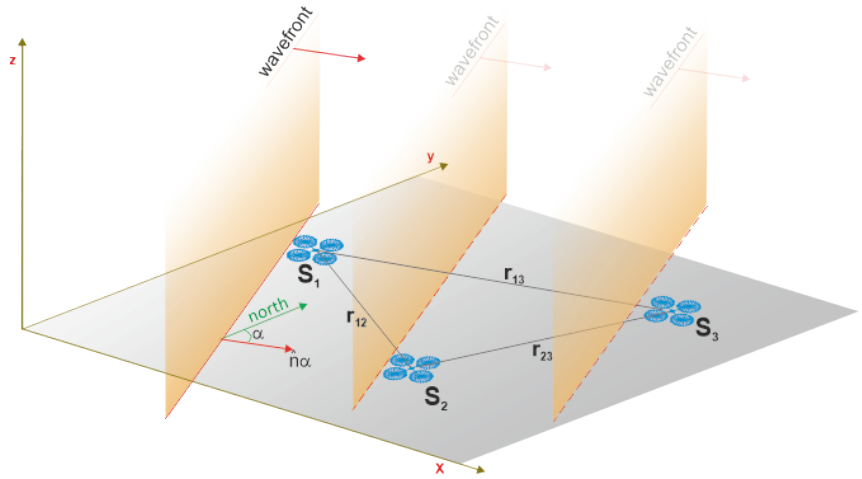

Figure 4.4. Schematic illustration example of a planar wavefront crossing an array with 3 microbarometers sensors (S_1, S_2 and S_3) and a rosette shape WNRS. The unit vector normal to wavefront ($\hat{n}_\alpha$) refers the propagation direction α respective to north and r_{ij} is the distance between sensors i and j.

In the second stage (**Progressivity**), if the signals are correlated and consistent, waveforms from other sensors at the station are progressively considered and are retained if the signals are sufficiently correlated and consistent. The analysis is initialized on the smallest groups of three sensors and as additional sensors are added, the obtained results are refined and improved. Figure 4.5 presents an example of selected subnetworks at the I42PT station. The consistency of the set of delays obtained using all the sensors n of a sub-network R_n is defined as the mean quadratic residual of the closure relations. If consistency is below a defined threshold (close zero), a detection is declared on R_n (Cansi and Le Pichon 2008).

As long the relative position of the array relative to the signal source is known and considering a plane wave propagation from a fixed location at a given specific velocity, it is possible to predict when the signal will arrive at each sensor and therefore the time differences of arrival from sensor to sensor. Once a detection is declared, the time delays producing that detection are known. PMCC calculations yielding time differences of arrival from sensor to sensor permit the trace velocity and azimuth to be estimated.

The best subnets are selected from among all possible combinations calculated from the remaining sensors. The principle is to sort them according to criteria of symmetry and size. The small aperture equilateral triangle is the best setting (Cansi and Le Pichon 2008, Runco *et al.* 2014).

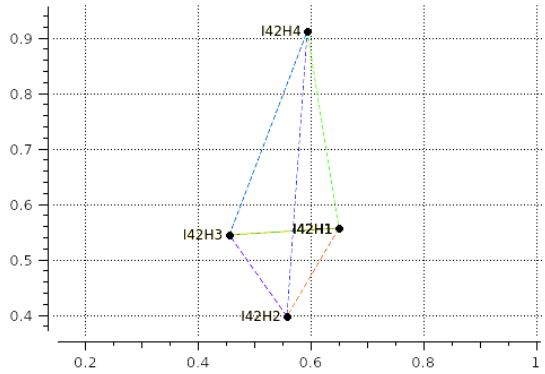

Figure 4.5. Selection of 3 initial subnetworks of the IMS I42PT infrasound station.

The third stage (**processing)** is performed consecutively in several frequency bands and in adjacent time windows covering the whole analyses period, using the PMCC algorithm, implemented for example in the DTK-GPMCC software (integrated in the NDC-In-A-Box package – NIAB). If waveforms are sufficiently correlated and consistent for a specific time window and frequency band, each elementary detection is stored in a so-called **pixel**, with a time, frequency, back- azimuth and apparent velocity. The pixel height represents the processing bandwidth, while the pixel width represents the time increment between adjacent windows. Each pixel also includes detection attributes such as azimuth, speed (trace velocity), consistency, root mean square (rms) amplitude, and Fisher statistic values.

The next stage of the detection processing consists of aggregating pixels with similar attributes into larger groups (*e.g.*, Brachet *et al.* 2010).

A set of several pixels in the time-frequency domain are considered to represent one detected wave. Several waves with different parameters may coexist in the same time window but in different frequency bands and each one must be identified separately. For this, a nearest-neighbour search method, which forms clusters of pixels (**families**) that are similar in the time, frequency, velocity and azimuth space domain (t, f, V, β) is used. Build pixel families can therefore be associated with the same infrasound arrival (Le Pichon and Cansi 2003). An example of a GPMCC-produced family is illustrated in Figure 4.6.

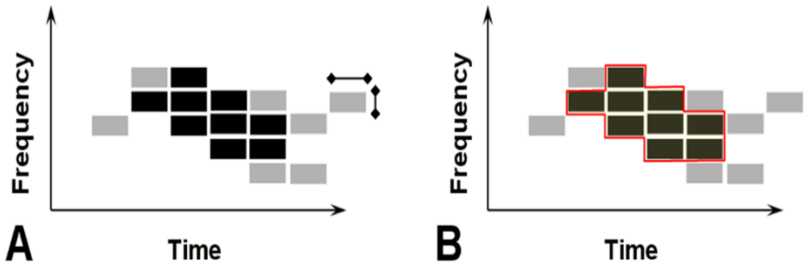

Figure 4.6. PMCC post processing: aggregation of close-enough pixels into a family (Le Pichon and Cansi 2003).

Attributes that influence the family grouping process include time, frequency, azimuth, and speed. If there are enough pixels in a family, it will result into a **detection**. When a detection is formed, several attributes are calculated for the family, including time duration of the family, frequency bandwidth, centre frequency, speed, azimuth, and F-stat.

Initially, the PMCC was processed in 10 linearly spaced frequency bands, in independent and multi-separated runs with different target signal frequencies, in the band between 0.1 and 0.4 Hz (Brachet and Coyne, 2006). For the PMCC algorithm to handle simultaneously low and high frequency signals, a new highly configurable version enables the length of the processing window and the detection parameters to be frequency band dependent. Enhanced by Le Pichon *et al.* (2010), this single calculation run can be carried out with 15 frequency bands spaced logarithmically between 0.01 and 5 Hz with a variable window length.

4.2.2. PMCC for volcanoes. Adjustments and automation array processing

In this work, specific adjustments were made to PMCC algorithm parameters to cope with the characteristics of infrasound signals generated by volcanic activity. These typically transient natural signals are associated with frequencies between 0.5 and 5 Hz (Le Pichon *et al.* 2009, Pilger *et al.* 2018) and requiring careful tuning of the detection parameters to reduce false alarms and ensure the coherence of signal groupings. To this end, the algorithm was configured to optimize three critical aspects: the duration of the correlation time window (WindowLength), the time shift between two successive windows (TimeStep), and the consistency threshold (Threshold Consistency), which defines the maximum acceptable deviation before a detection pixel is rejected. This value has a major impact on the detection performance and cannot be lower than the sampling period in a way to satisfy the closure relation and obtain a detection (Cansi and Le Pichon 2008). For this purpose, regarding the frequency-dependent parameters, 15 logarithm-spaced frequency bands were chosen (Matoza et al 2013) with frequency values ranging from 0.07 Hz to 5 Hz, a logarithmic distribution and time window lengths values ranging from 150 s to 25 s with a 1/f distribution dependent on the centre frequency of the bands, with 90 % window length overlap (10% time step) (Figure 4.7).

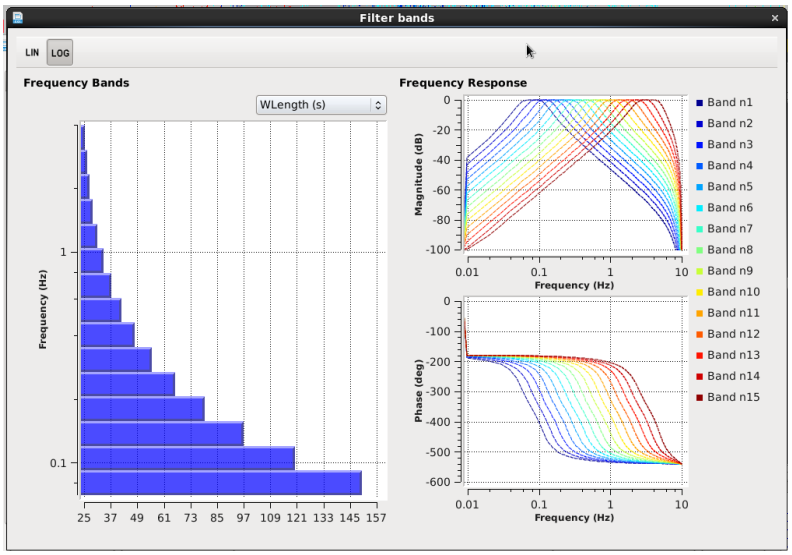

Figure 4.7. Fifteen bands with logarithmically spaced filter parameters configuration (0.07 Hz-4 Hz) with variable window length. On the left side the frequency bands attributes are displayed. On the right side the frequency response (magnitude and phase) filters are shown.

Regarding the family grouping - most of the pre-defined PMCC algorithm parameters remain unchanged, except for the thresholds controlling the minimum and maximum number of pixels per family (LFamMin and LFamMax), which were set to 30 and 3000, respectively. These options values were considered to avoid both the fragmentation of families of the same detection signal, or continuous clusters (such as microbarom) that can last several hours and days.

All detections resulting from the PMCC processing were compiled into bulletins, each listing a set of relevant parameters including minimum, mean, median, and maximum frequency, family size, arrival time (start and end), signal duration, apparent velocity, back-azimuth, correlation accuracy, peak-to-peak amplitude, number of sensors involved, and the Fisher statistical coefficient. An advantage of working with these bulletins lies in the lower or even elimination of wind noise, thereby reducing processing times (Figure 4.8).

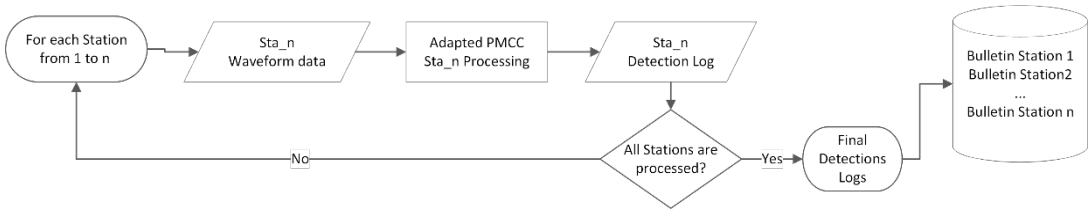

Figure 4.8. Flowchart illustrating Phase 2 of the method: station-level detection processing. For each available station (from 1 to n), waveform data are processed using the PMCC algorithm (Progressive Multi-Channel Correlation). The output is a detection log (or bulletin) for each station. The process loops through all available stations until complete. The resulting station bulletins are later used in correlation with the volcanic event onset times (t_o) identified in Phase 1.

4.2.3. Source location based on cross-bearing method

As the apparent phase velocity is given by the time delay between coherent signals arrivals to the different sensors, the back-azimuth indicates the bearing from the sensor to the source of a detected signal. A potential source region can be estimated if data is available from a minimum of two stations, and as more stations contribute to the detection, the more accurate the location will be, applying a cross-bearing method (Figure 4.9).

Unlike other natural processes, where infrasound sources can vary in function of the time of day or the seasons, such as microbarom or Mountain-Air Waves (MAW), volcanoes have a fixed location and monitoring its activity and characterising their behaviour generally depends on the source-to-receiver propagation conditions. Considering the inherent uncertainties associated with the detected back-azimuth (θ)—which may result from sensor malfunction, array response characteristics, or atmospheric wind conditions along the propagation path (*e.g.*, Le Pichon *et al.*, 2005a)—this work adopts a tolerance of θ ± 5° relative to the volcano's reference back-azimuth. In addition, a broader window of θ ± 10° was evaluated to assess the sensitivity of the analysis to directional deviations.

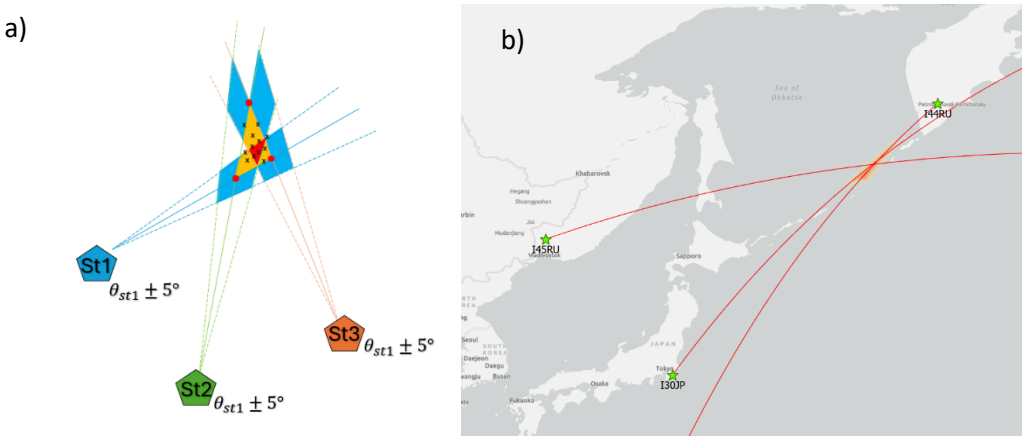

Figure 4.9. a) Cross-bearing method approach schematic illustration. Solid lines refer to the main azimuth to volcano and the dashed lines refers to 5° deviation b) Great circle bearings from three IMS stations example, related to the Chirinkotan events of November 2016.

4.3. Meteorological data

Infrasound propagation over long distances relies on atmospheric conditions, including the direction and amplitude of vertical wind gradients and background temperature fields (Brown *et al.* 2002, Drob *et al.* 2008). It is therefore important to know the atmospheric conditions when the events occur (Figure 4.10). Although infrasound channelling is mostly efficiently in the stratospheric waveguide, typically the observed waves propagate through

the lower 100 km of the Earth's atmosphere, including the troposphere and lower thermosphere, producing multiple arrivals at distant stations.

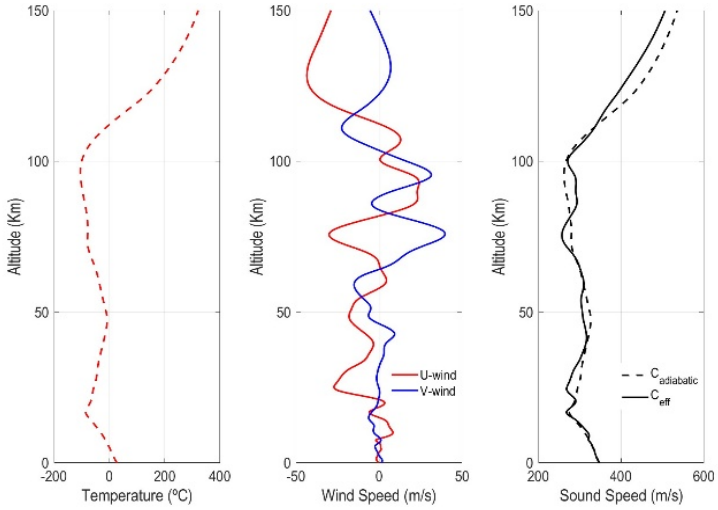

Figure 4.10. Atmospheric conditions on Temperature (ºC), zonal and meridional wind-speed and the adiabatic and effective sound speed (m/s) for Agung 2017 November 26th event.

The European Centre for Medium-Range Weather Forecasts (ECMWF) provides operational datasets in terms of data forecast, but also a huge number of historical observations on a global scale, using advanced modelling and data assimilation systems. To explore the stratospheric specifications regarding volcanic events, ERA-Interin (from 2011 to 2018) and ERA5 datasets (for 2019 and 2020) were employed. ERA-Interim provides data from 1979 to present, with a global spatial resolution of approximately 80 km in 60 vertical levels up to 0.1 hPa available in 6-hour analyses. ERA5 data is presented on a 31 km grid (0.28° × 0.28°) and using 137 levels from the surface up to a height of 80 km (0.01 hPa) hourly available (Hersbach *et al* 2020). Those datasets were an invaluable resource for studying atmospheric and climate dynamics over the period of 2011 to 2020.

For each of the 60 levels of the model, the temperature, the horizontal wind components and the logarithm of the surface pressure are stored. Atmospheric parameters retrieved are then used to calculate the effective speed of sound ratio $v_{eff-ratio}$ for each day (or period) for the locations of a selected volcanic event and selected IMS stations.

After acquiring the $v_{eff\text{-}ratio}$ (Figure 4.11), the attenuation coefficient (*Ap*) is obtained according to the distance between the grid nodes (0.75° x 0.75°) and the selected volcano.

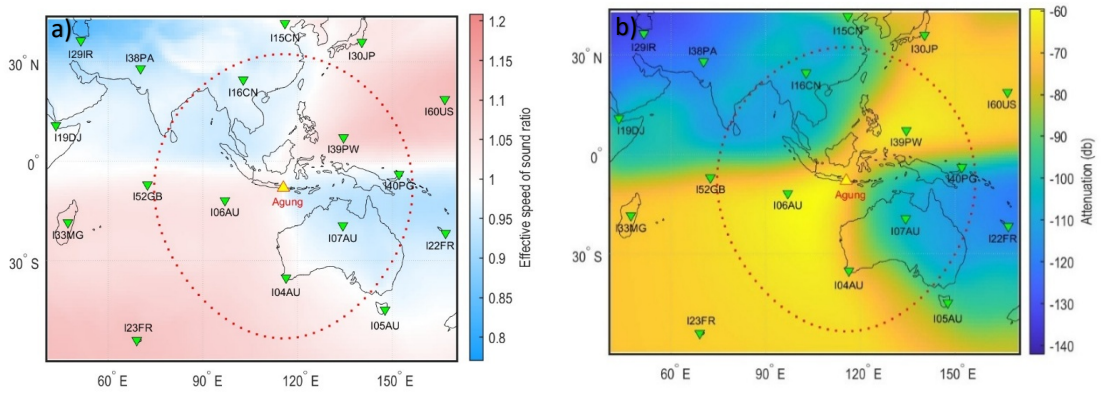

Figure 4.11. Example of effective speed of sound ratio (a) and attenuation (b) calculated for the 2017 November 26th event on Agung volcano.

As mentioned before, refractions towards the ground can be expected to occur at thermospheric altitudes. In this context, the AVO-G2S model was used with meteorological data to extend the atmospheric observations to the thermosphere. Using the infrasound ray tracing software INfraGA (Blom and Waxler, 2012), the wind speed and adiabatic speed of sound parameters were calculated for the time-period of each selected event. Raytracing was then used to show the expected back-azimuth of possible arrivals of EigenRays originating from the selected volcano and the nearest IMS station (Figure 4.12).

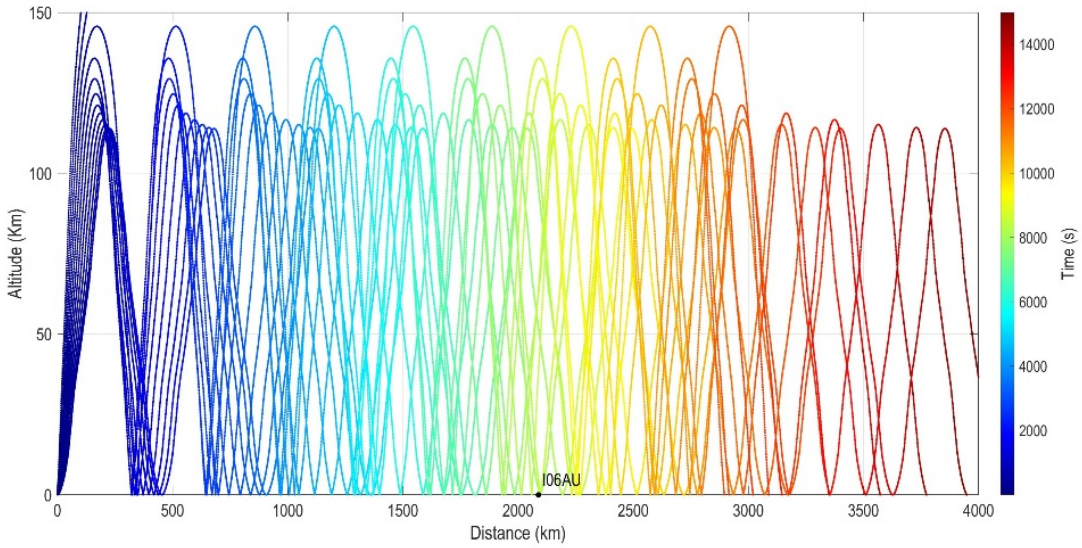

Figure 4.12. Example of ray racing calculated with InfraGA for the closest station of the 2017 November 26th Agung volcano event.

4.4. Data Processing

For each volcano in this study, a data sheet was prepared linking the volcano to the closest stations (within a radius of 4,500 kilometres, as specified before). Parameters such as distance, back-azimuth and waveform propagation times (considering a speed of 0,340km/s), are presented (Table 4.4)(See Appendix B).

Table 4.4. Example of the Ambae volcano distance, back-azimuth and wave propagation time to the closest stations.

Ambae Volcano	1st_sta	2nd_sta	3rd_sta	4th_sta	5th_sta	6th_sta	7th_sta
IMS Station	I22FR	I40PG	I36NZ	I05AU	I07AU	I60US	I39PW
Distance (Kms)	759	2123	3494	3569	3585	3838	4462
Backazimuth (°)	8	126	330	39	87	178	125
Prop. Time (Hour)	00:37:13	01:44:04	02:51:16	02:54:57	02:55:43	03:08:09	03:38:43

Progressing through Phase 2, data processing was generated based on MATLAB® script. New scripts were then created: (1) *Proc_VOLCsta_assoc.m*, for IMS infrasound data analysis, (2) *Proc_V_Att.m*, for elaboration the $V_{eff\text{-}ratio}$ and attenuation maps; (3) *Proc_met_prof.m* file, for meteo data analysis (Temperature, zonal and meridional winds and adiabatic and effective speed of sound).

This Phase 2 is centred on the *Proc_VOLCsta_assoc.m* script developed in MATLAB, designed to correlate the onset times of volcanic events with infrasound detections registered at IMS stations. The script uses two key inputs: (i) a volcanic event catalogue (Event_List), with all the results obtained from Phase 1, where the onset times (t_o) are included, and (ii) the detection lists generated by each station using the PMCC algorithm adapted for volcanoes (Station Bulletins).

The process starts by selecting a volcano from the catalogue of events. For the selected volcano, the script evaluates all the IMS stations individually. The geographical distance between the volcano and each station is determined, considering only stations within a maximum radius of 4500 km are considered. Stations without effective detections data are rejected. After evaluating all the stations, the list is sorted in ascending order of distance to be used in the following steps.

For each event associated with the volcano, the onset time (t_o) is taken. The script then verifies whether valid detection data is available for each station in the screened list. If no data is found, the script moves on to the next station. If data is available, processing is carried out between a time window of 12 hours before (t_start) and 24 hours after the start time ((t_end). The volcano's back-azimuth angle (θ_n) for each station is calculated based on the

geographical coordinates of each station and the volcano with two different directional tolerance ranges options employed: a default window of θ_n ± 5° and an extended range of θ_n ± 10° for a wider analysis.

The detection list for each station is then analysed to identify the detections that fall within both the specified time window and azimuth range. The screened detections are automatically saved and associated with the specific event and station. These outputs are later used in the interpretation and evaluation phases (Figure 4.13).

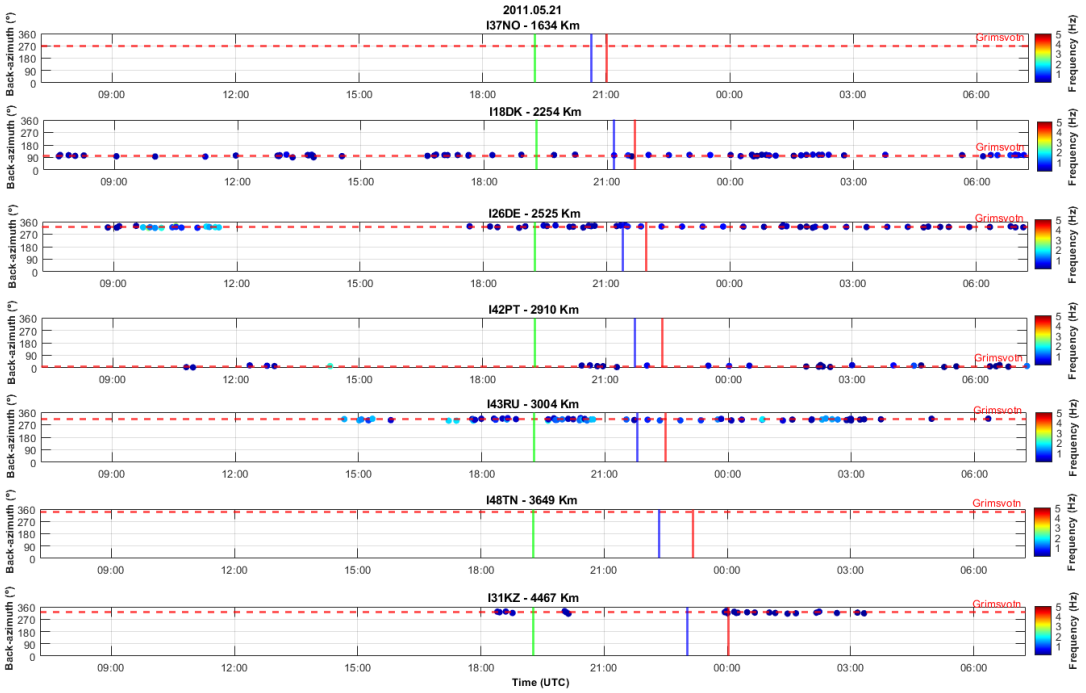

Figure 4.13. Example of the final processing image related with Grimsvotn eruption, in May 2011. IMS infrasound stations with valid data are present by distance within 4500 km limit; red dashed line is the volcano back-azimuth, vertical lines are the celerity of 260 (red) and 330 (blue) respectively. Dots are detections by frequency (Hz)and green verical line is refered to t_0.

To clearly understand the spatial characteristics of the infrasound signals identified by the algorithm and their association with volcanic sources, the detected events were classified into eight detection classes (A-H), based on the layout and distribution of the monitoring stations that registered the signals. These classes reflect the performance of the stations involved in the detections and provide information on the efficiency of atmosphere propagation, the energy of the explosive events and the reliability of the monitoring network. The classification scheme is described as follows (see Table 4.5 for a summary):

Class A is associated to detections at the closest station to the volcano. Signals being detected at the nearest station is of particularly importance, as it is indicative of a direct acoustic path and minor atmospheric attenuation. This class generally reflects propagation

that is close to the source and can be used as a key indicator to verify the time and existence of an event close to the source.

Class B includes detections identified at, at least one of the three closest stations. This class represents a more extensive spatial coverage area, giving an idea of the strength of the event and the influence of the atmosphere on the signal's propagation within such distances.

Class C includes detections registered at two of the three closest stations. Detections in this class likely reflect higher signal amplitudes or favourable atmospheric propagation conditions with a regional coverage potential.

Class D includes detections at the three closest stations. This pattern suggests a possibly high levels releases of acoustic energy and strong signal propagation in the near field.

Class E stands for detections at more than three stations in the network. These cases generally correspond to large explosive eruptions with enough energy to produce long-range infrasound signals that can be detected on a regional and global scale.

Class F includes detections identified at both close and distant stations. This configuration not only suggests energetic sources and favourable propagation paths, but may as well reflect atmosphere duct conditions, whether in the troposphere (*e.g.* jet streams), stratosphere or thermosphere. These ducts enable long-distance acoustic wave propagation beyond typical regional ranges.

Class G refers to detections only at distant stations (from the 3rd closest station onwards). This pattern may be associated with the physical features of the closest stations, like their location in shadow zones, failures in operation/performance or being located in high attenuation zones with $V_{eff\ ratios} < 1$. It can additionally reflect specific paths favourable to long-distance propagation.

Class H refers to detections at stations aligned with the volcano's back-azimuth, but where the estimated arrival times fall outside typical celerity propagation thresholds. This may indicate inaccuracies in the estimated origin time (t_o), or delays caused by complicated paths. This class might also show effects from uneven sound radiation or local filtering due to the landscape and wind direction.

Table 4.5. Summarises the detection classes used to categorise infrasound signals based on the spatial configuration of the stations. This classification helps to recognise the range from local to regional and long-range detections, giving information on acoustic energy, atmospheric propagation conditions and network performance.

Class	Detection Description	Key Implications
A	Only at the nearest station	Direct path, low attenuation. Reliable for confirming event origin.
B	At one of the 3 closest stations	Moderate spatial coverage and energy. Good local propagation.
C	At two of the three nearest stations	Strong amplitude signal or favorable propagation. Regional coverage.
D	At all three closest stations.	High energy and effective near-field propagation.
E	At more than three stations.	Large explosive events. Regional or global-scale infrasound propagation.
F	At both nearby and far stations	High energy and ducting conditions (troposphere, stratosphere and thermosphere).
G	Only beyond the 3rd closest station.	Possible shadow zones, station issues, or long-range propagation via specific paths.
H	Along the source azimuth, with untimely arrival times.	May reflect an erroneous time of origin (t_o) or complex propagation paths.

For the classes B, C, D, F and G, a detailed analysis was carried out using the DTK-GPMCC software (Figure 4.14), to ensure consistent detections (see section 4.2.1). For each event, the resulting detection attributes were added to the database. These attributes include the IMS station name, time of arrival, number of pixels and number of families detected, mean frequency, mean speed, azimuth (azimuth range, mean azimuth, observed mean azimuth, azimuth deviation) maximum amplitude, number of sensors used and correlation (Table 4.6 and 4.7). Also, polar plot according to back-azimuth (polar angle) and trace velocity (polar radius) related to detections time was retrieved (Figure 4.15).

Table 4.6. Predicted infrasound arrival.

station	Dist (km)	BackAz (°)	Event time (UTC)	Prop. Time (0,340km/s)	Exp. Arr_time (UTC)	arrival time (UTC)
I30JP	953	250	6:41:00	0:46:43	7:27:43	7:28:07

Table 4.7. Detection information.

Nb_fam	Nb_pix	BackAz_obs range (°)	Mean BackAz_obs (°)	BackAz _dev (°)	Mean Freq. (Hz)	Mean Speed (Km/s)	Max Amp (Pa)	Nb Sens.	Corr.
1,00	338	240-260	242	- 8	1,268	0,353	0,463	6	0,433

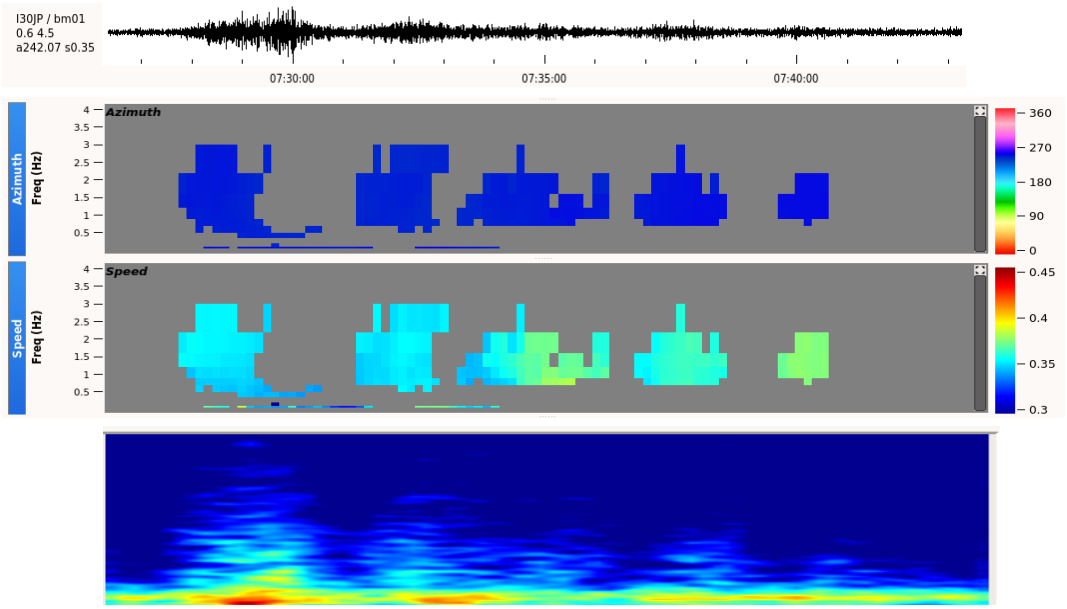

Figure 4.14. DTK- PMCC example of the 2011 January 27th Kirishimayama event waveform (time-domain beams based on volcano observed back-azimuth); detections based on expected travel time and back-azimuth; and spectrogram.

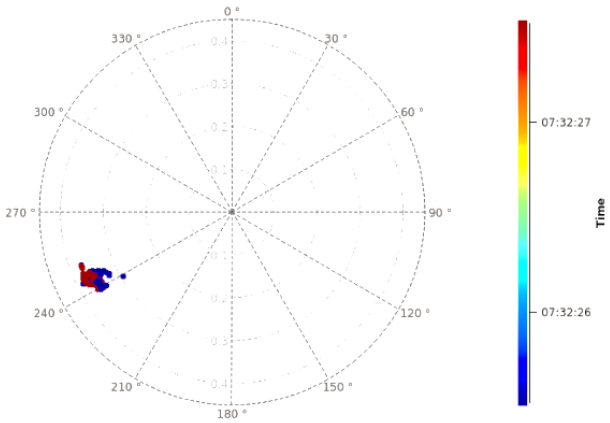

Figure 4.15. DTK- PMCC polar plot example of the 2011 January 27th Kirishimayama event.

As a final step, the results of the detections (*e.g.,* tables 4.6 and 4.7) will be correlated with the identified events in the LEB and SEL3 bulletins (*e.g.,* table 4.4). In addition to the analysis of the number of detections by IMS stations that can be associated to volcanic events, their validation or not on the basis of IDC bulletins will indicate how effective the assessment tool can be applied as a baseline for detection response and an early warning notification system (Figure 4.16).

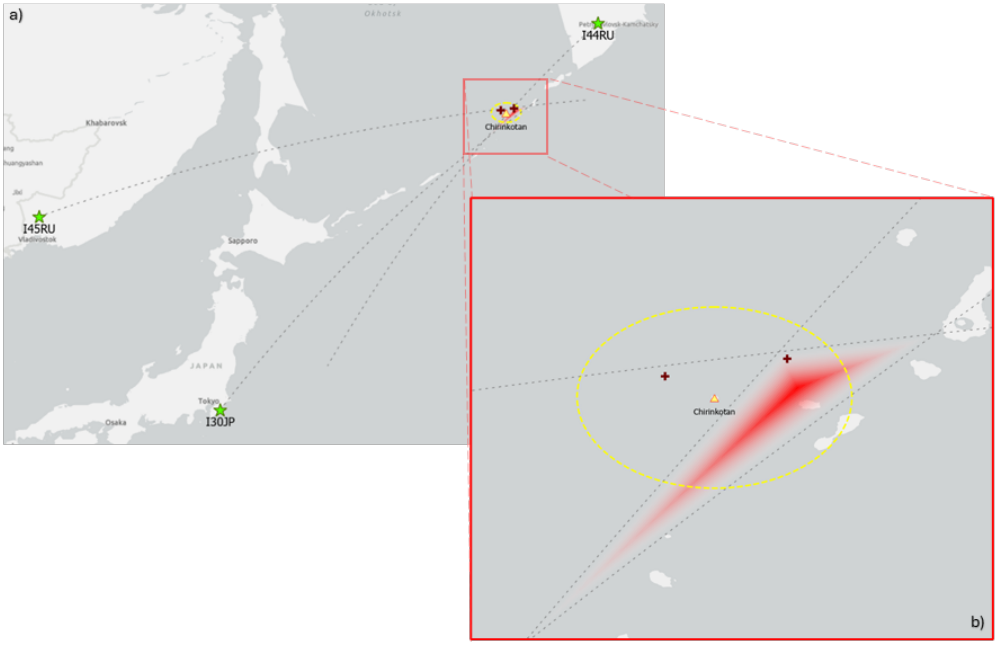

Figure 4.16. Chirinkotan 2016 eruption example: a) Three closest stations cross-bearing of the main back-azimuths and of 5° back-azimuths deviation. b) Ellipse of 50 km centred on volcano showing back-azimuths interpolation of best-fit reconstructed locations (red area) and LEB results locations (red crosses).

4.5. IDC Database

At the IDC, the waveform received from the infrasound station are subjected to quality control verifications and then processed by the DFX-PMCC (Data Feature eXtraction-Progressive Multi-Channel Correlation) application technology (Branchet et al, 2010) based on the PMCC algorithm (Cansi 1995). Incoming arrivals resulting from station-level processes are used as input for the network processing performed through the Global Association (GA) software. At this network level, events are built up from the combination of arrivals and published in the SEL2 and SEL3 automatic bulletins (Figure 4.17).

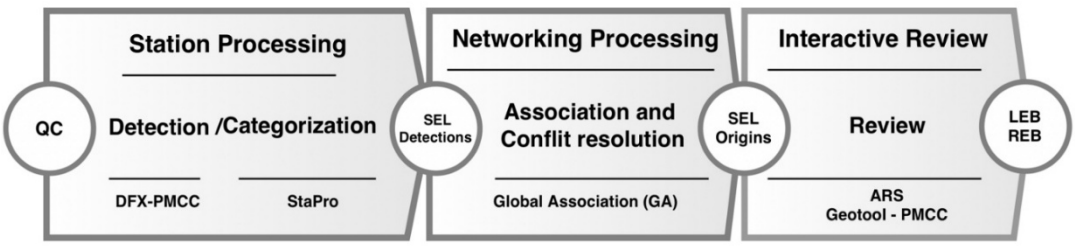

Figure 4.17. IDC Infrasound processing pipeline (Adapted from Mialle et al 2019).

The analyst review process is summarised in the Late Event Bulletin (LEB), and event definition criteria are then applied to produce the Reviewed Event Bulletin (REB). Events that

don't fulfil REB's event definition criteria (*e.g.,* minimum number of primary IDC station defining arrivals associated with them) are included in the LEB but are not listed in the REB.

In the scope of this work, SEL3 and REB IDC bulletins were collected via the CTBTO Secure Web Site (https://access.ctbto.org/portal/index.html). The LEB buletins were requested through the Verification Data and Products Messaging System (VDMS) Command Line Client application available in the NDC-in-a-Box software package (supplied by the PTS).

The events were stored in text files, with associated parameters such as Event Identification (Event Id), Event Location (Location), Date (yyyy,mm,dd), Time (hh:mm:ss.m), RMS, Latitude (Lat), Longitude(Lon), Azimuth of event (Az), Number of stations (Nsta), Detected stations code (Sta) and their distance (Dist), Phase, Arrival time (Time), Back-Azimuth (Baz), Slowness (Slow), SNR, Signal Amplitude (Amp), among others (Table 4.8). These data were subsequently used to compile a catalogue of events in order to be tentatively correlated with volcanic events identified on Phase 1 and detected and processed on the previous phase.

Table 4.8. LEB information example related with Ambae volcano activity.

Event Id	Location	Date	Time	RMS	Lat	Long	Az	Nsta
16493999	VANUATU ISLANDS	2018-10-30	07:43:05.56	193.5	-16.20	168.11	22	4

Sta	Dist	Phase	Time	Baz	Slow	SNR	Amp
I22FR	6.07	I	08:15:45.000	8.8	320.4	31.7	1.2
I40PG	19.75	I	09:40:10.714	125.4	271.9	3.9	29.9
I07AU	32.30	I	11:04:50.000	87.8	310.2	8.3	0.0
I21FR	50.91	I	13:10:41.786	260.8	300.1	10.2	0.1

The IDC CTBTO bulletins (LEB, SEL3 and REB) were collected to assess their ability to register and provide information on events that could be correlated with the volcanic events detected and processed on the previous step.

In this thesis, one of the main purposes is to verify if LEB is a reliable first approach indicator for an early warning notification system.

CHAPTER 5 |

Results

In this chapter we analyse the results of the detections obtained for eruptive events selected from Global Volcanism Program (GVP) and evaluate the effectiveness of the detection algorithm by comparing them with the onset times and with the events listed in the IDC bulletins.

In general, most of the events reported in the GVP database are associated with discrete explosions (n=116; 61%), while approximately 49 events (26%) are associated with sustained eruptive columns. Twelve events (6%) are related to lava fountaining at Mount Etna volcano, and two events are associated with lava dome collapses at the Paluweh (2012) and Sinabung (2018) volcanoes. The remaining 7% correspond to events that were not characterised beyond their date and VEI classification.

To assess the system's overall detection capability, a comparative analysis was made between the number of volcanic eruptions (67) and events (186) that were detected or not detected. Each eruptive period lasts from a few days to several years and encompasses several explosive volcanic events. Within these periods, the different discrete eruptive events identified show the episodic and complex dynamics of the volcanic systems. Among the 67 eruptive periods, 73.13 % (n = 49) were successfully identified, while 26.8 % (n = 18) were not detected (Figure 5.1). In contrast, of the 186 volcanic events, 54.8 % (n = 102) were identified and 45.2 % (n = 84) were not detected.

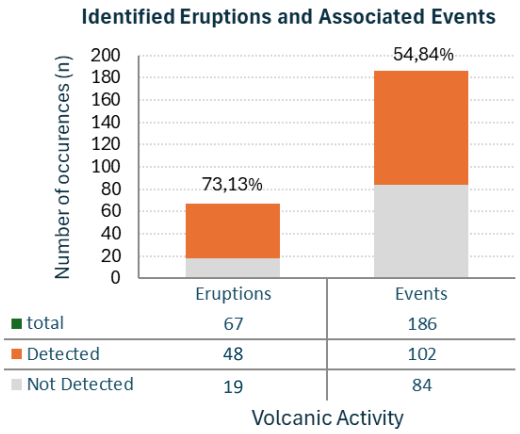

Figure 5.1. Volcanic activity identified during the study period, represented as eruptive periods and distinct events. Each eruptive period includes one or more events occurring over varying timescales. Stacked bar chart shows the number of detected (orange) and undetected (grey) occurrences for both categories.

5.1. Detections results

The following section summarizes the results of detection grouped in the 11 volcanic regions previously defined (see section 4.1). It evaluates the detectability of the associated infrasound signals across different detection scenarios and details the contribution of each IMS station to volcanic activity detection.

5.1.1. Northwest Pacific Volcanic Region

Across this region (Figure 5.2a), nine volcanoes and a total of 13 eruptive periods were identified, with each volcano showing between one to three eruptive events, with a total number of 56 selected events (Table 5.1). The eruptive periods span from a minimum of three days to a maximum of approximately four years. All eruptive periods reported for this group of volcanoes in the GVP have been classified as moderate to large explosive events, corresponding to a VEI 3.

The overall detection results of this group are shown in Figure 5.2b. Eruptions were successfully detected in 11 cases (84.6%; n = 13) and discrete events in 34 cases (60.7%; n = 56). No detections were recorded during the three-day eruptive episode at Chikurachki volcano in 2015, nor during the eruptive activity at Zhupanovsky, in 2016, and Karymsky, in 2020.

These results are further detailed by analysing the performance of the detection algorithm at the level of each volcano. An individual analysis for each volcano is presented in Appendix A.1 and B.1.

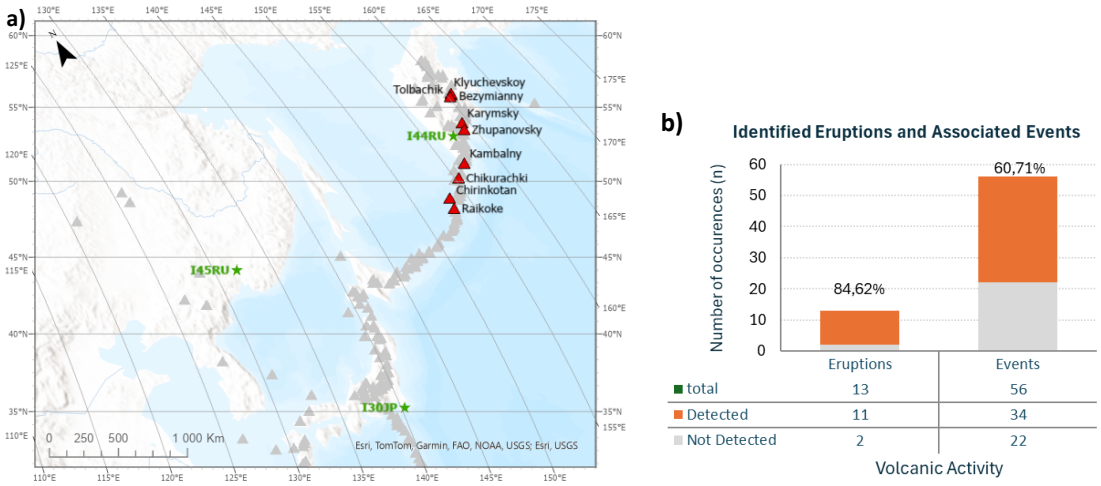

Figure 5.2. a) Location map with nine volcanoes (red triangles) identified as having eruptive activity during the selected period in the GVP, as well as the three closest IMS stations (green stars). b) Volcanic activity, shown as eruptive periods and events. The stacked bar chart represents the number of detected (orange) and undetected (grey) occurrences.

Table 5.1. Summary of volcanic eruption characteristics and detected events in the Northwest Pacific Volcanic Regions.

GVP number	Volcano_Name	Eruption time period	VEI	Duration	Events Detected
300250	Bezymianny	2012 Feb 12 - 2013 Jun 20	3	1 y, 4 m, 8 d	Yes
		2016 Dec 5 - 2021 Feb 1	3	4 y, 1 m, 27 d	Yes
290360	Chikurachki	2015 Feb 16 - 2015 Feb 18	3	3 d	Yes
290260	Chirinkotan	2016 Nov 29 - 2017 Apr 7	3	4 m, 9 d	Yes
300010	Kambalny	2017 Mar 24 - 2017 Apr 23	3	30 d	Yes
300130	Karimsky	2017 Jun 4 - 2018 Sep 30	3	1 y, 3 m, 26 d	Yes
		2020 Apr 1 - 2022 Aug 7	3	2 y, 4 m, 6 d	No
300260	Klyuchevskoy	2013 Aug 15 - 2013 Dec 20	3	4 m, 5 d	Yes
290250	Raikoke	2019 Jun 22 - 2019 Jul 1	3	10 d	Yes
300240	Tolbachik	2012 Nov 27 - 2013 Sep 5	3	9 m, 9 d	Yes
300120	Zhupanovsky	2014 Jun 6 - 2015 Aug 6	3	1 y, 2 m	Yes
		2015 Nov 28 - 2016 Mar 25	3	3 m, 26 d	Yes
		2016 Nov 20 - 2016 Nov 20	3	1 d	No

Obviously, the detectability varies for the different volcanoes (Figure 5.3). Bezymianny, Chikurachki, Chirinkotan, Kambalny, Klyuchevskoy, Raikoke and Tolbachik volcanoes had 100% of the eruptions detected. Among these, Raikoke, Chirinkotan and Tolbachik also had all the events detected, while Bezymianny had a slightly lower detection rate of 66.7 % (n = 9, with 6 detected). Karymsky had the lowest detection performance in the group. Only 50% of eruptions were

detected (n = 2), and the event detection rate was also 50% (n = 20, with 10 detected). Zhupanovsky showed a relatively high number of events (n = 12) and eruptions (n = 3), with detection rates of 66.7% for eruptions and 41.7% for events, indicating a moderate performance of the algorithm in this case.

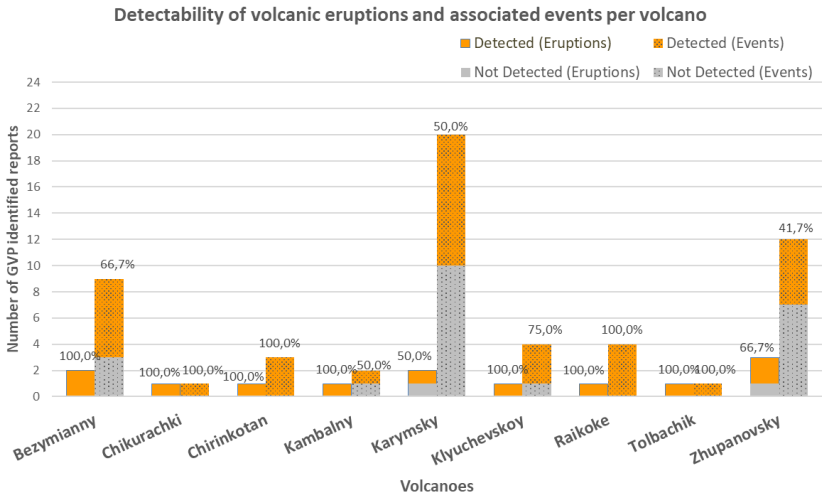

Figure 5.3. Detection of identified activity (eruptions and discrete events) for the nine volcanoes. The stacked bars show the number of GVP reports and the percentage of events identified by the algorithm are shown above each bar.

The 34 detected volcanic events were further characterized according to the eight non-exclusive detections classes (A to H) defined in table 4.5 (Figure 5.4a). Each class reflects the specific spatial configurations of stations around the volcano and hence the relative detectability conditions of the events. The Class A was the most frequently observed result, associated with 79.41% of the detected events. Also most frequently identified were classes B (47.06%), F (35.29%) and C (32.35%). The less common were the classes G (14.71%), E (8.82%) and D (5.88%). For 50% of the cases (17 events), the observed arrival times were beyond the considered celerity thresholds; therefore, they were only identified in the volcano back azimuth and were categorised under the H class.

The individual contribution of each station for the total number of detections was also analysed (Figure 5.4b). Station I44RU was responsible for the highest number of detections, identifying 27 of the 56 events (48.2%), followed by I53US, with 15 detections (26.8%), and I45RU with 12 detections (21.4 %). The other stations had a lower number of detections, with I30JP detecting 8 events (14.3%), and stations I58US and I34MG with 5 events each (8.9%). The I60US station recorded just 1 detection (1.8%), reflecting a minimal contribution to the overall data set.

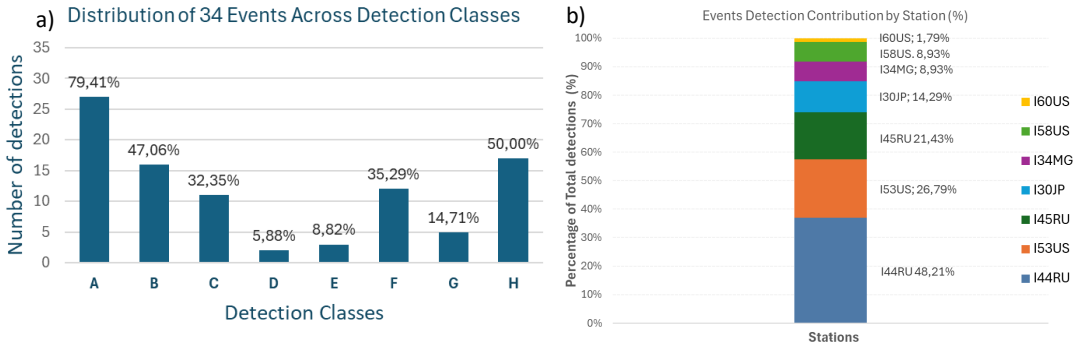

Figure 5.4. Detection statistics for the 34 detected volcanic events. a): Number of events per detection classes (A–H); percentages above bars indicate the proportion of total detections. Each event may be associated with multiple scenarios. Right: Contribution of detections by station (%).

5.1.2. Western Pacific Volcanic Region

Concerning the volcanoes of the western pacific region, we selected six volcanoes (Figure 5.5a) that had VEI>=3 activity between 2011 and 2020, for a total of 13 eruptive periods, with duration spanning from 11 days to almost 8 months (Table 5.2), and 24 discrete events (Figure 5.5b). The 2020 eruption of Taal was classified as VEI 4. All other eruptive periods reported for this group were categorised by moderate to large explosive events, corresponding to a VEI 3.

No detections were identified during the 17-days of the eruptive phase of Ontakesan volcano, in 2014. Similarly, no detections were associated with the eruptions of Kirishimayama, in 2018, Kuchinoerabujima, in 2018 and 2020, neither Soputan, in 2012 and 2015. An individual analysis for each volcano is presented in Appendix A.2 and B.2.

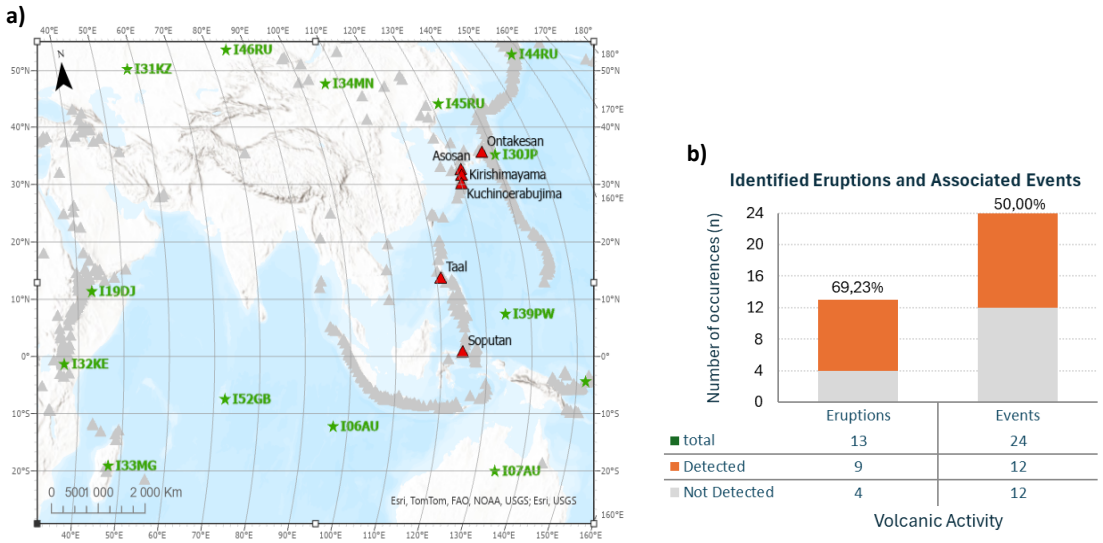

Figure 5.5. a) Location map with six volcanoes (red triangles) identified as having eruptive activity during the selected period in the GVP, as well as the three closest IMS stations (green stars). b) Volcanic activity, shown as eruptive periods and events. The stacked bar chart represents the number of detected (orange) and undetected (grey) occurrences.

Table 5.1 Summary of volcanic eruption characteristics and detected events in the Western Pacific Volcanic Regions.

GVP number	Volcano_Name	Eruption period time	VEI	Duration	Events Detected
282110	Asosan	2016 Oct 7 - 2016 Nov 12	3	1 m, 5 d	Yes
282090	Kirishimayama	2011 Jan 19 - 2011 Sep 7	3	7 m, 19 d	Yes
		2018 Mar 1 - 2018 Jun 22	3	3 m, 21 d	No
282050	Kuchinoerabujima	2015 May 29 - 2015 Jun 19	3	22 d	Yes
		2018 Oct 21 - 2019 Feb 3	3	3 m, 13 d	Yes
		2020 Jan 11 - 2020 May 13	3	4 m, 2 d	No
283040	Ontakesan	2014 Sep 27 - 2014 Oct 14	3	17 d	No
266030	Soputan	2011 Jul 3 - 2011 Aug 15	3	1 m, 12 d	Yes
		2012 Aug 26 - 2012 Sep 19	3	25 d	No
		2015 Jan 6 - 2015 Mar 9	3	2 m, 3 d	Yes
		2016 Jan 2 - 2016 Feb 7	3	1 m, 5 d	Yes
		2018 Oct 2 - 2018 Dec 16	3	2 m, 14 d	Yes
273070	Taal	2020 Jan 12 - 2020 Jan 22	4	11 d	Yes

The results of infrasound detections applied to this group of volcanoes are summarised in Figure 5.6. Volcanoes such as Asosan and Taal showed fully detectable activity, with 100% of eruptions and events detected (Asosan: n = 1 eruption, 2 events; Taal: n = 1 eruption, 2 events). The algorithm successfully identified the totality of the recorded activity, probably due to clear infrasonic signatures and adequate station coverage. Kirishimayama had 1 out of 2 eruptions detected (50%) and 3 out of 5 events (60%), while Kuchinoerabujima had a detection rate of 66.7% for eruptions (n = 3) and 50% for events (n = 4). Soputan Volcano was the most active of the group, with 5 eruptions and 10 events, of which 4 eruptions (80%) and 3 events (30%) were detected.

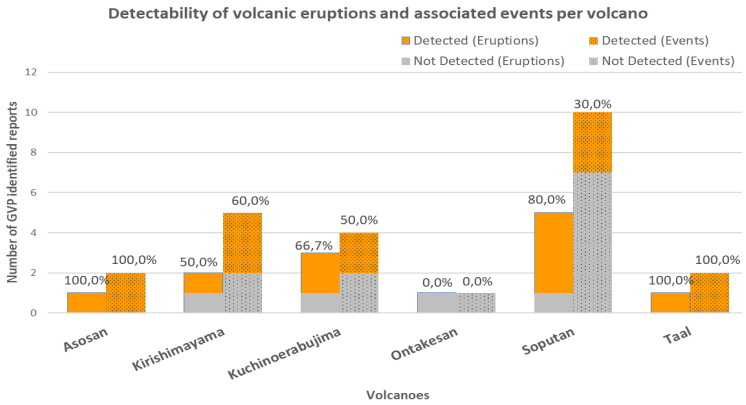

Figure 5.6. Detection of identified activity (eruptions and discrete events) for the six volcanoes. The stacked bars show the number of GVP reports and the percentage of events identified by the algorithm are shown above each bar.

For this group of volcanoes, the 12 identified events were classified (A-H). Class A was the most frequent, associated with 10 events (83.33%). Class C was present in 6 events (50%). Classes D and F were associated with 3 events each (25%), while classes B and E were associated with 1 event each (8.33%). No events observed for class G. Five events (41.67%) were identified only by their back-azimuths from the stations (Class H) (Figure 5.7a). The distribution of detections (n=25) throughout the several sites within a 4,500 km radius is shown in Figure 5.7b. With n = 8 (32 %), station I39PW had the most detections, followed by I30JP with n=7 (28%) and I45RU with n = 4 (16%). Less than 15% were identified at other stations, such as I34MN (n=3; 12%), I44RU (n=2; 8 %), and I04AU (n=1; 4%). No detections were identified at stations I07AU, I06AU, I40PG, I60US and I46RU.

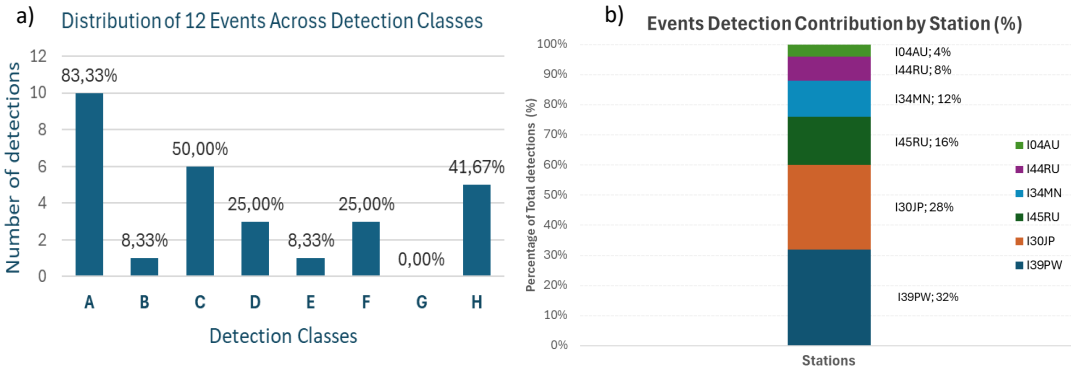

Figure 5.7. Detection statistics for the 12 detected volcanic events. a) Number of events per detection classes (A–H); percentages above bars indicate the proportion of total detections. Each event may be associated with multiple scenarios. b) Contribution of detections by station (%).

5.1.3. Southwest Pacific Volcanic Region

Concerning the volcanoes of the Southern Pacific Region, we selected five volcanoes (Figure 5.8a) that had VEI>=3 activity between 2011 and 2020, for a total of six eruptive periods and 25 discrete eruptive events (Table 5.3, Figure 5.8b). The eruptions were successfully detected in five cases (n = 5, 83.3%), while discrete events were detected in 12 of the 25 cases (48%). An individual analysis for each volcano is presented in Appendix A.3. and B.3.

According to GVP, the eruptions of Ambae, Tinakula and Manam (in 2010), were classified as moderate to large explosive events (VEI 3), while the three eruptive periods of Rabaul, Ulawun and Manan (in 2014) were classified as large explosive events (VEI 4).

Duration of the six eruptive periods ranged from a minimum of six days, in the case of the Tinakula eruption, to a maximum of approximately three years, six months, and 12 days for the 2014-2018 eruption of Manam volcano. All eruptions were detected at Ambae, Rabaul, Tinakula, and Ulawun volcanoes (1 of 1 eruption each, 100%) and one time at Manam volcano (1 of 2 eruptions, 50%).

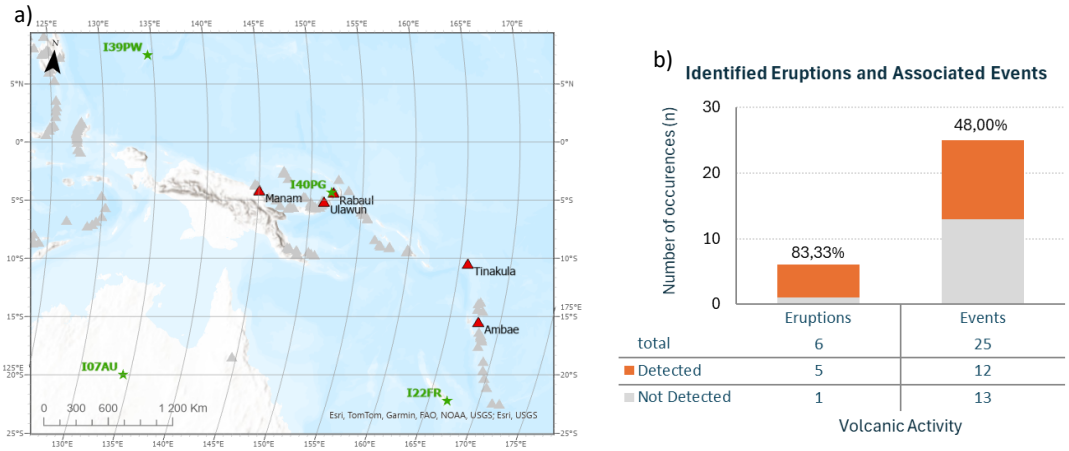

Figure 5.8. a) Location map with five volcanoes (red triangles) identified as having eruptive activity during the selected period in the GVP, as well as the three closest IMS stations (green stars). b) Volcanic activity, shown as eruptive periods and events. The stacked bar chart represents the number of detected (orange) and undetected (grey) occurrences.

Table 5.3. Summary of volcanic eruption characteristics and detected events in the Southwest Pacific Volcanic Regions.

GVP number	Volcano_Name	Eruption period time	VEI	Duration	Events Detected
257030	Ambae	2017 Sep 6 - 2018 Oct 30	3	1 y, 1 m, 24 d	Yes
251020	Manam	2010 Aug 10 - 2013 Dec 15	3	3 y, 4 m, 5 d	No
		2014 Jun 29 - 2018 Jan 10	4	3 y, 6 m, 12 d	Yes
252140	Rabaul	2014 Jul 7 - 2014 Sep 18	4	2 m, 11 d	Yes
256010	Tinakula	2017 Oct 21 - 2017 Oct 26	3	6d	Yes
252120	Ulawun	2019 Jun 26 - 2019 Oct 5	4	3 m, 9 d	Yes

Regarding the distinct volcanic events, the detection rates varied significantly among the different volcanoes (Figure 5.9). All events associated with both Rabaul and Ulawun volcanoes were detected (1 in 1, 100 %). For Manam volcano, 2 out of 4 events (50%) were detected during the 2014 and 2017 episodes, while for Tinakula volcano only 1 out of 2 events (50%) was detected. The lowest detection rate occurred at Ambae volcano, where only 7 out of 17 events were detected (41.2%), which likely reflects variations in event intensities or unfavourable atmosphere conditions that limited signal propagation. No infrasound detections were identified during Manam's eruptive phase between 2010 and 2013.

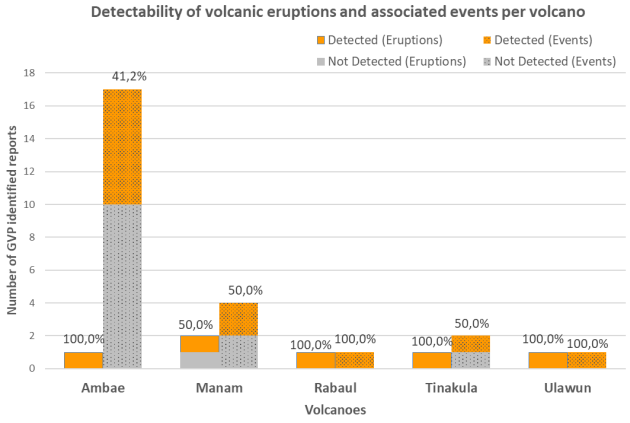

Figure 5.9. Detection of identified activity (eruptions and discrete events) for the five volcanoes. The stacked bars show the number of GVP reports and the percentage of events identified by the algorithm are shown above each bar.

A total of 12 events were detected and classified according to the different detections classes (Figure 5.10a). Class A was the most frequent, associated with 10 events (83.33%). Class C was observed in 6 events (50%), followed by classes B and H, both associated with 4 events (33.33 per cent), with class H reflecting the subset of cases influenced by directional propagation effects. Class F, was present in two events (16.67%). Class H was also associated with 4 events (33.33%), Classes D, E and G were not observed in this group.

Figure 5.10b, shows the percentage of detections attributed to the nine stations analysed. Nine detections (39.13%) were identified at station I22FR, followed by I40PG with n = 7 (30.43%) and I39PW with n = 3 (13.04%). At stations I07AU, I04AU, I30JP and I05AU only one (4.35%) detection was identified at each. Stations I36NZ and I60US did not register any detections. These results show the strong role of stations I22FR and I40PG in the detection of events within this group.

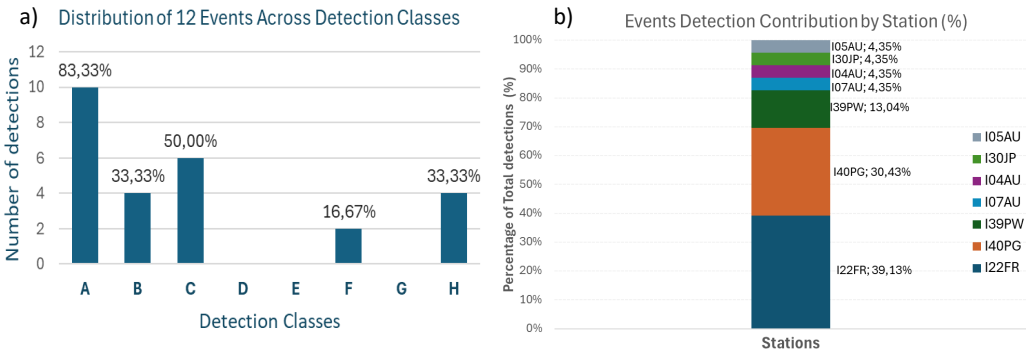

Figure 5.10. Detection statistics for the 12 detected volcanic events. a) Number of events per detection classes (A–H); percentages above bars indicate the proportion of total detections. Each event may be associated with multiple scenarios. b) Contribution of detections by station (%).

5.1.4. Eastern Pacific Volcanic Region

Concerning the Eastern Pacific Region, a large (VEI 4) explosive event was identified for Wolf volcano in the GVP (Table 5.4 and Figure 5.11). Despite the eruptive phase lasting one month and 21 days, no infrasound detections were identified by the algorithm.

Table 5.4. Summary of volcanic eruption characteristics and detected events in the Eastern Pacific Volcanic Regions.

GVP number	Volcano_Name	Eruption period time	VEI	Duration	Events Detected
353020	Wolf	2015 May 25 - 2015 Jul 16	4	1 m, 21 d	No

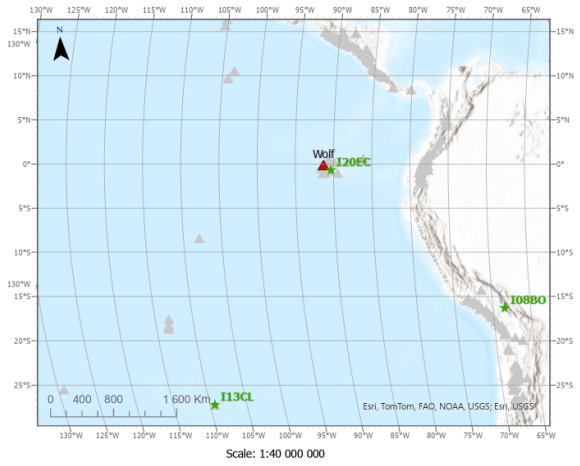

Figure 5.11. Location map of Wolf Volcano (red triangle) identified as having eruptive activity during the selected period in the GVP. The three stations (green star) closest to this volcano (I08BO, I13CL and I13CL) are more than 3,000 kilometres away. I20EC was lately certified (2017), not operational during the eruption period.

5.1.5. Sunda-Banda Volcanic Region

The results of the group detections are summarised in Figure 5.12a. Eleven eruptive periods were identified, with each volcano showing between one to three distinct events (Table 5.5). Eruptive periods ranged from as short as one day (Merapi in 2013) to as long as approximately seven and a half years (Semeru volcano). Five of the eruptions were classified as VEI 4, while the remaining six were classified as moderate to large explosive events (VEI 3).

A total of 11 eruptions and 19 discrete events were identified across eight volcanoes (Figure 5.12b). Eruptions were successfully detected in 5 out of 11 cases (45.45 %), while discrete events were detected in 9 out of 19 cases (47.3%). An individual analysis for each volcano is presented in Appendix A.5. and B.5.

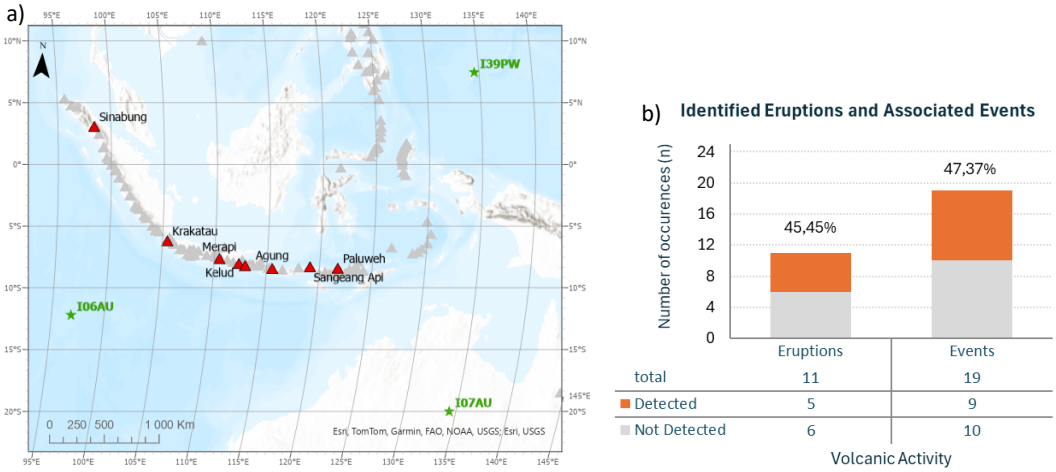

Figure 5.12. a) Location map with eight volcanoes (red triangles) identified as having eruptive activity during the selected period in the GVP, as well as the three closest IMS stations (green stars). b) Volcanic activity, shown as eruptive periods and events. The stacked bar chart represents the number of detected (orange) and undetected (grey) occurrences.

Table 5.5. Summary of volcanic eruption characteristics and detected events in the Sunda-Banda Volcanic Regions.

GVP number	Volcano_Name	Eruption period time	VEI	Duration	Events Detected
264020	Agung	2017 Nov 21 - 2019 Jun 13	3	1 y, 6 m, 23 d	No
263280	Kelud	2014 Feb 13 - 2014 Feb 15	4	3 d	Yes
262000	Krakatau	2018 Jun 18 - 2020 Apr 17	3	1 y, 9 m, 30 d	No
263250	Merapi	2013 Nov 18 - 2013 Nov 18	3	1 d	No
		2014 Mar 9 - 2014 Apr 20	3	1 m, 11 d	Yes
		2018 May 11 - 2020 Jun 21	3	2 y, 1 m, 10 d	Yes
264150	Paluweh	2012 Oct 8 - 2013 Oct 31	3	1 y, 23 d	No
264050	Sangeang Api	2014 May 30 - 2015 Nov 5	4	1 y, 5 m, 6 d	Yes
263300	Semeru	2017 Jun 6 - 2024 Dec 19 (ongoing)	4	7 y, 6 m, 13 d	No
261080	Sinabung	2013 Sep 15 - 2018 Jun 22	4	4 y, 9 m, 7 d	No
		2019 Feb 6 - 2019 Jun 9	4	4 m, 3 d	Yes

Eruptions were detected at Kelud and Sangeang Api volcanoes (1 of 1 eruption each, 100%), at Merapi volcano (2 of 3 eruptions, 66.7%) and at Sinabung volcano (1 of 2, 50%). In terms of distinct events, all events were identified correctly for Kelud and Sangeang Api volcanoes (2 of 2 and 3 of 3, 100%), 2 out of 3 events for Sinabung volcano (66.7%), and 2 out of 4 events for Merapi volcano (50%). No infrasound detections were identified during different periods of activity of Agung (2017), Krakatau (2018), Paluweh (2012), and Semeru (2017) volcanoes. Additionally, no detections were associated with the Merapi eruption in 2013 or Sinabung's sustained activity between 2013 and 2018 (Figure 5.13).

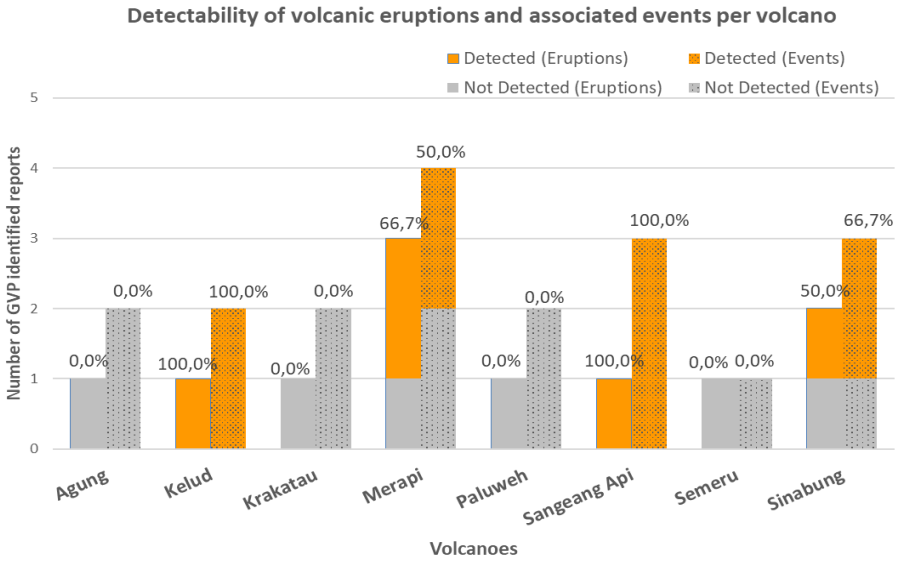

Figure 5.13. Detection of identified activity (eruptions and discrete events) for the eight volcanoes. The stacked bars show the number of GVP reports and the percentage of events identified by the algorithm are shown above each bar.

Nine detected events were classified by the different classes (Figure 5.14a). Class C (detection at two of the three closest stations) was the most frequent, observed in 6 events (66.67%), followed by class A associated with 5 events (55.56%). Class H was associated with 3 events (33.33%) while classes E and F were detected in 2 events each (22.22%). Classes D and G were associated with 1 event each (11.11%) and Class B was not observed in this group.

Figure 5.14b shows the percentage of individual contribution of each station. Stations I06AU and I39PW detected the highest number of events, each with n = 5 (23.81%). Station I52GB followed with n = 4 (19.05%), while I07AU and I04AU each with n = 3 (14.29%). At station I40PG only one (n = 1, 4.35%) detection was identified across the time.

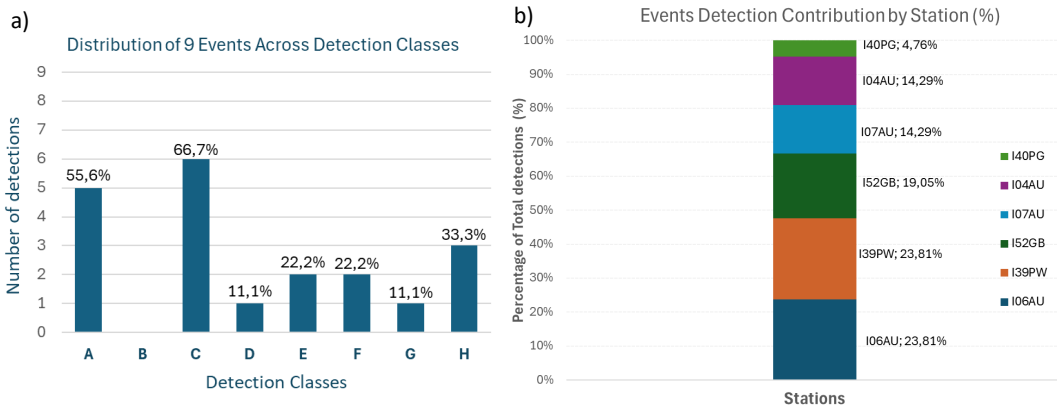

Figure 5.14. Detection statistics for the nine detected volcanic events. a) Number of events per detection classes (A–H); percentages above bars indicate the proportion of total detections. Each event may be associated with multiple scenarios. b) Contribution of detections by station (%).

5.1.6. Eastern Africa Volcanic Region

Concerning the Eastern African Region, a large (VEI 4) explosive event was identified in the GVP for Nabro volcano (and Figure 5.11, Table 5.6). The eruption was detected by the algorithm at 3 of the 7 stations within a radius of 4,500 km: I32KE, I48TN and I31KZ. The nearest station I19DJ (≈264 km away) did not register any detections, as well as stations I33MG, I52GB and I35NA, probably as a result of the low atmospheric propagation levels at the time of the event. A detailed analysis is present in Appendix A.6. and B.6.

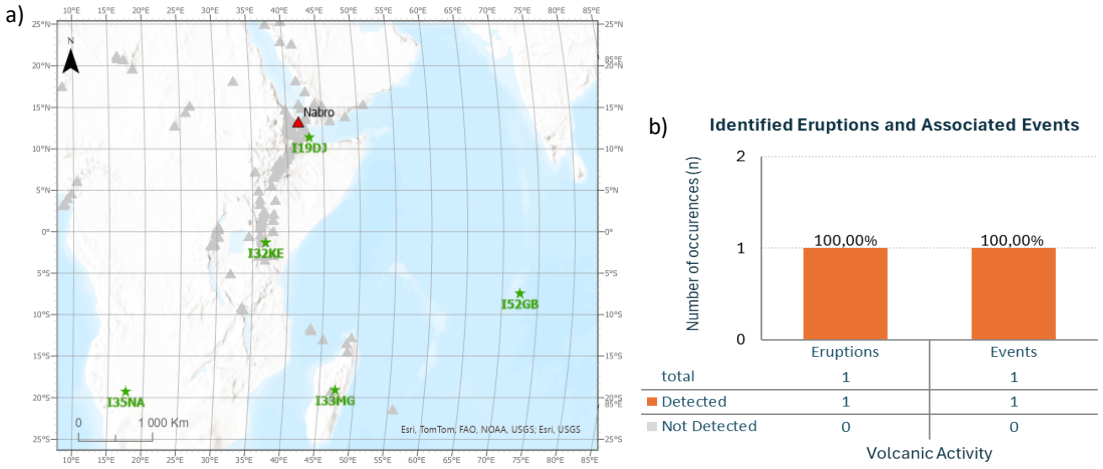

Figure 5.15. a) Location map of Nabro volcano (red triangle) identified as having eruptive activity during the selected period in the GVP, as well as the three closest IMS stations (green stars). b) Volcanic activity, only one eruption and event were identified.

Table 5.6. Summary of volcanic eruption characteristics and detected events in the Eastern Africa Volcanic Regions.

GVP number	Volcano_Name	Eruption period time	VEI	Duration	Events Detected
221101	Nabro	2011 Jun 13 - 2012 Jun 3	4	11 m, 21 d	Yes

5.1.7. Atlantic Ocean Volcanic Region

Concerning the Atlantic Ocean Volcanic region, a single, large (VEI 4) eruption - associated with Grimsvötn volcano (Figure 16a) was identified by the GVP (Table 5.7). The eruption lasted five days, during which infrasound signals were detected at various stages of the eruptive sequence. An individual analysis is presented in Appendix A.7. and B.7.

Table 5.7. Summary of volcanic eruption characteristics and detected events in the Atlantic Volcanic Regions.

GVP number	Volcano_Name	Eruption period time	VEI	Duration	Events Detected
373010	Grimsvotn	2011 May 21 - 2011 May 25	4	5 d	yes

The only event reported (Figure 5.16b), is referring to the onset of the Grimsvötn volcano eruption at 19:36 UTC, detected at 5 of the 7 stations: I18DK, I26DE, I42PT, I43RU and I31KZ. No detections were identified at the closest station I37NO (≈1,638 km away) nor at station I48TN (≈3,649 km away). The event was simultaneously classified in classes C, E and H, showing detections at two of the three closest stations, and at more than three stations within a radius of 4,500 km. At other stations, detections were identified in the volcano back-azimuth, but with arrival times falling outside the selected celerity thresholds.

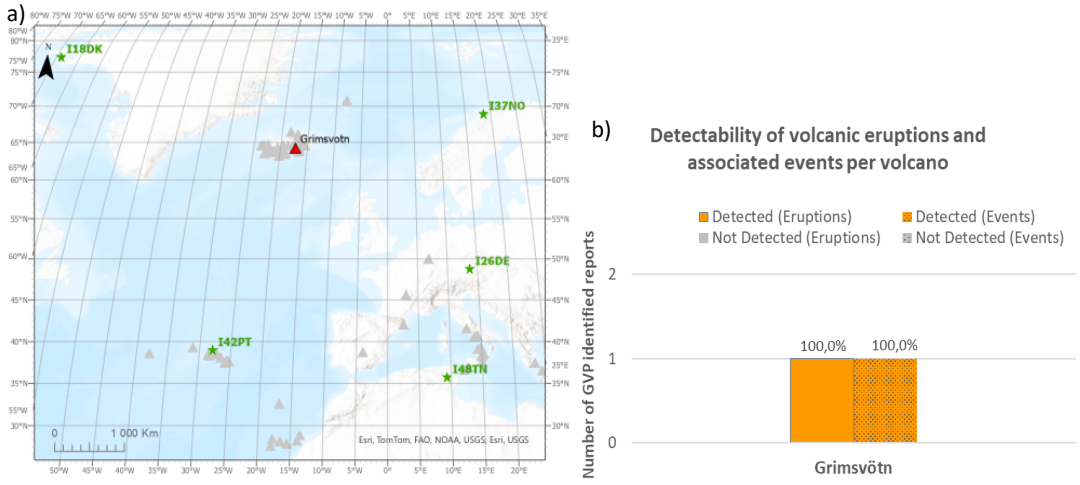

Figure 5.16. a) Location map of Wolf Volcano (red triangle) identified as having eruptive activity during the selected period in the GVP.

5.1.8. European Volcanic Region

Concerning the European Volcanic Region, the GVP reports activity for Etna volcano (Figure 5.17a) with two VEI 3 eruptive periods and a total of 18 discrete events. The first eruptive period lasted approximately two years and eight months, while the second lasted around eight years, nine months, and 14 days (Table 5.8).

Eruptions were successfully detected in the two periods (100%), while discrete events were detected in 10 out of 18 cases (55.56%). An individual analysis for each volcano is presented in Appendix A.8. and B.8.

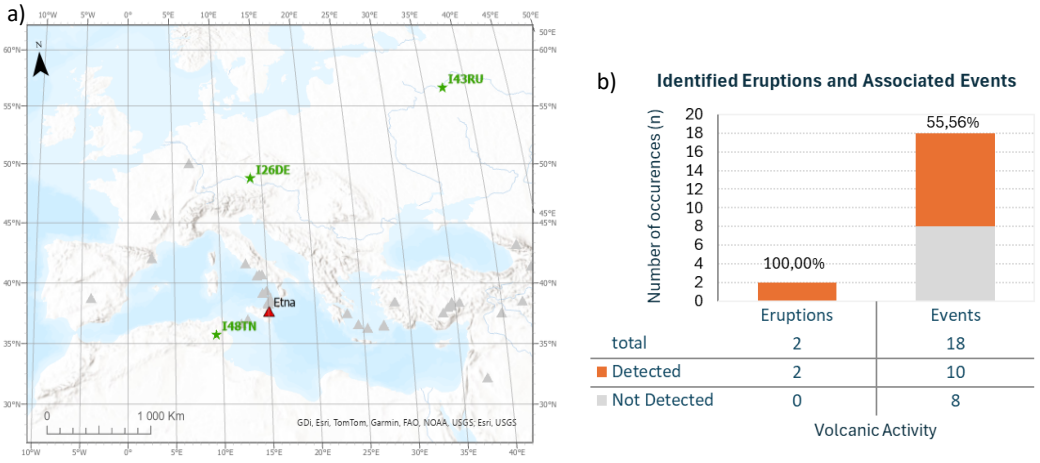

Figure 5.17. Location map of Mount Etna volcano (red triangle) identified as having eruptive activity during the selected period in the GVP.

Table 5.8. Summary of volcanic eruption characteristics and detected events in the European Volcanic Regions.

GVP number	Volcano_Name	Eruption period time	VEI	Duration	Events Detected
211060	Etna	2010 Aug 25 - 2013 Apr 27	3	2 y, 8 m, 2 d	yes
		2013 Sep 3 - 2022 Jun 17	3	8 y, 9 m, 14 d	yes

The 10 detected events were classified across the different detection classes (Figure 5.18a). Class A was the most often observed, identified in 7 events (70%). Class C was identified in 4 events (40%), followed by class B and F, each associated with 3 events (30%). Class H was associated with 6 events (60%). Classes D, E and G were not observed.

The individual contribution of each station for the total number of detections was analysed (Figure 5.18b). As expected, stations I48TN and I26DE recorded the highest number of detections, each with n = 6 (33.33%), followed by I31KZ with n = 3 (16.67%) and I43RU with n =

2 (11.11%). At station I42PT only one detection (4.35%) was detected during the analysis period. No detections were identified at stations I37NO, I17CI and I19DJ.

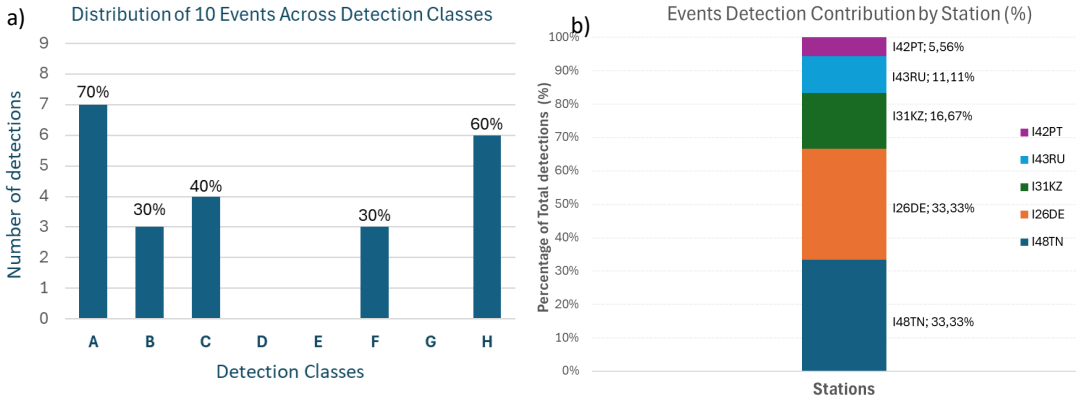

Figure 5.18. Detection statistics for the 10 detected volcanic events. a) Number of events per detection classes (A–H); percentages above bars indicate the proportion of total detections. Each event may be associated with multiple scenarios. b) Contribution of detections by station (%).

5.1.9. North America Volcanic Region

Across this region (Figure 5.19a), five volcanoes had activity according to the GVP, with a total of nine eruptive periods, with Pavlof volcano accounting for four of them (Table 5.9) and 13 discrete events. Eruption duration ranged from as short as a single day, such as the 2016 Cleveland volcano eruption, to as long as approximately two years, seven months, and 19 days, also at Cleveland volcano, between 2016 and 2019.

Eruptions were successfully detected in 6 out of 9 cases (66.67 %), while discrete events were detected in 9 out of 13 cases (69.23%) (Figure 5.19b). All periods in the GVP were classified as moderate to large explosive events, corresponding to a VEI 3.

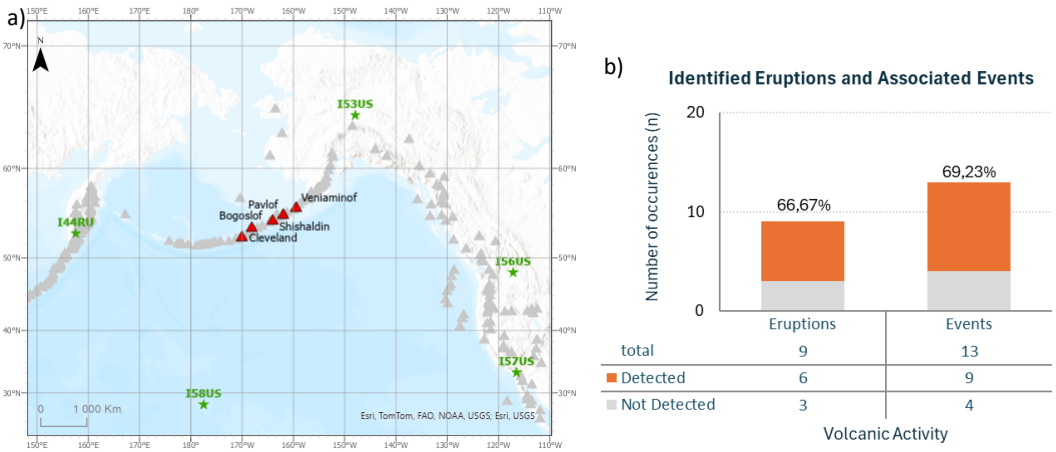

Figure 5.19. Location map with five volcanoes (red triangles) identified as having eruptive activity during the selected period in the GVP, as well as the three closest IMS stations (green stars). b) Volcanic activity, shown as eruptive periods and events. The stacked bar chart represents the number of detected (orange) and undetected (grey) occurrences.

Table 5.9. Summary of volcanic eruption characteristics and detected events in the North America Pacific Volcanic Regions.

GVP number	Volcano_Name	Eruption period time	VEI	Duration	Events Detected
311300	Bogoslof	2016 Dec 20 - 2017 Aug 30	3	8 m, 10 d	Yes
311240	Cleveland	2016 Apr 16 - 2019 Jan 20	3	2 y, 9 m, 4 d	no
		2020 Jun 1 - 2020 Jun 1	3	1 d	yes
312030	Pavlof	2013 May 13 - 2013 Jun 26	3	1 m, 13 d	no
		2014 May 31 - 2014 Jun 6	3	7 d	yes
		2014 Nov 12 - 2014 Nov 15	3	4 d	yes
		2016 Mar 27 - 2016 Jul 30	3	4 m, 3 d	yes
311360	Shishaldin	2019 Jul 23 - 2020 May 4	3	9 m, 11 d	yes
312070	Veniaminof	2013 Jun 13 - 2013 Oct 12	3	3 m, 29 d	No

The algorithm successfully identified all eruptions and distinct events associated with Bogoslof volcano (100% detection rate). Concerning Shishaldin volcano, 1 out of 1 eruption (100%) and 2 out of 3 (66.7%) distinct events were detected. Concerning Cleveland Volcano, 1 out of 2 eruptions and 1 of 2 distinct events were identified (50% each). For Pavlof volcano, 3 of 4 eruptions (75%) and 5 of 7 distinct events (71.4%) were detected.

No infrasound detections were identified during Cleveland's 2016-2029 eruptive period and the Pavlof May–June 2013 eruptive period. Veniaminof volcano had no eruptions or distinct events that were identified by the algorithm (Figure 5.20).

The absence of detections, particularly during the prolonged 2016 Cleveland activity, may be linked to the moderate eruptive strength combined with unfavourable propagation conditions, as suggested by elevated attenuation values and marginal $V_{eff\text{-}ratio}$ distributions along the paths to IMS stations. An individual analysis for each volcano is presented in Appendix A.9. and B.9.

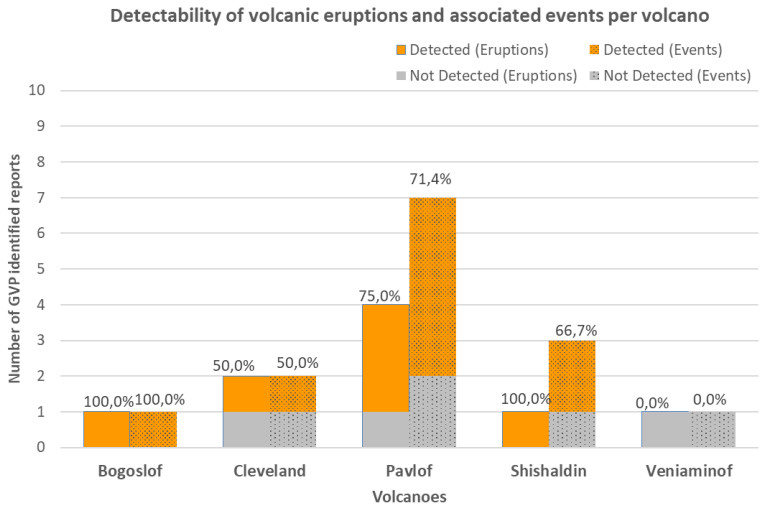

Figure 5.20. Detection of identified activity (eruptions and discrete events) for the five volcanoes. The stacked bars show the number of GVP reports and the percentage of events identified by the algorithm are shown above each bar.

The nine detected events were classified according to different detection classes as shown in Figure 5.21a. Class A was the most frequently observed, accounting for 8 events (88.89%), followed by class B with 5 events (55.6%) associated. Class F included 4 events (44.4%), and Class C was associated with 3 events (33.33%). A single event (11.11%) was linked to Class H. Classes D and E were not represented among the detected events.

The percentage of detections across the 11 stations were analysed (Figure 5.21b). I53US recorded the highest number of detections with n = 8 (50%), followed by stations I44RU, I57US, I18DK each with n = 2 (13%). At station I56US and I59US only one detection (6%) was identified during the analysis period. No detections were identified at stations I58US, I45RU, I60US, I30JP and I10CA.

Figure 5.21. Detection statistics for the 9 detected volcanic events. a): Number of events per detection classes (A–H); percentages above bars indicate the proportion of total detections. Each event may be associated with multiple scenarios. b) Contribution of detections by station (%).

5.1.10. Middle America-Caribbean Volcanic Region

In this region, three volcanoes, each associated with a single period of activity, were identified in the GVP (Figure 5.22a). The eruptive periods ranged from a minimum of approximately seven months for the San Miguel volcanic eruption to a maximum of approximately four years, eight months, and 29 days for the Turrialba eruption between 2015 and 2019 (Table 5.10). All eruptions were classified as moderate to large explosive events VEI 3.

A total of three eruptions and six discrete events were identified during the study period (Figure 5.22b).

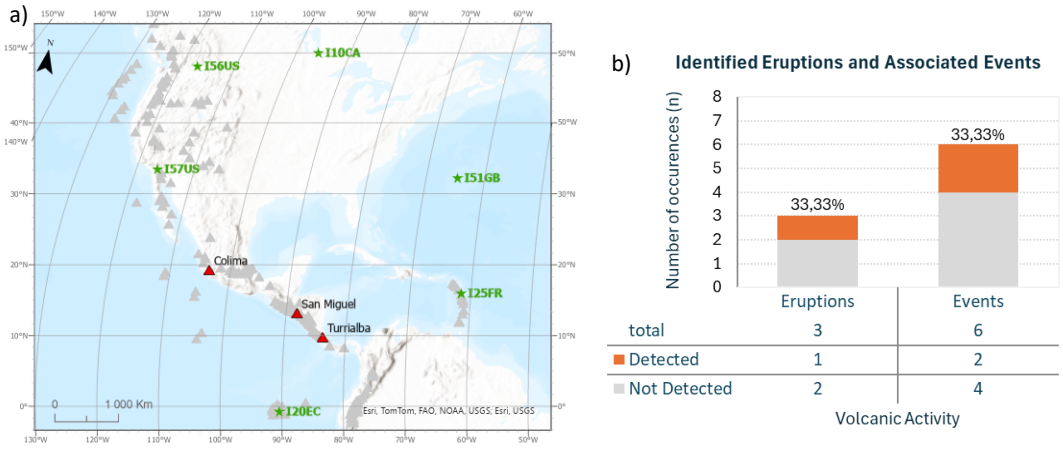

Figure 5.22. Location map with three volcanoes (red triangles) identified as having eruptive activity during the selected period in the GVP, as well as the three closest IMS stations (green stars). b) Volcanic activity, shown as eruptive periods and events. The stacked bar chart represents the number of detected (orange) and undetected (grey) occurrences.

Table 5.10. Summary of volcanic eruption characteristics and detected events in the Middle America-Carabbean Volcanic Regions.

GVP number	Volcano_Name	Eruption period time	VEI	Duration	Events Detected
341040	Colima	2013 Jan 6 - 2017 Mar 7	3	4 y, 2 m, 1 d	No
343100	San Miguel	2013 Dec 29 - 2014 Jul 28	3	6 m, 29 d	No
345070	Turrialba	2015 Mar 8 - 2019 Dec 7	3	4 y, 8 m, 29 d	Yes

Among all cases analysed in this group, only the eruption and one of the two distinct events at Turrialba Volcano were detected by the algorithm. No eruptions or distinct events were identified at Colima or San Miguel. A detailed, individual analysis for each volcano is provided in Appendix A.10. and B.10.

The only event detected in this group was classified into class B, associated with a short-duration explosion at Turrialba Volcano, observed exclusively at station I08BO, located 3,373 km away. No detections were recorded at any other station.

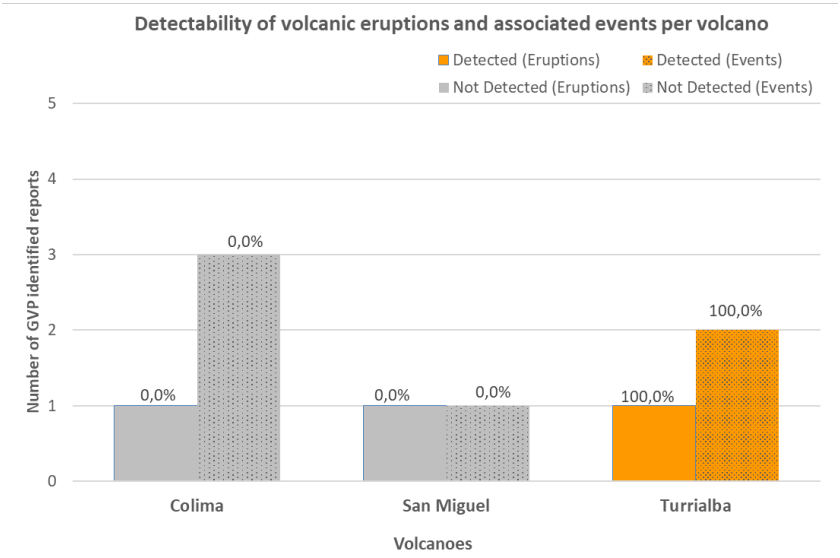

Figure 5.23. Detection of identified activity (eruptions and discrete events) for the three volcanoes. The stacked bars show the number of GVP reports and the percentage of events identified by the algorithm are shown above each bar.

5.1.11. South America Volcanic Region

Six volcanoes were identified in this group (Figure 5.24a), with a total of eight eruptive periods, three of then occurring at Tungurahua volcano (Table 5.11) and 22 discrete events were identified (Figure 5.24b). These eruptive periods ranged from a minimum of one month and four days for the Calbuco eruption to a maximum of approximately eight years, one month, and 13 days (as of December 2024) for the ongoing Sabancaya eruption.

According to the GVP, the eruption of Puyehue-Cordón Caulle between June 4, 2011, and April 21, 2012, was classified as a very large explosive event (VEI 5). In comparison, the 2015 eruption of Calbuco was categorized as a large explosive event (VEI 4). The remaining six eruptive periods were classified as moderate to large explosive events (VEI 3).

Eruptions were successfully detected in 6 out of 8 cases (75%), while discrete events were detected in 13 out of 22 cases (59.1%). An individual analysis for each volcano is presented in Appendix A.11. and B.11.

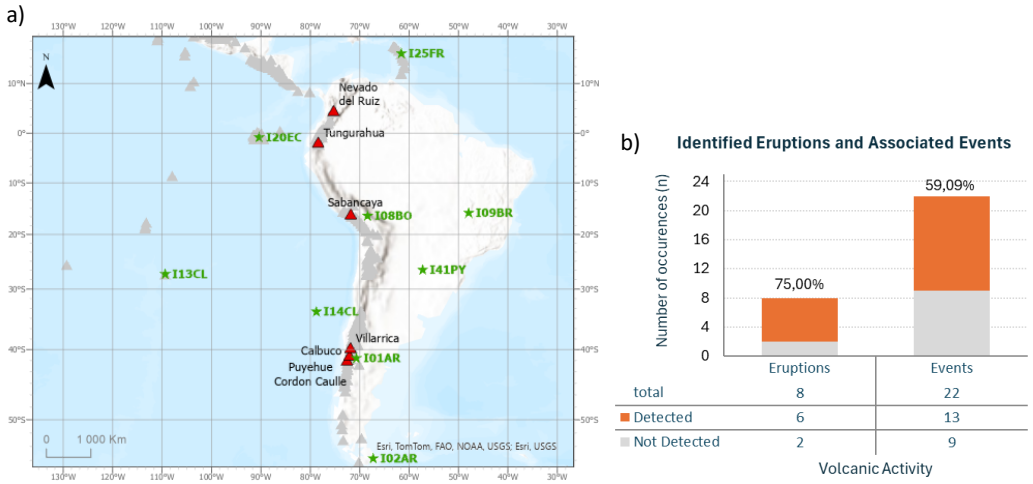

Figure 5.24. Location map with six volcanoes (red triangles) identified as having eruptive activity during the selected period in the GVP, as well as the three closest IMS stations (green stars). b) Volcanic activity, shown as eruptive periods and events. The stacked bar chart represents the number of detected (orange) and undetected (grey) occurrences.

Table 5.11. Summary of volcanic eruption characteristics and detected events in the South America Volcanic Regions

GVP number	Volcano_Name	Eruption period time	VEI	Duration	Events Detected
358020	Calbuco	2015 Apr 22 - 2015 May 26	4	1 m, 4 d	Yes
351020	Nevado del Ruiz	2012 Feb 22 - 2013 Jul 12	3	1 y, 4 m, 20 d	No
357150	Puyehue Cordon Caulle	2011 Jun 4 - 2012 Apr 21	5	10 m, 17 d	Yes
354006	Sabancaya	2016 Nov 6 - ongoing	3	8 y, 1 m, 13 d	No
352080	Tungurahua	2011 Apr 20 - 2011 May 26	3	1 m, 6 d	Yes
		2011 Nov 27 - 2012 Sep 4	3	9 m, 8 d	yes
		2012 Dec 14 - 2016 Mar 16	3	3 y, 3 m, 2 d	Yes
357120	Villarrica	2014 Dec 2 - 2024 Dec 13	3	10 y, 11 d	Yes

The algorithm successfully detected all eruptions of the Calbuco, Puyehue-Cordón Caulle, and Villarrica volcanoes (1 out of 1 eruption for each). Eruptions associated with Tungurahua were also fully detected (3 out of 3). Regarding discrete events, the algorithm detected 2 out of 2 events for Calbuco, the single event for Puyehue-Cordón Caulle, 9 out of 15 for Tungurahua, and 1 out of 2 for Villarrica. In contrast, no infrasound detections were identified for eruptions or discrete events associated with Nevado del Ruiz (2012 and 2013) or Sabancaya (2016–ongoing) (Figure 5.25).

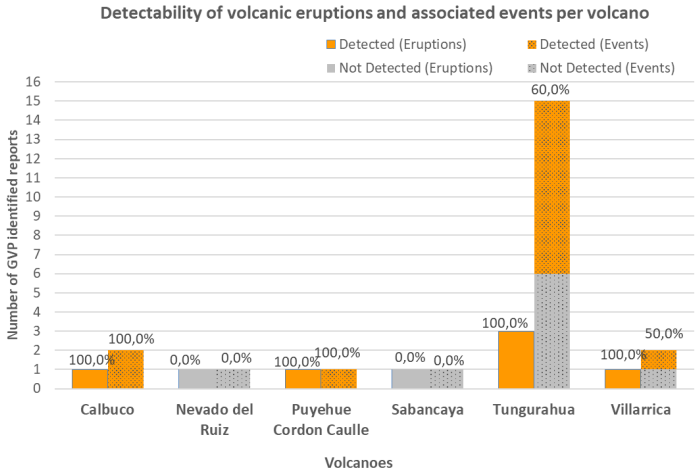

Figure 5.25. Detection of identified activity (eruptions and discrete events) for the six volcanoes. The stacked bars show the number of GVP reports and the percentage of events identified by the algorithm are shown above each bar.

A total of 13 detected discrete events were classified according to the detection classes (Figure 5.26a). Class B, was the most frequently observed, accounting for 8 events (61.5%), followed by class A with 7 events (53.8%) associated. Class F was identified in 6 events (46.2%), class G in 5 events (38.5%), while class H was associated with 4 events (30.8%). Classes C, D and E were not represented among the detected events.

The distribution of detections (n = 27) across the seven monitoring stations were analysed (Figure 5.26b). Station I08BO recorded the highest number of detections with n = 8 (29.63%), followed by I09BR with n = 7 (25.93%) and I13CL with n = 6 (22.22%). Stations I14CL, I02AR and I41PY each contributed with n = 2 detections (7.41%). No infrasound detections were identified at station I51GB.

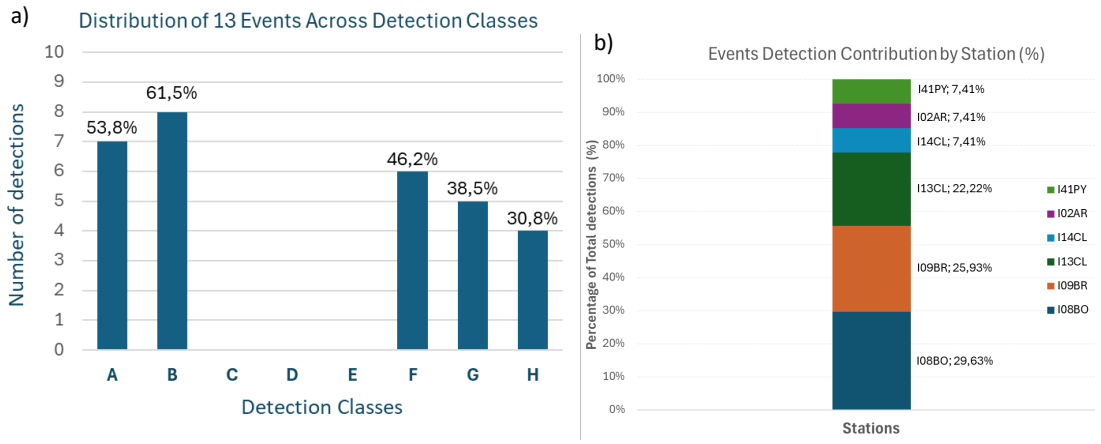

Figure 5.26. Detection statistics for the 13 detected volcanic events. a) Number of events per detection classes (A–H); percentages above bars indicate the proportion of total detections. Each event may be associated with multiple scenarios. b) Contribution of detections by station (%).

5.2. The IDC bulletins

The events listed in the IDC bulletins are presented below based on the GVP event onset time, categorized by volcanic region, and ordered chronologically by year. Only events that met all the predefined criteria were included in the analysis. The associated parameters have been previously described in Chapter 4. For each event, the corresponding volcano identified through the applied detection algorithm is indicated. This association is based on the temporal correspondence with the dates and times reported by the GVP, as well as their spatial proximity—each volcano is located within 250 km of the listed event location.

5.2.1. SEL3 bulletins results

At the IDC, following the final stages of station-level processing, the resulting arrivals are combined to generate events, which are published in the form of automatic bulletins. Among these, the SEL3 bulletin is the most comprehensive, as it integrates data from all waveform technologies

Through the analysis of the IDC's automatic bulletin (SEL3), 13 events were identified as potentially related to the eruptive periods under study. Among the volcanoes covered from the 11 volcanic regions (Table 5.12), no events were identified in association with those located in the Western Pacific, Eastern Pacific, Atlantic Ocean, North America or Middle America–Caribbean regions. A total of 10 potentially active volcanoes across five volcanic regions were identified as being associated with the events under analysis.

Table 5.12. Events from the SEL3 bulletin detected by infrasound IMS stations during the study period, potentially associated with volcanic activity. Includes event ID, time, location, number of detecting stations (Nstat), and associated volcano.

		Det Algorithm			SEL3 Bulletin				Associated Volcano
N	Date	t0 Time	Lat	Long	Event ID	Time	Lat	Long	
Northwest Pacific Volcanic Regions									
1	27.11.2012	16:30	55.835	160.326	9249051	16:05:10.52	53.0326	156.2218	Tolbachik
2	08.03.2015	01:35	55.589	159.15	11747175	01:05:40.88	54.0880	160.4485	Zupanovsky
3	20.01.2019	16:10	55.972	160.595	16850607	16:12:48.50	56.0002	161.4751	Bezymyanny
4	15.03.2019	17:30	55.972	160.595	17084823	17:22:16.60	57.2312	163.5009	Bezymyanny
Southwest Pacific Volcanic Regions									
5	31.07.2015	01:30	-4.08	145.037	12214688	01:42:55.37	-4.1302	147.6341	Manan

Sunda-Banda Volcanic Regions									
6	13.02.2014	16:30	-7.935	112.314	10508515	16:14:27.28	-8.8563	107.2361	Kelud
7	30.05.2014	07:55	-8.2	119.07	10868012	08:01:45.90	-8.6107	121.0899	Sangeang Api
Eastern Africa Volcanic Regions									
8	12.06.2011	21:00	13.37	41.7	7631072	21:37:12.12	13.1451	41.7011	Nabro
European Volcanic Regions									
9	16.03.2013	17:15	37.748	14.99	9587195	17:53:31.37	37.6047	15.1313	Etna
10	03.04.2013	12:30	37.748	14.99	9640825	12:02:03.85	37.6298	14.7508	Etna
11	20.04.2013	15:13	37.748	14.99	9699989	15:36:56.90	38.0404	15.8117	Etna
South America Volcanic Regions									
12	03.03.2015	06:10	-39.42	-71.93	11730991	06:21:59.42	-38.4170	-73.8310	Villarica
13	22.04.2015	21:04	-41.33	-72.618	11899578	21:58:17.85	-37.8049	-70.8286	Calbuco

5.2.2. LEB buletins results

The LEB contains the outcome of a post-processing review performed by IDC analysts after automated bulletins become available. By using specific interactive software, such as the Analyst Review Station (ARS), the analysts validate the automated results, identify inconsistencies or data mismatches and integrate, if necessary, additional pre-processed raw data to refine and enhance the final results.

By analyzing the IDC's LEB bulletin, 52 events were identified as potentially related to the eruptive periods of 28 volcanoes, representing approximately 61% of the volcanoes under study (n = 46; Table 5.13). Among these, no events were found to be associated with those located in the Eastern Pacific region (Wolf volcano) or in the Central America–Caribbean region (Colima, San Miguel and Turrialba volcanoes).

The listed events were identified and associated with volcanic activity distributed across the different volcanic regions analysed. For instance, 19 events can be associated with volcanoes spanning from the North Pacific volcanic region (7 out of 9 volcanoes; 77.8%) to the South American volcanic region (4 out of 6; 66.7%). In the Western Pacific and Sunda-Banda volcanic regions, 6 and 5 events were identified, respectively, each involving 50% of the volcanoes in these groups. The Southwest Pacific volcanic region had the highest percentage association (excluding the Tinakula volcano), with 4 of the 5 volcanoes (80%) corresponding to a total of 7 events. In the North American volcanic region 3 events were correlated with 3 out of 5 volcanoes (60%). Additionally, two events associated with Nabro volcano were identified (East Africa volcanic region), one related to Grímsvötn volcano (Atlantic Ocean region) and two events

associated to the Europe region (Mount Etna), each representing total coverage (100%) in their respective groups.

Table 5.13. Events from the LEB bulletin detected by infrasound IMS stations during the study period. potentially associated with volcanic activity. Includes event ID, time, location, number of detecting stations (Nstat) and associated volcano.

		Det Algorithm			LEB Bulletin				Associated Volcano
N	Date	t0 Time	Lat	Long	Event ID	Time	Lat	Long	
Northwest Pacific Volcanic Regions									
1	01.09.2012	19:16	55.972	160.595	8994206	19:35:08	55.78	160.72	Bezymiany
2	18.10.2013	06:05	56.056	160.642	10189079	07:19:08	56.11	160.92	Klyuchevskoy
3	07.11.2014	21:55	55.589	159.15	11390881	21:55:04	53.61	159.36	Zhupanovsky
4	07.11.2014	21:55	55.589	159.15	11390967	22:19:53	53.65	159.39	Zhupanovsky
5	08.03.2015	01:35	55.589	159.15	11747175	01:02:58	54.14	160.77	Zhupanovsky
6	28.11.2016	14:00	48.98	153.48	13817267	14:47:31	49.17	153.84	Chirinkotan
7	31.03.2017	11:46	48.98	153.48	14262685	11:43:57	49.09	153.23	Chirinkotan
8	02.04.2017	18:50	51.306	156.875	14271161	18:33:33	51.26	156.87	Kambalny
9	16.06.2017	04:53	55.972	160.595	14522762	04:46:49	57.86	162.84	Bezymiany
10	08.08.2017	11:20	54.049	159.443	14703159	11:24:04	55.00	161.43	Karymsky
11	09.08.2017	06:00	54.049	159.443	14705944	05:59:14	54.92	161.39	Karymsky
12	12.08.2017	17:40	54.049	159.443	14730649	17:19:21	54.09	159.62	Karymsky
13	20.12.2017	03:55	55.972	160.595	15252881	03:46:17	56.31	161.53	Bezymiany
14	20.01.2019	16:10	55.972	160.595	16850607	16:12:48	56.00	161.48	Bezymiany
15	15.03.2019	17:30	55.972	160.595	17105580	17:21:49	55.97	161.47	Bezymiany
16	15.03.2019	17:30	55.972	160.595	17105579	17:34:17	55.95	161.38	Bezymiany
17	21.06.2019	17:50	48.292	153,25	17516349	17:47:18	48.15	152.18	Raikoke
18	21.06.2019	23:00	48.292	153,25	17527209	23:36:47	48.05	151.75	Raikoke
19	21.10.2020	20:22	55.972	160.595	19576321	20:24:34	55.42	160.38	Bezymiany
Western Pacific Volcanic Regions									
20	27.01.2011	06:41	31.934	130.862	7090211	06:36:45	31.14	132.07	Kirishimayama
21	28.01.2011	03:47	31.934	130.862	7093337	03:45:05	31.65	132.06	Kirishimayama
22	31.01.2011	22:54	31.934	130.862	7106236	22:55:23	31.64	132.65	Kirishimayama
23	07.10.2016	16:46	32.8849	131.085	13646309	16:51:59	33.47	132.44	Asosan
24	12.01.2020	07:00	14.0106	120.997	18382877	06:50:19	15.12	121.64	Taal
25	12.01.2020	08:00	14.0106	120.997	18387665	08:07:00	14.59	122.01	Taal
Southwest Pacific Volcanic Regions									
26	28.08.2014	17:30	-4.2459	152.1937	11163687	17:28:56	-2.96	152.16	Rabaul
27	31.07.2015	01:30	-4.08	145.037	12234181	01:22:41	-4.11	145.94	Manam
28	26.07.2018	10:00	-15.389	167.835	16079613	09:56:10	-17.21	168.35	Ambae
29	27.07.2018	00:03	-15.389	167.835	16084737	00:08:30	-16.89	168.42	Ambae
30	01.09.2018	09:15	-15.389	167.835	16258257	09:12:07	-16.32	168.07	Ambae

31	30.10.2018	07:30	-15.389	167.835	16493999	07:43:05	-16.20	168.12	Ambae
32	25.06.2019	04:30	-5.05	151.33	17546582	04:16:31	-5.03	151.37	Ulawun
Sunda-Banda Volcanic Regions									
33	13.02.2014	15:50	-7.935	112.314	10508515	16:00:56	-8.11	109.55	Kelud
34	13.02.2014	16:30	-7.935	112.314	10508831	16:17:48	-8.54	109.77	Kelud
35	27.03.2014	06:12	-7.54	110.446	10677125	06:19:00	-7.86	109.06	Merapi
36	30.05.2014	07:55	-8.2	119.07	10868012	07:57:53	-7.83	119.94	Sangeang Api
37	19.02.2018	01:53	3,17	98,392	15477095	02:04:26	1.36	96.95	Sinabung
Eastern Africa Volcanic Regions									
38	12.06.2011	21:00	13.37	41.7	7632257	20:36:37	14.56	41.48	Nabro
39	12.06.2011	21:00	13.37	41.7	7666797	21:39:01	13.06	41.17	Nabro
Atlantic Ocean Volcanic Region									
40	21.05.2011	19:16	64.416	-17.316	7579127	19:16:58	64.69	-17.37	Grimsvotn
European Volcanic Regions									
41	16.03.2013	17:15	37.748	14.99	9587195	17:50:29	37.52	14.98	Mount Etna
42	03.04.2013	12:30	37.748	14.99	9640825	12:02:03	37.52	14.98	Mount Etna
North America Volcanic Regions									
43	28.03.2016	06:30	55.417	-161.894	13017585	06:37:32	55.63	-160.75	Pavl*of*
44	21.12.2016	00:30	53.93	-168,03	13949557	00:34:59	52.98	-165.78	Bogosl*of*
45	02.06.2020	06:31	52.825	-169.944	19009870	06:29:15	52.31	-171.17	Cleveland
South America Volcanic Regions									
46	30.04.2011	07:12	-1.467	-78.442	7564131	07:22:31	-2.61	-77.40	Tunguragua
47	04.06.2011	18:45	-40.59	-72.117	7606421	18:39:02	-39.67	-67.74	Puyehue Cordon Calle
48	14.07.2013	11:46	-1.467	-78.442	9918277	11:50:47	-2.88	-77.54	Tunguragua
49	01.02.2014	22:39	-1.467	-78.442	10510840	23:37:02	-1.87	-79.87	Tunguragua
50	03.03.2015	06:10	-39.42	-71.93	11730991	06:16:51	-38.67	-73.46	Villarrica
51	22.04.2015	21:04	-41.33	-72.618	11899444	21:27:57	-41.86	-67.95	Calbuco
52	23.04.2015	04:00	-41.33	-72.618	11899991	04:02:36	-41.60	-71.08	Calbuco

5.2.3. REB Bulletins results

The Reviewed Event Bulletin (REB) includes lists of events detected by IMS seismic, hydroacoustic and infrasound stations, providing detailed information on the time of origin, location, magnitude and signal attributes associated with each event. REB is the waveform-based end product, once analysts applied event definition criteria over the results in the LEB. Events that do not fulfil the REB definition criteria - such as those not detected by at least three primary stations or with a cumulative weight of less than 4.6 - are kept in the LEB but are excluded from the published REB.

The same procedure was applied to the REB — the IDC's analyst-reviewed bulletin. As a result, 31 events were identified as potentially related to eruptive periods of 21 volcanoes under study (Table 5.14). Among the volcanoes identified in the course of this work, no events were identified in association with those located in the Southwest Pacific, Eastern Pacific, or Middle America–Caribbean volcanic regions.

Table 5.14. Events from the REB bulletin detected by infrasound IMS stations during the study period, potentially associated with volcanic activity. Includes event ID, time, location, number of detecting stations (Nstat), and associated volcano.

		Det Algorithm			REB Bulletin				Associated Volcano
N	Date	t0 Time	Lat	Long	Event ID	Time	Lat	Long	
Northwest Pacific Volcanic Regions									
1	01.09.2012	19:16	55.972	160.595	8994206	19:35:08.30	55.78	160.72	Bezymiany
2	07.11.2014	21:55	55.589	159.15	11390881	21:55:04.55	53.61	159.36	Zhupanovsky
3	08.03.2015	01:35	55.589	159.15	11747175	01:02:58.20	54.14	160.77	Zhupanovsky
4	28.11.2016	14:00	48.98	153.48	13817267	14:47:31.94	49.17	153.84	Chirinkotan
5	20.12.2017	03:55	55.972	160.595	15252881	03:46:17.18	56.31	161.53	Bezymiany
6	15.03.2019	17:30	55.972	160.595	17105580	17:21:49.30	55.97	161.47	Bezymiany
7	21.06.2019	19:00	48.292	153,25	17516354	19:39:04.13	48.69	152.92	Raikoke
8	21.06.2019	20:50	48.292	153,25	17527288	21:07:10.26	48.40	152.49	Raikoke
9	21.06.2019	23:00	48.292	153,25	17527209	23:36:47.97	48.05	151.75	Raikoke
10	21.10.2020	20:22	55.972	160.595	19576321	20:24:34.55	55.42	160.38	Bezymiany
Western Pacific Volcanic Regions									
11	27.01.2011	06:41	31.934	130.862	7090211	06:36:45.02	31.14	132.07	Kirishimayama
12	28.01.2011	03:47	31.934	130.862	7093337	03:45:05.08	31.65	132.06	Kirishimayama
13	07.10.2016	16:46	32.8849	131.085	13646309	16:51:59.20	33.47	132.44	Asosan
14	12.01.2020	07:00	14.0106	120.997	18382877	06:50:19.06	15.12	121.64	Taal
15	12.01.2020	08:00	14.0106	120.997	18387665	08:07:00.40	14.59	122.01	Taal
Sunda-Banda Volcanic Regions									
16	13.02.2014	15:50	-7.935	112.314	10508515	16:00:56.96	-8.11	109.55	Kelud
17	13.02.2014	16:30	-7.935	112.314	10508831	16:17:48.11	-8.54	109.77	Kelud
18	30.05.2014	07:55	-8.2	119.07	10868012	07:57:53.43	-7.83	119.94	Sangean Api
19	19.02.2018	01:53	3,17	98,392	15477095	02:04:26.79	1.36	96.95	Sinabung
Eastern Africa Volcanic Regions									
20	12.06.2011	21:00	13.37	41.7	7666797	21:39:01.13	13.06	41.17	Nabro
Atlantic Ocean Volcanic Region									
21	21.05.2011	19:16	64.416	-17.316	7579127	19:16:58.05	64.69	-17.37	Grimsvotn
European Volcanic Regions									
22	16.03.2013	17:15	37.748	14.99	9587195	17:50:29.00	37.63	15.09	Etna
23	03.04.2013	12:30	37.748	14.99	9640825	12:02:03.68	37.64	14.77	Etna
North America Volcanic Regions									
24	21.12.2016	00_30	53.93	-168,03	13949557	00:34:59.10	52.98	-165.78	Bogoslof
South America Volcanic Regions									

25	04.06.2011	18:45	-40.59	-72.117	7606421	18:39:02.29	-39.67	-67.74	Puyehue Cordon Calle
26	14.07.2013	11:46	-1.467	-78.442	991827	11:50:47.92	-2.88	-77.54	Tungurauhua
27	01.02.2014	22:39	-1.467	-78.442	10510840	23:37:02.53	-1.87	-79.87	Tungurauhua
28	03.03.2015	06:10	-39.42	-71.93	11730991	06:16:51.89	-38.67	-73.46	Villarrica
29	22.04.2015	21:04	-41.33	-72.618	11899444	21:27:57.72	-41.86	-67.95	Calbuco
30	23.04.2015	04:00	-41.33	-72.618	11899991	04:02:36.53	-41.60	-71.08	Calbuco

The residual time analysis between the onset time (t0) used by the algorithm and the times registered in the bulletins shows differences across SEL3, LEB, and REB (Figure 5.27). SEL3 shows mainly negative residuals, with an average deviation of -10.83 minutes showing detections with a time prior to the t0 used by the algorithm. Most events fall into the < -15 min and -15 to -5 min categories. The LEB shows a more balanced distribution, with a mean residual of +0.78 minutes, reflecting the adjustments made by the analysts, putting the detection time closer to t0, with most events falling between -5 and +15 minutes. The REB, as a reviewed outcome, with more rigid criteria for detecting events, has an average residual of slightly more than +2.17 minutes, indicating consistent but minor positive changes compared to t0. Its distributions are more clustered, indicating better time accuracy through comprehensive manual validation.

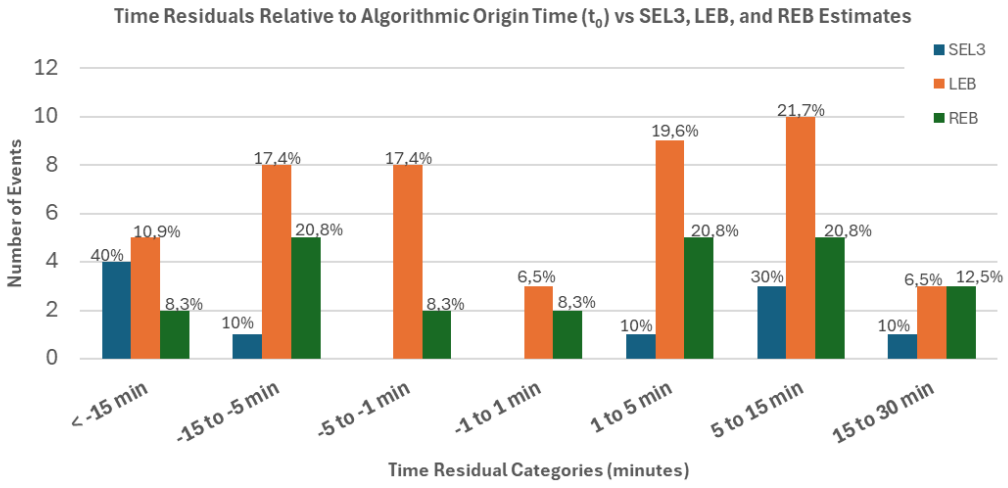

Figure 5.27. Time residuals chart relative to the event onset time (t0), used by the algorithm in this work, and the event times estimated by SEL3 (automatic), LEB (analyst-reviewed), and REB (final validated).

The results showed a clear improvement in time accuracy from the automatic to the reviewed phases, as expected. The variation reduction and the residual clustering from SEL3 to REB validate the impact of analyst interaction on event time enhancement. These residual times reveal a valid reference for assessing the reliability and accuracy of the event's onset time (t0) at all levels of processing. The results presented in this chapter focus on the infrasound signals detections associated with volcanic activity, based on the detection algorithm developed in this study. The detections were analysed with respect to the volcanoes identified in 11 different volcanic regions, allowing an effective assessment of the IMS network performance in different geographical contexts, types and intensity of volcanic activity. Furthermore, a quantitative overview of the spatial distribution of IMS stations in relation to the selected volcanoes was also presented to contextualise the observed patterns.

In parallel, and regarding the IDC bulletins, events potentially related to the eruptive periods were identified and associated with volcanic activity under study. The listed events were selected based on their proximity - within 250 km of the volcanic source - and temporal consistency with times difference with a maximum around +/- 10 minutes related to the estimated origin time (t0). Together, these results provide an initial validation of the approach.

Nevertheless, these results also point to the variability across events and different regions, which can result from changes in the eruption dynamics, signal propagation conditions, or the IMS network's coverage capability. These findings are discussed in the following chapter, where the implications of the results are discussed, with reference to methodological constraints, the propagation effects of the signal and the broader implications for infrasound monitoring associated with explosive volcanic activity and early warning strategies.

CHAPTER 6 |

Discussion and Conclusions

In this chapter we discuss the results presented in Chapter 5, highlighting how the detection algorithm developed for this study was able to identify global-scale volcanic activity higher or equal to VEI 3, based on the onset time of GVP reports and IMS infrasound station data. Also, eruptive styles, atmospheric conditions and the propagation effects will be discussed.

6.1. Effectiveness of the algorithm

In sub-section 6.1.1, the overview of the global results is summarized, comprising total statistics for the distinct volcanic regions, like the number of eruptions detected per year, the average duration of events and their temporal distribution over the study period, in order to evaluate the algorithm consistency across time and its ability to identify volcanic activity with VEI ≥3. Section 6.1.2 then focuses on analysing the detection patterns observed at specific IMS stations, focusing on the five IMS stations that represented almost half of all detections throughout the study period. This combined approach supports a robust validation of the algorithm, demonstrating its effectiveness in the automated detection of volcanic events using infrasound data across multiple temporal and spatial scales.

6.1.1. Overall Detection Results

The results achieved support the algorithm's effectiveness to detect volcanic events or higher, with its performance largely shaped by the source to receiver distance, along with the atmospheric conditions at the time of the event. This effectiveness is particularly observed in favourable infrasound propagation conditions in the presence of atmospheric waveguides.

The annual distribution of volcanic events associated with infrasound detections was analysed by distinguishing between undetected events (Nd) and detected events (Det), based on data from the selected IMS stations. The number of events per year corresponds to the total number of eruptions or eruption-related phenomena expected to produce detectable infrasound signals. The success rate is given by the number of successfully identified events in relation to the total number of events in each year. As shown by Figure 6.1, the algorithm demonstrated high reliability in multiple years - particularly in 2011, 2014, 2015 and 2019 - with detection rates exceeding 87 per cent and reaching 100 per cent in 2019. The results indicate a good performance of the algorithm in identifying infrasound signals generated by explosive volcanic activity across periods of high and low eruptive frequency. On the other hand, years such as 2013 and 2018 revealed a lower effectiveness, with a considerable level of unidentified events associated with them. In 2020, 50% of the events were detected and 50% were not. Additionally, the total number of eruption-related events shows a declining trend after 2016, which likely reflects a real decrease in volcanic activity rather than algorithmic limitations. The yearly values of detected (Det) and undetected (Nd) events used in this analysis are provided, as for the underlying detection statistics reference.

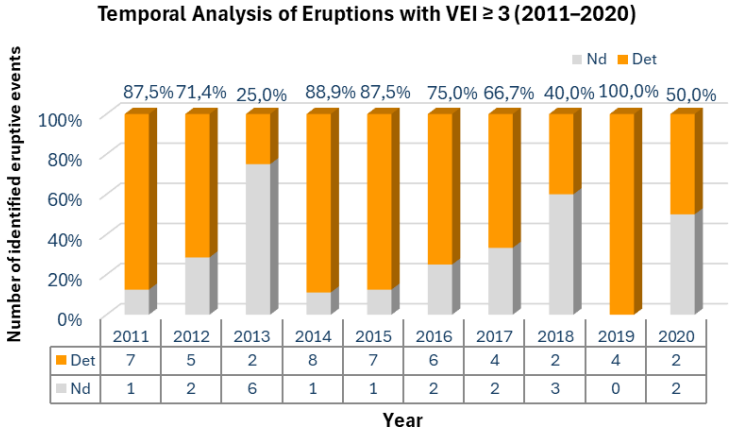

Figure 6.1. Annual distribution of volcanic events (VEI ≥ 3) detected by the algorithm between 2011 and 2020.Bars represent the number of events detected (orange) and not detected (grey) by the algorithm each year.

To assess the system's overall detection capability, a comparative analysis was made of the number of volcanic events and eruptions that were detected or not detected (Figure 6.2). Each eruptive period encompasses several events of volcanic activity, lasting from a few days to several years (Figure 6.3). Within these periods, the different discrete eruptive events identified show the episodic and complex dynamics of the volcanic systems (Figure 6.4).

Among the 67 eruptive periods, 70.15% (n = 47) were successfully detected, while 29.8 % (n = 20) were not detected. In contrast, of the 186 volcanic events, 54.8 % (n = 102) were detected and 45.2 % (n = 84) were not.

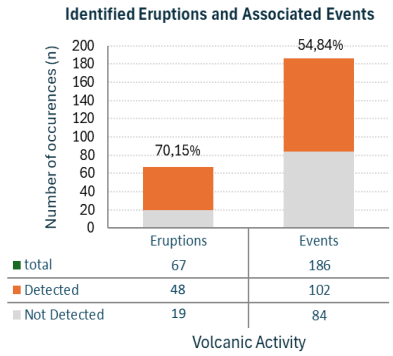

Figure 6.2. Volcanic activity identified during the study period, represented as eruptive periods and distinct events. Each eruptive period includes one or more events occurring over varying timescales. Stacked bar chart shows the number of detected (orange) and undetected (gray) occurrences for both categories.

Overall, the algorithm demonstrated positive performance regarding eruptions across all years. For analysis purposes and to better characterise the duration of eruptions based in our data (ranging from 1 day to more than 1 year), and to correlate with their detections, in this work we detailed the classical division in volcanology on short-lived (from a few seconds to days) and long-lived eruptions (months, years, or even centuries) in duration classes (Figure 6.3): **Class I** (≈1 to 36 days) with 19 eruptions (28 %); **Class II** (1 to 12 months) with 25 eruptions (37 %); **Class III** (1 to 2.5 years) with 10 eruptions (15%); **Class IV** (2.5 to 5 years) with 9 eruptions (13%); **Class V** (5 to 7.5 years) with no eruptions (0%); **Class VI** (7.5 to 9 years) with 3 eruptions (4%); and **Class VII** (more than 9 years), with 1 eruption (1%). The distribution of eruption durations is skewed toward shorter events, with a median of 2.15 years, with a strong concentration of eruptions of less than 1 year. In fact, almost two thirds of all eruptions (62 %) lasted less than 1 year and most of them less than a few months.

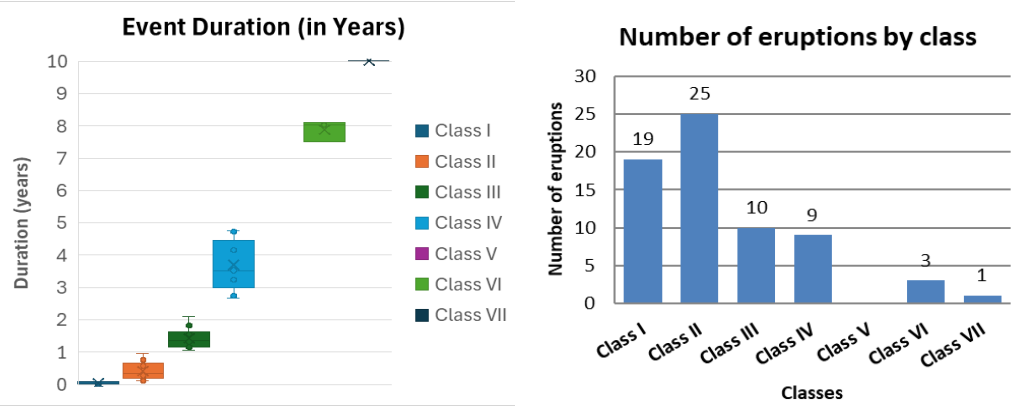

Figure 6.3. The graphics above shows the distribution of eruptions lengths (in years) in different classes. These include Class I (~1-36 days), Class II (~1-12 months), Class III (1-2.5 years), Class IV (2.5-5 years), Class V (5-7.5 years, no events), Class VI (7.5-9 years), and Class VII (>9 years). Graphic at the right side shows the number of eruptions by Class.

Figure 6.4 presents the overall location of the 46 volcanoes analysed in this study, along with all the IMS infrasound stations (blue pentagrams) used. Each volcano is categorised based on the effectiveness of the algorithm in detecting the discrete events during the respective eruption period.

For a total of 26 volcanoes, the algorithm successfully detected all their eruptions, include eruptions such as Cleveland (2020), Villarica (2014), Chirinkotan (2016), and Tolbachik (2012), demonstrating the system's capability to identify diverse eruptive events under varying geographic and atmospheric contexts, pointing to favourable conditions for long-distance infrasound propagation and effective network coverage.

On the other hand, for 9 volcanoes not all eruptions were identified by the algorithm, probably due to variations in the eruption intensities, in the atmospheric conditions at the time of the event, or in the layout of the used network of stations.

For 11 volcanoes the algorithm did not detect any events, even though they were active during the studied period. Such cases can be explained by factors such as low-energy eruption, complex propagation patterns, or sparse network coverage. This points out the heterogeneity in the algorithm's effectiveness in global detection and underlines the importance of considering the source's features, the network's layout and the atmosphere's status at the time of the event.

An overview of the obtained outcomes for the 67 identified eruptions associated with periods of eruption of the 46 volcanoes under analysis is provided in the table of the Annex C.

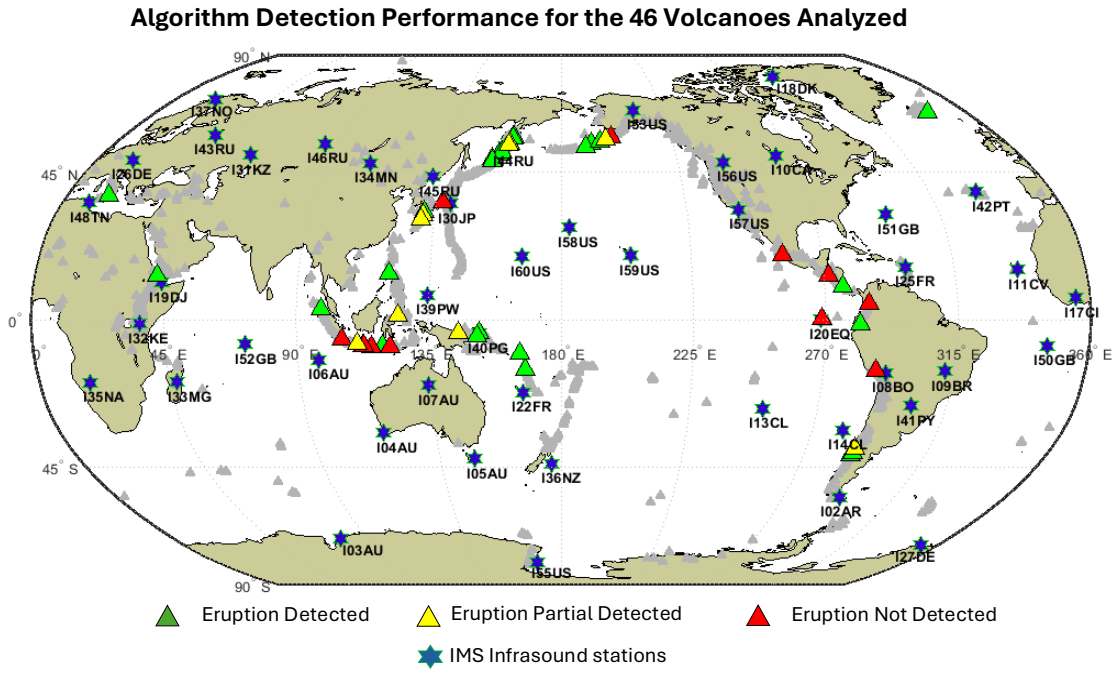

Figure 6.4. Location world map of the volcanoes and IMS infrasound stations (blue pentagrams) used in this work, with the volcanoes with all eruptions detected (green triangles), partially detected eruptive periods (yellow triangles), and volcanoes with no detections (red triangles).

6.1.2. Specific cases in detection patterns across IMS stations

Based on the proposed algorithm, this section presents the spatial and temporal distribution of infrasound detections attributed to volcanic eruptions, focusing on the five IMS stations that accounted for almost half of all detections during the studied period (Figure 6.5). The analysis summarises the overall response of each station in terms of the number of detections, associated volcanoes or volcanic regions. By considering parameters such as the back-azimuth, the distance to the source and the VEI of the eruption, the objective is to show that location and proximity to active volcanic areas influence the detection capabilities and performance of regional monitoring.

Station I44RU (4 array elements, ≈1.9 km aperture) alone contributed with 31 identified detections involving 12 distinct volcanoes. Being the closest station of all the nine volcanoes in the Northwest Pacific Volcanic Region, it detected at least one distinct event associated with each. Recorded back-azimuths ranged from 29° (*Bezymianny volcano*) to 212° (*Raikoke volcano*), with source distances spanning from 110 km (*Zhupanovsky volcano*) to approximately 620 km (*Raikoke volcano*). In the North America group, the station detected events associated with eruptions of the *Cleveland* and *Pavlof volcanoes* at distances exceeding 2,000 km, with back-azimuths between 68° and 78°. Additionally, detections related to the *Kirishimayama volcano* (Western Pacific Group) were observed at ≈3,200 km and a back-azimuth of 233°. All the events corresponded to VEI 3 eruptions.

Station I53US (8 array elements, ≈1.97 km aperture) accounted for 24 detections involving 10 distinct volcanoes across two volcanic groups: North America and Northwest Pacific. For the North America group, eight detections were attributed to four volcanoes. As the closest station of five volcanoes in this group, I53US detected at least one event from four of them (excluding *Veniaminof volcano*, for which no detections were identified). Back-azimuths ranged from 222° (*Pavlof volcano*) to 236° (*Cleveland volcano*), with distances from ~1,305 km (*Pavlof volcano*) to 1,832 km (*Cleveland volcano*). For the Northwest Pacific group, six of nine volcanoes were associated with detections at I53US, where it was the third-closest station. Events had back-azimuths ranging from 268° (*Chirinkotan volcano*) to 281° (*Raikoke volcano*), and distances from ≈2,900 km (e.g., *Klyuchevskoy volcano*) to ~3,800 km (*Chirinkotan volcano*).

Station I39PW (7 array elements, ≈2.44 km aperture) registered 18 distinct events involving 13 volcanoes across three volcanic regions: Western Pacific, Southwest Pacific, and Sunda-Banda. As the closest station, it detected eruptions from Soputan volcano (2011, 2015, 2016), Taal volcano (2020), and Rabaul volcano, with back-azimuths ranging from 123° (Rabaul volcano) to 297° (Taal volcano), and distances from 1,300 km (Soputan volcano) to 2,356 km (Rabaul volcano). As the second-closest station, it also detected explosive activity from Manam volcano (2015) and Ulawun volcano (2019), both in the Southwest Pacific group. Back-azimuths ranged from 123° (Ulawun volcano, ≈2,326 km) to 137° (Manam volcano, ≈1,700 km). The VEI 4 eruption of Sangeang Api volcano (May 30, 2014) was also identified at a distance of ≈ 2,445 km and a back-azimuth of 225°. As the third- and fourth-closest station, it registered VEI 3 eruptions from Asosan volcano and Kuchinoerabujima volcano (Western Pacific), and Merapi volcano (Sunda-Banda), all located more than 2,500 km distant. Notably, the station also detected VEI 4 eruptions from Kelud volcano (2014) and Sinabung volcano (2019), both in the Sunda-Banda group. In total, I39PW detected seven of the 10 VEI 4 eruptions listed in the GVP

database, with distances ranging from 1,645 km (Taal volcano) to 4,000 km from Sinabung volcano, with a back-azimuth of 5°.

Station I30JP (6 array elements, ≈2.12 km aperture) recorded 16 distinct events linked to 10 volcanoes across the Northwest Pacific, Western Pacific, and Southwest Pacific regions. As the closest station to the Western Pacific region, it recorded signals from three eruptions of Kirishimayama volcano (January 2011) at ≈953 km (back-azimuths 242–244°), and one from Asosan volcano (October 2016) at ≈891 km (back-azimuth 256°). As the second-closest station, it identified two events from the VEI 4 eruption of Taal volcano (January 2020), at ≈3,050 km (back-azimuths 221–224°). In the Northwest Pacific group, acting as the third-closest station, it detected activity from six of the nine studied volcanoes, with back-azimuths ranging from 27° (Klyuchevskoy volcano) to 33° (Raikoke volcano), and distances from 1,794 km (Raikoke volcano) to 2,774 km (Klyuchevskoy volcano). Only one event from the Southwest Pacific group was identified: the 2013 eruption of Manam volcano, at ~4390 km.

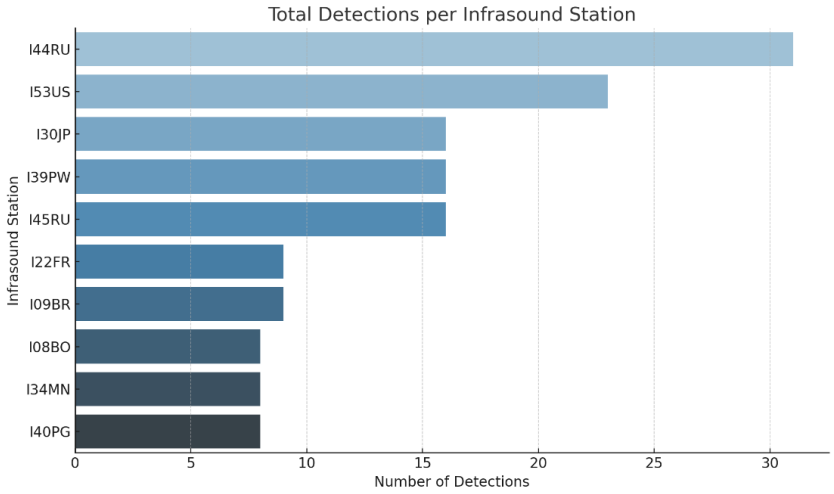

Figure 6.5. Number of detections of the five IMS stations that contribute to almost 50% of the total detected events.

The analysis of the five IMS stations with the highest detection rates points towards the importance of station proximity, layout and geographical location. Stations such as I44RU and I53US, with 4 and 8 array elements respectively and located relatively close to active volcanic clusters in the Pacific Northwest and North America, registered the highest number of detections. Stations such as I39PW (7 elements) and I30JP (6 elements), although further away from most eruptive sources, demonstrated the ability to detect long-range, high-explosive eruptions, emphasising the potential influence of wide-open, distributed array elements on far-field detection performance.

Additionally, when evaluating detection patterns in the IMS network, it is also important to consider the propagation conditions in the atmosphere along the path between the source and the receiving station. As example, stations located in acoustic shadow zones - regions where atmospheric conditions prevent infrasound energy from being transmitted either through tropospheric, stratospheric or thermospheric ducts - may be inhibited from registering signals, even when located quite close to the source. Thus, the understanding of detection (or non-

detection) patterns involves a combined assessment of the spatial configuration and propagation environment, as shown by ray tracing or other acoustic modelling tools, as proved by earlier studies (e.g. Le Pichon et al. 2005), which emphasise the strong influence of seasonal wind structures and atmospheric variability on the propagation of long-range infrasound. A particularly illustrative case is that of station I44RU (Figure 6.6). According to the ray tracing simulations performed for the Zhupanovsky – I44RU path, no eigenrays were observed to reach the station under any propagation mode - whether through tropospheric ducts, stratospheric returns, neither thermospheric refraction. This persistent lack of simulated acoustic paths reveals that I44RU is in an acoustic shadow zone for this source-receiver set-up. Also, that phenomenon has been observed in recurring events, despite atmospheric dynamics, reinforcing the conclusion that the absence of detections is a consequence of an unfavourable propagation path and not due to a potential failure or limits in the station's equipment.

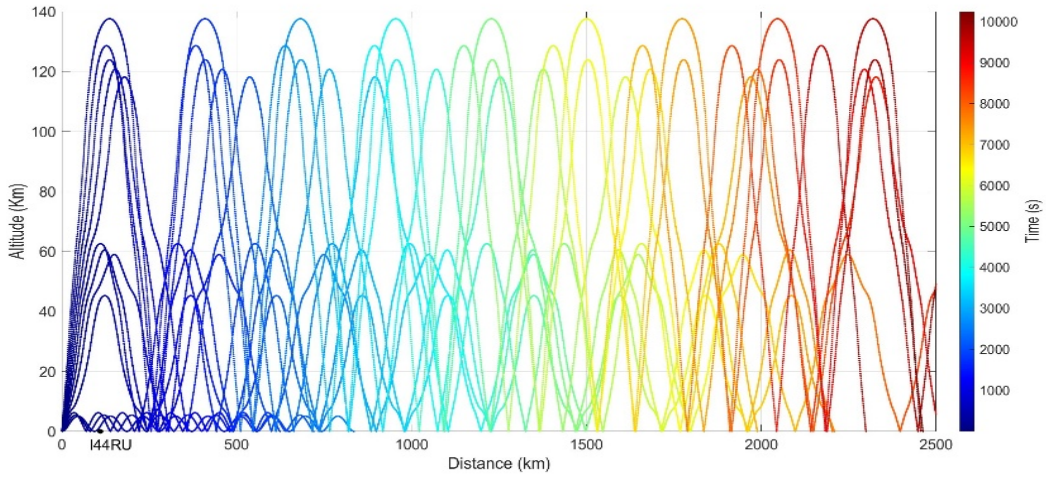

Figure 6.6. Ray tracing simulation between Zhupanovsky volcano and IMS station I44RU. The figure shows modelled acoustic ray paths through tropospheric ducts, stratospheric returns, and thermospheric refraction. None of the rays reach I44RU, indicating that the station is located within an acoustic shadow zone. This supports the interpretation that the absence of detections is due to unfavourable propagation conditions rather than sensors malfunction.

The capability of stations to detect events in multiple volcanic regions demonstrates the potential of the IMS network for regional and even global volcanic monitoring. These results emphasise the important role played by stations with varying configurations and locations, reinforcing the impact of network design in improving overall capabilities for detecting explosive volcanic activity.

6.2. Detection Outcomes by Eruption Type and Intensity

This section analyses the heterogeneous types of eruptive events successfully detected by the algorithm, with particular focus on their VEI and eruptive style. For their analysis, the VEI values were grouped into detected (Det) and undetected (Nd) eruptive periods, as shown in Figure 6.7. The results show that VEI 3 is the most frequent in all the identified eruptions, with a total of 54 eruptive periods, of which 16 were undetected and 38 were detected. This corresponds to a detection rate of 70.37%, representing most eruptions in the analysed data, implying that eruptions with VEI3 are the most common in our data set, but also includes the highest number of undetected events, suggesting variability in signal strength and eruptive dynamics within this VEI class. VEI 4 was observed in 12 cases, with 9 successfully eruptions detected (75%) and 2 undetected. Although less frequent than VEI 3, VEI 4 still represents a considerable number of events, indicating eruptions of moderate magnitude often associated with clear infrasonic signals. The algorithm successfully detected the VEI 5 eruption of the Puyehue-Cordón Caulle volcano, which occurred from June 2011 to April 2012. Though this result is supported by a single eruption, it agrees with what was expected, considering that VEI 5 eruptions commonly generate intense and sustained infrasonic signals that can be detected over long-range distances.

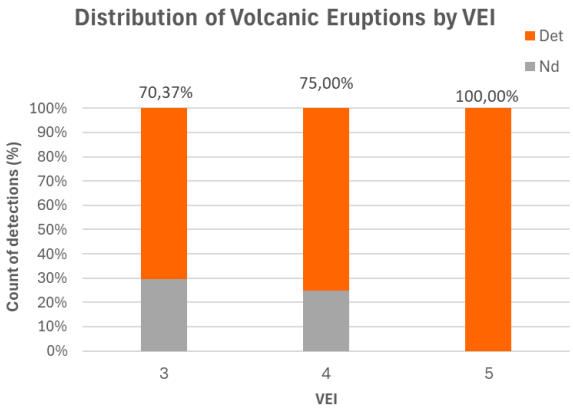

Figure 6.7. Detected (Det) and non-detected (Nd) eruptions, categorized by Volcanic Explosivity Index (VEI).

As outlined in Chapter 1, Section 1.2, different styles of volcanic activity, which may or not generate enough energy to produce and propagate infrasound waves. Hawaiian eruptive style, despite its low explosiveness - which implies limited propagation of infrasound waves over long distances - has been successfully detected by the algorithm in a few cases. This includes the lava fountaining at Mount Etna volcano (2013 and 2016), as well as lava lake activity. Strombolian activity at Villarrica volcano (2015) has been detected at distances of approximately 3,700 km at stations IS42 and I13CL, respectively. Strombolian and Vulcanian gas-driven outbursts represented approximately 89.8 % of the discrete events associated with VEI 3 (n = 167),

although only 87 events (50.62%) were identified by the algorithm based on GVP reports (Figure 6.8). These results reflect the heterogeneity of the events, the classification associated with their intensity, the station network's geographical coverage and the atmospheric conditions. Among large explosive events (VEI 4), the algorithm successfully identified 14 out of 18 subplinian discrete events, including the Grimsvötn and Nabro eruptions in 2011, Kelud in 2014, and Taal volcano in the Philippines in 2020. On the other hand, two eruptions — Wolf (2015) and Semeru (2017) — were not identified by the algorithm. The network coverage near these volcanoes (e.g., the nearest station to Wolf volcano is located approximately 3,000 km away) and unfavourable atmospheric conditions at the time of the events may explain the lack of detections. A single Plinian event, reported in the GVP and classified as a very large explosive event (VEI 5) was identified on June 4th, 2011, associated to Puyehue Cordon Caulle volcano eruption. Infrasound detections were observed at one of the three closest stations, I41PY, as well as at station I09BR, located approximately 3,623 km from the source.

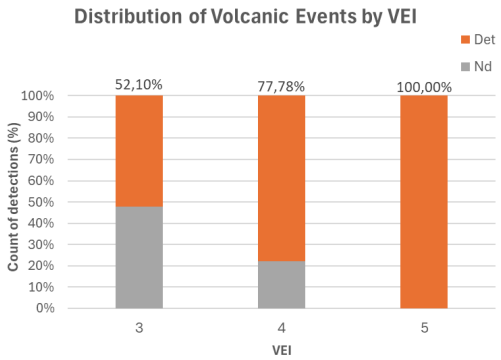

Figure 6.8. Detected (Det) and non-detected (Nd) discrete events, categorized by Volcanic Explosivity Index (VEI).

Hawaiian and Strombolian eruptions produce low-amplitude, short-duration infrasound signals that are tricky to detect because they are often masked by ambient noise. Volcanic eruptions, such as the Mount Ontake eruption of 2014 (VEI 3), generate more energy and usually produce short, impulsive signals. However, this event was not detected by the infrasound stations, probably due to the low acoustic energy released. In contrast, sub-Plinian and Plinian eruptions, such as Grímsvötn, in 2011 (Figure 6.9) or Kelud (2014), generated high-amplitude, long-duration infrasound signals that were recorded over long distances. Wolf (2015) eruption was not detected despite the same VEI, possibly due to the distance (≈3,000 km) from the nearest infrasound stations and the low propagation of the signal.

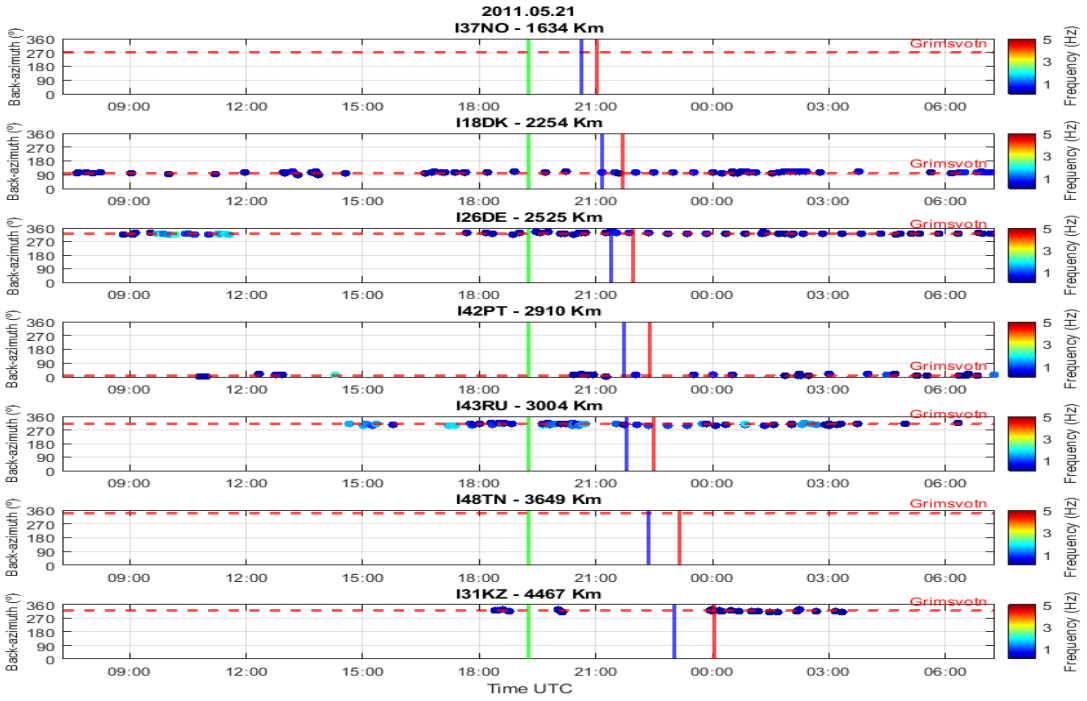

Figure 6.9. Detections identified by the proposed algorithm related to the VEI 4 Grimsvötn eruption (May 2011). IMS infrasound stations with valid data are shown within a 4500 km radius. The red dashed line indicates the back-azimuth direction to volcano. Vertical lines correspond to theoretical celerities of 260 m/s and 330 m/s. Dots represents detections, color-coded by frequency (Hz). No detections were identified at I37NO and I48TN stations, apparently due to operational problems at these arrays.

By comparing the detected events with their respective VEI and eruptive styles, very useful information can be extracted in terms of the performance and sensitivity of the detection algorithm. The results prove that the algorithm performs reliably, mainly for moderate to high-intensity volcanic events, while also revealing its sensitivity to transitions in eruptive dynamics and signal characteristics. Successful detections are significantly interrelated with VEI. The VEI 5 Plinian eruption of the Puyehue-Cordón Caulle volcano (the only one in the dataset) was successfully detected and three quarters of the VEI 4 eruptions, mainly of Vulcanian and Plinian eruptive styles, were successfully detected.

Among the eruptions analysed, VEI 3 and VEI 4 events represented most of the dataset, accounting respectively for approximately 80% and 17.9% of cases, while only a single VEI 5 eruption was reported. VEI 5 and VEI 4 eruptions showed high detection, indicating that the algorithm performs well in identifying energetic and coherent explosive events. In contrast, VEI 3 eruptions, though most frequent, exhibited a lower detection rate, reflecting greater variability in signal strength and eruptive behaviour. These results highlight a clear positive relationship between eruptive explosivity and detection success, while also emphasizing that detectability depends on other factors, such as eruption duration, acoustic energy radiated, and the coverage of the infrasound monitoring network.

To conclude, the algorithm has demonstrated robust detection capabilities for more intense eruptions but also identifies points for improvement in dealing with the complexity and variability of global volcanic activity. Future improvements should take into consideration

integrating qualitative eruption indicators and geographic-based propagation conditions (e.g., regional atmospheric structure, wind profiles, and topographic effects) to enhance the reliability of detection across a broader spectrum of eruptive styles.

6.3. Limitations in Event Detection

6.3.1. Network Coverage

A comprehensive overview of the IMS stations used in the study was outlined in the previous chapters (Section 4.2). In this analysis, the data from 43 out of the 54 currently certified IMS infrasound stations were systematically processed (Figure 6.10). These stations were sorted on the basis on criteria covering data availability, their operational status throughout the study period and their spatial relevance to the volcanic regions under analysis.

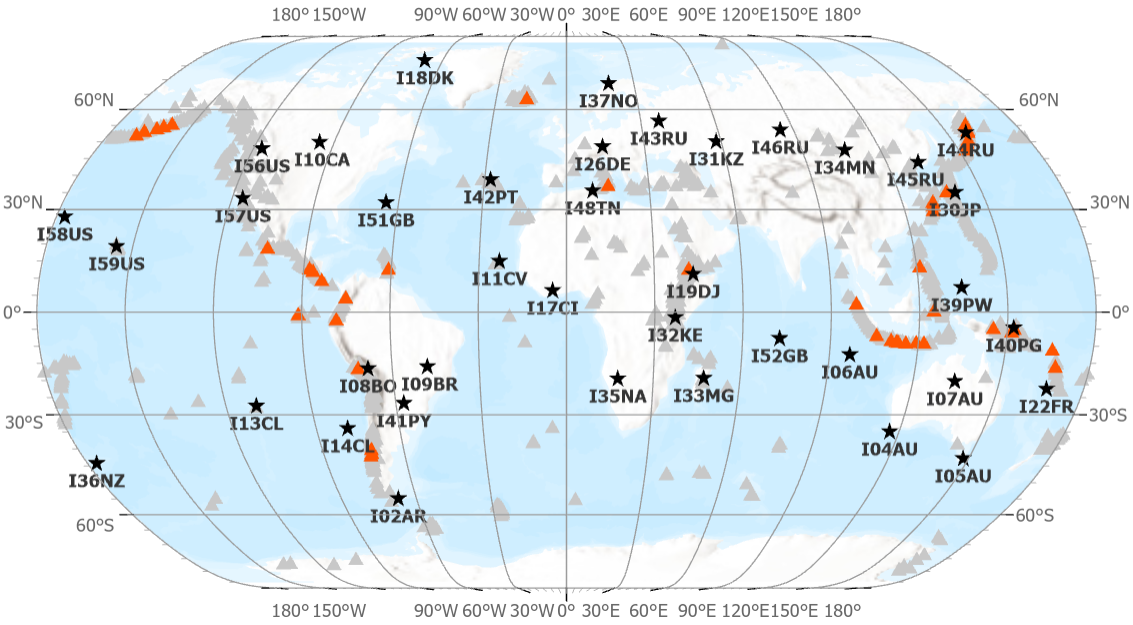

Figure 6.10. Location of the 43 IMS infrasound stations analysed (black stars) and volcanoes identified in this study (orange triangles). Other Holocene volcanoes that did not meet the selection criteria defined for the analysis are also shown (grey triangles). (Base map: World Natural Earth, GCS WGS 1984, Esri).

Within a 4,500 km radius from each volcano (n = 46), the number of associated IMS stations ranges from a minimum of three stations (6.5% of volcanoes: Sinabung, Turrialba, and Wolf) to a maximum of nine stations (2.2%, Bogoslof volcano). The mean number of stations is 6, which is also the most frequent value. The interquartile range (IQR) goes from 5 to 7 stations, covering 71.8 % of all the volcanoes. This distribution (Figure 6.11) reflects relatively uniform IMS coverage, with minimal variations and few outliers.

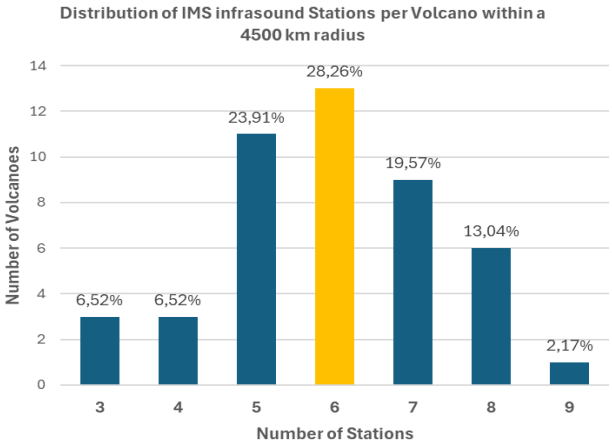

Figure 6.11. Number of infrasound stations associated with each volcano within a radius of 4,500 kilometres. The percentages are shown above each bar. The mode (6 stations) is highlighted in yellow.

The distance between the volcanoes and the three nearest IMS stations was clustered into intervals to assess their spatial coverage (Figure 6.12). With regard to the closest station, only one volcano (2.2%) was identified with a station located at a distance less than 100 km (I40PG for Rabaul volcano). Most stations are located at distances ranging from 1,000 to 2,000 km (20 cases, 43.5%), followed by stations with distances between 205-1000 km (14 cases, 30.4%) and distances between 100-250 km (8 cases, 17.4%). In three cases (6.5%), the closest station is further than 2,000 km: I06AU for the Agung, I57US for the Colima and I07AU for Sangeang Api. No stations were further than 3,000 km distant from any volcano.

As for the second closest station, the distances are more clustered in the 2,000-3,000 km range (25 cases, 54.3%), followed by 1,000-2,000 km (15 stations, 32.6%) and 3,000-4,000 km (4 stations, 8.7%). Only two stations (4.3%) were between 205 and 1,000 km, and none were below 100 km or beyond 4,000 km.

Regarding the third closest station, the largest number of stations are located at distances between 2,000-3,000 km (27 stations, 58.7%), followed by stations within 3,000-4,000 km (13 stations, 28.3%) and 1,000-2,000 km (5 stations, 10.9%). Only a third closest station (2.2%) was identified beyond 4,000 km (I39PW for Sinabung volcano). These results indicate a progressive increase in the distance between the volcano and the nearest subsequent IMS stations, with most of the second and third nearest stations located more than 2,000 km away.

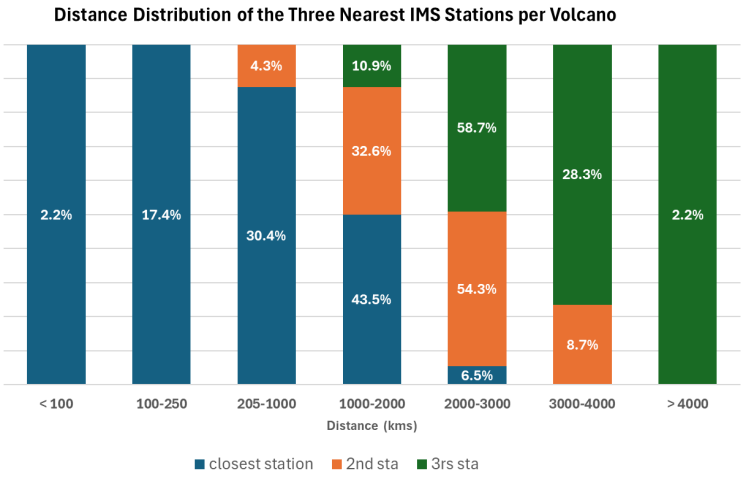

Figure 6.12. Volcanoes by distance to their three closest IMS infrasound stations. Most of the first-closest stations are located between 1,000 and 2,000 kilometres from the volcano. For the second-closest stations, the distances are more clustered in the 2,000-3,000 km range. Similarly, most of the third-closest stations are also in the 2,000-3,000 km distance range, indicating that the station density increases beyond 1,000 km.

6.3.2. Infrasound Propagation

The detection of infrasound over long distances is highly impacted by atmospheric propagation conditions (Drob et al. 2003), such as the vertical wind structure, which varies seasonally and with the direction of propagation. Ducting between the ground and troposphere, the stratosphere and thermosphere waveguides can significantly enhance the efficiency of acoustic energy transmission, allowing signals to travel thousands of kilometres with low attenuation (Le Pichon et al. 2004). Frequencies in the range of 1 to 3 Hz are commonly observed in stratospheric arrivals while lower frequencies (<1Hz) are noted in thermosphere arrivals, due to high altitude rarefaction leading to stronger attenuation of higher frequencies. However, even highly energetic eruptions may go undetected if atmospheric conditions are unfavourable for establishing a propagation channel toward the monitoring stations. As an example, Figure 6.13 shows the results obtained by the algorithm's script (*Pro_met_prof.m*) for the atmospheric profiles (temperature, wind speed and sound speed) for two different events (winter and summer) associated with the Mount Etna volcano. The direction of the stratospheric zonal winds blow from West to East in winter and inversely in summer.

.

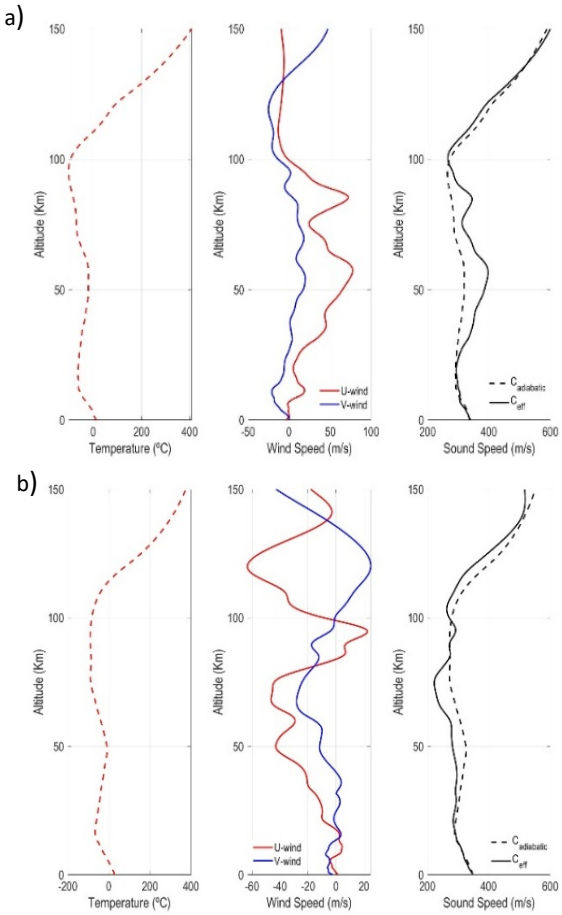

Figure 6.13. Processed results of atmospheric profiles over Mount Etna for temperature (°C), zonal (u) and meridional (v) wind speed and adiabatic and effective speed of sound in winter (event on 15.11.2011) (a), and summer, (event on 19.08.2011); (b) Zonal stratospheric winds are observed to blow from west to east in winter and inversely in summer, directly impacting the effective speed of sound.

These variations strongly affect the attenuation of infrasound rays on their path from the volcano to the monitoring station. The C_{eff} drives the refraction of acoustic energy in the stratopause zone towards the ground, and it is highly constrained by the direction of stratospheric winds, which generally follow seasonal patterns. Refractions towards the ground can also be expected to occur at thermospheric altitudes. When acoustic waves propagation is in the wind direction, $V_{eff-ratio}>1$, a stratospheric duct evolves, enabling transmission. On the other end, when wind reverses and sound propagate against the wind direction, $V_{eff-ratio} < 1$, the attenuation of the thermospheric arrivals is high and energy is strongly dissipated (Le Pichon et al., 2012).

As an illustrative example, Figure 6.14 shows the output generated by the script algorithm in relation to the atmospheric wind speed for two different events associated with the Villarica volcano. These events occurred under distinct seasonal conditions: one during the austral summer, characterised by stratospheric zonal winds predominantly from west to east, and the second one during the austral winter, during which this flow is reversed. The image also indicates

that the tropospheric duct, associated with the tropospheric jet stream, tends to be more effective through the winter months, enhancing propagation at low altitude.

This seasonal variation in the wind dynamics is clearly expressed in the corresponding attenuation and effective sound speed ratio ($V_e$ff) maps. For the event of March 3, 2015, although the closest station (I14CL) successfully detected the signal, several other nearby stations did not. In contrast, the event was recorded at more distant stations, including I08BO (2,605 km) and I13CL (3,711 km) (Appendix A.11.6), suggesting the presence of favourable long-range propagation paths despite regional limitations closer to the source.

The absence of detections at the closest stations, like I41PY and I09BR, may be an effect of their location within regions characterized by high attenuation and low V_{eff} values, pointing to unfavourable propagation conditions. In the same way, I02AR is located close to the boundary of favourable conditions; despite attenuation levels higher than 70 dB, the marginal values of the effective sound speed ratio suggest limited detection capability (Appendix A.11.6). It is also important to evaluate the impact of the array layout. A low number of sensor elements in some IMS arrays may further reduce detection sensitivity, especially under marginal propagation conditions and higher noise. Additionally, station I01AR, although shown on the map for completeness, was not operational at the time of the 2015 event - it only became active in 2019.

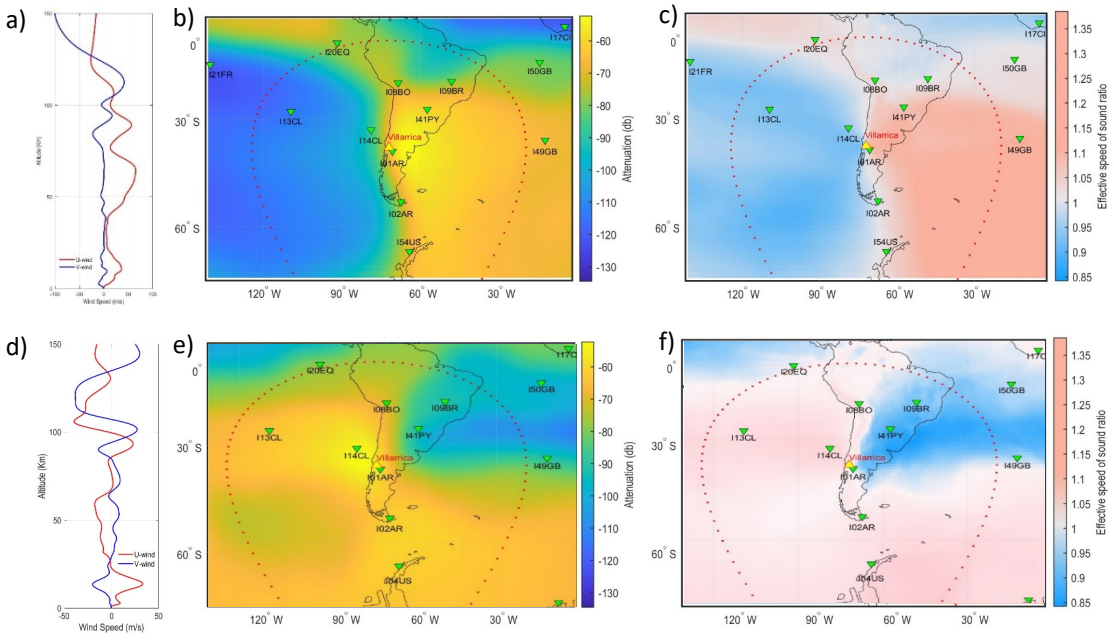

Figure 6.14. Example of atmospheric profiles over Villarrica Volcano in:austral winter (event of 30.08.2017) :a) zonal(u) and meridional(v) wind speed, b) attenuation, c) Effective speed of sound; and austral summer (event in 03.03.2015): d) zonal(u) and meridional(v) wind speed, e) attenuation, f) Effective speed of sound.

The results presented in this section emphasise the critical importance of atmospheric propagation dynamics in the long-range monitoring. Seasonal variations in the direction of the zonal stratospheric wind, as well as the structure of sound speed patterns, significantly affect the efficiency of signal propagation and the overall detectability of volcanic events at IMS stations. It

becomes evident that the $V_e$ff-ratio is a key parameter in understanding when and where infrasound signals are refracted back toward the ground. The seasonal asymmetry in detection capabilities is further demonstrated by the 2015 Villarica case, in which the event was not detected at several nearby stations, but was successfully recorded at more distant IMS arrays, suggesting that long-range propagation paths were more efficient than short-range ones under those specific atmospheric conditions. This result shows that sometimes proximity alone is no guarantee of detection, especially in the presence of noise or unfavourable wind patterns.

Moreover, the influence of station-specific characteristics, such as array configuration and sensor density, must also be considered. Stations with fewer sensor elements may exhibit reduced sensitivity, particularly under marginal propagation conditions. These observations are not isolated cases. Several other volcanic events across different regions and seasons exhibit similar behaviors, where the $V_e$ff-ratio structure, atmospheric attenuation, and station positioning critically affect detection outcomes. Additional examples and detailed $V_{eff\text{-}ratio}$ maps supporting this analysis are provided in Appendix A.11, offering a broader perspective on the atmospheric constraints influencing detection success across the IMS network.

In conclusion, although eruption energy and signal propagation are important, the atmosphere works as a selective filter and propagation dynamics are critical for effective signal reception. Understanding these limitations is essential to better assessing the data and enhancing monitoring procedures. In accordance with these interpretations, the following section explores how these atmospheric dynamics manifest themselves on a broader scale and seasonal perspective.

6.3.2.1.Seasonal Distribution of Eruptions and Associated Infrasound Detections

This section examines the seasonal distribution of volcanic eruptions and associated discrete infrasound detections in the main volcanic regions, with the aim of assessing the influence of seasonality in the two hemispheres on the detectability of infrasonic events. The dataset was categorized by hemisphere (North and South) and into seasons (Winter and Summer), allowing the identification of temporal patterns potentially correlated with atmospheric propagation conditions and regional eruptive activity (Figure 6.15).

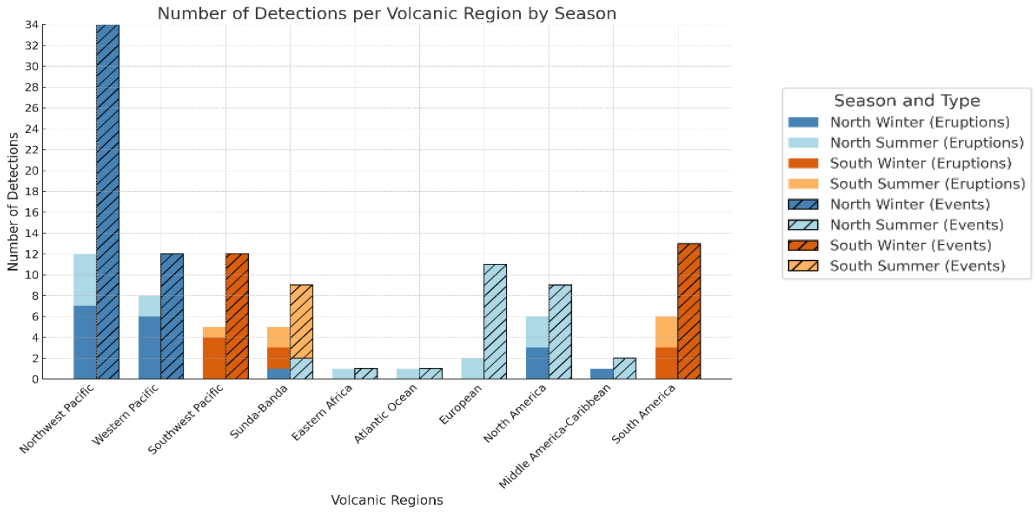

Figure 6.15. Seasonal distribution of eruptions (solid bars) and associated discrete infrasound detections (hashed bars) across multiple volcanic regions. The dataset was categorized by hemisphere (North and South) and season (Winter and Summer) to examine potential atmospheric and regional influences on detectability.

The figure illustrates distinct seasonal patterns according to the volcanic regions. For the cases of the distribution of detected eruptions by hemispheres and seasons, it must be noted that eruptions can begin in one specific season (e.g. Northern Hemisphere summer), while their associated events are only detected in a subsequent season (e.g. Northern Hemisphere winter)

This analysis highlights that volcanic eruptions and discrete infrasound events may not be confined to the same seasonal interval. In some cases. This time lag can be influenced by stratospheric wind patterns, which vary according to season and hemisphere, altering the efficiency of infrasound propagation across hemispheres.

In the Northern Hemisphere, 31 eruptions (66%) and 79 discrete events (77.5%) were identified by the algorithm, mainly during the Northern Hemisphere winter, probably favoured by the long-range infrasound propagation atmospheric conditions. The Northwest Pacific volcanic region was the most active globally, with 11 eruptions (23.4 %) and 34 associated events (33.3%), followed by the Western Pacific volcanic region with 9 eruptions (19.1 %) and 12 associated events (11.8%).

Several regions, such as North America, Europe, and Central America-Caribbean, exhibit detections predominantly during the Northern Hemisphere summer, which may be related both

to network configuration and seasonal variability in propagations conditions. In the North American volcanic region, 6 eruptions (9%) and 9 events (8.8%) were identified, and in the European Region (only referring to the Mount Etna volcano), although only 2 eruptions were identified, a relatively number of 10 discrete events (9.8 %) were detected.

The Central America-Caribbean, Eastern Africa and Atlantic Ocean regions contributed minimally, with 1 eruption (1.5%) or event (1%) per region, but correspond to the VEI 4 eruptions of Nabro and Grimsvötn volcanoes in 2011. These were short-lived eruptions with the detected discrete events associated with the initial explosive onset of the eruptions.

In the Southern Hemisphere, 16 eruptions (34%) and 23 discrete events (22.5%) were identified by the algorithm. In the Southwest Pacific and South America regions, 5 (7.5%) and 6 (9%) eruptions and 12 events (11.8%), respectively, were detected exclusively during the Southern Hemisphere winter, which is consistent with the expected seasonal propagation enhancements.

In the Sunda-Banda arc region, 5 eruptions (7.5%) and 9 events (8.8%) were identified, with detections occurring across the Southern summer, Southern winter and even isolated detections during the Northern winter and Northern summer, reflecting its location closer to the equatorial region and exposure to both seasonal hemispherical variances. Also suggesting the presence of the region-specific dynamics.

No activity was detected in the Eastern Pacific region, possibly due to a combination of lower eruptive activity during the analysis period and long oceanic distances to the nearest stations, which potentially limited the detection capability.

In conclusion, the analysis supports the presence of a strong hemispherical and seasonal impact on volcanic detections using infrasound. Most eruptions and discrete events occurred in the Northern Hemisphere, mainly during winter, given the favourable source-to-station atmospheric propagation. The Northwest and Western Pacific regions were the most active and most effectively detected.

In the Southern Hemisphere, the detected events were less numerous and occurred mainly in the austral winter. The Sunda-Banda region, which lies in the equatorial region, showed detections in all seasons. Regions such as East Africa and the Atlantic Ocean had limited detections due to the duration of the eruptions.

Overall, the results highlight the importance of atmospheric conditions and the location of the eruption.

6.4. Classification Categories Analysis

Based on the detections identified by used algorithm, the events were classified into eight different classes (A to H, see section 4.4). To characterise the spatial variability of the detections, a classification scheme was developed, grouping the events according to the number and distribution of stations that recorded each detection, considering the proximity and back-azimuth of the signal. The aim of this classification is to better understand the robustness of the detections and the influence of atmosphere propagation conditions (Figure 6.16).

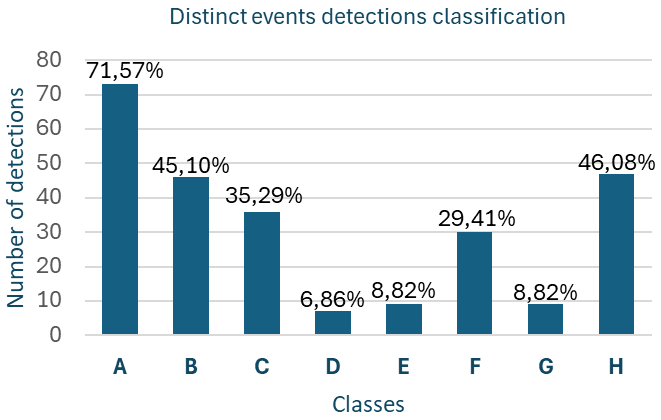

Figure 6.16. Distribution chart of the identified events, classified according to eight class. Classs A to D reflect the detection density between the three closest stations, with class A (only at the closest station) with the highest number of events observed. Class E, which includes detections identified at more than three stations. Class F and G refer to detections at nearby and distant stations or only at distant stations, potentially linked to atmospheric ducts or station faults. Class H includes the observations associated to volcano back-azimuth with onset times falling outside celerity thresholds. The percentages above each bar represent the relative frequency of each class for the 102 events, considering that each detected event can be associated to more than one class.

The classes cover detections identified at the nearest station (Class A) to detections identified only in the back-azimuth direction of the volcano (Class H). Each detected event can be associated to more than one class.

Class A accounts for 71.6% of all cases and emphasises the key role of nearby station locations - particularly the nearest station - highlighting the importance of station proximity in improving detection performance. Of the 73 events, 35 were detected only at the nearest station (e.g., at I48TN in relation to Mount Etna in August 2011; at I14CL in relation to Villarrica in 2015 or at I43US for Bogoslof in December 2016). This subset of detections highlights both the importance of station proximity and the intensity of events that can generate infrasound signals capable of being detected locally, even under limited propagation conditions. In these cases, signal detection was possible despite high attenuation or unfavourable atmosphere propagation conditions. From the total events of Class A, 27 events were also identified at the two closest stations (Class C), indicating slightly wider propagation conditions (e.g. Mount Etna in May 2016; Sinabung in February 2018 or Cleveland on 6 December 2020). From this group, we also have in 4 events detections identified at the nearest station and at the third nearest station (also Class C), with no detections at the intermediate station. This lack of detection can be explained, for example, by noise or shadow zone, by unfavourable atmospheric conditions, as the station is in a region with an $V_{eff\ ratio}$ lower than 1, preventing the downward refraction of acoustic energy. Other possible reasons might be technical temporary issues that affected the station during the event period (e.g. Kambalny, April 2017, VEI 3; Kelud, February 2014, VEI 4). These spatial coverage variations, all of them involving the nearest station, highlight the dependency of infrasound signal propagation on the conditions of the atmosphere and the network's geometry and performance, as previously discussed.

Class B (45.1%), C (35.3%), and F (29.4%) demonstrate the algorithm’s ability to detect events across wider or more spatially dispersed station configurations.

Classes C (35.3%), and D (6.9%), totalling 43 events, are the focus of the analysis, as they will be cross-checked with the IDC bulletins for validation. From the various parameters analysed for each volcano (Appendix B), two are presented here in detail: propagation time delay and the correlation parameter. The propagation delay corresponds to the time difference between the expected travel time of the infrasonic signal - calculated based on the distance between the source and the station and a reference sound speed (0.340 km/s) and the arrival time effectively recorded (Figure 6.17). It is useful for identifying the influence of atmosphere conditions, such as wind direction on the propagation of the signal. The correlation parameter evaluates the strength consistency of the detected waveform. It´s a signal quality indicator: high correlation values suggest clear and coherent arrivals, while low values can reflect noise, signal distortion or propagation anomalies. These two parameters contribute to a better understanding of how infrasound propagates through the atmosphere and the reliability of detections in different volcanic regions and seasons.

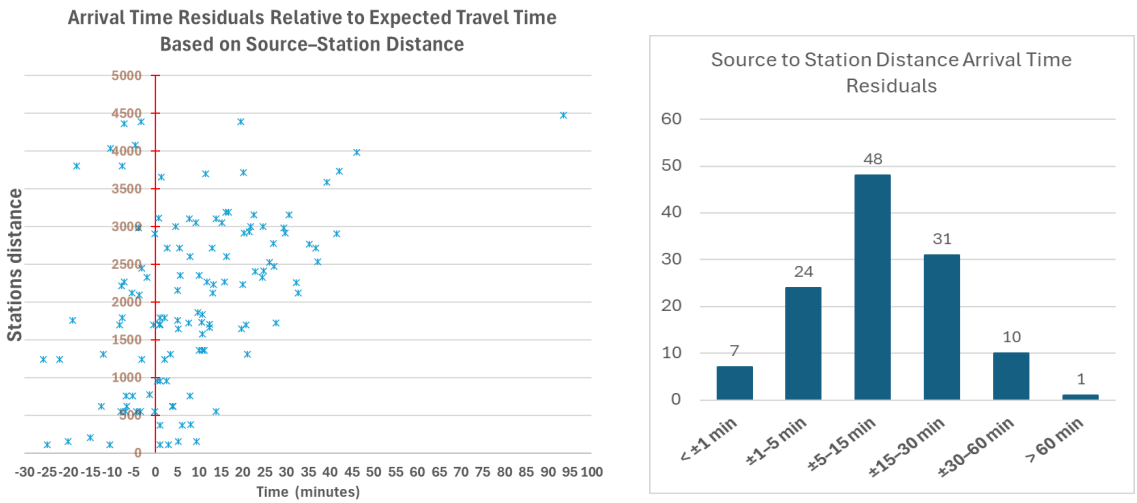

Figure 6.17. Arrival time residuals (in minutes) plotted as a function of source–station distance (in kilometres). Residuals were calculated as the difference between the observed infrasound arrival time and the expected travel time assuming a standard sound speed model (0.340 km/s).

For each of the 43 events, the correlation values obtained at each station were analysed to evaluate the coherence of the identified infrasound signals. So, the number of analyses performed corresponds to the number of stations that detected each group of events. High correlation values indicate coherent and clear detections, while low correlations may indicate interference from noise. Regions with a higher number of events, such as the Northwest Pacific, Western Pacific and Southwest Pacific, allow for a more reliable statistical assessment (Figure 6.18).

The Northwest Pacific had the highest number of analyses (41) across 14 events, with a median correlation of 0.57, with values ranging from 0.21 to 0.77. Despite the variability, the median score was relatively high, suggesting generally good coherence in detected signals, possibly aided by favourable source–station geometry and propagation conditions.

The Western Pacific region (19 analyses of 6 events) performed well with moderately median and correlation values mostly above 0.6, but varying between 0.25 and 0.95, pointing to consistent detection performance, but with variable detection conditions in some cases, most probably affected either by the network layout or the environmental conditions that affected the signal propagation patterns.

The Southwest Pacific (18 analyses, 9 events) and Sunda-Banda (19 analyses, 6 events) regions both showed stable and high coherence, both with median correlation of around 0.58. The general quality of these detections remains moderate to good, likely influenced by their location relative to the global infrasound network and favourable propagation paths, to station configuration, and to prevailing atmospheric conditions.

Although with fewer events identified, the regions of Europe, Atlantic Ocean and East Africa also exhibited moderate to good correlation values. For example, the European region (10 analyses, 4 events) showed median values (0.428), probably reflecting the variable conditions of infrasound propagation despite the characteristics of strong and repetitive signals associated with a well-monitored source such as the Mount Etna volcano. Regarding the Atlantic region, the Grímsvötn volcano showed a mean correlation above 0.62, with values ranging from 0.55 to 0.72, with the event being detected at all stations with available data within a radius of 4500 km. The correlation values for the East African region (Nabro volcano) ranged from 0.3 to 0.6, with a mean correlation of 0.59, indicating a moderate detection quality.

The North American region, with 6 analyses from 3 events, had moderate correlation values between 0.43 and 0.64, with a median of 0.58. Despite the limited number of detections, the results suggest a relatively stable signal quality.

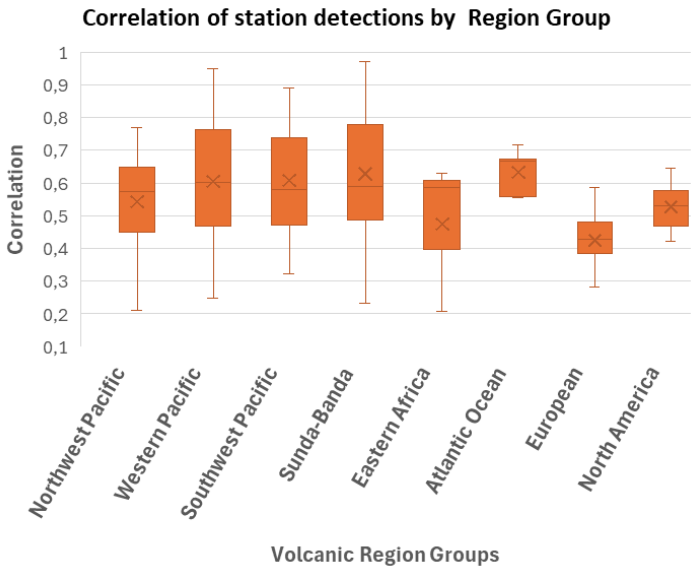

Figure 6.18. Stations data correlation for infrasound detections across volcanic regions (classes C and D).

In summary, the correlation analysis reveals regional variations that could be associated with the station layout, network coverage and source-receiver atmospheric propagation patterns, as well as local atmospheric variables. Regions with more dense monitoring stations and with more frequent volcanic activity, such as the Northwest and Southwest Pacific, tend to have higher and more consistent correlations. On the other hand, regions with fewer stations or more complex propagation environments tend to show higher variability. These results highlight the value of correlation as a key parameter in validating infrasound detections and for characterising propagation in different volcanic environments.

To assess the consistency of our detection algorithm with reliable reference data, the Late Event Bulletin (LEB) from the International Data Centre (IDC) of the CTBTO was chosen as a comparison base, mainly because it provides a good combination of both completeness and reliability. When compared to SEL3, which lists automatically generated events which may include false or misdefined events, the LEB lists events that have been reviewed and validated by analysts, enhancing its precision and consistency. It was also compared to the Reviewed Event Bulletin (REB), in which only events that meet more restrictive screening criteria are included, while LEB uses more flexible criteria for including events. This leads to a more extensive and diverse catalogue of events, including those events that are relevant to this study and as they are beyond the scope of nuclear monitoring, are often excluded from the REB. Overall, the LEB provides a useful and robust dataset for evaluating the performance of t_o-based algorithm.

The time differences (in minutes) between the detection algorithm onset time (t_o) and the LEB event origin time are presented below (Figure 6.19). Time differences are distributed around zero, reflecting a strong agreement between the detections made by the algorithm based on t_o and the events listed in the LEB.

A mean difference of 1.37 minutes and a median of 0.5 minutes, indicate a slightly positive trend, meaning that LEB events tend to be picked up later than those detected by our algorithm. Although most of the values are well clustered, the standard deviation of 14.8 minutes reflects some variability, mainly because a few outliers.

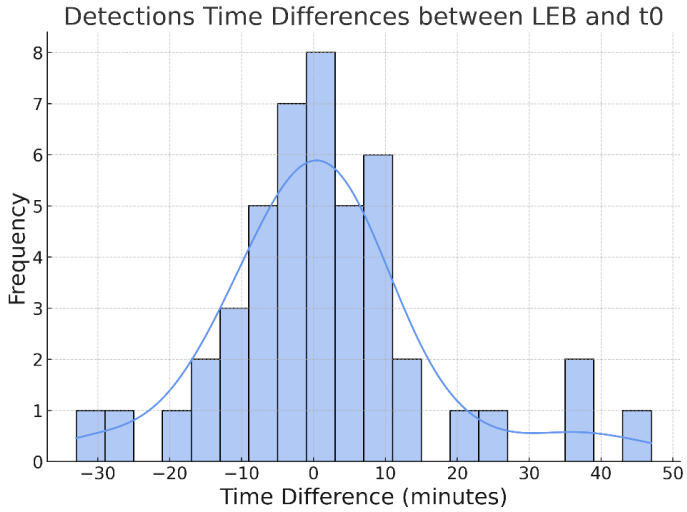

Figure 6.19. Time difference (in minutes) between the LEB event origin time and the algorithm onset time (t_0). Positive values mean the LEB detection times came after t_0; negative values mean it came before.

To summarise, the achieved results have shown strong time agreement and support the consistent performance of the detection algorithm when compared to LEB events. Most of the detections are closely aligned in time, and the few outliers are possibly a result of unexpected variations linked to propagation effects or the IMS stations used. The LEB therefore proved to be a robust and suitable reference for assessing infrasound event detection associated with volcanic activity. This overall consistence reinforces confidence in the reliability of the algorithm.

Class E (8.8%), with detections that occurred at more than three stations, was less frequent—only 11 events—mostly involving eruptions of higher intensity (six VEI 3 and five VEI 4 events).

Class G (8.8%), corresponding to detections only at distant stations, suggests the presence of specific propagation ducting. Some of these detections were excluded from further analysis due to anomalous waveform characteristics at long distances, such as high-frequency content or low detection correlation.

Class H accounts for 46,08% of all the cases and it refers to detections at stations aligned with the volcanoes back-azimuth, but where the estimated arrival times fall outside typical celerity propagation thresholds. This may reflect GVP erroneous event origin time, inaccuracies in the estimated onset time (t_o), or delays caused by complex propagation paths (Figure 6.20).

This class might also show effects from uneven sound radiation or local filtering due to the landscape and wind direction.

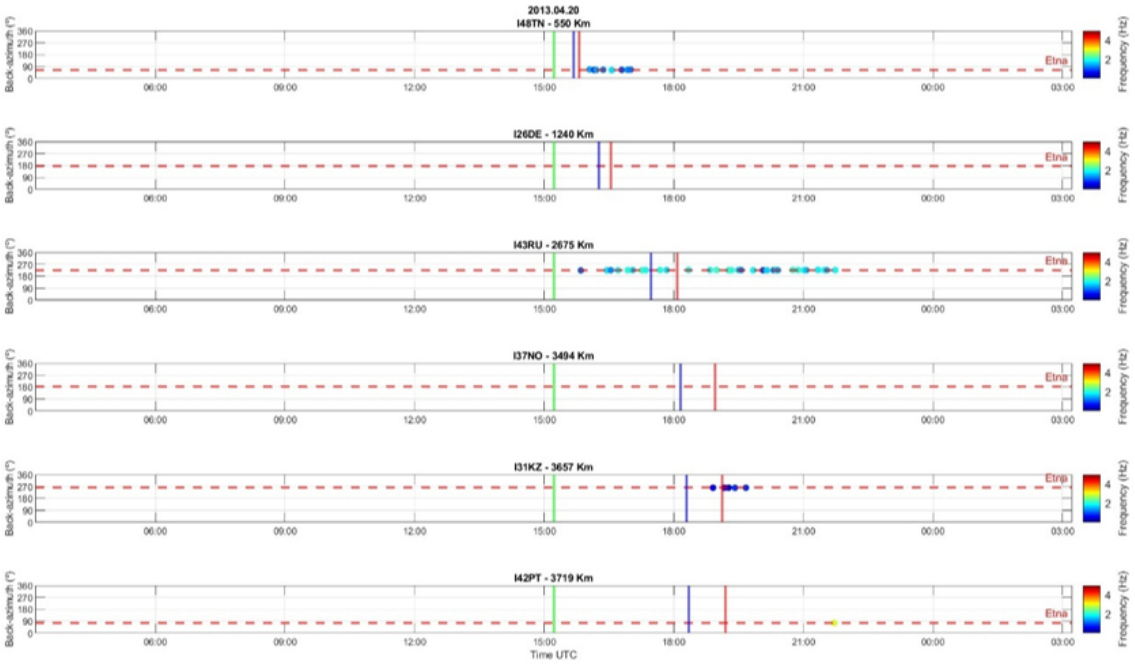

Figure 6.20. Class H detections associated with the Etna 2013 event on 20 April, classified in H Class, where it is clearly observed that the signal arrival times at the nearest station (I48TN), 550km away are beyond the celerity thresholds (blue and red vertical lines), but are probably valid detections. The red dashed line is the volcano's back-azimuth, the green vertical line is the t_0 time and each dot is a detection colored by frequency (Hz).

To improve the detection algorithm based on the onset time (t_o), Class H was introduced, enabling detections at stations aligned with the volcano's back-azimuth to be added, even if the arrival times fall outside the expected atmospheric propagation interval. This can occur due to a variety of reasons, such as the event start time (t_o) provided by the GVP may not be always accurate, particularly for long lasting eruptions with poor timelines or eruptions that occur over multiple phases. Delays can also be caused by a complex propagation path or by local conditions, such as wind or topography, which slow down or filter the acoustic waves. Although these detections are beyond the expected time window, most of them take place within 1 to 2 hours of the estimated t_o, i.e. we're looking at the wrong onset time and they're likely to be valid detections. Adding this class results will allow identification of possible infrasound signals associated with volcanic eruptions. As a result, the detection algorithm becomes more robust and efficient, especially in real-life environments where conditions are not ideal. Applying the improved detection algorithm, based on this class, led to a clear performance enhancement at all levels of the analysis in the number of volcanoes, as well as in terms of detections success of eruptions and discrete events. The number of the volcanoes with identified eruptive activity increased from 26 to 30, which corresponds to an increase from 56.5 % (26/46) to 65.2 % (30/46), representing an absolute gain of 8.7 % in terms of coverage. In the case of the eruptions, detections have increased from 46 to 50 (out of 67), which represents an improvement of 3.3 % (71.6 % to 74.9 %). The most significant improvement resulted with the events, where the overall number of detections increased from 102 to 128, for a total of 186 events. This increased the detection rate resulted in an improvement of 14 % (54.8 % to 68.8 %).

The addition of class H detections plays an essential role in increasing the flexibility and range of the detection algorithm beyond conventional thresholds. It allows the recovery of detections that would previously have been discarded simply because they didn't meet the celerity criteria or the GVP onset time t_0 was inaccurate. Clear examples of this include discrete infrasound signals associated with the eruptions of Karymsky (2017), Krakatau (2018), Manam (2014-2017), Mount Etna (2010-2013) and Zhupanovsky (2015-2016). In many of these cases, the detections were recorded outside the expected propagation celerity window, but within a window of up to 1 or 2 hours before or after the estimated onset time (t_o), strongly supporting the identification of their origin. This extended approach significantly increases the sensitivity of the detection algorithm, allowing for a more comprehensive identification of volcanic activity, both in terms of location and time.

6.5. Characterization of Source-to-Station Distances and Associated Infrasound Propagation Times

As stated before, the best approach to evaluate the results obtained in this work facing the IDC bulletins, is to compare them with the LEB. For that, it is crucial to relate the distance between the studied volcanoes with their third nearest station. Assuming that the signal propagates at the speed of 0.340 km/s, the aim is to analyse the spatial distribution of these distances and estimate the corresponding propagation times.

The obtained dispersion ranges between 1,525 km (Calbuco) and 4,035 km (Sinabung), with an average of approximately 2,737 km that indicate a quite consistent spatial distribution with some outliers at more distant ranges. The associated travel times vary from approximately 1 hour and 14 minutes to around 3 hours and 17 minutes. On average, the signal takes around 2 hours and 16 minutes to travel from the volcanic source to the third station.

According to the Violin plot on Figure 6.21, distances to the third closest station for volcanoes in the Northwest Pacific volcanic Region range from 1,794 km to 2,774 km, corresponding to infrasound travel times between approximately 1 hour 28 minutes and 2 hours 16 minutes. The average propagation time in this region is around 1 hour 56 minutes, reflecting medium-range travel paths through oceanic and atmospheric layers with moderate attenuation.

In the Western Pacific, the station distances extend from 2,482 km up to 3,507 km, yielding propagation times between 2h 2m and 2h 52m, with an average around 2h 19m. Those distances tend to be vast, which could be seen as an indicator of moderately sparse station coverage, leading to the waves propagating through extended atmospheric ducts.

The Southwest Pacific region exhibits a broader range of distances, from 2,104 km to 3,494 km, with corresponding travel times from 1h 43m to 2h 51m. These values reflect the presence of detections close to the source as well as after long distance propagation, probably influenced by the prevailing wind conditions in the upper atmosphere.

In contrast, the Sunda-Banda region registered the longest propagation paths in the dataset, ranging from 2,476 km to 4,035 km, which results in propagation times between around 2h 1m and 3h 18m. The average distance of 3,061 km is evidence of longer infrasound propagation paths, most probably driven by effective stratospheric ducts, despite atmospheric losses.

The North American volcanic region shows less variation, with distances from 2,802 km to 3,141 km and propagation times between 2h 17m and 2h 34m. The narrow range reflects relatively centralized activity or uniform station distribution, facilitating consistent monitoring.

In the Middle America-Caribbean region, distances are similarly high, between 3,156 km and 3,413 km, corresponding to travel times from 2h 35m to 2h 47m. The high values suggest efficient long-distance propagation, though the effectiveness of detection may depend on noise, seasonal wind patterns and stratified atmospheric layers.

The South American volcanic region stands out with the shortest minimum distance of 1,525 km (travel time: 1h 15m), while the maximum reaches 2,684 km (2h 12m). The mean distance of 2,013 km yields an average travel time of approximately 1h 39m, indicating a mix of local and regional signal paths that benefit from reduced attenuation in the lower atmosphere.

These results confirm that despite significant atmospheric attenuation, infrasound from volcanic events can propagate over several thousand kilometres, with travel times extending up to three hours until the third nearest station. The combination of source-station geometry and atmospheric propagation conditions plays a critical role in determining detection capabilities and should be considered in network design and signal interpretation.

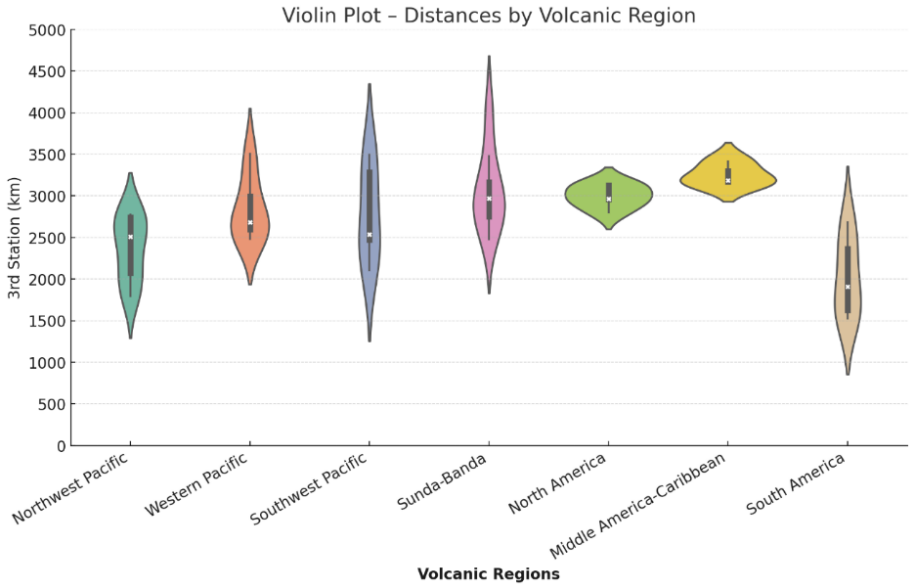

Figure 6.21. Violin plot showing the distribution of distances (in kilometres) to the third nearest infrasound station for each volcanic region. The regions are arranged geographically from Northwest Pacific to South America. Each violin represents the kernel density estimation of the distribution, with wider sections indicating a higher concentration of values. The median is marked by a central line, while the minimum and maximum values are indicated by the lower and upper extremes of each shape.

The characterisation of source-station distances and associated propagation times gives valuable insights regarding the applicability and the response capability of infrasound-based volcanic monitoring. By looking at the source-station distances of each of the 46 volcanoes and the third nearest IMS station, it is possible to estimate the expected propagation time of the signal and, therefore, the minimum time delay necessary for a potential alert based simply on infrasound recordings.

Across the various volcanic regions, travel times range from approximately 1 hour and 14 minutes (as observed in South America) to over 3 hours (in the Sunda-Banda region), assuming a constant sound speed (0.340 km/s). These values represent the minimum time required for a signal to reach a third station, which is required to support validation of detected signals and to reduce the risk of false alerts.

In regions such as South America, where the mean distance to the third station is only around 2,013 km, monitoring systems may benefit from faster detection capabilities, with average signal arrival times close to 1 hour and 39 minutes. This improves the potential for timely alert issuance, especially for explosive eruptions. In regions such as the Sunda-Banda arc and Central America-Caribbean, mean distances are greater than 3,000 kilometres and detection latency is higher, which could potentially compromise the efficiency of near-real-time monitoring

systems. It must be noted that these estimations assume an Ideal horizontal propagation pattern. However, in practice, the atmosphere's variability plays a critical role in signal propagation. Even strong eruptions may go undetected if the signal path crosses regions of high attenuation or unfavourable wind alignment. A key parameter in this context is the effective sound speed ratio (V_{e}ff).

In an ideal monitoring model, the closest three stations to each volcano would not only be geographically nearby but also located within favourable atmospheric propagation zones—that is, areas with $V_{\text{eff-ratio}} > 1$ and minimal signal loss. Therefore, a real-time understanding of atmospheric propagation conditions at the time of the event is essential to interpret detections correctly and ensure that the stations contributing to the alert are indeed within viable transmission paths. This shifts the paradigm from a purely geometric network model to a dynamic, propagation-aware detection strategy, where proximity is weighted together with acoustic viability.

Thus, for the volcanoes under study, the time window between eruption onset and detection at the third nearest station defines a lower bound for alert response, typically ranging from 1 to 3 hours, depending on both station geometry and propagation efficiency. Optimizing this response time requires not only strong signals and well-distributed stations, but also integration of atmospheric models that can dynamically assess whether infrasound is likely to reach the network under prevailing conditions.

FINAL CONSIDERATIONS

Volcanic eruptions are one of the most impressive, powerful, intense natural phenomena on Earth, posing a potential threat to hundreds of millions of people.

Volcanic eruptions exhibit a wide range of styles, from effusive events (e.g., fluid lava flows or lava domes) to violent explosive eruptions that generate rapidly ascending columns, expanding volcanic clouds, and pyroclastic density currents. Each eruptive style represents a distinct volcanic hazard, with potential impacts varying from local (less than a few kilometres) to regional scales (hundreds of kilometres or more).

Volcanoes are efficient sources of infrasound, with signals ranging in duration from short-lived transient bursts (lasting only a few seconds) to long-lasting atmospheric perturbations (several hours), with pressure amplitudes spanning from just a few Pascals to several hundred Pascals. From Hawaiian to Plinian eruption styles, volcanic activity perturbs the atmosphere and generates infrasonic waves that can be detected at various distances. Large-scale volcanic eruptions have the potential to generate atmospheric pressure waves that propagate around the Earth, such as reported examples of the Krakatau volcano eruption in 1883, Bezymianny volcano in 1956, Mount Saint Helens in 1980, El Chichon in 1992, or more recently the Hunga Tonga-Hunga Ha'apai volcano in January 2022.

Despite significant progress in developing real-time, multiparametric volcanic monitoring networks over the past decades, only a small fraction of the 1281 world's potentially active volcanoes from the GVP database is currently monitored in real time and even fewer are equipped with comprehensive, multiparametric systems. Many active volcanoes, particularly those in remote areas, lack conventional ground-based monitoring infrastructure. In these cases, remote sensing techniques remain the only practical means of surveillance and eruption detection. Among them, infrasound has proven to be a valuable tool for detecting and monitoring explosive volcanic activity.

Previous research has shown their effectiveness in propagation in atmospheric waveguides, allowing signals generated by explosive eruptions to be registered at stations thousands of kilometres away. The atmosphere here plays an important role in the propagation and eventual detection of infrasound at the range of monitoring stations, in particular in the Stratosphere, were the stratospheric jets turn it the most critical layer for the source-to-receiver infrasound propagation.

Given this framework, this work aimed to evaluate the effectiveness of remote detection of explosive volcanic activity using infrasound monitoring. An automatic detection algorithm was applied to eruptions reported in the Global Volcanism Program (GVP) database for the period 2011-2020, with a Volcanic Explosivity Index (VEI) ≥ 3. The analysis was based on data from the IMS infrasound stations, operated by CTBTO. The IMS infrasound data has provided the perfect opportunity to test the effectiveness of the detection algorithm on volcanoes across the Globe.

Active volcanoes that had eruptive activity with VEI≥ 3 from 2011 to 2020 were identified and selected from the GVP database. During the period of interest, there were 360 eruptions (or confirmed eruptive activity) from 138 volcanoes. Among these, 67 eruptions originating from 46 volcanoes had a VEI ≥ 3 and were therefore selected for this study (53 events were classified with VEI = 3, 13 events with VEI = 4 and 1 event with VEI = 5).

Following the 46 volcanoes selection, these were grouped into 11 pre-defined GVP zones, according to their geographical distribution and geodynamic setting, which included 67 eruptions and 186 associated discrete events.

For infrasound data, although the CTBTO IMS infrasound network during the study period consisted of 53 certified stations, only data from 43 IMS infrasound stations at a source-receiver distance of up to 4,500 km from each selected volcano met the required criteria and were analysed. Therefore, 9 IMS certified stations were not considered, once their maximum distance from any of the selected volcanoes (IS03, IS21, IS23, IS24, IS27, IS47, IS49, IS50 and IS55). The selected arrays have a median aperture of 2.15 kilometres, spanning from 1.13 kilometres (IS32) to 3.37 kilometres (IS60). The number of elements of each array varies from 4 to 10. Altogether, the daily volume of raw data reaches more than 508×10^6 samples, in a 20 Hz sampling rate.

To assess detection capability and improve the association between signals and events, a specific algorithm was developed based on the Progressive Multi-Channel Correlation (PMCC) method. This algorithm was adjusted to consider the state of the atmosphere at the time of each event, by incorporating meteorological reanalysis data from the ECMWF models (ERA-Interim and ERA5) and the Ground-to-Space (G2S) empirical model for application of ray tracing techniques to simulate infrasonic signal propagation.

A set of Matlab scripts was created to automate the different process steps of the algorithm that perform the association between infrasonic detections and volcanic events; generates $V_{eff\text{-}ratio}$ maps and attenuation patterns; and runs through atmospheric parameters.

The algorithm for infrasound data analysis performs as follows: (1) array processing: For each available station, waveform data is processed based in PMCC algorithm to generate a final station detection bulletin; (2) select the volcano to be analysed; (3) select the list of explosive events associated with the selected volcano to extract the onset time t0 of each event; (4) select the station detection lists that fulfil the maximum distance of 4500 km with valid data available; (5) process a time window t_0-t_{start} to t_0 + t_{end}, looking for detections; (6) evaluation of the processed detections based on the volcano-station back-azimuth with a deviation of ±5° and ±10°; and (7) final processing of station detections.

Data from the 60 levels of the atmospheric model, the temperature, the horizontal wind components and the logarithm of the surface pressure were retrieved and stored for the 186 discrete events. Atmospheric parameters retrieved were then used to calculate the effective speed of sound ratio $v_{eff-ratio}$ for each day for the locations of the selected 186 events and selected IMS stations. Ray tracing was used to obtain the expected back-azimuth of the possible arrivals of the eigenrays in the nearest IMS station, with origin in the selected volcano, being performed for all the 186 discrete events.

The algorithm demonstrated high reliability in multiple years - particularly in 2011, 2014, 2015 and 2019 - with detection rates exceeding 87 % and reaching 100 % in 2019. The results indicate a good performance of the algorithm in identifying infrasound signals generated by explosive volcanic activity across periods of high and low eruptive frequency.

The results showed that 102 events were detected (54.8%) from 47 eruptions (70.15%). In the Northern Hemisphere, 31 eruptions (66%) and 79 discrete events (77.5%) were identified by the algorithm, mainly during the Northern Hemisphere winter. The Northwest Pacific volcanic region was the most active globally, followed by the Western Pacific volcanic region. Several regions, such as North America, Europe, and Central America-Caribbean, exhibit detections predominantly during the Northern Hemisphere summer, which may be related both to network

configuration and seasonal variability in propagations conditions. The Central America-Caribbean, Eastern Africa and Atlantic Ocean regions contributed minimally, with 1 eruption or event per region. In the Southern Hemisphere, 16 eruptions (34%) and 23 discrete events (22.5%) were identified by the algorithm. While in Southwest Pacific and South America regions, events were detected exclusively during the Southern Hemisphere winter, which is consistent with the expected seasonal propagation enhancements: in the Sunda-Banda arc region detections occurred across the Southern summer, Southern winter and even isolated detections during the Northern winter and Northern summer, reflecting its location closer to the equatorial region and exposure to both seasonal hemispherical variances. Also in equatorial zone, no activity was detected in the Eastern Pacific region, possibly due to a combination of lower eruptive activity during the analysis period and long oceanic distances to the nearest stations, which potentially limited the detection capability.

The analysis of the five IMS stations with the highest detection rates points towards the importance of station proximity, layout and geographical location. Stations such as I44RU and I53US, with 4 and 8 array elements respectively and located relatively close to active volcanic clusters in the Pacific Northwest and North America, registered the highest number of detections. Stations such as I39PW (7 elements) and I30JP (6 elements), although further away from most eruptive sources, demonstrated the ability to detect long-range, high-explosive eruptions, emphasising the potential influence of wide-open, distributed array elements on far-field detection performance. Additionally, when evaluating detection patterns in the IMS network, it is also important to consider the propagation conditions in the atmosphere along the path between the source and the receiving station. As example, stations located in acoustic shadow zones - regions where atmospheric conditions prevent infrasound energy from being transmitted either through tropospheric, stratospheric or thermospheric ducts - may be inhibited from registering signals, even when located quite close to the source. Thus, the understanding of detection (or non-detection) patterns involves a combined assessment of the spatial configuration and propagation environment, as shown by ray tracing or other acoustic modelling tools, as proved by earlier studies, which emphasise the strong influence of seasonal wind structures and atmospheric variability on the propagation of long-range infrasound.

Regarding the magnitude of events, VEI 3 is the most frequent in all the identified eruptions with a detection rate of 70.37%, e.g. the lava fountaining at Mount Etna volcano (2013 and 2016), or the Strombolian activity at Villarrica volcano (2015). However, the eruption of the Mount Ontake in 2014, which generated more energic events, also VEI 3, was not detected by the infrasound stations, probably due to the low acoustic energy released. Although less frequent than VEI 3, VEI 4 still represents a considerable number of events, indicating eruptions of moderate magnitude often associated with clear infrasonic signals, such as the Grimsvötn and Nabro eruptions in 2011, Kelud in 2014, and Taal volcano in the Philippines in 2020. On the other hand, two eruptions — Wolf (2015) and Semeru (2017) — were not identified by the algorithm. The algorithm successfully detected the VEI 5 eruption of the Puyehue-Cordón Caulle volcano, which occurred from June 2011 to April 2012. The algorithm has demonstrated robust detection capabilities for more intense eruptions but also identifies points for improvement in dealing with the complexity and variability of global volcanic activity.

The number of associated IMS stations for each volcano ranges from a minimum of three stations (Sinabung, Turrialba, and Wolf - 6.5% of the total of the volcanoes) to a maximum of nine stations (Bogoslof volcano – 2.2%). The mean number of stations is 6, which is also the most

frequent value. The interquartile range (IQR) goes from 5 to 7 stations, covering 71.8 % of all the volcanoes. This distribution reflects relatively uniform IMS coverage, with minimal variations and few outliers.

The detection of infrasound over long distances is highly impacted by atmospheric propagation conditions, such as the vertical wind structure, which varies seasonally and with the direction of propagation. Even highly energetic eruptions may be undetected if atmospheric conditions are unfavourable for establishing a propagation channel toward the monitoring stations. Through the results obtained by the algorithm's script for the atmospheric profiles, we can clearly see in several events that the variations of the stratospheric zonal winds strongly affect the transmission loss of infrasound rays on their path from the volcano to the monitoring station. The $V_{eff-ratio}$ drives the refraction of acoustic energy from the stratopause zone towards the ground, and it is highly constrained by the direction of stratospheric winds, which generally follow seasonal patterns. This seasonal variation in the wind dynamics is clearly expressed in the corresponding attenuation and effective sound speed ratio (V_{eff}) maps. These results emphasise the critical importance of atmospheric propagation dynamics in the long-range monitoring. Seasonal variations in the direction of the zonal stratospheric wind, as well as the structure of sound speed patterns, significantly affect the efficiency of signal propagation and the overall detectability of volcanic events at IMS stations. It becomes evident that the $V_{eff-ratio}$ is a key parameter in understanding when and where infrasound signals are refracted back toward the ground. Moreover, the influence of station-specific characteristics, such as array configuration and sensor density, must also be considered. Stations with fewer sensor elements may exhibit reduced sensitivity, particularly under marginal propagation conditions and high noise. These observations are not isolated cases. Several volcanic events across different regions and seasons exhibit similar behaviors, where the $V_{eff-ratio}$ structure, atmospheric attenuation, and station positioning critically affect detection outcomes. In summary, although eruption energy and signal propagation are important, the atmosphere works as a selective filter and propagation dynamics are critical for effective signal reception. Understanding these limitations is essential to better assessing the data and enhancing monitoring procedures.

Based on the detections identified by the algorithm, the events were classified into eight different classes to characterise the spatial variability of the detections.

Class A accounts for 71.6% of all cases and emphasises the key role of nearby station locations - particularly the nearest station - highlighting the importance of station proximity in improving detection performance. Class B (45.1%), C (35.3%), and F (29.4%) demonstrate the algorithm’s ability to detect events across wider or more spatially dispersed station configurations. Classes C (35.3%), and D (6.9%), totalling 43 events, were the focus of the analysis, as they were cross-checked with the CTBTO’s International data Centre (IDC) bulletins for validation. To assess the consistency of our detection algorithm with reliable reference data, the Late Event Bulletin (LEB) from the IDC was chosen as a comparison base, mainly because it provides a good combination of both completeness and reliability. The achieved results have shown strong time agreement and support the consistent performance of the detection algorithm when compared to LEB events. Most of the detections are closely aligned in time, and the few outliers are possibly a result of unexpected variations linked to propagation effects or the IMS stations used. Class E (8.8 %), with detections that occurred at more than three stations, was less frequent and mostly involving eruptions of higher intensity.

Class H accounts for 46.08 % of all the cases and it refers to detections from stations aligned with the volcanoes back-azimuth, but where the estimated arrival times fall outside typical celerity propagation thresholds. Here, GVP erroneous event origin time, inaccuracies in the estimated onset time (t_o), or delays caused by complex propagation paths can influence those situations. The addition of this class plays an essential role in increasing the flexibility and range of the detection algorithm beyond conventional thresholds. It allows the recovery of detections that would previously have been discarded. As a result, the detection algorithm becomes more robust and efficient, leading to a clear performance enhancement at all levels of the analysis in the number of volcanoes, as well as in terms of detections success of eruptions and discrete events. The number of the volcanoes with identified eruptive activity increased from 26 to 30, representing an improvement of 8.7 % of coverage. The number of eruptions and events increased from 46 to 50 and 102 to 128 respectively, representing improvements of 3.3% and 14%.

The detection algorithm developed and applied in this work has proven to be an effective instrument for detecting infrasound events in a wide range of volcanic regions worldwide and demonstrates its potential for global volcanic monitoring. Its conception allows for automation based on the IMS stations nearest each volcano, giving a practical and scalable framework for routine monitoring. Additionally, the algorithm can be adapted to specific volcanoes or regions, as it can include regional propagation conditions by using available atmospheric profiles. This adaptability and flexibility make it suitable for integration into early warning systems and real-time monitoring programs.

Future improvements can also take into consideration the integration of qualitative eruption indicators and geographic-based propagation conditions to enhance the reliability of detection across a broader spectrum of eruptive styles.

BIBLIOGRAPHY

Allstadt, K. E., Matoza, R. S., Lockhart, A. B., Moran, S. C., Caplan-Auerbach, J., Haney, M. M., Thelen, W. A., & Malone, S. D. (2018). Seismic and acoustic signatures of surficial mass movements at volcanoes. In *Journal of Volcanology and Geothermal Research* (Vol. 364). https://doi.org/10.1016/j.jvolgeores.2018.09.007

Amante, C. and Eakins, B. W.: ETOPO1 1 Arc-Minute Global Relief Model: Procedures, Data Sources and Analysis. *NOAA Technical Memorandum NESDIS NGDC-24*, *National Geophysical Data Center*, NOAA, https://doi.org/10.7289/V5C8276M, 2009.

Ancey, C. (2001). Snow Avalanches. In: Balmforth N.J., Provenzale A. (eds.) Geomorphological Fluid Mechanics. *Lecture Notes in Physics,* vol. 582. Springer, Berlin, Heidelberg. https://doi.org/10.1007/3-540-45670-8_13.

Anderson, T. & Flett, J.S. (1903). Report on the eruptions of the Soufriere, in St. Vincent, in 1902, and on a visit to Montagne Pelee, in Martinique - Part I. *Philosophical Transactions of the Royal Society of London, Series A*, 200: pp. 353–553.

Arendt, S., and D. Fritts (2000). Acoustic radiation by ocean surface waves. *Journal of Fluid Mechanics*, 415, 1-21.

Arhens, C. D. (2009). *Meteorology today: an introduction to weather, climate, and the environment*. Belmont, CA: Brooks/Cole.

Arnoult, K. M., J. V. Olson, C. A. Szuberla, S. R. McNutt, M. Garces, D. Fee, and M. Hedlin (2010). *Infrasound observations of the recent explosive eruptions of Okmok and Kasatochi volcanoes*, Alaska, *Journal of Geophysical Research*, doi:10.1029/2010JD013987, in press.

Arrowsmith, S. J. & Hedlin, M. A. H. (2005). Observations of infrasound from surf in southern California, *Geophysical Research Letters*. 32, L09810, doi:10.1029/2005GL022761.

Arrowsmith, S. J., D. ReVelle, W. Edwards, and P. Brown (2008). Global detection of infrasonic signals from three large bolides, *Earth Moon Planets*, 102(1–4), 357–363, doi:10.1007/978-0-387-78419-9_50.

Assink, J. D., Evers, L. G., Holleman, I., & Paulssen, H. (2008). Characterization of infrasound from lightning. *Geophysical Research Letters*. 35(15). https://doi.org/10.1029/2008GL034193.

Assink J. D., Waxler R., Drob D. (2012). On the sensitivity of infrasonic travel times in the equatorial region to the atmospheric tides. *Journal of Geophysical Research*, 117. D01110, doi:10.1029/2011JD016107.

Assink, J. D., A. Le Pichon, E. Blanc, M. Kallel, and L. Khemiri (2014). Evaluation of wind and temperature profiles from ECMWF analysis on two hemispheres using volcanic infrasound, *Journal of Geophysical Research: Atmospheres*, 119, 8659–8683, doi:10.1002/2014JD021632.

Assink, J., Averbuch, G., Shani-Kadmiel, S., Smets, P., & Evers, L. (2018). A Seismo-Acoustic Analysis of the 2017 North Korean Nuclear Test. *Seismological Research Letters*, *89*(6), 2025–2033. https://doi.org/10.1785/0220180137

Atchley, A. A. (2005). Not Your Ordinary Sound Experience: A Nonlinear-Acoustics Primer. *Acoustics Today*, *1*(1), 19. https://doi.org/10.1121/1.2961122

Balachandran, N., Donn, W.L. (1971). Characteristics of infrasonic signals from rockets. *Geophysical Journal of the Royal Astronomical Society*.26:135–148

Balachandran, N., Donn, W. L. & Rind, D. H. (1977). Concorde Sonic Booms as an Atmospheric Probe. *Science*, 197(4298), 47 LP-49. http://science.sciencemag.org/content/197/4298/47.abstract.

Balachandran, N. K. (1983). *Acoustic and gravity waves in the neutral atmosphere and the ionosphere, generated by severe storms*. NASA NTRS/ Source: https://ntrs.nasa.gov/citations/19830023934.

Baldwin, M. P., Ayarzagüena, B., Birner, T., Butchart, N., Butler, A. H., Charlton-Perez, A. J., Domeisen, D. I. v., Garfinkel, C. I., Garny, H., Gerber, E. P., Hegglin, M. I., Langematz, U., & Pedatella, N. M. (2021). Sudden Stratospheric Warmings. *Reviews of Geophysics*, *59*(1). https://doi.org/10.1029/2020RG000708

Bass, B., Avolio, B., Jung, D., Berson, Y. (2003). Predicting Unit Performance by Assessing Transformational and Transactional Leadership. *The Journal of applied psychology*. 88. 207-18. 10.1037/0021-9010.88.2.207.

Bass, H. E., Bhattacharyya, J., Garcés, M. A., Hedlin, M., Oslon, J. & Woodward, R. L. (2006). Infrasound *Acoustic Today* 2 (1): 9–19. https://doi.org/10.1121/1.2961130.

Bedard Jr, A. J. (1988). Infrasound from natural sources. *In Proceedings from the 1988 International Conference on Noise Control Engineering*, Avignon, France.

Bedard Jr, A. J. (1989). Detection of avalanches using atmospheric infrasound, *Proceedings of the Western Snow Conference*, edited by: Shafer, B., *Western Snow Conference*, April 1989, Colorado State University, Fort Collins, CO, USA, 52–58.

Bedard Jr, A. J. (1998). Infrasonic detection of severe weather. *In Proceedings of the 19th conference on severe local storms*. *American Meteor Society*, Minneapolis, MN, Paper 6.6.

Bedard, A. J., Jr., Bartram, B. W., Keane, A. N., Welsh, D. C., Nishiyama, R. T. (2004). The infrasound network (ISNet): Background, design, details, and display capability as a 88D adjunct tornado detection tool. *Preprints*, *22nd Conf. on Severe Local Storms,* Hyannis, MA, *American Meteor Society*, 1.1.

Belli, G., Walter, F., McArdell, B., Gheri, D., & Marchetti, E. (2022). Infrasonic and seismic analysis of debris-flow events at Illgraben (Switzerland): Relating signal features to flow parameters and to the seismo-acoustic source mechanism. *Journal of Geophysical Research: Earth Surface*, 127, e2021JF006576. https://doi.org/10.1029/2021JF006576

Benioff, H., & Gutenberg, B. (1939). Observations with Electromagnetic Microbarographs. *Nature*, *144*(3645), 478–478. https://doi.org/10.1038/144478a0

Blom P., Waxler R. (2012). Impulse propagation in the nocturnal boundary layer: Analysis of the geometric component. *The Journal of the Acoustical Society of America,* 131. 3680–3690. https://doi.org/10.1121/1.3699174.

Blom, P. (2014). *GeoAc: Numerical tools to model acoustic propagation in the geometric limit* [Software]. Los Alamos National Laboratory (LANL).

Blom P., Waxler R. (2017). Modeling the refraction of microbaroms by the winds of a large maritime storm. *The Journal of the Acoustical Society of America*, 142. 3520–3529. https://doi.org/10.1121/1.5016809.

Bolt, B. A., & Tanimoto, T. (1981). Atmospheric oscillations after the May 18, 1980 eruption of Mount St. Helens, Eos Trans. AGU, 62(23), 529–530.

Bonadonna, C., Macedonio, G., & Sparks, R. S. J. (2002). Numerical modelling of tephra fallout associated with dome collapses and Vulcanian explosions: application to hazard assessment on Montserrat. *Geological Society, London, Memoirs*, *21*(1), 517–537. https://doi.org/10.1144/GSL.MEM.2002.021.01.23

Bonadonna, C., Cioni, R., Costa, A., Druitt, T., Phillips, J., Pioli, L., Andronico, D., Harris, A., Scollo, S., Bachmann, O., Bagheri, G., Biass, S., Brogi, F., Cashman, K., Dominguez, L., Dürig, T., Galland, O., Giordano, G., Gudmundsson, M., … Wallenstein, N. (2016). MeMoVolc report on classification and dynamics of volcanic explosive eruptions. *Bulletin of Volcanology*, *78*(11), 84. https://doi.org/10.1007/s00445-016-1071-y

Bowman, J. R., Baker, G. E., & Bahavar , M. (2005). Ambient infrasound noise, *Geophysical Research Letters*, 32, L09803, doi:10.1029/2005GL022486.

Brachet, N., & Coyne, J. (2006, setembro). Latest developments in the automatic and interactive processing of infrasound data at the IDC Infrasound Technology Workshop (ITW), Fairbanks, AK, Estados Unidos.

Brachet N, Brown D, Le Bras R, Mialle P, Coyne J (2010). Monitoring the earth's atmosphere with the global IMS infrasound network. In: Le Pichon A., Blanc E., Hauchecorne A. (eds.) *Infrasound Monitoring for Atmospheric Studies*. Springer, Dordrecht, pp. 73–114.

Braun, T. & Ripepe, M. (1993). Interaction of seismic and air waves as recorded at Stromboli Volcano. *Geophysical Research Letters*, 20: 65–68. https://doi.org/10.1029/92GL02543.

Brekhovskikh, L. M., & Godin, O. A. (1999). *Acoustics of Layered Media II* (Vol. 10). Springer Berlin Heidelberg. https://doi.org/10.1007/978-3-662-03889-5

Brown D., Katz C., Le Bras R., Flanagan M., Wang J., Gault A. (2002). Infrasonic signal detection and source location at the prototype international data centre". *Pure and Applied Geophysics*, 159: 1081–1125. https://doi.org/10.1007/978-3-0348-8144-9_10.

Brown, S. K., Crosweller, H. S., Sparks, R. S. J., Cottrell, E., Deligne, N. I., Ortiz Guerrero, N., Hobbs, L., Loughlin, S. C.& Siebert, L. (2014). Characterisation of the Quaternary eruption record: Analysis of the Large Magnitude Explosive Volcanic Eruptions (LaMEVE) database. *Journal of Applied Volcanology, 3*(1), 5. https://doi.org/10.1186/2191-5040-3-5

Buckingham, M. J. &. Garcés, M. (1996). Canonical model of volcano acoustics. *Journal of Geophysical Research*. 101, 8129-8151.

Campus, P. (2004). The IMS infrasound network and its potential for detection of events: examples of a variety of signals recorded around the world. *Inframatics,* 6:14–22.

Campus, P. & Christie, D. (2010). Worldwide Observations of Infrasonic Waves. In: Le Pichon A., Blanc E., Hauchecorne A. (eds.) *Infrasound Monitoring for Atmospheric Studies*. Springer, Dordrecht. DOI: https:// doi10.1007/978-1-4020-9508-5_6.

Cannata, A., Montalto, P., Privitera, E., Russo, G., & Gresta, S. (2009). Tracking eruptive phenomena by infrasound: May 13, 2008 eruption at Mt. Etna. *Geophysical Research Letters*, *36*(5). https://doi.org/10.1029/2008GL036738

Cannata, A., Spedalieri, G., Behncke, B., Cannavò, F., di Grazia, G., Gambino, S., Gresta, S., Gurrieri, S., Liuzzo, M., & Palano, M. (2015). Pressurization and depressurization phases inside the plumbing system of Mount Etna volcano: Evidence from a multiparametric approach. *Journal of Geophysical Research: Solid Earth*, *120*(9), 5965–5982. https://doi.org/10.1002/2015JB012227

Cansi Y (1995). An automatic seismic event processing for detection and location: the PMCC method. *Geophysical Research Letters*. 22(9):1021–1024.

Cansi, Y., & Klinger, Y. (1997). *An automated data processing method for mini-arrays*. European-Mediterranean Seismological Centre (EMSC).

Cansi, Y., & Le Pichon, A. (2008). Infrasound event detection using the progressive multi-channel correlation algorithm. In D. Havelock, S. Kuwano, & M. Vorländer (Eds.), *Handbook of Signal Processing in Acoustics* (pp. 1425–1435). Springer. https://doi.org/10.1007/978-0-387-30441-0_77.

Caplan-Auerbach, J. & McNutt, S.R. (2003). New insights into the 1999 eruption of Shishaldin volcano, Alaska, based on acoustic data. *Bulletin of Volcanology,* 65(6): 405–417.

Caplan-Auerbach, J., Bellesiles, A., Fernandes, JK., (2010). Estimates of eruption velocity and plume height from infrasonic recordings of the 2006 eruption of Augustine Volcano, Alaska. *Journal of Volcanology and Geothermal Research.* 189(1–2):12 18. https://doi.org/10.1016/j.jvolgeores.

Carley, J. C. (2011). *Some notes on acoustics*. University of Bath.

Caudron, C., Taisne, B., Garcés, M., Alexis, L. P., & Mialle, P. (2015). On the use of remote infrasound and seismic stations to constrain the eruptive sequence and intensity for the 2014 Kelud eruption. *Geophysical Research Letters*, *42*(16), 6614–6621. https://doi.org/10.1002/2015GL064885.

Ceplecha, Z. (1998). Meteor phenomena and bodies. *Space Science Reviews*, 84, 327–471. https://doi.org/10.1023/A:1005069928850.

Ceranna L., Le Pichon A., Green D. N., Mialle P. (2009). The Buncefield explosion: a benchmark for infrasound analysis across Central Europe. *Geophysical Journal International*, 177: 491–508. doi:10.1111/j.1365-246X.2008.03998.x

Ceranna, L., Matoza, R., Hupe, P., Le Pichon, A., Landès, M. (2019). Systematic Array Processing of a Decade of Global IMS Infrasound Data. In: Le Pichon, A., Blanc, E., Hauchecorne, A. (eds) *Infrasound Monitoring for Atmospheric Studies.* Springer, Cham. https://doi.org/10.1007/978-3-319-75140-5_13

Chimonas, G. (1977). A Possible Source Mechanism for Mountain-Associated Infrasound. *Journal of the Atmospheric Sciences*, 34(5):806-811. https://doi.org/10.1175/1520-0469.

Chouet, B., Hamisevicz, N., & McGetchin, T. R. (1974). Photoballistics of volcanic jet activity at Stromboli, Italy, *Journal of Geophysical Research*, 79 (32), 4961–4976, doi:10.1029/JB079i032 p04961.

Chouet, B. A., & Matoza, R. S. (2013). A multi-decadal view of seismic methods for detecting precursors of magma movement and eruption. *Journal of Volcanology and Geothermal Research*, *252*, 108–175. https://doi.org/10.1016/j.jvolgeores.2012.11.013

Christie, D. R., Vivas Veloso, J. A., Campus, P., Bell, M., Hoffmann, T,. Langlois, A., Martysevich, P., Demirovic, E., and Carvalho, J. (2001). Detection of atmospheric nuclear explosions: The infrasound component of the International Monitoring System. *Kerntechnik.* 66. 96-101. 10.1515/kern-2001-0058.

Chrzanowski, P., Greene, G., Lemmon, K. T., & Young, J. M. (1961). Traveling pressure waves associated with geomagnetic activity. *Journal of Geophysical Research*, *66*(11), 3727–3733. https://doi.org/10.1029/JZ066i011p03727

Chunchuzov, I., Kulichkov, S., Perepelkin, V., Popov, O., Firstov, P., Assink, J. D., & Marchetti, E. (2015). Study of the wind velocity-layered structure in the stratosphere, mesosphere, and lower thermosphere by using infrasound probing of the atmosphere. *Journal of Geophysical Research: Atmospheres*, *120*(17), 8828–8840. https://doi.org/10.1002/2015JD023276

Cioni, R., Pistolesi, M., Rosi, M. (2015). Plinian and Subplinian Eruptions. In: Sigurdsson, H., Houghton, B., Rymer, H., Stix, J., McNutt, S. (Eds.), *The Encyclopedia of Volcanoes*, pp. 519–535.

Clarke, A. B., Esposti Ongaro, T., & Belousov, A. (2015). *Vulcanian Eruptions. The Encyclopedia of Volcanoes, 505–518.* doi:10.1016/b978-0-12-385938-9.00028-6.

Cook, R. K. (1971). Infrasound radiated during the Montana Earthquake of 1959 August 18. *Geophysical Journal of the Royal Astronomical Society*. 26, 191-198.

Dabrowa, A. L., Green, D.N., Rust, A.C., Phillips, J.C. (2011). A global study of volcanic infrasound characteristics and the potential for long-range monitoring. *Earth and Planetary Science Letters*. 310. 369-379. DOI:10.1016/j.epsl.2011.08.027.

De Angelis S., Fee D., Haney M., Schneider D. (2012). Detecting hidden volcanic explosions from Mt. Cleveland Volcano, Alaska with infrasound and ground-coupled airwaves. *Geophysical Research Letters*. 39 (L21312). DOI:10.1029/2012GL053635.

De Angelis, S., Lamb, O., Lamur, A., Hornby, A., Aulock, F., Chigna, G., Lavallée, Y., Rietbrock, A. (2016). Characterization of moderate ash-and-gas explosions at Santiaguito volcano, Guatemala, from infrasound waveform inversion and thermal infrared measurements. *Geophysical Research Letters*. 43 (12):6220–6227.

De Angelis, S., Diaz-Moreno, A., Zuccarello, L. (2019). Recent Developments and Applications of Acoustic Infrasound to Monitor Volcanic Emissions. *Remote Sensing*. 11. 1302. DOI: 10.3390/rs11111302.

de Carlo, M., Hupe, P., le Pichon, A., Ceranna, L., & Ardhuin, F. (2021). Global Microbarom Patterns: A First Confirmation of the Theory for Source and Propagation. *Geophysical Research Letters*, *48*(3). https://doi.org/10.1029/2020GL090163

de Groot-Hedlin C. (2008). Finite-difference time-domain synthesis of infrasound propagation through an absorbing atmosphere. *The Journal of the Acoustical Society of America*. 124. 1430-1441. DOI: 10.1121/1.2959736.

de Groot-Hedlin, C.D., Hedlin, M.A., Walker, K.T., Drob, D.P. & Zumberge, M.A. (2008). Evaluation of infrasound signals from the shuttle Atlantis using a large seismic network. *The Journal of the Acoustical Society of America, 124 3*, 1442-51.

de Groot-Hedlin C. D., Hedlin, M. A. H., Drob, D. P. (2010). Atmospheric Variability and Infrasound Monitoring. In: Le Pichon A., Blanc E., Hauchecorne A. (eds) *Infrasound Monitoring for Atmospheric Studies*. Springer, Dordrecht. DOI: https://doi.org/10.1007/978-1-4020-9508-5_15.

de Groot-Hedlin C., Hedlin, M. A. H., Walker, K. (2011). Finite difference synthesis of infrasound propagation through a windy, viscous atmosphere: application to a bolide explosion detected by seismic networks. *Geophysical Journal International*. 185 (1). 305–320. https://doi.org/10.1111/j.1365-246X.2010.04925.x.

de Groot-Hedlin, C.D., & Hedlin, M.A. (2014). Infrasound detection of the Chelyabinsk meteor at the USArray. *Earth and Planetary Science Letters, 402*, 337-345.

Delle Donne, D., Ripepe, M., de Angelis, S., Cole, P. D., Lacanna, G., Poggi, P., & Stewart, R. (2014). Chapter 9 Thermal, acoustic and seismic signals from pyroclastic density currents and Vulcanian explosions at Soufrière Hills Volcano, Montserrat. *Geological Society, London, Memoirs*, *39*(1), 169–178. https://doi.org/10.1144/M39.9

Dessler, A. J. (1973). Infrasonic thunder, *Journal of Geophysical Research*. 78, 1889 – 1896.

Dibble, R. (1989). Infrasonic recordings of Strombolian eruptions of Erebus, Antarctica, March–December 1984, covering the jump in activity on 13 September 1984, in *Volcanic Hazards, Assessment and Monitoring*, edited by J. Latter, pp. 536– 553, *Springer-Verlag*, Berlin.

Dibble, R. R., Kienle, J., Kyle, P. R., & Shibuya, K. (1984). Geophysical studies of Erebus volcano, Antarctica, from 1974 December to 1982 January. *New Zealand Journal of Geology and Geophysics*, *27*(4), 425–455. https://doi.org/10.1080/00288306.1984.10422264

Donn, W. & Shaw D. (1967). Exploring the atmosphere with nuclear explosions. *Reviews of Geophysics and Space Physics*,5:53–82.

Donn, W. & Rind, D. (1979). Monitoring Stratospheric Winds with Concorde-Generated Infrasound. *Journal of Applied Meteorology*, 18(7): 945-952. https://doi.org/10.1175/1520-0450.

Donn, W. & Balachandran, N. (1981). Mount St. Helens eruption of 18 May 1980: air waves and explosive yield. *Science*, 213:539–541.

Douville H. (2009). Stratospheric polar vortex influence on Northern Hemisphere winter climate variability. *Geophysical Research Letters*. 36 (18). https://doi.org/10.1029/2009GL039334.

Drob, D. P., Picone J. M., Garcés M. (2003). Global morphology of infrasound propagation. *Journal of Geophysical Research*. 108. D2. 4680. DOI:10/1029/2002JD003307

Drob, D. P., Emmert J. T., Crowley G., Picone J. M., Shepherd G. G., Skinner W., Hays P., Niciejewski R.J., Larsen M., She C. Y., Meriwether J. W., Hernandez G., Jarvis M. J., Sipler D.P., Tepley C. A., O'Brien M. S., Bowman J. R., Wu Q., Murayama Y., Kawamura S., Reid I. M., Vincent R. A. (2008). An empirical model of the Earth's horizontal wind fields: HWM07. *Journal of Geophysical Research*. 113. A12304. doi:10.1029/2008JA013668.

Drob, D. P., Broutman D., Hedlin M. A., Winslow N. W., Gibson R. G. (2013). A method for specifying atmospheric gravity wavefields for long-range infrasound propagation calculations. *Journal of Geophysical Research: Atmospheres*. 118. 3933–3943. DOI:10.1029/2012JD018077.

Drob, D. P., Emmert J.T., Meriwether J.W., Makela J.J., Doornbos E., Conde M., Hernandez G., Noto J., Zawdie K. A., McDonald S. R., Huba J. D., Klenzing J. H. (2015). An update to the Horizontal Wind Model (HWM): The quiet time thermosphere. *Earth and Space Science*. 2. 301–319. DOI:10.1002/2014EA000089.

Edwards, W. N., P. G. Brown, and D. O. ReVelle (2006). Estimates of meteoroid kinetic energies from observations of infrasonic airwaves, *Journal of Atmospheric and Solar-Terrestrial Physics*. 68, 1136 – 1160.

Evans, J. E. (1991). Development of a real-time ATC volcanic ash advisory system based on the future aviation weather system: in Casadevall, T. J., (ed.), Volcanic ash and aviation safety: Proceedings of the first international symposium on volcanic ash and aviation safety, U.S. *Geological Survey Bulletin.* 2047, p. 157-161.

Evers, LG. (2008). *The inaudible symphony: on the detection and source identification of atmospheric infrasound*. [Dissertation (TU Delft), Delft University of Technology]. TU Delft, DEOS.

Evers, L. G., and Haak, H. W. (2005). The detectability of infrasound in The Netherlands from the Italian volcano Mt. Etna: *Journal of Atmospheric and Solar-Terrestrial Physics*, 67, 259–268, doi: 10.1016/j.jastp.2004 .09.002.

Evers, L., Ceranna, L., Haak, H., Le Pichon, A. & Whitaker, R. (2007). A Seismoacoustic Analysis of the Gas-Pipeline Explosion near Ghislenghien in Belgium. *Bulletin of the Seismological Society of America*, 97(2), 417-425.

Evers, L. & Haak, H.W. (2010). The Characteristics of Infrasound, its Propagation and Some Early History. In: Le Pichon A., Blanc E., Hauchecorne A. (eds) *Infrasound Monitoring for Atmospheric Studies.* Springer, Dordrecht. DOI: https://doi.org/10.1007/978-1-4020-9508-5_1.

Evers, L. G., van Geyt, A. R. J., Smets, P., & Fricke, J. T. (2012). Anomalous infrasound propagation in a hot stratosphere and the existence of extremely small shadow zones. *Journal of Geophysical Research: Atmospheres*, *117*(D6). https://doi.org/10.1029/2011JD017014

Fairfield, C. (1980). OMSI sound project, the acoustic effects of the Mount St. Helens eruption on May 18, 1980. *Ore Geology*. 12, 200–202.

Farges, T., Blanc, E., le Pichon, A., Neubert, T., & Allin, T. H. (2005). Identification of infrasound produced by sprites during the Sprite2003 campaign. *Geophysical Research Letters*, *32*(1), 1–4. https://doi.org/10.1029/2004GL021212.

Farges, T. & Blanc, E. (2010). Characteristics of infrasound from lightning and sprites near thunderstorm areas. *Journal of Geophysical Research: Space Physics*, 115(A6).

Fee, D., Garcés, M., Patrick, M., Chouet, B., Dawson, P. & Swanson, D. (2010a). Infrasonic harmonic tremor and degassing bursts from Halema'uma'u Crater, Kilauea Volcano, Hawaii. *Journal of Geophysical Research,* 115, B11316, doi:10.1029/2010JB007642.

Fee, D., Garcés, M., Steffke, A., (2010b). Infrasound from Tungurahua Volcano 2006–2008: Strombolian to Plinian eruptive activity. *Journal of Volcanology and Geothermal Research*, 193 (1–2), 67–81. http://dx.doi.org/10.1016/j.jvolgeores.2010.03.006.

Fee D, Steffke A, Garcés, M. (2010c). Characterization of the 2008 Kasatochi and Okmok eruptions using remote infrasound arrays. *Journal of Geophysical Research: Atmospheres*. 115(D2). https://doi.org/10.1029/ 2009jd013621.

Fee, D., Garces, M., Orr, T., & Poland, M. (2011a). Infrasound from the 2007 fissure eruptions of Kīlauea Volcano, Hawai'i. *Geophysical Research Letters*, *38*(6), n/a-n/a. https://doi.org/10.1029/2010GL046422

Fee, David & Mcnutt, S. & Lopez, Taryn & Arnoult, Kenneth & Szuberla, Curt & Olson, John. (2011b). Combining local and remote infrasound recordings from the 2009 Redoubt Volcano eruption. *Fuel and Energy Abstracts*. 259. 10.1016/j.jvolgeores.2011.09.012.

Fee, D., Matoza, R. S. (2013). An overview of volcano infrasound: From Hawaiian to Plinian, local to global. *Journal of Volcanology and Geothermal Research.* 249. 123-139. https://doi.org/10.1016/j.jvolgeores.2012.09.002.

Fee, D., Yokoo, A., & Johnson, J. B. (2014). Introduction to an Open Community Infrasound Dataset from the Actively Erupting Sakurajima Volcano, Japan. *Seismological Research Letters*, *85*(6), 1151–1162. https://doi.org/10.1785/0220140051.

Fee, D., Izbekov, P., Kim, K., Yokoo, A., Lopez, T., Prata, F., Kazahaya, R., Nakamichi, H., & Iguchi, M. (2017). Eruption mass estimation using infrasound waveform inversion and ash and gas measurements: Evaluation at Sakurajima Volcano, Japan. *Earth and Planetary Science Letters*, *480*, 42–52. https://doi.org/10.1016/j.epsl.2017.09.043

Fee, D., Toney, L., Kim, K., Sanderson, R. W., Iezzi, A. M., Matoza, R. S., de Angelis, S., Jolly, A. D., Lyons, J. J., & Haney, M. M. (2021). Local Explosion Detection and Infrasound Localization by Reverse Time Migration Using 3-D Finite-Difference Wave Propagation. *Frontiers in Earth Science*, *9*. https://doi.org/10.3389/feart.2021.620813

Few, A. A. (1985). *The production of lightning-associated infrasonic acoustic sources in thunderclouds. Journal of Geophysical Research, 90(D4), 6175.* doi:10.1029/jd090id04p06175.

Firstov, P.P., Kravchenko N.M. (1996). Estimation of the amount of explosive gas released in volcanic eruptions using air waves. *Journal of Volcanology and Seismology*. 17:547–560.

Freire, S., Florczyk, A. J., Pesaresi, M., & Sliuzas, R. (2019). An Improved Global Analysis of Population Distribution in Proximity to Active Volcanoes, 1975–2015. *ISPRS International Journal of Geo-Information*, *8* (8), 341. https://doi.org/10.3390/ijgi8080341.

Friedlander, F. G. (1946). The diffraction of sound pulses. I. Diffraction by a semi-infinite plate. *Proceedings of the Royal Society of London A*. 186. 322–344. https://doi.org/10.1098/rspa.1946.0046.

Fu, S., Chen, L., Woldai, T., Yin, K., Gui, L., Li, D., Du, J., Zhou, C., Xu, Y., Lian, Z. (2020). Landslide hazard probability and risk assessment at the community level: A case of western Hubei, China. *Natural Hazards*. *Earth's Systems*. 20(2), 581-601. https://doi.org/10.5194/nhess-20-581-2020.

Gainville, O., Blanc, E., Le Pichon, A., Piserchia, P. F. & Blanc-Benon, P. H. (2007). Acoustic propagation and atmosphere characteristics derived from infrasonic waves generated by the Concorde. In *19th International Congress on Acoustics*. https://doi.org/10.1121/1.1404434.

Gainville, O., Blanc-Benon P., Scott J. (2012). Infrasound propagation in realistic atmosphere using nonlinear ray theory. *AIP Conference Proceedings.* 1474. 343–346. https://doi.org/10.1063/1.4749365.

Garcés, M., Hagerty, M. & Schwartz, S. (1998). Magma acoustics and time-varying melt properties at Arenal Volcano, Costa Rica. *Geophysical Research Letters*. 25 (13), 2293 2296.

Garcés M., Iguchi M., Ishihara K., Morrissey M., Sudo Y., Tsutsui T. (1999). Infrasonic precursors to a Vulcanian eruption at Sakurajima Volcano, Japan. *Geophysical Research Letters*, 26. 16. 2537-2540. https://doi.org/10.1029/1998GL005327.

Garcés, M., Hetzer, C., Merrifield, M., Willis, M. & Aucan, J. (2003). Observations of surf infrasound in Hawaii*, Geophysical Research Letters,* 30(24), 2264, doi:10.1029/2003GL018614.

Garcés M., Bass H., Drob D., Hetzer C., Hedlin M., Le Pichon A., Lindquist K., North R., Olson, J. (2004). *Forensic studies of infrasound from massive hypersonic sources*. EOS 85(43):433.

Garcés, M., Aucan, J., Fee, D., Caron, P., Merrifield, M., Gibson, R., Bhattacharyya, J. & Shah, S. (2006). Infrasound from large surf, *Geophysical Research Letters*, 33, L05611, doi:10.1029/2005GL025085.

Garcés, M., Fee, D., Steffke, A., McCormack, D., Servranckx, R., Bass, H., et al. (2008). Capturing the Acoustic Fingerprint of Stratospheric Ash Injection. *Eos, Transactions American Geophysical Union*, 89(40), 377-378. http://dx.doi.org/10.1029/2008EO400001

Genco, R., Ripepe, M. (2010). Inflation-deflation cycles revealed by tilt and seismic records at Stromboli volcano. *Geophysical Research Letters*, 37. https://doi.org/10.1029/2010GL042925

Georges, T. (1973). Infrasound from convective storms: Examining the evidence. *Reviews of Geophysics and Space Physics*, 11:571–594.

Georges, T. M., Beasley, W. H. (1977). Refraction of infrasound by upper-atmospheric winds. *The Journal of the Acoustical Society of America*, Vol. 61, No. 1. DOI:10.1121/1.381263

Gheri, D., Marchetti, E., Belli, G., Pichon, A.L., Boulenger, V., Hupe, P., Ceranna, L., Mialle, P., & Héreil, P. (2023). Monitoring of Indonesian volcanoes with the IS06 infrasound array. *Journal of Volcanology and Geothermal Research*.

Godin, O. A. (2002). An effective quiescent medium for sound propagating through an inhomogeneous, moving fluid. *The Journal of the Acoustical Society of America*, 112. 1269-1275. https://doi.org/10.1121/1.1504853.

Goerke, V. H., Young, J. M. & Cook, R. K. (1965). Infrasonic observations of the May 16, 1963, volcanic explosion on the island of Bali. *Geophysical Research Letters*, 70(24): 6017–6022, DOI:10.1029/JZ070i024p06017.

Goerke, V. H. and Woodward, M. W. (1966). Infrasonic observation of a severe weather system. *Monthly Weather Review*, 94, 395-398.

Gorshkov, G. S. (1959). Gigantic eruption of the Volcano Bezymianny. *Bulletin of Volcanology*. 20, 77–109.

Gossard, E., & Hooke, W. H. (1975). *Waves in the atmosphere: atmospheric infrasound and gravity waves: their generation and propagation*. Elsevier Scientific Pub. Co.

Green, D.N., Bowers, D. (2010). Estimating the detection capability of the International Monitoring System infrasound network. *Journal of Geophysical Research,* 115:D18116. https://doi.org/10.1029/ 2010JD014017.

Green, D.N., Matoza, R.S., Vergoz, J., Le Pichon, A. (2012). Infrasonic propagation from the 2010 Eyjafjallajökull eruption: investigating the influence of stratospheric solar tides. *Journal of Geophysical Research*, 117: D21202. https://doi.org/10.1029/2012JD017988.

Green, D.N., Evers, L.G., Fee, D., Matoza, R. S., Snellen M., Smets P., Simons, D. (2013). Hydroacoustic, infrasonic and seismic monitoring of the submarine eruptive activity and sub-aerial plume generation at South Sarigan, May 2010. *Journal of Volcanology and Geothermal Research*, 257. 31–43. http://dx.doi.org/10.1016/j.jvolgeores.2013.03.006.

Grover, F. H., & P. D. Marshall (1968). Ground to air coupled waves from a distant earthquake, *Nature*, 220(5168), 686 – 687.

Gudmundsson, M. T., R. Pedersen, K. Vogfjord, B. Thorbjarnardottir,S. Jakobsdottir, & M. J. Roberts (2010). Eruptions of Eyjafjallajökull Volcano, Iceland, *Eos, Transactions, American Geophysical Union*, 91(21), 190–191, doi:10.1029/2010EO210002.

Gutenberg, B. (1945). Atmospheric pressure waves near Pasadena. *Bulletin of the American Meteorological Society,* 26(10), 385–388.

Hansen, C. H. (2001). Fundamentals of acoustics. In: Goelzer, B.I.F., Hansen, C.H. and Sehrndt (Eds), *Occupational Exposure Noise: Evaluation, Prevention and Control. World Health Organisation Special Report,* S64:23-28. Federal Institute of Occupational Safety and Health. Germany: G. A. Editors

Harris, A., Ripepe, M. (2007). Synergy of multiple geophysical approaches to unravel explosive eruption conduit and source dynamics–A case study from Stromboli. *Chemie der Erde-Geochemistry*, 67(1):1–35.

Harris, A. J. L., Delle Donne, D., Dehn, J., Ripepe, M., & Worden, A. K. (2013). Volcanic plume and bomb field masses from thermal infrared camera imagery. *Earth and Planetary Science Letters*, *365*, 77–85. https://doi.org/10.1016/j.epsl.2013.01.004

Haskell, N.A. (1951). Asymptotic Approximation for the Normal Modes in Sound Channel Wave Propagation. *Journal of Applied Physics*, 22. 157–168. https://doi.org/10.1063/1.1699918.

Hedin, A. E., Fleming, E. L., Manson, A. H., Schmidlin, F. J., Avery, S. K., Clark, R. R., Franke, S. J., Fraser, G. J., Tsuda, T., Vial, F., & Vincent, R. A. (1996). Empirical wind model for the upper, middle and lower atmosphere. *Journal of Atmospheric and Terrestrial Physics*, *58*(13), 1421–1447. https://doi.org/10.1016/0021-9169(95)00122-0

Hedlin, M. A. H., and K. Walker (2012). A study of infrasonic anisotropy and multipathing in the atmosphere using seismic networks, *Philosophical Transactions of the Royal Society A*, 371, 20110542, doi:10.1098/rsta.2011.0542.

Hersbach, H., Bell, B., Berrisford, P., Hirahara, S., Horányi, A., Muñoz-Sabater, J., Nicolas, J., Peubey, C., Radu, R., Schepers, D., Simmons, A., Soci, C., Abdalla, S., Abellan, X., Balsamo, G., Bechtold, P., Biavati, G., Bidlot, J., Bonavita, M., … Thépaut, J-N. (2020). ERA5 hourly data on model levels from 1940 to present [Conjunto de dados]. Copernicus Climate Change Service (C3S) Climate Data Store (CDS). doi.org

Hicks, S. P., Matos, S. B., Pimentel, A., Belli, G., Gheri, D., Tsekhmistrenko, M., et al. (2023). Exclusive seismoacoustic detection and characterization of an unseen and unheard fireball over the North Atlantic. *Geophysical Research Letters*, *50*, e2023GL105773. https://doi.org/10.1029/2023GL105773

Holton, J. R., Haynes, P. H., McIntyre, M. E., Douglass, A. R., Rood, R. B., & Pfister, L. (1995). Stratosphere-troposphere exchange. *Reviews of Geophysics*, *33*(4), 403–439. https://doi.org/10.1029/95RG02097

Hupe, P. (2018). *Global infrasound observations and their relation to atmospheric tides and mountain waves*, PhD thesis, Ludwig-Maximilians-Universität München, Germany, 189 pp., https://doi.org/10.5282/edoc.23790, 2018.

Hupe, P., Ceranna, L., Le Pichon, A., Matoza, R. S., and Mialle, P. (2022). International Monitoring System infrasound data products for atmospheric studies and civilian applications, *Earth System Science Data*, 14, 4201–4230, https://doi.org/10.5194/essd-14-4201-2022.

Iezzi, A. M., Schwaiger, H. F., Fee, D., & Haney, M. M. (2019). Application of an updated atmospheric model to explore volcano infrasound propagation and detection in Alaska. *Journal of Volcanology and Geothermal Research*, *371*, 192–205. https://doi.org/10.1016/j.jvolgeores.2018.03.009

Iguchi, M. & Ishihara, K. (1990). Comparison of earthquakes and air shocks accompanied with explosive eruptions at Sakurajima and Sawunosejima volcanoes. *Anime News Network Ann. Disaster Prevention Research Institute*, Kyoto University, 33 (B-1): 1–12.

Ishihara, Y., Hiramatsu, Y., Yamamoto, M., Furumoto, M., Fujita, K., (2012). Infrasound/seismic observation of the Hayabusa reentry: Observations and preliminary results. *Earth, Planets and Space* **64**, 655–660. https://doi.org/10.5047/eps.2012.01.003.

Jesus, M., Belli, G., Gheri, D., Matos, S., Wallenstein, N., & Marchetti, E. (2025). The use of a low-cost, small-aperture array as an auxiliary tool to improve infrasound monitoring in the Azores region. *Pure and Applied Geophysics*, vol. 182, no. 12, Springer, pp. 5049–5064, 2025. doi:10.1007/s00024-024-03469-1.

Johnson, J., Lees, J. & Gordeev, E. (1998). Degassing explosions at Karymsky Volcano, Kamchatka. *Geophysical Research Letters*, 25, (21): 3999-4002.

Johnson, J. & Lees, J. (2000). Plugs and chugs; seismic and acoustic observations of degassing explosions at Karymsky, Russia and Sangay, Ecuador. *Journal of Volcanology and Geothermal Research*, 101 (1–2), 67–82.

Johnson, J. B. (2003). Generation and propagation of infrasonic airwaves from volcanic explosions. *Journal of Volcanology and Geothermal Research,* 121. 1-14. https://doi.org/10.1016/S0377-0273(02)00408-0.

Johnson, J., Aster, R. & Kyle P. (2004). Volcanic eruptions observed with infrasound. *Geophysical Research Letters*, 31, L14604, DOI:10.1029/2004GL020020.

Johnson, J. B., & Malone, S. D. (2007). *Ground-coupled acoustic airwaves from Mount St. Helens provide constraints on the May 18, 1980 eruption. Earth and Planetary Science Letters, 258(1-2), 16–31.* doi:10.1016/j.epsl.2007.03.001.

Johnson, J., Aster, R., Jones, K. R., Kyle, P., & McIntosh, B. (2008). Acoustic source characterization of impulsive Strombolian eruptions from the Mount Erebus lava lake. *Journal of Volcanology and Geothermal Research*, *177*(3), 673–686. https://doi.org/10.1016/j.jvolgeores.2008.06.028

Johnson, J. & Ripepe, M. (2011). Volcano infrasound: a review. *Journal of Volcanology Geothermal Research*, 206 (34): 61–69. http://dx.DOI.org/10.1016/.2011.06.006.

Johnson, J. B., Palma, J. L. (2015). Lahar infrasound associated with Volcán Villarica's 3 March 2015 eruption. *Geophysical Research Letters*, 42. 6324-6331. https://doi.org/10.1002/2015GL065024.

Johnson, J. B., Watson, L. M., Palma, J. L., Dunham, E. M., & Anderson, J. F. (2018). Forecasting the Eruption of an Open-Vent Volcano Using Resonant Infrasound Tones. *Geophysical Research Letters*, *45*(5), 2213–2220. https://doi.org/10.1002/2017GL076506

Johnson, J.B. (2019). Local volcano infrasound monitoring. In: *Infrasound Monitoring for Atmospheric Studies: Challenges in Middle Atmosphere Dynamics and Societal Benefits*: Second Edition, Springer International Publishing, pp 989–1022. https://doi.org/10.1007/978-3-319-75140-5_32.

Johnson, J.B., Roca, A., Pineda, A., Mérida, R., Escobar-Wolf, R., Anderson, J.F., Mock, J., Bosa, A., Bejar, G., and Waite, G. (2023). Infrasound detection of approaching lahars: *Scientific Reports*, v. 13, no. 6476, https://doi.org/10.1038/s41598-023- 32109-2.

Jolly, A. D., Matoza, R. S., Fee, D., Kennedy, B. M., Iezzi, A. M., Fitzgerald, R. H., et al. (2017). Capturing the acoustic radiation pattern of strombolian eruptions using infrasound sensors aboard a Tethered Aerostat, Yasur volcano, Vanuatu. *Geophysical Research Letters*, 44(19), 9672–9680. https://doi.org/10.1002/2017GL074971

Jones, K. R., & Johnson, J. B. (2011). Mapping complex vent eruptive activity at Santiaguito, Guatemala using network infrasound semblance. *Journal of Volcanology and Geothermal Research*, *199*(1–2), 15–24. https://doi.org/10.1016/j.jvolgeores.2010.08.006

Jones, K.R., Johnson, J.B., Aster, R., Kyle, P.R., McIntosh, W.C. (2008). Infrasonic tracking of large bubble bursts and ash venting at Erebus volcano, Antarctica. *Journal of Volcanology and Geothermal Research*, 177(3):661–672.

Kamo, K., Ishihara, K., & Tahira, M. (1994). Infrasonic and seismic detection of explosive eruptions at Sakurajima Volcano, Japan, and the PEGASAS-VE early-warning system, in *Proc. of the First International Symposium on Volcanic Ash and Aviation Safety, United States Geological Survey Bulletins,* Seattle, Washington, July 1991, Vol. 2047, 357–365.

Kanamori, H., Mori, J., & Harkrider, D. G. (1994). Excitation of atmospheric oscillations by volcanic eruptions, *Journal of Geophysical Research* 99(B11).

Kebeasy, R. (2008). The CTBTO International Monitoring System and Global Seismicity. In: Husebye, E.S. (eds) Earthquake Monitoring and Seismic Hazard Mitigation in Balkan Countries. NATO Science Series: IV: *Earth and Environmental Sciences*, vol 81. Springer, Dordrecht. https://doi.org/10.1007/978-1-4020-6815-7_7

Kim, K., Lees, J.M. (2011). Finite-difference time-domain modelling of transient infrasonic wavefields excited by volcanic explosions. *Geophysical Research Letters,* 38: L06804. https://doi.org/10.1029/.

Kim, K., Lees, J.M., Ruiz, M. (2012). Acoustic multipole source model for volcanic explosions and inversion for source parameters. *Geophysical Journal International*: 1192–1204. https://doi.org/10.1111/j.1365-246X.2012.05696.x.

Kim, K., Lees, J.M. (2014). Local volcano infrasound and source localization investigated by 3D simulation. *Seismological Research Letters*, 85(6):1177–1186. https://doi.org/10.1785/0220140029.

Kim, K., Fee, D., Yokoo, A., Lees, J.M. (2015). Acoustic source inversion to estimate volume flux from volcanic explosions. *Geophysical Research Letters,* 42:5243–5249 https://doi.org/10.1002/2015GL064466

Kinney, G. F., & Graham, K. J. (1985). *Explosive Shocks in Air*. Springer Berlin Heidelberg. https://doi.org/10.1007/978-3-642-86682-1

Kinsler, L. E., Frey, A. R., Coppens, A. B., & Sanders, J. V. (2000). Fundamentals of acoustics (4.ª ed.). Wiley.

Kogelnig, A., Hübl, J., Suriñach, E., Vilajosana, I., & McArdell, B. W. (2014). Infrasound produced by debris flow: Propagation and frequency content evolution. *Natural Hazards*, 70(3), 1713–1733. https://doi.org/10.1007/.

Konstantinou, K. & Schlindwein, V. (2002). *Nature*, wavefield properties and source mechanism of volcanic tremor: a review. *Journal of Volcanology Geothermal Research*,119: 161–187.

Kriester, B. (1972). Large scale circulation patterns of the stratosphere. *Space Science Reviews*. 13. 258-273.

Lacanna, G., Ripepe, M. (2013). Influence of near-source volcano topography on the acoustic wavefield and implication for source modelling. *Journal of Volcanology and Geothermal Research*, 250. 9-18. http://dx.doi.org/10.1016/j.jvolgeores.2012.10.005.

Lamb, O. D., de Angelis, S., & Lavallée, Y. (2015). Using infrasound to constrain ash plume rise. *Journal of Applied Volcanology*, *4*(1), 20. https://doi.org/10.1186/s13617-015-0038-6

Landès, M., Le Pichon, A., Shapiro, N. M., Hillers, G., and Campillo, M. (2014). Explaining global patterns of microbarom observations with wave action models, *Geophysical Journal International*, 199, 1328–1337, https://doi.org/10.1093/gji/ggu324.

Larson, R. J., L. B. Craine, Thomas, J. E, Wilson, C. R. (1971). Correlation of winds and geographic features with production of certain infrasonic signals in the atmosphere, *Geophysical Journal of the Royal Astronomical Society*, 26, 201 – 214.

Le Pichon, A., Garcés, M., Blanc, E., Barthélémy, M. & Drob, D. (2002). Acoustic propagation and atmosphere characteristics derived from infrasonic waves generated by the Concorde. *The Journal of the Acoustical Society of America*, 111(1), 629–641. https://doi.org/10.1121/1.1404434.

Le Pichon, A., & Cansi, Y. (2003a). Infrasound monitoring and global atmospheric dynamics. InfraMatics, (3), 11–18.

Le Pichon, A., Guilbert, J., Vallée, M., Dessa, J. & Ulziibat, M. (2003b). Infrasonic imaging of the Kunlun Mountain for the great 2001 China earthquake. *Geophysical Research Letters*, 30(15): 1814.

Le Pichon, A., Maurer, V., Raymond, D. & Hyvernaud, O. (2004). Infrasound from ocean waves observed in Tahiti. *Geophysical Research Letters*, 31, L19103, doi:10.1029/2004GL020676.

Le Pichon, A., Blanc, E., Drob, D., Lambotte, S., Dessa, J., Lardy, M., Bani, P. & Vergniolle, S. (2005a). Infrasound monitoring of volcanoes to probe high-altitude winds, *Journal of Geophysical Research*, 110, D13106, doi:10.1029/2004JD005587.

Le Pichon, A., Herry, P., Mialle, P., Vergoz, J., Brachet, N., Garcés, M. & Ceranna, L. (2005b). Infrasound associated with 2004-2005 large Sumatra earthquakes and tsunami. *Geophysical Research Letters*, 32(19):1–5. https://doi.org/10.1029/2005GL023893.

Le Pichon A., Mialle P., Guilbert J., Vergoz J. (2006). Multistation infrasonic observations of the Chilean earthquake of 2005 June 13. *Geophysical Journal International*. 167 (2). 838–844. https://doi.org/10.1111/j.1365-246X.2006.03190.x.

Le Pichon A, Vergoz J, Blanc E, Guilbert J, Ceranna L, Evers L, Brachet N. (2009). Assessing the performance of the International Monitoring System infrasound network: geographical coverage and temporal variabilities. *Journal of Geophysical Research*, 114: D08112. https://doi.org/10.1029/ 2008JD010907.

Le Pichon, A., Matoza, R.S., Brachet, N., and Cansi, Y. (2010). Recent Enhancements of the PMCC Infrasound Signal Detector, *InfraMatics*, 26, 5–8.

Le Pichon A., Vergoz J., Brachet N., Gaillard P., Cansi Y., Guilbert J. (2011). A description of the infrasound data processing at the french cea/dase. 2011 *Monitoring Research Review*: Ground-Based Nuclear Explosion Monitoring Technologies.

Le Pichon, A., Ceranna, L., Vergoz, J. (2012). Incorporating numerical modeling into estimates of the detection capability of the IMS infrasound network. *Journal of Geophysical Research*, 117: D05121. https://doi. org/10.1029/2011JD016670.

Le Pichon, A., Ceranna, L., Pilger, C., Mialle, P., Brown, D., Herry, P., and Brachet, N. (2013). The 2013 Russian fireball largest ever detected by CTBTO infrasound sensors, *Geophysical Research Letters*, 40, 1–6, https://doi.org/10.1002/grl.50619.

Le Pichon, A., Pilger, C., Ceranna, L., Marchetti, E., Lacanna, G., Souty, V., Vergoz, J., Listowski, C., Hernandez, B., Mazet-Roux, G., Dupont, A., and Hereil, P. (2021). Using dense seismo-acoustic network to provide timely warning of the 2019 paroxysmal Stromboli eruptions, *Scientific Reports-UK*, 11, 14464, https://doi.org/10.1038/s41598-021-93942-x.

Lees JM, Gordeev EI, Ripepe M. (2004). Explosions and periodic tremor at Karymsky volcano, Kamchatka, Russia. *Geophysical Journal International*, 158(3):1151–1167.

Lighthill J. (1978). Waves in Fluids. *Cambridge University Press*. New York.

Lingevitch, J. F., Collins, M. D., and Siegmann, W. L. (1999). Parabolic equations for gravity and acousto-gravity waves, *Acoustical Society of America Journal*, vol. 105, no. 6, pp. 3049–3056, 1999. doi:10.1121/1.424634.

Liszka, L. (2004). On the possible Infrasound Generation by Sprites. *Journal of Low Frequency Noise Vibration and Active Control*, pp 85-93.

Liszka, L. (2008). Infrasound: A summary of 35 years of infrasound research. Institutet for Rymdfysic, Swedish Institute os Space Physics, *IRF Scientific Report 291*, Umea, Sweden.

Lonzaga, J. B., Waxler R. M., Assink J. D., Talmadge C. L. (2015). Modelling waveforms of infrasound arrivals from impulsive sources using weakly non-linear ray theory. *Geophysical Journal International*. 200 (3). 1347–1361. https://doi.org/10.1093/gji/ggu479.

Lyons, J. J., Iezzi, A., Fee, D., Schwaigner, H. F., Wech, A. G., Haney, M. M. (2020). Infrasound generated by the 2016–2017 shallow submarine eruption of Bogoslof volcano, Alaska. *Bulletin of Volcanology*. 82. 19. https://doi.org/10.1007/s00445-019-1355-0.

Lyons, J. J., Waite, G. P., Rose, W. I. & Chigna, G. (2010). Patterns in open vent, Strombolian behavior at Fuego volcano, Guatemala, 2005–2007. *Bulletin of Volcanology,* 72 (1): 1–15.

Maher, S. P., Matoza R. S., de Groot-Hedlin, C. D., Gee, K. L., Fee, D., Yokoo, A. (2020). Investigating spectral distortion of local volcano infrasound by nonlinear propagation at Sakurajima Volcano, Japan. *Journal of Geophysical Research*: *Solid Earth*. 125. e2019JB018284. https://doi.org/10.1029/2019JB018284.

Marchetti, E., Ripepe, M., Harris A.J.L., Delle Donne, D. (2009). Tracing the differences between Vulcanian and Strombolian explosions using infrasonic and thermal radiation energy. *Earth and Planetary Science Letters*, 279(3):273–281.

Marchetti, E., Genco, R., & Ripepe, M. (2012). Ground to atmosphere coupling during the 2009 L'Aquila earthquake (central Italy): Infrasonic observations at 150 km distance. *Journal of Geophysical Research: Solid Earth*, *117*(B09304), 1–13. doi.org

Marchetti., E., Ripepe, M., Delle Donne, D., Genco, R., Finizola, A., & Garaebiti, E. (2013). Blast waves from violent explosive activity at Yasur Volcano, Vanuatu, *Geophysical Research Letters*, 40, 5838–5843, doi:10.1002/2013GL057900.

Marchetti, E., Lacanna, G., Le Pichon, A., Piccinini, D., Ripepe, M. (2016). Evidence of Large Infrasonic Radiation Induced by Earthquake Interaction with Alluvial Sediments. *Seismological Research Letters*; 87 (3): 678–684. doi: https://doi.org/10.1785/0220150223

Marchetti, E., Ripepe, M., Campus, P., Le Pichon, A., Brachet, N., Blanc, E., Gaillard, P., Mialle, P., Husson, P. (2019). Infrasound monitoring of volcanic eruptions and contribution of ARISE to the volcanic ash advisory centers. In: Le Pichon A, Blanc E, Hauchecorne A (eds) *Infrasound monitoring for atmospheric studies, 2nd edn*. Springer, Dordrecht, pp 1141–1162.

Marcial, S., Melosantos, A.A., Hadley, K.C., LaHusen, R.G., and Marso, J.N. (1996). Instrumental lahar monitoring at Mount Pinatubo in Newhall, C.G., and Punongbayan, R.S., eds., *Fire and mud—Eruptions and lahars of Mount Pinatubo, Philippines*: Seattle, University of Washington Press, p. 1015–1022.

Marty, Julien & Martysevich, Pavel & Kramer, A. & Haralabus, G. (2012). Engineering and development projects for the sustainment and enhancement of the IMS infrasound network. 11204-. *Geophysical Research Abstracts*, Vol. 14.EGU General Assembly 2012.

Marty, J. (2019). The IMS Infrasound Network: Current Status and Technological Developments, in: *Infrasound Monitoring for Atmospheric Studies – Challenges in Middle-atmosphere Dynamics and Societal Benefits*, edited by: Le Pichon, A., Blanc, E., and Hauchecorne, A., 3–62, Springer, https://doi.org/10.1007/978-3-319-75140-5_1.

Marty, J., Doury, B., and Kramer, A. (2021). Low and High Broadband Spectral Models of Atmospheric Pressure Fluctuation, *Journal of Atmospheric Oceanic Technology*, 38, 1813–1822, https://doi.org/10.1175/jtech-d-21-0006.1

Mason, B. G., Pyle, D. M., Dade, W. B., and Jupp, T. (2004). Seasonality of volcanic eruptions, *Journal of Geophysical Reshearch*, 109, B04206, doi:10.1029/2002JB002293.

Matos, S. (2018) - *The use of infrasound in volcano monitoring. Contribution for future application in the Azores Islands.* Dissertação de Mestrado em Vulcanologia e Riscos Geológicos, Faculdade de Ciências e Tecnologia, Universidade dos Açores.

Matos, S., Wallenstein, N., Marchetti, E., and Ripepe, M. (2020). Location of Stromboli volcano July 2019 paroxysm event based on long-range infrasound detections in several IMS stations, EGU General Assembly 2020, Online, 4–8 May 2020, EGU2020-10156, https://doi.org/10.5194/egusphere-egu2020-10156, 2020

Matos, S., Wallenstein, N., Marchetti, E., and Ripepe, M. (2020). Location of Stromboli volcano July 2019 paroxysm event based on long-range infrasound detections in several IMS stations, EGU General Assembly 2020, Online, 4–8 May 2020, EGU2020-10156, https://doi.org/10.5194/egusphere-egu2020-10156

Matoza, R., Hedlin, M., Garcés, M. (2007). An infrasound array study of Mount St. Helens. *Journal of Volcanology and Geothermal Research*, 160, 249–262.

Matoza, R. S., Vergoz, J., le Pichon, A., Ceranna, L., Green, D. N., Evers, L. G., Ripepe, M., Campus, P., Liszka, L., Kvaerna, T., Kjartansson, E., & Höskuldsson, Á. (2011a). Long-range acoustic observations of the Eyjafjallajökull eruption, Iceland, April-May 2010. *Geophysical Research Letters*, *38*(6), n/a-n/a. https://doi.org/10.1029/2011GL047019

Matoza, R., Le Pichon A., Vergoz J., Herry P., Lalande J. M., Lee H., Che I., Rybin A. (2011b). Infrasonic observations of the June 2009 Sarychev Peak eruption, Kuril Islands: Implications for infrasonic monitoring of remote explosive volcanism. *Journal of Volcanology and Geothermal Research*. 200. 35-48. DOI: 10.1016/j.jvolgeores.2010.11.022.

Matoza, R. S., Landès M., Le Pichon, A., Ceranna L., Brown, D. (2013). Coherent ambient infrasound recorded by the International Monitoring System. *Geophysical Research Letters*. 40. 429-433. DOI:10.1029/2012GL054329.

Matoza, R. S., Green, D. N., Le Pichon, A., Shearer, P. M., Fee, D., Mialle, P., & Ceranna, L. (2017). Automated detection and cataloging of global explosive volcanism using the International Monitoring System infrasound network. *Journal of Geophysical Research: Solid Earth*, *122*(4), 2946–2971. https://doi.org/10.1002/2016JB013356

Matoza, R., Fee D., Green D., Mialle P. (2019). Volcano Infrasound and the International Monitoring System. In: Le Pichon A., Blanc E., Hauchecorne A. (eds) *Infrasound Monitoring for Atmospheric Studies - Challenges in Middle Atmosphere Dynamics and Societal Benefits*. Springer, Cham. DOI: 10.1007/978-3-319-75140-5_33.

Matoza, R.S., Roman, D.C. (2022). One hundred years of advances in volcano seismology and acoustics. *Bulletin of Volcanol*ogy, 84, 86. https://doi.org/10.1007/s00445-022-01586-0

Mauk, F. J. (1983). Utilization of seismically recorded infrasonic-acoustic signals to monitor volcanic explosions: The El Chichon Sequence 1982—A case study, *Journal of Geophysical Research*, 88 (B12), 10385–10401, DOI:10.1029/JB088iB12p10385.

McKee, K., Fee, D., Yokoo, A., Matoza, R. S., & Kim, K. (2017). *Analysis of gas jetting and fumarole acoustics at Aso Volcano, Japan. Journal of Volcanology and Geothermal Research, 340, 16–29.* doi: 10.1016/j.jvolgeores.2017.03.029.

Mialle, P. (2007). *Contribution d'un modèle 3D de trace de rayons dans un milieu complexe pour la localisation de sources infrasonores*. *Unpublished Doctor Thesis*. Université de Nice Sophia-Antipolis, France.

Mialle, P., Brachet, P., Gaillard, A., Le Pichon, A., Blanc, D., Tailpied, E., & Friha, N. (2015). Towards a volcanic notification system with infrasound data: Use of infrasound data in support of the VAACs in the framework of ARISE project. In *World meteorological organization 7th international workshop on volcanic ash (IWVA/7)*, Anchorage, Alaska.

Mialle, P., Brown, D., and Arora, N. (2019). Advances in Operational Processing at the International Data Centre, in: *Infrasound Monitoring for Atmospheric Studies – Challenges in Middle-atmosphere Dynamics and Societal Benefits*, edited by: Le Pichon, A., Blanc, E., and Hauchecorne, A., 209–248, Springer, https://doi.org/10.1007/978-3-319-75140-5_6.

Moran, S., Matoza, R., Garces, M., Hedlin, M., Bowers, D., Scott, W., Sherrod, D. & Vallance, J. (2008). Seismic and acoustic recordings of an unusually large rockfall at Mount St. Helens, Washington. *Geophysical Research Letters*, 35 (19).

Morrissey, M. & Chouet, B. (1997). Burst conditions of explosive volcanic eruptions recorded on microbarographs. *Science,* 275 (5304): 1290 1293.

Morrissey, M.M. & Mastin, L.G. (2000). Vulcanian eruptions, in *Encyclopedia of Volcanoes*, pp. 463–475, ed. Sigurdsson, H., Academic Press.

Muench, H. S. (1965). Stratospheric Energy Processes and Associated Atmospheric Long-Wave Structure in Winter. *Environmental Research Papers* (No. 95). University of Washington. Seattle.

Murayama, N. (1968). Propagation of atmospheric pressure waves produced by the explosion of volcano Bezymianny of March 30, 1956 and transport of the volcanic ashes. Q. J. Seismol. 33, 1–11 *(PDF) Atmospheric pressure waves in the field of volcanology*.

Mutschlecner, J. & Whitaker, R. (2005). Infrasound from earthquakes. *Journal of Geophysical Research: Atmospheres,* 110(1):1–11. https://doi.org/10.1029/2004JD005067.

Needham, C.E. (2010). Blast Wave Propagation. In: *Blast Waves. Shock Wave and High Pressure Phenomena*. Springer, Berlin, Heidelberg. https://doi.org/10.1007/978-3-642-05288-0_7.

Newhall, C.G., Self, S., (1982). The volcanic explosivity index (VEI): an estimate of explosive magnitude for historical volcanism. *Journal of Geophysical Research*. 87, 1231e1238.

Nishida, K., Ichihara M. (2016). Real-time infrasonic monitoring of the eruption at a remote island volcano using seismoacoustic cross correlation. *Geophysical Journal International*. 204. 748-752. https://doi.org/10.1093/gji/ggv478.

Olson, J. V., R. W. Wilson, and R. A. Hanson (2003). Infrasound associated with the 2002 Denali fault earthquake, Alaska, *Geophysical Research Letters*, 30(23), 2195, doi:10.1029/2003GL018568.

Omori, F. (1912). The eruptions and earthquakes of the Asama-yama. Bulletin of the Imperial Earthquake Investigation Committee, 6(1), 1–147.

Pallister, J., McNutt, S.R. (2015). Synthesis of Volcano Monitoring, Chapter 66 of *Encyclopedia of Volcanoes, 2nd Edition*, Sigurdsson, H., B. Houghton, S.R. McNutt, H. Rymer, and J. Stix (eds.), Elsevier, p. 1151-1171.

Pasko, V. (2012). Infrasonic waves generated by supersonic auroral arcs. *Geophysical Research Letters*, 39(19). https://doi.org/10.1029/2012GL053587.

Pavlovski, O. A. (1998). "Radiological Consequences of Nuclear Testing for the Population of the Former USSR (Input Information, Models, Dose, and Risk Estimates)". *Atmospheric Nuclear Tests*. Springer Berlin Heidelberg. pp. 219–260. doi:10.1007/978-3-662-03610-5_17. ISBN 978-3-642-08359-4.

Perret, F. (1950). *Volcanological Observations*. Carnegie Institution of Washington Publication 549, Washington, D. C., 1950.

Perttu, A., Taisne, B., De Angelis, S., Assink, J.D., Tailpied, D., Williams, R.A. (2020). Estimates of plume height from infrasound for regional volcano monitoring. *Journal of Volcanology and Geothermal Research*, 402:106997. https://doi.org/10.1016/j.jvolgeores.2020.106997.

Petersen, T., De Angelis, S., Tytgat, G., & McNutt, S. (2006). Local infrasound observations of large ash explosions at Augustine Volcano, Alaska, during January 11–28, 2006, *Geophysical Research Letters*, 33, L12303, Doi: 10.1029/2006GL026491.

Petersen, Jon & Sölveling, Gustaf & Clarke, John-Paul & Johnson, Ellis & Shebalov, Sergey. (2012). An Optimization Approach to Airline Integrated Recovery. *Transportation Science*. 46. 482-500. 10.2307/23362876.

Picone, J. M., A. E. Hedin, D. P. Drob, A. C. Aikin (2002). NRLMSISE-00 empirical model of the atmosphere: Statistical comparisons and scientific issues. *Journal of Geophysical Research*, 107(A12). 1468. DOI:10.1029/2002JA009430.

Pierce, A. (1981). *Acoustics: An Introduction to Its Physical Principles and Applications*. McGraw-Hill. ISBN 0-07-049961-6.

Pilger, C., Gaebler, P., & Ceranna, L. (2018). Real-time infrasound processing with the PMCC algorithm and a dedicated processing pipeline. In *CTBT: Science and Technology 2017 Conference (SnT2017)*. CTBTO Preparatory Commission.

Pilger, C., Gaebler, P., Hupe, P., Ott, T., and Drolshagen, E. (2020). Global Monitoring and Characterization of Infrasound Signatures by Large Fireballs, *Atmosphere*, 11, 83, https://doi.org/10.3390/atmos11010083.

Ponceau, D., & L. Bosca, L. (2010). Low-Noise Broadband Microbarometers, In: A. Le Pichon, E. Blanc and A. Hauchecorne, Eds., *Infrasound Monitoring for Atmospheric Studies*, Springer, Berlin, 2010, pp. 119-139. doi:10.1007/978-1-4020-9508-5_4

Posmentier, E.S., (1967). A theory of microbaroms. *Geophysical Journal of the Royal Astronomical Society*, 13:487–501.

Posmentier, E. (1971). Preliminary observations of 1–16 Hz natural background infrasound and signals from Apollo 14 and aircraft. *Geophysical Journal of the Royal Astronomical Society*, 26:173–177.

Procunier, R. W. (1971). *Observations of Acoustic Aurora in the 1-16 Hz Range. Geophysical Journal of the Royal Astronomical Society, 26(1-4), 183–189.* doi:10.1111/j.1365-246x.1971.tb03392.x

Pyle, D.M. (2000). Sizes of volcanic eruptions. In: Sigurdsson H et al. (eds) *Encyclopedia of volcanoes*. Academic Press, pp 263–269.

Reed, J. (1987). Air pressure waves from Mount St. Helens eruptions. *Journal of Geophysical Research*, 92 (D10), 11979–11982.

ReVelle, D. (1796). On meteor-generated infrasound, *Journal of Geophysical Research*, 81, 1217–1237.

Richards, A.F. (1963). Volcanic sounds, investigation and analysis. *Journal of Geophysical Research: Solid Earth*, 68:919–928.

Richardson, J., Fitzgerald, K., Waite, G., & Pennington, W. (2010). Acoustic and seismic observations of calving events at Bering Glacier, Alaska. *Special Paper of the Geological Society of America, 462*, 327-335. http://doi.org/10.1130/2010.2462(17).

Ripepe, M., Poggi, P., Braun, T., Gordeev, E. (1996). Infrasonic waves and volcanic tremor at Stromboli. *Geophysical Research Letters*, 23(2):181–184.

Ripepe, M., Coltelli, M., Privitera, E., Gresta, S., Moretti, M. & Piccinini, D. (2001b). Seismic and infrasonic evidences for an impulsive source of the shallow volcanic tremor at Mt. Etna, Italy. *Geophysical Research Letters,* 28 (6): 1071–1074.

Ripepe, M., Harris, A. & Carniel, R. (2002a). Thermal, seismic and infrasonic evidences of variable degassing rates at Stromboli volcano. *Journal of Volcanology Geothermal Research*, 118(3– 4), 285–297.

Ripepe, M., Marchetti, E. (2002b). Array tracking of infrasonic sources at Stromboli volcano. *Geophysical Research Letters*, 29 (22). 2076. 181-184. American Geophysical Union. DOI: 10.1029/2002GL015452.

Ripepe, M., Marchetti, E. & Ulivieri G. (2007). Infrasonic monitoring at Stromboli volcano during the 2003 effusive eruption: Insights on the explosive and degassing process of an open conduit system. *Journal of Geophysical Research*, 112, B09207, doi:10.1029/2006JB004613.

Ripepe, M. & Delle Donne, D. & Harris, A. & Marchetti, E. & Ulivieri, G. (2008). Dynamics of Strombolian Activity. Washington DC. *American Geophysical Union Geophysical Monograph Series*. 182. 39-48. 10.1029/182GM05.

Ripepe, M., De Angelis, S., Lacanna, G. & Voight, B. (2010a). Observation of infrasonic and gravity waves at Soufrière Hills Volcano, Montserrat. *Geophysical Research Letters*, 37, L00E14, doi:10.1029/ 2010GL042557.

Ripepe, M., Marchetti, E., Bonadonna, C., Harris, A., Pioli, L. & Ulivieri, G. (2010b). Monochromatic infrasonic tremor driven by persistent degassing and convection at Villarrica Volcano, Chile. *Geophysical Research Letters*, 37, L15303. http://dx.DOI.org/ 10.1029/2010gl043516.

Ripepe, M., Bonadonna, C., Folch, A., Delle Donne, D., Lacanna, G., Marchetti, E., Höskuldsson, A. (2013). Ash-plume dynamics and eruption source parameters by infrasound and thermal

imagery: the 2010 Eyjafjallajökull eruption. *Earth and Planetary Science Letters*, 366:112–121. https://doi.org/10.1016/j.epsl.2013.02.005.

Ripepe, M., Marchetti, E., Delle Donne, D., Genco, R., Innocenti, L., Lacanna, G., Valade, S. (2018). Infrasonic early warning system for explosive eruptions. *Journal of Geophysical Research: Solid Earth*, 123(11):9570–9585. https://doi.org/10.1029/2018JB015561.

Rowe, C., Aster, R., Kyle, P., Dibble, R. & Schlue, J. (2000). Seismic and acoustic observations at Mount Erebus Volcano, Ross Island, Antarctica. *Journal of Volcanology Geothermal Research,* 101(1– 2): 105– 128.

Ruiz, M., Lees, J. & Johnson, J. (2006). Source constraints of Tungurahua volcano explosion events. *Bulletin of Volcanology* 68 (5): 480–490.

Runco, A., Le Pichon, A., Durante, F., & Gualtieri, L. (2014). Probing the atmosphere using infrasound: New insights from the 2009–2010 sudden stratospheric warming. Journal of Geophysical Research: Atmospheres, 119(24), 13,853–13,871. doi.org

Sabatini, R., Bailly C., Marsden O., Gainville O. (2016). Characterization of absorption and non-linear effects in infrasound propagation using an augmented Burgers' equation, *Geophysical Journal International*. 207 (3). 1432–1445, https://doi.org/10.1093/gji/ggw350.

Schwaiger, Hans & Iezzi, Alexandra & Fee, David. (2019). AVO-G2S: A modified, open-source Ground-to-Space atmospheric specification for infrasound modeling. *Computers & Geosciences*. 125. 10.1016/j.cageo.2018.12.013.

Scott, K.M., Macias, J.L., Vallance, J.W., Naranjo, J.A., Rodriguez, S., McGeehin, J.P. (2001). Catastrophic debris Flows transformed from landslides in volcanic terrains: mobility, hazard assessment, and mitigation strategies. *United States Geological Survey Professional Pappers* 1630, 67 pp., 19 pgs., 9 tabs.

Scott, E., Hayward, C., Kubichek, R., Hamann, J., Pierre, J., Comey, B. & Mendenhall, T. (2007). Single and multiple sensor identification of avalanche-generated infrasound. Cold Regions. *Science and Technology,* 47(1–2 SPEC. ISS.), 159–170. https://doi.org/10.1016/j.coldregions.2006.08.005.

Scott, Julian & Blanc-Benon, Philippe & Gainville, Olaf. (2017). Weakly nonlinear propagation of small-wavelength, impulsive acoustic waves in a general atmosphere. *Wave Motion*. 72. 10.1016/j.wavemoti.2016.12.005.

Siebert, L., Simkin, T., & Kimberly, P. (2010). *Volcanoes of the World*. University of California Press.

Silber, E., Brown, P. & Krzeminski, Z. (2015). Optical observations of meteors generating infrasound: Weak shock theory and validation. *Journal of Geophysical Research: Planets*, 120(3), 413–428. https://doi.org/10.1002/2014JE004680.

Simkin, T., & Fiske, R. S. (1983). KRAKATAU 1883: A Centennial Retrospective on the Eruption and its Atmospheric Effects. *Weatherwise*, *36*(5), 244–254.

Smets, P. S. M., Assink, J. D., Le Pichon, A., & Evers, L. G. (2016). ECMWF SSW forecast evaluation using infrasound. *Journal of Geophysical Research: Atmospheres*, *121*(9), 4637–4650. https://doi.org/10.1002/2015JD024251

Smets, P. (2018). Infrasound and the Dynamical Stratosphere: A new application for operational weather and climate prediction. *Doctoral thesis*. Faculty of Civil Engineering and Geoscience.

Delft University of Technology. https://doi.org/10.4233/uuid:517f8597-9c24-4d01-83ed-0f430353e905.

Sutherland, L. C., Bass, H. E. (2004). Atmospheric absorption in the atmosphere up to 160 km. *The Journal of the Acoustical Society of America,* 115. 1012-1032. https://doi.org/10.1121/1.1631937.

Symons, G. (1888). *The eruption of Krakatoa and subsequent phenomena*, Trübner, London.

Taddeucci, J., Edmonds, M., Houghton, B., James, M. R., & Vergniolle, S. (2015). Hawaiian and Strombolian Eruptions. *The Encyclopedia of Volcanoes*, 485–503. doi:10.1016/b978-0-12-385938-9.00027-4.

Tahira, M. (1982). A study of the infrasonic wave in the atmosphere: (II) Infrasonic waves generated by the explosions of the Volcano Sakurajima. *Journal of the Meteorological Society of Japan*, 60 (3): 896–907.

Tahira, M. (1988). A study of the long range propagation of infrasonic waves in the atmosphere. I, Observation of the volcanic infrasonic waves propagating through the thermospheric duct. *Journal of the Meteorological Society of Japan,* vol. 66:17-26.

Tahira, M., Nomura, M., Sawada, Y. & Kamo, K. (1996). Infrasonic and acoustic-gravity waves generated by the Mount Pinatubo eruption of June 15, 1991. In: Newhall, C.G., Punongbayan, R.S. (Eds.), *Fire and Mud*. University of Washington Press, Seattle, pp. 601–614.

Tailpied D., Le Pichon A., Marchetti E., Ripepe M., Kallel M., Ceranna L., Brachet N. (2013). Remote Infrasound Monitoring of Mount Etna: Oserved and Predicted Network Detection Capability. *InfraMatics*. 2. 1-11. DOI: 10.4236/inframatics.2013.21001.

Taisne, B., Perttu, A., Luo, Y., De Angelis, S. (2025). The Use of Infrasound in Volcano Monitoring. In: Spica, Z., Caudron, C. (eds) Modern Volcano Monitoring. *Advances in Volcanology*. Springer, Cham. https://doi.org/10.1007/978-3-031-86841-2_7

Tsuya, H., 1955. Geological and petrological studies of volcano Fuji, V. *Bulletin of the Earthquake Research Institute*, Tokyo 33, 341 and 383.

Ulivieri, G., Ripepe, M., Marchetti, E. (2013) Infrasound reveals transition to oscillatory discharge regime during lava fountaining: implications for early warning. *Geophysical Research Letters*, 40(12):3008–3013. https://doi.org/10.1002/grl.50592.

Verbeek (1884) The Krakatoa eruption. *Nature*, 30(757):10–15.

Vergniolle, S. and Brandeis, G. (1994). Origin of the sound generated by Strombolian explosions. *Geophysical Research Letters,* 21 (18): 1959–1962. http://dx.DOI.org/ 10.1029/94gl01286.

Vergniolle, S., Caplan-Auerbach, J. (2006) Basaltic thermals and subplinian plumes: constraints from acoustic measurements at Shishaldin volcano, Alaska. *Bulletin of Volcanology*, 68(7–8):611–630.

Vergoz J., Le Pichon A., Millet C. (2019). The Antares Explosion Observed by the USArray: An Unprecedented Collection of Infrasound Phases Recorded from the Same Event. In: Le Pichon, A., Blanc, E., Hauchecorne, A. (eds) *Infrasound Monitoring for Atmospheric Studies*. Springer, Cham. https://doi.org/10.1007/978-3-319-75140-5_9.

Vergoz, J., Hupe, P., Listowski, C., Le Pichon, A., Garcés, M. A., Marchetti, E., et al. (2022). IMS observations of infrasound and acoustic-gravity waves produced by the January 2022 volcanic

eruption of Hunga, Tonga: A global analysis. *Earth and Planetary Science Letters*, 591, 117639. https://doi.org/10.1016/j.epsl.2022.117639

Walker, G.P.L. (1973). Explosive volcanic eruptions - a new classification scheme. *Geologische Rundschau*, 2:431–446.

Walker, G.P.L. (1980). The Taupo pumice: product of the most powerful known (ultraplinian) eruption? *Journal of Volcanology and Geothermal Research,* 8:69–94.

Walker, K. T., Hedlin M. A. H., de Groot-Hedlin C., Vergoz J., Le Pichon A., Drob P. (2010a). Source location of the 19 February 2008 Oregon bolide using seismic networks and infrasound arrays. *Journal of Geophysical Research*. 115. B12329. DOI:10.1029/2010JB007863.

Walker, K., Hedlin, M. (2010b). A review of wind-noise reduction methodologies. In: Le Pichon A., Blanc E., Hauchecorne A. (eds) *Infrasound Monitoring for Atmospheric Studies*. Springer, Dordrecht. DOI: https://doi.org/10.1007/978-1-4020-9508-5_5.

Wallenstein, N., Gaspar, J.L., Kramer, A., Carvalho, J., Campus, P., Haralabus, G., Gregório, J., and IS42 Team (2011). IS42 Graciosa (Azores): A new IMS certified infrasound station in the North Atlantic. *European Geosciences Union General Assembly 2011*, Vienna, Austria, 03 – 08 April (Poster). *Geophysical Research Abstracts*, Vol. 13, EGU2011–12386.

Wallenstein, N. & Campus, P. (2017). IS42 station: infrasound "sentinel" on the North Atlantic - Fourth ARISE2 Workshop Science Meeting / GRIF-RUN 2017. *Geophysical Research Infrastructures Forum*, La Reunion Island (France), 2-6 October 2017 (poster).

Watson, L.M., Iezzi, A.M., Toney, L. (2022). Volcano infrasound: progress and future directions. *Bulletin of Volcanology,* 84, 44 https://doi.org/10.1007/s00445-022-01544-w.

Waxler, R., Hetzer C., Velea, D. (2015). *Atmospheric Infrasound Propagation* Package Version 1.1.

Waxler, R., Assink, J., Velea, D. (2017). Modal expansions for infrasound propagation and their implications for ground-to-ground propagation. *The Journal of the Acoustical Society of America*, 141 (2). 1290-1307. http://dx.doi.org/10.1121/1.4976067.

Waythomas, C. F., W. E. Scott, S. G. Prejean, D. J. Schneider, P. Izbekov, and C. J. Nye (2010). The 7–8 August 2008 eruption of Kasatochi Volcano, central Aleutian Islands, Alaska, *Journal of Geophysical Research*, 115, B00B06, doi:10.1029/2010JB007437.

Whipple, F. (1930). The great Siberian meteor and the waves, seismic and aerial, which it produced. *Royal Meteorological Society Quarterly Journa*l 56:287-304.

Whitaker, S. (1996). The Forchheimer equation: A theoretical development. *Transport in Porous Media*. 25. 27–61. https://doi.org/10.1007/BF00141261.

Whitaker, R. W., & J. P. Mutschlecner (2008). A comparison of infrasound signals refracted from stratospheric and thermospheric altitudes, *Journal of Geophysical Research*, 113, D08117, doi:10.1029/2007JD008852.

Wilson, C. (1967). Infrasonic pressure waves from aurora: a shock wave model. *Nature* 216, (131–133).

Wilson, C. (1971). Auroral Infrasonic Waves and Poleward Expansions of Auroral Substorms at Inuvik, N.W.T., Canada. *Geophysical Journal of the Royal Astronomical Society*, 26: 179–181. DOI:10.1111/j.1365-246X.1971.tb03391. x.

Wilson, D. K. (2003). The sound-speed gradient and refraction in the near-ground atmosphere. *The Journal of the Acoustical Society of America*, 113. 750-757. https://doi.org/10.1121/1.1532028.

Wilson, C. Olson, J., & Stenbaek-Nielsen, H. (2005). High trace-velocity infrasound from pulsating auroras at Fairbanks, Alaska. *Geophysical Research Letters*, 32, L14810, doi:10.1029/2005GL023188.

Wilson, C. R., Olson, J. V., Szuberla, C. A. L., McNutt, S., Tytgat, G., & Drob, D. P. (2006). Infrasonic array observations at I53US of the 2006 Augustine Volcano eruptions. *Inframatics*, no. 13, p. 11-25.

Worland, R. S., & Wilson, D. D. (1999). The speed of sound in air as a function of temperature. *The Physics Teacher*, 37(1), 53–57. https://doi.org/10.1119/1.880153.

Woulff, G., McGetchin, TR. (1976). Acoustic noise from volcanoes: theory and experiment. *Geophysical Journal of the Royal Astronomical Society*, 45:601–616.

Wright, W. M. (1983). Propagation in air of *N* waves produced by sparks. *The Journal of the Acoustical Society of America*, 73. 1948-1955. https://doi.org/10.1121/1.389585.

Yamamoto, R. (1954). Paper XIV: The microbarographic oscillations produced by the explosions of hydrogen-bombs (The radioactive dust from the nuclear detonation). Bulletin of the Institute for Chemical Research, Kyoto University**32 (Supplementary Issue), 120–133.

Yokoo, A., T. Tameguri, and M. Iguchi (2009). Swelling-up of lava plug associated with Vulcanian eruption at Sakurajima Volcano, as revealed by infrasound record - Case study on eruption on January 2, 2007, *Bulletin of Volcanology*, 71, 619–630.

Yokoyama, I. (1981). A geophysical interpretation of the 1883 Krakatau eruption. *Journal of Volcanology and Geothermal Research*. 9, 359–378.

Young, J. & Greene, G. (1982). Anomalous infrasound generated by the Alaskan earthquake of 28 March 1964. *The Journal of the Acoustical Society of America*, 71:334–339.

WEBGRAPHY

Alaska Volcano Observatory. Available at https://avo.alaska.edu/. [accessed between 2021-2025]

Atmospheric Layers (2017). National Aeronautics and Space Administration - NASA Available at Earth's Atmosphere: A Multi-layered Cake - NASA Science [accessed on 07/09/2022]

Commissariat à l'energie Atomique et aux Energies Alternatives, Departement Analyse,Surveillance, Environnement CEA/DASE. Available at www-dase.cea.fr [accessed on 12/10/2021]

CTBTO Web Portal – Secure Web Portal – Available at https://access.ctbto.org/portal/index.html. [accessed between 2021 -2025]

Global Volcanism Program, 2025. [Database] Volcanoes of the World (v. 5.2.6; 5 Feb 2025). Distributed by Smithsonian Institution, compiled by Venzke, E. https://doi.org/10.5479/si.GVP.VOTW5-2024.5.2. [accessed between 2021 -2025]

Hetzer, C.H., Drob, D.P., and Zabel, K. (2019). The NCPA-G2S Request System. https://g2s.ncpa.olemiss.edu. [accessed between 2023- 2024].

Infrasound Laboratory University of Hawaii. Available at https://www.isla.hawaii.edu/. [accessed 20/5/2023]

Kamchatka Volcanic Eruption Response Team. Available at http://www.kscnet.ru/ivs/kvert/z. [accessed 20/5/2023]

MATLAB overview (2023). Available at https://www.mathworks.com/products/matlab, [accessed on 18/02/2023]

National Oceanic and Atmospheric Administration – NOAA. (2017). Layers of the Atmosphere. Available at: https://www.srh.noaa.gov/jetstream/atmos/layers.html [accessed 12/08/2022]

Preparatory Commission for the Comprehensive Nuclear-Test-Ban Treaty Organization – CTBTO (2021). The treaty. Available at: https://www.ctbto.org/the-treaty [accessed on 08/10/2021]

Salinas, L. (2010). United Airlines Flight Dispatch, Congressional Hazards Caucus, Available at http://www.agiweb.org.

SREA 2024 – Serviço Regional de Estatística dos Açores. Available at: https://srea.azores.gov.pt

Siebert, L., Simkin, T. (2002). Volcanoes of the world: an illustrated catalogue of Holocene volcanoes and their eruptions, Smithsonian Institution, Global Volcanism Program digital information series, GVP-3. [accessed 10/04/2022]

Space Research Institute Russian Academy of Sciences. Available at http://jr.rse.cosmos.ru.

Volcano Research Centre, ERI, Univ. TOKYO. Available at https://www.eri.u-tokyo.ac.jp/VRC/index_E.html. [accessed 10/11/2021].

Annexes

Annex A

Algorithm Workflow

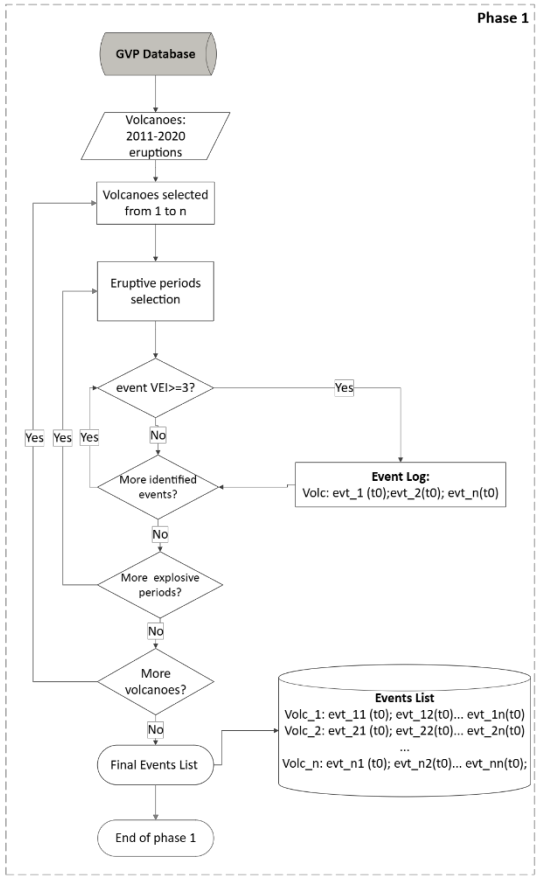

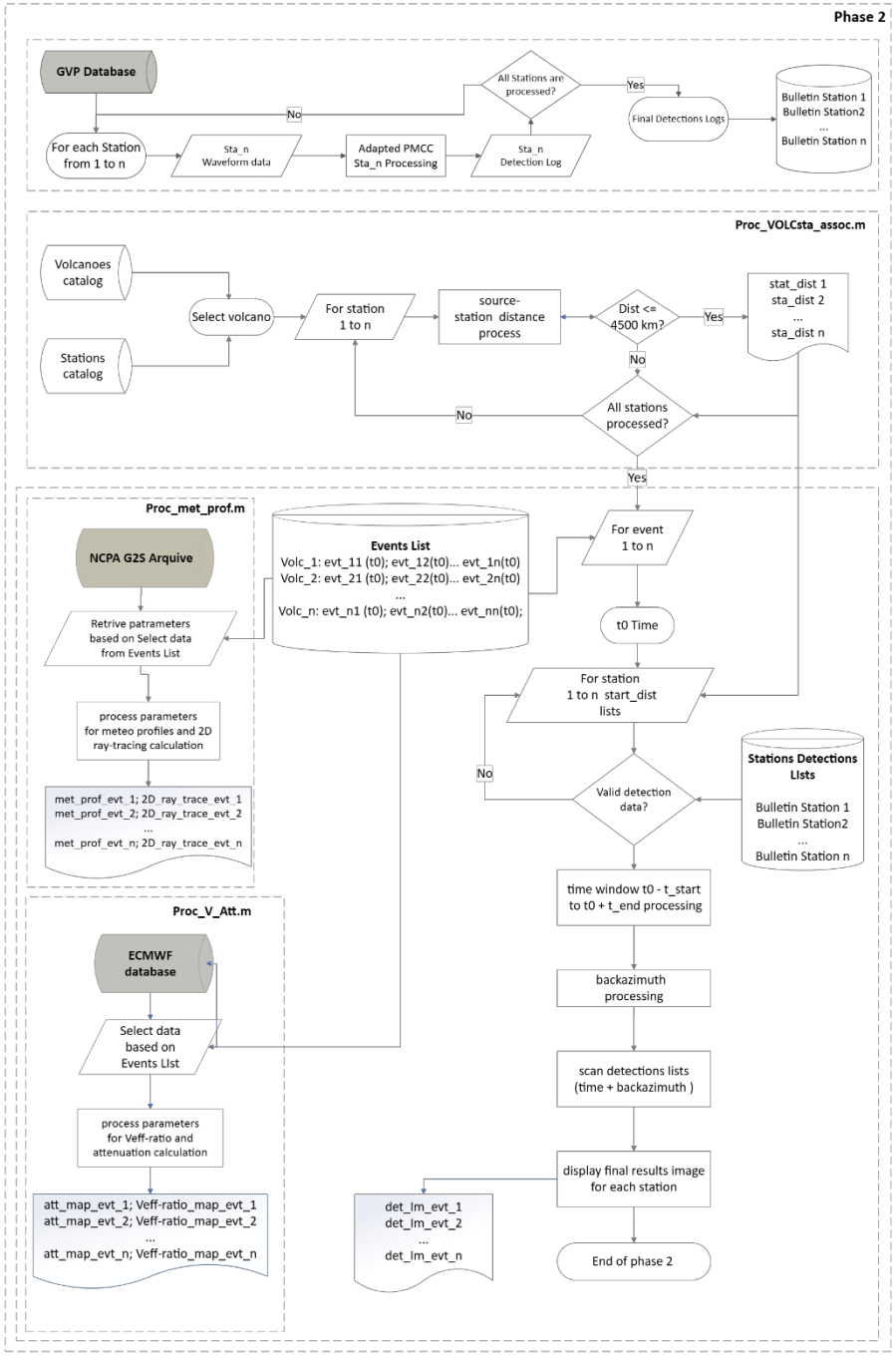

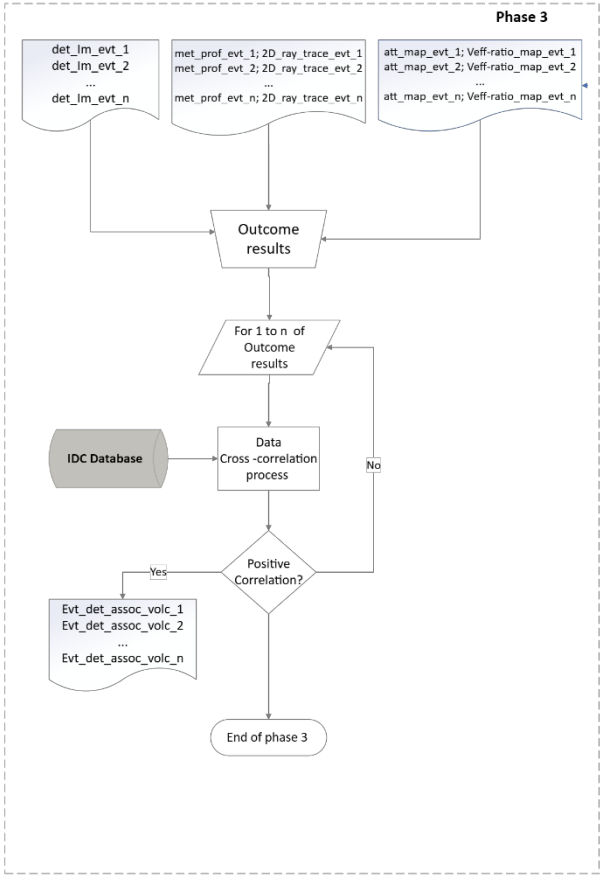

Workflow Illustrating the three Phases of the algorithm.*Proc_met_prof.m, Proc_V_Att.m and Proc_Volcsta_assoc.m* are elaborated scripts for data procedures.

Annex B

Events list

Table B – List of 186 discrete events analyzed by the algorithm, grouped according to volcanic regions. Each row includes the name of the associated volcano, the event date, the onset time (t_o), the VEI, detected (*yes* or *no*), the infrasound stations located within a 4500 km, and the final detection class assigned to the event.

n	group	Volcano_Name	Date (dd.mm.yyyy)	t0 (UTC)	VEI	event detect	1st sta	2nd sta	3rd sta	4th sta	5th sta	6th sta	7th sta	8th sta	9th sta	Class
1	1	Bezymianny	08.03.2012	21:40	3	no	-	-	-	-	-	-	-			H
2	1		01.09.2012	19:16	3	yes	+	-	+	+	+	-	-			A-C-E-F
3	1		15.12.2016	10:00	3	no	-	-	-	-	-	-	-			-
4	1		09.03.2017	03:23	3	no	-	-	-	-	-	-	-			H
5	1		16.06.2017	04:53	3	yes	+	+	-	-	-	-	-			A-C-H
6	1		20.12.2017	03:55	3	yes	+	-	-	+	-	-	-			A-B-H
7	1		20.01.2019	16:10	3	yes	++	-	-	++	-	-	-			A-B-F
8	1		15.03.2019	17:30	3	yes	-	-	++	++	-	-	-			B-F
9	1		21.10.2020	20:22	3	yes	+	-	-	+	-	-	-			A-B-F
10	1	Chikurachki	15.02.2015	22:00	3	yes	+	-	-	-	-	-	-			H
11	1	Chirinkotan	28.11.2016	14:00	3	yes	+	+	+	-	+	-	-			A-D-E-F
12	1		21.03.2017	04:20	3	yes	-	-	-	-	+	-	-			G-H
13	1		31.03.2017	11:46	3	yes	+	+	-	+	-	-	-			A-C-F
14	1	Kambalny	24.03.2017	21:20	3	no	-	-	-	-	-	-	-			H
15	1		02.04.2017	18:50	3	yes	+	-	+	-	-	-	-			A-B-H
16	1	Karymsky	03.06.2017	12:40	3	no	-	-	-	-	-	-	-			-
17	1		05.06.2017	05:50	3	yes	+	-	-	-	-	-	-			A
18	1		08.06.2017	21:20	3	no	-	-	-	-	-	-	-			-
19	1		24.06.2017	21:40	3	yes	+	-	-	-	-	-	-			A-B
20	1		26.06.2017	19:40	3	yes	+	-	-	-	-	-	-			A-B
21	1		03.07.2017	16:20	3	no	-	-	-	-	-	-	-			H
22	1		10.07.2017	19:10	3	yes	+	-	-	-	-	-	-			A-B-H
23	1		11.07.2017	17:30	3	yes	+	-	-	-	-	-	-			A-B
24	1		19.07.2017	12:30	3	no	-	-	-	-	-	-	-			H
25	1		27.07.2017	01:00	3	no	-	-	-	-	-	-	-			-
26	1		02.08.2017	22:10	3	no	-	-	-	-	-	-	-			-
27	1		08.08.2017	11:20	3	yes	+	+	-	++	-	-	-			A-B
28	1		09.08.2017	06:00	3	yes	+	+	-	-	-	+	-			A-C-F
29	1		12.08.2017	17:40	3	yes	+	+	-	-	-	++	-			A-C-H
30	1		19.09.2017	17:40	3	no	-	-	-	-	-	-	-			-
31	1		22.09.2017	21:30	3	no	-	-	-	-	-	-	-			-
32	1		03.12.2017	18:30	3	yes	-	-	-	+	+	-	-			G-H
33	1		14.12.2017	20:30	3	no	-	-	-	-	-	-	-			-
34	1		14.07.2018	21:20	3	no	-	-	-	-	-	-	-			-
35	1		08.11.2020	14:08	3	no	-	-	-	-	-	-	-			-
36	1	Klyuchevskoy	15.08.2013	06:30	3	yes	+	-	-	-	-	-	-			A-B
37	1		11.10.2013	08:20	3	yes	+	-	-	+	-	-	-			A-G-H
38	1		18.10.2013	06:05	3	yes	+	+	-	+	+	-	-			A-C-F-H
39	1		19.11.2013	02:16	3	no	-	-	-	-	-	-	-			-
40	1	Raikoke	21.06.2019	17:50	3	yes	+	+	-	-	-	-	-			A-C
41	1		21.06.2019	19:00	3	yes	++	+	++	-	-	-	-			A-C-H
42	1		21.06.2019	20:50	3	yes	+	+	+	-	-	-	-			A-C-D-H
43	1		21.06.2019	23:00	3	yes	-	+	+	+	-	+	-			C-E-F-H
44	1	Tolbachik	27.11.2012	16:30	3	yes	+	-	++	++	-	-	-			A-B-H
45	1	Zhupanovsky	06.06.2014	15:00	3	no	-	-	-	-	-	-	-			-
46	1		07.11.2014	21:55	3	yes	+	-	-	+	-	-	-			A-G
47	1		25.11.2014	00:14	3	yes	++	++	-	+	-	-	-			A-B-F-H
48	1		28.12.2014	23:30	3	no	-	-	-	-	-	-	-			-
49	1		08.03.2015	01:35	3	yes	+	-	-	+	-	-	-			A-B-F
50	1		25.03.2015	04:29	3	no	-	-	-	-	-	-	-			-
51	1		12.07.2015	20:38	3	no	-	-	-	-	-	-	-			-
52	1		30.11.2015	03:47	3	yes	+	-	-	+	-	-	-			A-H
53	1		19.01.2016	04:46	3	no	-	-	-	-	-	-	-			H
54	1		21.01.2016	05:46	3	yes	-	-	-	++	+	-	-			G-H
55	1		12.02.2016	20:22	3	no	-	-	-	-	-	-	-			H
56	1		20.11.2016	02:29	3	no	-	-	-	-	-	-	-			H

n	group	Volcano_Name	Date (dd.mm.yyyy)	t0 (UTC)	VEI	event detect	1st sta	2nd sta	3rd sta	4th sta	5th sta	6th sta	7th sta	8th sta	9th sta	Class
57	2	Asosan	07.10.2016	12:52	3	yes	+	-	-	++	-	-	-			A-B-F-H
58	2		07.10.2016	16:46	3	yes	+	+	-	+	-	-	-			A-C-F
59	2	Kirishimayama	26.01.2011	09:50	3	no	-	-	-	-	-	-	-			-
60	2		27.01.2011	06:41	3	yes	+	+	+	-	++	-	-			A-D-E-F
61	2		28.01.2011	03:47	3	yes	++	+	+	-	-	-	-			A-D
62	2		31.01.2011	22:54	3	yes	++	+	++	-	++	-	-			A-D-F
63	2		01.03.2018	02:00	3	no	-	-	-	-	-	-	-			H
64	2	Kuchinoerabujima	29.05.2015	00:59	3	yes	+	-	+	-	-	-	-	-		B-H
65	2		17.01.2019	00:20	3	yes	+	-	-	-	-	-	-	-		A-H
66	2		29.01.2019	08:00	3	no	-	-	-	-	-	-	-	-		-
67	2		02.02.2020	20:21	3	no	-	-	-	-	-	-	-	-		-
68	2	Ontakesan	27.09.2014	02:52	3	no	-	-	-	-	-	-	-	-		-
69	2	Soputan	02.07.2011	09:00	3	no	-	-	-	-	-	-				-
70	2		02.07.2011	22:00	3	yes	+	-	-	-	-	-				A
71	2		26.08.2012	11:36	3	no	-	-	-	-	++	-				G
72	2		05.01.2015	06:47	3	no	-	-	-	-	-	-				-
73	2		18.01.2015	03:38	3	no	-	-	-	-	-	-				-
74	2		07.03.2015	09:09	3	yes	++	-	-	-	-	-				A
75	2		04.01.2016	22:38	3	no	-	-	-	-	-	-				-
76	2		04.01.2016	12:53	3	yes	+	-	-	-	-	-				A-H
77	2		03.10.2018	00:47	3	no	-	-	-	-	-	-				-
78	2		15.12.2018	17:02	3	no	-	-	-	-	-	-				H
79	2	Taal	12.01.2020	07:00	4	yes	+	+	-	-	-	-	-			A-C-H
80	2		12.01.2020	08:00	4	yes	+	+	-	-	-	+	-			A-C-f-H
81	3	Ambae	06.09.2017	21:10	3	no	-	-	-	-	-	-	-			-
82	3		09.10.2017	18:02	4	no	-	-	-	-	-	-	-			-
83	3		10.10.2017	06:26	3	no	-	-	-	-	-	-	-			-
84	3		13.10.2017	08:15	3	no	-	-	-	-	-	-	-			-
85	3		15.10.2017	16:30	3	no	-	-	-	-	-	-	-			-
86	3		06.11.2017	21:58	3	no	-	-	-	-	-	-	-			-
87	3		23.02.2018	22:31	3	yes	+	+	-	-	-	-	-			A-C
88	3		18.03.2018	19:31	3	yes	+	-	-	-	-	-	-			A-H
89	3		30.03.2018	22:00	3	no	-	-	-	-	-	-	-			-
90	3		05.04.2018	14:00	3	yes	+	-	-	+	-	-	-			A-B
91	3		17.07.2018	00:30	3	no	-	-	-	-	-	-	-			-
92	3		17.07.2018	07:34	3	no	-	-	-	-	-	-	-			-
93	3		17.07.2018	11:02	3	no	-	-	-	-	-	-	-			-
94	3		26.07.2018	10:00	3	yes	+	+	-	-	-	-	-			A-B
95	3		27.07.2018	00:00	3	yes	+	-	-	-	-	-	-			A-B
96	3		01.09.2018	09:15	3	yes	+	+	-	-	-	-	-			A-C
97	3		30.10.2018	07:30	3	yes	+	+	-	-	+	-	-			A-C
98	3	Manam	12.01.2013	00:00	3	yes	-	-	-	-	-	-	++	-		G
99	3		14.04.2013	22:04	3	no	-	-	-	-	-	-	-	-		-
100	3		31.07.2015	01:30	4	yes	+	+	-	-	-	-	-	-		A-B
101	3		04.05.2017	07:00	3	no	-	-	-	-	-	-	-	-		H
102	3	Rabaul	28.08.2014	17:30	4	yes	-	+	+	-	-	-				C
103	3	Tinakula	20.10.2017	23:40	3	yes	-	+	-	-	-	-	-			-
104	3		20.10.2017	19:20	3	yes	+	+	-	-	-	-	-			A-C
105	3	Ulawun	25.06.2019	04:30	4	yes	+	+	-	-	-	-				A-C
106	4	Wolf	25.05.2015	06:58	4	no	-	-	-	-	-					-
107	5	Agung	25.11.2017	09:20	3	no	-	-	-	-	-					-
108	5		26.11.2017	21:50	3	no	-	-	-	-	-					
109	5	Kelud	13.02.2014	15:50	4	yes	+	-	+	+	+	-				A-C-F
110	5		13.02.2014	16:30	4	yes	+	+	-	+	+	-				A-C-F
111	5	Krakatau	25.06.2018	00:14	3	no	-	-	-	-	-					-
112	5		22.12.2018	14:30	3	no	-	-	-	-	-					H
113	5	Merapi	18.11.2013	21:53	3	no	-	-	-	-	-					-
114	5		27.03.2014	06:12	3	yes	+	+	-	-	-					A-C
115	5		11.05.2018	00:40	3	yes	-	-	++	+	-					G
116	5		20.05.2018	18:25	3	no	-	-	-	-	-					-
117	5	Paluweh	02.02.2013	15:00	3	no	-	-	-	-	-					-
118	5		09.08.2013	20:27	3	no	-	-	-	-	-					-
119	5	Sangeang Api	30.05.2014	07:55	4	yes	+	+	+	++	-					A-C-D
120	5		31.05.2014	14:42	3	no	-	-	-	-	-					A-H
121	5		31.05.2014	05:30	3	yes	+	-	-	-	-					A-H
122	5	Semeru	06.06.2017	23:50	4	no	-	-	-	-	++	-				-
123	5	Sinabung	18.11.2013	00:04	4	no	-	-	-							-
124	5		19.02.2018	01:53	4	yes	+	+	-							A-C
125	5		09.06.2019	09:28	4	yes	-	+	+							C

n	group	Volcano_Name	Date (dd.mm.yyyy)	t0 (UTC)	VEI	event detect	1st sta	2nd sta	3rd sta	4th sta	5th sta	6th sta	7th sta	8th sta	9th sta	Class
126	6	Nabro	12.06.2011	21:00	4	yes	-	+	-	+	-	+	-			B-E-H
127	7	Grimsvotn	21.05.2011	19:16	4	yes	-	+	+	++	+	-	+			C-E-H
128	8	Etna	11.01.2011	15:00	3	yes	+	-	-	-	-	-	-	-		A
129	8		12.01.2011	22:25	3	no	-	-	-	-	-	-	-	-		-
130	8		19.08.2011	00_02	3	yes	+	-	-	-	-	-	-	-		A
131	8		28.09.2011	14:00	3	yes	-	+	-	-	-	-	-	-		H
132	8		15.11.2011	10:55	3	no	-	-	-	-	-	-	-	-		-
133	8		08.02.2012	20:30	3	no	-	-	-	-	-	-	-	-		-
134	8		18.03.2012	06:00	3	no	-	-	-	-	-	-	-	-		-
135	8		31.03.2012	21:30	3	no	-	-	-	-	-	-	-	-		-
136	8		16.03.2013	17:15	3	no	-	-	-	-	-	-	-	-		H
137	8		03.04.2013	12:30	3	yes	+	+	-	-	+	-	-	-		A-C-H
138	8		08.04.2013	20:52	3	yes	+	-	-	-	+	-	-	-		A-H
139	8		20.04.2013	15:13	3	yes	-	-	+	-	+	-	-	-		B-F-H
140	8		03.12.2015	02:00	3	no	-	-	-	-	-	-	-	-		H
141	8		04.12.2015	09:00	3	yes	-	-	+	-	-	-	-	-		B-H
142	8		18.05.2016	10:50	3	yes	+	+	-	-	-	-	-	-		A-C-H
143	8		19.05.2016	06:00	3	yes	+	+	-	-	-	+	-	-		A-C-H
144	8		21.05.2016	03:15	3	yes	+	+	-	-	-	-	-	-		A-C
145	8		24.05.2016	23:00	3	yes	-	+	-	-	-	-	-	-		B-H
146	9	Bogoslof	21.12.2016	00:30	3	yes	+	-	-	-	-	-	-	-	-	A-F-H
147	9	Cleveland	02.06.2020	06:31	3	yes	+	+	-	-	-	-	-	-		A-C
148	9	Pavlof	13.05.2013	16:00	3	no	-	-	-	-	-	-	-	-		-
149	9		25.06.2013	06:50	3	no	-	-	-	-	-	-	-	-		-
150	9		31.05.2014	19:36	3	yes	+	-	-	-	-	-	-	-		A
151	9		05.06.2014	02:05	3	yes	+	-	-	-	-	-	+	-		A-F
152	9		12.11.2014	01:50	3	yes	++	-	-	-	-	++	++	-		G-H
153	9		28.03.2016	23:50	3	yes	+	-	-	-	-	-	-	-		A-C
154	9		28.03.2016	06:30	3	yes	+	+	-	-	-	-	-	-		A-C
155	9	Shishaldin	12.12.2019	16:00	3	yes	-	-	-	-	-	+	-	-		-
156	9		07.01.2020	14:00	3	yes	-	-	-	-	+	-	-	-		-
157	9		19.01.2020	08:28	3	yes	+	-	-	+	-	-	+	-		A-F
158	9	Veniaminof	30.08.2013	14:00	3	no	-	-	-	-	-	-	-	-		-
159	10	Colima	13.01.2013	18:15	3	no	-	-	-	-	-	-				-
160	10		29.01.2013	09:45	3	no	-	-	-	-	-	-				-
161	10		21.11.2014	19:15	3	no	-	-	-	-	-	-				-
162	10	San Miguel	29.12.2013	16:30	3	no	-	-	-	-	-	-				-
163	10	Turrialba	12.03.2015	17:00	3	no	-	-	-	-	-					-
164	10		12.03.2015	20:00	3	yes	-	+	-	-	-					C
165	11	Calbuco	22.04.2015	21:04	4	yes	-	-	-	++	-	+				G-H
166	11		23.04.2015	04:00	4	yes	+	-	-	+	++	+				A-B
167	11	Nevado del Ruiz	29.05.2012	08:00	3	no	-	-	-	-	-	-	-			-
168	11	Puyehue Cordon Caulle	04.06.2011	18:45	5	yes	-	+	+	-	+	-				G-H
169	11	Sabancaya	07.11.2016	02:26	3	no	-	-	-	-	-	-	-	-		-
170	11	Tungurahua	22.04.2011	20:12	3	no	-	-	-	-	-	-	-	-		-
171	11		25.04.2011	03:30	3	no	-	-	-	-	-	-	-	-		-
172	11		30.04.2011	07:12	3	yes	+	-	-	-	-	-	-	-		A-F
173	11		27.11.2011	22:18	3	yes	+	-	-	-	-	-	-	-		A
174	11		04.02.2012	10:50	3	yes	+	-	-	-	-	-	-	-		A
175	11		26.07.2012	12:00	3	no	-	-	-	-	-	-	-	-		-
176	11		05.08.2012	12:21	3	no	-	-	-	-	-	-	-	-		-
177	11		14.12.2012	19:36	3	no	-	-	-	-	-	-	-	-		-
178	11		16.12.2012	10:53	3	yes	+	-	-	-	-	+	-	-		A-F
179	11		14.07.2013	11:46	3	yes	-	+	-	+	-	-	-	-		B-F
180	11		01.02.2014	22:39	3	yes	+	-	-	-	+	+	-	-		A-B
181	11		01.02.2014	22:12	3	yes	-	-	-	-	-	-	-	-		G
182	11		04.04.2014	23:01	3	yes	-	-	-	++	-	-	-	-		H
183	11		04.04.2014	23:16	3	yes	-	-	-	++	-	-	-	-		H
184	11		26.02.2016	18:33	3	no	-	-	-	-	-	-	-	-		-
185	11	Villarrica	03.03.2015	06:10	3	yes	+	-	-	++	-	+				A-F
186	11		30.08.2017	12:24	3	no	-	-	-	-	-	-				-

Annex C

Volcanoes detection performance

Table C - Table presenting the eruptive period data for each volcano analysed. For each volcano, the table includes: the name, the eruptive period data, the detection status of each period (marked as **Det** for detected and **NDet** for not detected), and the overall detection outcome. Each case is categorised as **Detected** (all periods identified), **Partially Detected** (some periods identified), or **Not Detected** (none identified).

Volcano_Name	eruption time period	Eruption detected	Overall Detection
Northwest Pacific Volcanic Region			
Bezymianny	2012 Feb 12 - 2013 Jun 20	Det	Detected
	2016 Dec 5 - 2021 Feb 1	Det	
Chikurachki	2015 Feb 16 - 2015 Feb 18	Det	Detected
Chirinkotan	2016 Nov 29 - 2017 Apr 7	Det	Detected
Kambalny	2017 Mar 24 - 2017 Apr 23	Det	Detected
Karymsky	2017 Jun 4 - 2018 Sep 30	Det	Parciallyly Detected
	2020 Apr 1 - 2022 Aug 7	Ndet	
Klyuchevskoy	2013 Aug 15 - 2013 Dec 20	Det	Detected
Raikoke	2019 Jun 22 - 2019 Jul 1	Det	Detected
Tolbachik	2012 Nov 27 - 2013 Sep 5	Det	Detected
Zhupanovsky	2014 Jun 6 - 2015 Aug 6	Det	Parcially Detected
	2015 Nov 28 - 2016 Mar 25	Det	
	2016 Nov 20 - 2016 Nov 20	Ndet	
Western Pacific Volcanic Region			
Asosan	2016 Oct 7 - 2016 Nov 12	Det	Detected
Kirishimayama	2011 Jan 19 - 2011 Sep 7	Det	Parcially Detected
	2018 Mar 1 - 2018 Jun 22	Ndet	
Kuchinoerabujima	2015 May 29 - 2015 Jun 19	Det	Parciallyly Detected
	2018 Oct 21 - 2019 Feb 3	Det	
	2020 Jan 11 - 2020 May 13	Ndet	
Ontakesan	2014 Sep 27 - 2014 Oct 14	Ndet	Not Detected
Soputan	2011 Jul 3 - 2011 Aug 15	Det	Parciallyly Detected
	2012 Aug 26 - 2012 Sep 19	Ndet	
	2015 Jan 6 - 2015 Mar 9	Det	
	2016 Jan 2 - 2016 Feb 7	Det	
	2018 Oct 2 - 2018 Dec 16	Det	
Taal	2020 Jan 12 - 2020 Jan 22	Det	Detected
Southwest Pacific Volcanic Region			
Ambae	2017 Sep 6 - 2018 Oct 30	Det	Detected
Manam	2010 Aug 10 - 2013 Dec 15	Ndet	Parcially Detected
	2014 Jun 29 - 2018 Jan 10	Det	
Rabaul	2014 Jul 7 - 2014 Sep 18	Det	Detected
Tinakula	2017 Oct 21 - 2017 Oct 26	Det	Detected
Ulawun	2019 Jun 26 - 2019 Oct 5	Det	Detected

Volcano_Name	eruption time period	Eruption detected	Overall Detection
Eastern Pacific Volcanic Regions			
Wolf	2015 May 25 - 2015 Jul 16	Ndet	Not Detected
Sunda-Banda Volcanic Region			
Agung	2017 Nov 21 - 2019 Jun 13	Ndet	Not Detected
Kelud	2014 Feb 13 - 2014 Feb 15	Det	Detected
Krakatau	2018 Jun 18 - 2020 Apr 17	Ndet	Not Detected
Merapi	2013 Nov 18 - 2013 Nov 18	Ndet	Parcially Detected
	2014 Mar 9 - 2014 Apr 20	Det	
	2018 May 11 - 2020 Jun 21	Det	
Paluweh	2012 Oct 8 - 2013 Oct 31	Ndet	Not Detected
Sangeang Api	2014 May 30 - 2015 Nov 5	Det	Detected
Semeru	2017 Jun 6 - 2024 Dec 19 (ongoing)	Ndet	Not Detected
Sinabung	2013 Sep 15 - 2018 Jun 22	Det	Detected
	2019 Feb 6 - 2019 Jun 9	Det	
Eastern Africa Volcanic Region			
Nabro	2011 Jun 13 - 2012 Jun 3	Det	Detected
Atlantic Ocean Volcanic Region			
Grimsvotn	2011 May 21 - 2011 May 25	Det	Detected
European Volcanic Region			
Etna	2010 Aug 25 - 2013 Apr 27	Det	Detected
	2013 Sep 3 - 2022 Jun 17	Det	
North America Volcanic Region			
Bogoslof	2016 Dec 20 - 2017 Aug 30	Det	Detected
Cleveland	2020 Jun 1 - 2020 Jun 1	Det	Detected
Pavlof	2013 May 13 - 2013 Jun 26	Ndet	Parcially Detected
	2014 May 31 - 2014 Jun 6	Det	
	2014 Nov 12 - 2014 Nov 15	Det	
	2016 Mar 27 - 2016 Jul 30	Det	
Shishaldin	2019 Jul 23 - 2020 May 4	Det	Detected
Veniaminof	2013 Jun 13 - 2013 Oct 12	Ndet	Not Detected
Middle America-Caribbean Volcanic Region			
Colima	2013 Jan 6 - 2017 Mar 7	Ndet	Not Detected
San Miguel	2013 Dec 29 - 2014 Jul 28	Ndet	Not Detected
Turrialba	2015 Mar 8 - 2019 Dec 7	Det	Detected
South America Volcanic Region			
Calbuco	2015 Apr 22 - 2015 May 26	Det	Detected
Nevado del Ruiz	2012 Feb 22 - 2013 Jul 12	Ndet	Not Detected
Puyehue Cordon Caulle	2011 Jun 4 - 2012 Apr 21	Det	Detected
Sabancaya	2016 Nov 6 - 2024 Dec 19 (ongoing)	Ndet	Not Detected
Tungurahua	2011 Apr 20 - 2011 May 26	Det	Detected
	2011 Nov 27 - 2012 Sep 4	Det	
	2012 Dec 14 - 2016 Mar 16	Det	
Villarrica	2014 Dec 2 - 2024 Dec 13 (ongoing)	Det	Detected

UNIVERSIDADE DOS AÇORES
Faculdade de Ciências e Tecnologia

Rua da Mãe de Deus
9500-321 Ponta Delgada
Açores, Portugal

2025

Infrasound real-time long-range erupting volcanoes monitoring

Sandro Branquinho de Matos